3d Transition Metal and Lanthanoid Complexes of Tritopic C_3-Symmetric Ligands as Molecular Magnets to Advance the Basis for Quantum Technologies

DISSERTATION

zur Erlangung des akademischen Grades *doctor rerum naturalium* (Dr. rer. nat.)

vorgelegt dem Rat der Chemisch-Geowissenschaftlichen Fakultät der
Friedrich-Schiller-Universität Jena
von M. Sc. Benjamin Kintzel
geboren am 01.07.1990 in Erfurt

Gutachter:

1. Prof. Dr. Winfried Plass, Friedrich-Schiller-Universität Jena

2. Jun.-Prof. Dr. Robert Kretschmer, Friedrich-Schiller-Universität Jena

3. Prof. Dr. Eva Rentschler, Johannes Gutenberg Universität Mainz

Tag der öffentlichen Verteidigung: 07.07.2021

„Alles ist Wechselwirkung."

Alexander Von Humboldt, Tagebücher der Amerikanischen Reise,
1. August 1803.

„Ich hielt es für besser, etwas zu leisten, als nichts zu

versuchen weil man nicht alles leisten kann."

Alexander Von Humboldt, Die freie Bergschule zu Steben,
13. März 1794.

Contents

LIST OF PUBLICATIONS

Peer-reviewed Publications

- (P1) **"Molecular Electronic Spin Qubits from a Spin-frustrated Trinuclear Copper Complex"** Benjamin Kintzel, Michael Böhme, Junjie Liu, Anja Burkhardt, Jakub Mrozek, Axel Buchholz, Arzhang Ardavan and Winfried Plass, *Chemical Communications*, 2018, **54**, 12934−12937 (DOI: 10.1039/c8cc06741d).

- (P2) **"Electric Field Control of Spins in Molecular Magnets"** Junjie Liu, Jakub Mrozek, William K. Myers, Grigore A. Timco, Richard E. P. Winpenny, Benjamin Kintzel, Winfried Plass and Arzhang Ardavan, *Physical Review Letters*, 2019, **122**, 037202 (DOI: 10.1103/PhysRevLett.122.037202).

- (P3) **"Pentanuclear Nickel(II) Complex with two Vertex-Shared Triaminoguanidine Fragments and Symmetric Capping Ligand"** Michael Böhme, Adrian E. Ion, Benjamin Kintzel, Axel Buchholz, Helmar Görls and Winfried Plass, *Zeitschrift für anorganische und allgemeine Chemie*, 2020, **646**, 999−1009 (DOI: 10.1002/zaac.202000054).

- (P4) **"Spin-Electric Coupling in a Cobalt(II)-Based Spin Triangle Revealed by Electric Field-Modulated ESR"** Benjamin Kintzel, Maria Fittipaldi, Michael Böhme, Alberto Cini, Lorenzo Tesi, Axel Buchholz, Roberta Sessoli, Winfried Plass, *Angewandte Chemie International Edition*, 2021 (DOI: 10.1002/anie.202017116).

Cover Artworks

- *Chemical Communications*, 2018, **54**, 12934−12937.

Public Talks

- **"Polynuclear 3d and 4f Metal Complexes for Potential Molecular Spintronics Applications"** 10th European School on Molecular Nanosciences, El Escorial-Madrid (Spain), 7th − 12th May 2017.

- **"Tritopic C_3 Symmetric Ligands as Versatile Building Blocks for Dy-Based Molecular Magnets"** 14. Koordinationschemikertreffen, Heidelberg (Germany), $11^{th} - 13^{th}$ March 2018.

Poster Presentations

- **"Troubleshooting Approaches for Dy(III) Based Single Ion Magnets"** European f-Element Network (EuFEN4), Lisbon (Portugal), $9^{th} - 12^{th}$ April 2015.

- **"Structural Variation of Dy(III) Complexes: Alkali-Metal Ions as a Tuning Tool for Magnetism?"** 12. Koordinationschemikertreffen, Kiel (Germany), 28th February $- 1^{st}$ March 2016.

- **"Tritopic C_3 symmetric Ligands as Versatile Building Blocks for Molecular Magnets Based on Dysprosium(III)"** EuCheMS Inorganic Chemistry Conference 4, Copenhagen (Denmark), $2^{nd} - 5^{th}$ July, 2017.

- **"3d Metal Complex Based Spin Triangles & Hourglasses for Potential Molecular Spintronics Applications"** 6th European Conference on Molecular Magnetism, Bucharest (Romania), $27^{th} - 31^{st}$ August, 2017.

- **"Triangular Spin Topology: Workbench Towards SMMs, Toroics or Quantum Gates"** 2nd European Conference on Molecular Spintronics, Peñíscola (Spain), $21^{st} - 24^{th}$ October, 2018.

- **"Understanding Magnetic Relaxation in Polynuclear Dy(III) Complexes with C_3 symmetric Ligands"** 7th European Conference on Molecular Magnetism, Florence (Italy), $15^{th} - 18^{th}$ September, 2019.

INTRODUCTION

"Unter allem, was aus der Erde gegraben wird, ist nichts wunderbahreres als der Magnet." (Amongst everything, which is dug out of the earth, there is nothing as wonderful as the magnet.) These words introduced Christian Wolff's work "Vernünftige Gedanken von den Würckungen der Natur" of 1734 and they remain true even now. Although, of course, nowadays' magnetic materials are no longer simply dug up from our earth's lithosphere, but are rather synthesized via chemical pathways and physical treatments the fascination of their unique properties and widespread applications persists unbroken. Inasmuch this work aims for the creation and evaluation of novel molecular magnetic materials by means of coordination chemistry, the following four-part introduction is intended to briefly illustrate the route from 'magnets dug out of the earth' to 'state-of-the-art molecular magnets'. By shedding additional light on two subjects of recent scientific research, which are of outstanding importance for this work, it eventually motivates the targets and approaches deliberately followed.

1.1 Magnetism - From Rocks to Molecules

In the field of magnetism, history has impressively shown, that a certain understanding of the nature and mechanism of particular phenomena can be a crucial prerequisite to making use of them. Namely, the capability of the mineral magnetite to attract iron has been known and documented numerous times already in the ancient world, first by Thales of Milet in the 6th century BC. Nevertheless, it remained an overall useless object until its anisotropic property to align nearly ideally along the north-south axis of the earth in the very same orientation whenever floating was discovered. Thus, the magnetic compass was born. Its usage for navigation was first documented around the 12th century AD in Europe. In an unadulterated view, already in this earliest of all inventions utilising magnetism, the concept of "magnetic interaction" is exploited, for it is the presence of the large magnetic earth that governs the preferential direction of the magnetic needle. The results of this invention were groundshaking and beyond any doubt it can be considered a key innovation of the medieval era. Additionally it remained the only available tool for measuring magnetic fields and related phenomena in the

sense of making them visible until the 19th century.[1,2]

The crusader engineer Petrus Peregrinus wrote a first milestone monograph on the topic in the 13th century. Correctly describing the different poles of a magnet and how to determine them as well as their corresponding effect of attraction and repulsion, this became the basis for the discovery of geomagnetism. However, it took more than 300 years until William Gilbert published his theory and experimental proof of the earth being a magnet itself in 1600. Only at that point in time the setup of the 'device' magnetic compass was fully understood. Coincidentally, it was in the 17th century that the two words embodying the concept of this paragraph were first introduced. The earliest mention of the word "magnetism" was by William Barlow in 1616, while Pierre Gassendi was the first to establish the French word "molécule" in 1650. Also the hypothesis of Galileo Galilei's student Benedetto Castelli that magnetic materials are built of so-called elemental magnets in 1640 is worth highlighting.[1]

More visionary thoughts were contributed during the 18th century. Exemplarily the scientist Johann Wilhelm Ritter, who was mainly working in Jena, was the first to talk of "magnetic lines" to characterise magnetic fields and claimed that magnetic effects of materials increase upon lowering of the temperature.[3] However, veritably groundshaking experimental results and the respective rationalisations were mainly achieved in the 19th century. Ritter's close friend, the Danish professor Hans Christian Oersted published his observations of the magnetic field caused by electric currents in 1820. This opened a flood of discoveries and comprehension in relation to magnetism and electricity, which are all around in our everyday life still today. Hereinafter some examples also relevant for this work are emphasized. William Sturgeon constructed the first artificial electromagnet in 1825, which is to date the most important concept for generating large magnetic fields necessary for many analytical methods, e.g. ESR spectroscopy. In 1831 the magnetic induction was observed and described by Michael Faraday, which is the basic measuring principle of a SQUID magnetometer. The first documented magnetic telegraph line was established in 1834 between the offices of Carl Friedrich Gauß and Wilhelm Eduard Weber in Göttingen, prior to this Gauß had invented a prerequisite: the first magnetometer. The two of them also developed the "cgs" unit system, which is commonly applied in magnetochemistry. Now, the principle of the magnetic telegraph was the next key innovation based on magnetism, which enabled the transmission of information at the speed of light over large distances. It can therefore be considered the hour of birth of information technology, which still today forms the largest field of applications of magnetism and prospective application for molecular magnets.[1]

Hitherto, materials that had been regarded as "magnetic" were predominantly naturally abundant minerals showing remanent magnetisation such as magnetite as well as iron and some of its alloys, which were susceptible to becomimg permanently magnetised. Michael Faraday was the first to categorise a variety of known materials by their behaviour when exposed to magnetic fields in 1851. Substances, which aligned parallel to the magnetic flux lines he called "paramagnetic" and those aligning crosswise to the magnetic flux lines he called diamagnetic. He also ordered them according to the relative strength of the effect and henceforth, the science of magnetic materials arose. Obeying André-Marie Ampère's theory of molecular currents,

Wilhelm Beetz in 1860 correctly explained the phenomenon of saturation of magnetisation with the parallel alignment of all "molecular magnets" the material consists of. James Alfred Ewing introduced the word "hysteresis" for the magnetisation circular of magnetic materials in 1882. Following Faraday's pathway of investigating magnetic materials, Pierre Curie could uncover pioneering insights on the temperature dependence of magnetic susceptibilities of diamagnets, paramagnets and ferromagnets (term was introduced by Du Bois in 1892). The magnetic susceptibility is generally considered the ratio of magnetisation (M) and applied magnetic field (H_a):

$$\chi = \frac{M}{H_a} \tag{1.1}$$

The Curie temperature defining the sharp transition of a ferromagnet to paramagnetic behaviour was named after him. He also found a first quantitative correlation about susceptibility (χ) of paramagnets the Curie law, which includes the Curie constant C:[4]

$$\chi = \frac{C}{T} \tag{1.2}$$

Finally, the discovery of the electron by Joseph John Thompson as well as the triplet splitting of atomic spectral lines in magnetic fields by Pieter Zeeman (Zeeman effect) both in 1897 crowns the 19th century's progress, which consequentially paves the way for the microscopic understanding of magnetic materials, its exploitation and design.[1,5,6]

In the very beginning of the past century, Paul Langevin developed a first electron-based theory of paramagnetism and diamagnetism in 1905. Accordingly all electron-based magnetic moments of a paramagnet orient statistically in the absence of a magnetic field. Its susceptibility is positive and temperature dependent as follows from Curie's law. By means of a magnetic field applied, magnetisation can be generated, until all magnetic moments are aligned parallel to the field direction, which is the state of saturation. In contrast, electron-based magnetic moments, that cancel out cause a negative susceptibility, which is mostly temperature independent. Hence, the susceptibilty of any paramagnetic material consists of at least a diamagnetic (χ_{dia}) and a paramagnetic contribution (χ_{para}), which always have to be considered for magnetometry.

$$\chi = \chi_{dia} + \chi_{para} \tag{1.3}$$

The theory was extended for ferromagnetism by Pierre Weiss 1907, who was the first to describe the long range order of electron-based magnetic moments. For this he introduced the so-called mean field theory implying that each carrier of a magnetic moment is affected by its neighbours. The spontaneous magnetisation in the material therefore occurs due to cooperativity between the individual magnetic moments. Weiss also found the magnetic domains in ferromagnets and the relation of their susceptibility above the Curie temperature with temperature, the

Curie-Weiss law:

$$\chi = \frac{C}{T - T_{\mathrm{C}}} \tag{1.4}$$

Together with his collaborator Piccard he discovered the magnetocaloric effect in 1917, which is in the focus of researchers nowadays for magnetic refrigeration devices[7] and forms an interesting field of application of magnetic materials not further discussed within this work. It may be emphasized that Langevin and Weiss founded all their thoughts on classical mechanics exclusively assuming angular momentum as source of magnetism, without even knowing about the concept of electronic spin. Along that line it shall be noted, that there are more types of long range magnetic orders in solids known today. First of all, antiferromagnetism was explained in 1930 by Pierre Weiss's doctoral student Louis Neél and means the antiparallel alignment of all magnetic moments with respect to their closest neighbours. This leads to an anisotropy of susceptibility below the so-called Neél temperature, which marks the transition of the material to paramagnetism. Neél also described ferrimagnetism in 1948, which is analogous to antiferromagnetism, but the two resulting sublattices of antiparallel magnetic moments feature different absolute values. Thus the apparent magnetic behaviour is a ferromagnetic one. Interestingly, the historic archetypal magnet, magnetite, is actually a ferrimagnet. In systems of lower magnetic lattice dimension phenomena like helical or spiral magnetic order are known. The spin glass is a special metastable state, where exclusively a short-ranged order of magnetic moments is present, but none in the long-range.[1,6,8]

In parallel, the era of the development of quantum mechanics went full speed, which is a story for itself and not outlined here. But of course these concepts cannot be uncoupled. Niels Bohr stated in 1911, that microscopic magnetism cannot be understood with classical physics, since the electrons cannot circle arbitrarily around the atomic nucleus, which was underlined by his atomic model from 1913. The Stern-Gerlach experiment successfully conducted in 1922, once again enabled by the application of a magnetic field and the presence of a magnetic moment in the used silver atoms, proved that statement as well as the whole theory of quantum mechanics. Eventually, with the discovery of the electronic spin by George Eugene Uhlenbeck and Samuel Abraham Goudsmit in 1925, which turned out to have twice the magnitude of magnetic moment compared to the "classical" angular momentum, all ingredients for the deep quantum mechanical understanding of magnetism were now gathered. However, for this work only cornerstones which are relevant need to be pointed out. First of all, an expression for the absolute magnetic moment of an electron combining its spin s and its orbital angular momentum l to the total angular momentum J is found to be:

$$\mu_J = -g_J \frac{e}{2m_{\mathrm{e}}} \hbar J \tag{1.5}$$

In here, e is the elemental charge, m_{e} is the electron mass and g_J is the Landé factor, which becomes two for pure spin contribution and one for pure orbital contribution. Extending this to an atom or ion and at the same time combining all natural constants included in the Bohr

Magneton μ_B results in the expression:

$$\mu_J = \mu_B g_J \sqrt{J(J+1)} \tag{1.6}$$

At this point, it has to be raised that the atomic nucleus may, of course, also have a magnetic moment as was first experimentally proven by Otto Stern in 1933,[9,10] which interacts with the magnetic moment of the electron shell. Nuclear magnetism enables nowadays indispensable analytic techniques like nuclear magnetic resonance (NMR) spectroscopy and magnetic resonance imaging. This is another example of magnetism to give rise to extraordinarily important innovations. However, for most magnetic phenomena treated within this work it plays a subordinated role and will therefore be neglected in the following mathematic descriptions. Thus, a Hamiltonian for an isolated atom in a magnetic field B can be devised,

$$\widehat{H} = \widehat{H_0} + \mu_B g_J \cdot J \cdot B + \frac{e^2}{8m_e} \sum_i (B \times r_i)^2 \tag{1.7}$$

where $\widehat{H_0}$ sums up the electronic kinetic energy and potential energy, hence the atom without a magnetic field. The second term is the paramagnetic term, it lowers the energy of the system when exposed to a magnetic field. In contrast, the third term refers to the diamagnetic moment augmenting the energy of the system in a magnetic field, with r_i being the magnitude of the position vector of the ith electron. With the help of van Vleck's equation by John Hasbrouck Van Vleck,[11] which quantum mechanically describes the magnetic susceptibility of a quantum object such as an atom, a microscopic interpretation of experimental susceptibilities becomes feasible. If the temperature independent contributions are accounted for separately, from this equation an expression for the Curie constant C included in eq. (1.2) can be derived.

$$C = \frac{n g_J^2 \mu_B^2}{3k_B} J(J+1) \tag{1.8}$$

For this, n is the number of independent atoms in a unit ensemble and k_B is Boltzmann's constant. Based on this, the magnetisation of a system, which is an actually measurable observable, can be related to a dependence on magnetic field and temperature (eq. (1.9)).

$$M = n g_J \mu_B J B_J(x) \tag{1.9}$$

The discrete value of $x = g_J \mu_B B / k_B T$ bears the temperature dependence and B_J is the so-called Brillouin function (eq. (1.10)), which is necessary to obtain the magnetisation for certain J values.[12]

$$B_J = \frac{2J+1}{2J} \coth\left(\frac{2J+1}{2J}x\right) - \frac{1}{2J}\coth\left(\frac{x}{2J}\right) \tag{1.10}$$

In this form, the expressions are only valid for an ensemble of individual, non-interacting atoms. Of course, in functional magnetic materials and molecular magnets the desired properties

mostly rely on interactions between the magnetic centres. The mechanisms and consequences of magnetic interaction are discussed in the next section. Right here some more light will be shed on how chemistry entered into the world of magnetism, since up to this point, the physical development and understanding of magnetism have been predominantly discussed.[1,6,13]

Built on the theoretical basis that was just described, magnetism was first utilised in chemistry as an analytical tool for solid inorganic compounds. Measuring magnetic moments and susceptibilities mostly by means of magnetic balances like the Gouy balance revealed information about the electronic configuration of individual ions or atoms, especially the number of unpaired electrons. Such methods were first established by the German chemist Wilhelm Klemm, who described them in the 1936 textbook "Magnetochemie".[14] His pioneering work in that field summarised in this book is generally considered the beginning of modern magnetochemistry.[15]

Magnetochemistry further evolved from an analytical tool into a research field of designing and understanding more complex magnetic properties within molecular species for itself. This process started with the description of the temperature dependence of the magnetic susceptibility[16] as well as the structure[17] of the complex salt $[Cu_2(OAc)_4(H_2O)_2]$. The rapid decrease of the susceptibility with temperature could be attributed to an antiferromagnetic interaction within a "molecular cluster" instead of long range ordering by Bleaney and Bowers aided by ESR spectroscopy.[18] They also found the exchange interaction operative to be a superexchange via bridging donor atoms as proposed by Anderson.[19] Based on that they introduced the exchange term (see eq. (1.11)) into the effective spin Hamiltonian for the spin states of one molecular cluster and derived the so-called Bleaney-Bowers equation (eq. (1.12)) with the magnetic exchange coupling constant J_{ex} included.

$$\widehat{H} = -J_{ex}\hat{S}_1\hat{S}_2 \tag{1.11}$$

$$\chi = \frac{2Ng^2\mu_B^2}{k_BT\left[3 + \exp\left(-\frac{2J_{ex}}{kT}\right)\right]} \tag{1.12}$$

It was the first case to reproduce the temperature dependence of the magnetic susceptibility of a bulk material by description of an isolated molecular cluster and therefore is usually considered the birth of molecular magnetism. Exchange-coupled "molecular clusters", which we nowadays rather designate as polynuclear coordination compounds or complexes with bulky organic ligands, of 3d transition metals dominated the research in that field until the 1990s and hence the mechanisms of magnetic exchange interactions are illuminated in more detail in the following section.

1.2 Magnetically Coupled Transition Metal Complexes - Frustration for Innovation

A central aspect of molecular magnetism is magnetic exchange interaction within one molecule. The different types of magnetic interaction are introduced briefly, before their exploitation for the design of molecular magnets is illustrated and some recent trends being crucial for this work are emphasized.

1.2.1 Types of Magnetic Interaction

The only classical type of magnetic interaction is the dipolar interaction, describing the energy gain E_{dip} of two point symmetric magnetic dipole moments μ_1 and μ_2, which are separated by r_{12} and form the angle α between the direction of the moments and the vector connecting them (see fig. 1.1) as follows:

$$E_{dip} = -\frac{\mu_1 \cdot \mu_2 \left[3\cos^2\alpha - 1\right]}{r_{12}^3} \tag{1.13}$$

It is a highly anisotropic (α, see fig. 1.1), through-space, long-range interaction, meaning it does not need any transmitting medium or conditions, but is always operative. However, due to the cubic dependence on the distance of the dipoles ($\sim r^{-3}$) its size is neglectable for most molecular magnets based on transition metals. Yet, it may contribute significantly to magnetic interactions in case of lanthanoids. This is further discussed in section 1.3.[6,13]
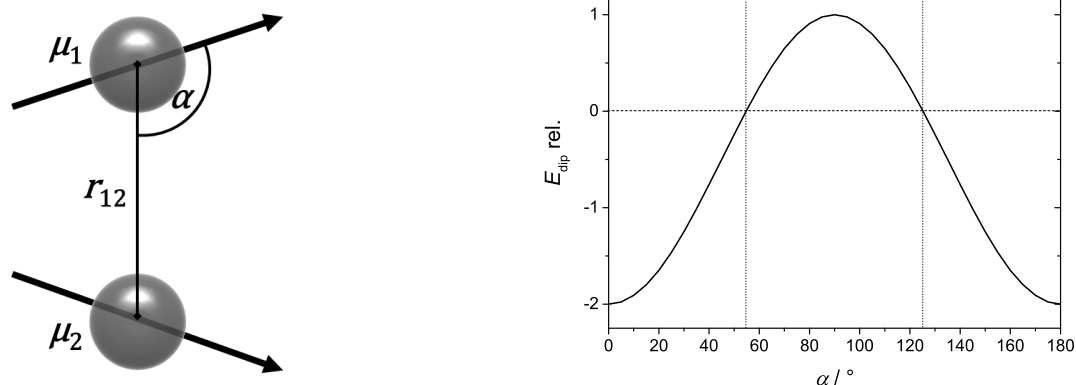

Figure 1.1: Left: Schematic representation of two magnetic dipoles μ_1 and μ_2 e.g. paramagnetic atoms and relating parameters affecting the magnetic dipolar interaction. **Right:** Depiction of the angular dependence on α of the relative dipolar interaction energy E_{dip} rel. obeying eq. (1.13).

All other interactions are called exchange interactions, since they rely on peculiarities of the electronic shell of the respective atoms. The direct exchange is related to the overlap integrals of the atomic orbitals bearing the involved electronic spins, the so-called magnetic orbitals. For non-zero overlap integrals (kinetic exchange), the exchange coupling parameter J_{ex} after eq. (1.11) is negative obeying Pauli's principle leading to a ground state spin (S_{GS})

subtracting the individual spins (S_i) of the coupled atoms. In contrast, zero overlap integrals or orthogonality of the magnetic orbitals (potential exchange) leads to a usually weaker positive J_{ex} and $S_{GS} > S_i$. This direct exchange requires proximity of the pertaining atoms, since the orbital overlap decreases tremendously with distance ($J_{ex} \sim r^{-10}$).[20]

So for most molecular magnets, direct exchange is irrelevant, but the similar superexchange mechanism utilising filled orbitals of bridging ligands as mediators is most influential.[19] As becomes obvious from fig. 1.2 the sign and magnitude of the superexchange interaction is strongly dependent on the symmetry of the magnetic orbitals bearing the unpaired electrons and the bridging angle of the mediating donor atom. Some general rules for the qualitative prediction of the interaction were developed based on experimental observations on inorganic solids fulfilling certain symmetry conditions by Goodenough and Kanamori.[21–23] A simplified orbital model exemplifying ideal cases of 180° and 90° bridging of two metal ions M_1 and M_2 with half filled d_{z^2} orbitals via a closed shell oxygen donor is schemed in fig. 1.2.[6,13]
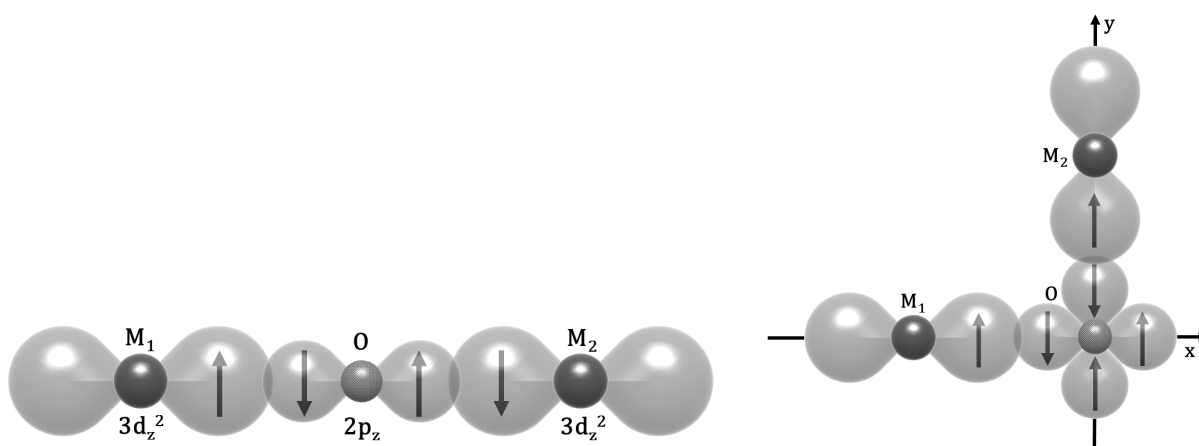
Figure 1.2: Scheme of a simplified orbital model of two metal ions M_1 and M_2 with half filled d_{z^2} orbitals bridged via a closed shell oxygen donor O in a 180° (left) and 90° (right) angle leading to antiferromagnetic and ferromagnetic exchange, respectively.

In general, these interactions have to be evaluated for all included magnetic orbitals individually. If both types of superexchange interactions are operative between two metal ions with more than one magnetic orbital, the overall exchange is often dominated by the stronger antiferromagnetic contribution. When unquenched orbital angular momenta come into play, the simplified superexchange model breaks down and more complex models are necessary,[24] which are not further detailed here.

In the special case of an exchange interaction between two equal atoms in different oxidation states the so-called double exchange mechanism first described by Zener[25] can occur. It features a true delocalisation of electrons into the empty neighbouring orbital and mediates comparably strong ferromagnetic interactions. In contrast to superexchange it additionally gives rise to electric conductivity within the coupled system. Although, due to its special prerequisites, the effect does not frequently appear in molecular magnets, there are some reported examples found in literature.[26–28]

However, for this work another contribution to the magnetic interaction is of higher impor-

tance, which is an antisymmetric component of the superexchange introduced by Dzyaloshinsky and Moriya[29,30] and therefore often referred to as Dzyaloshinsky-Moriya (DM) interaction. It occurs, if there is no inversion symmetry on the line connecting two ions bearing the spins S_1 and S_2, and is related to the spin–orbit interaction of the pertinent atoms. The contribution to the effective Hamiltonian of a system can be described as:

$$\widehat{H}_{DM} = G(S_1 \times S_2) \tag{1.14}$$

G is a vector giving the magnitude of the DM interaction. It tends to align S_1 and S_2 perpendicular to each other and to G resulting in a canting of the otherwise collinear spins (see fig. 1.3). The size of G is usually small in comparison to J_{ex} but generates an additional splitting of spin states whenever occurring and a net magnetic moment in the ground state of an antiferromagnetically coupled homodimer.[6,13]
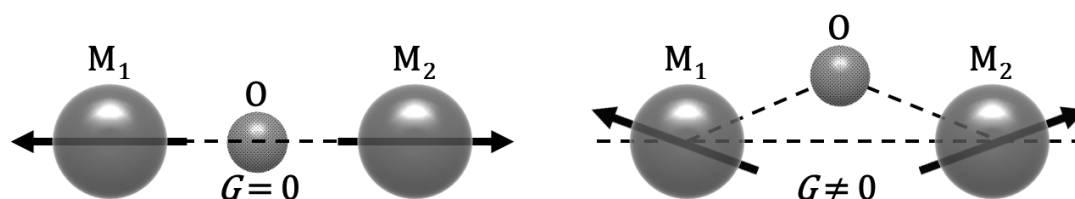
Figure 1.3: Schematic alignment of spin moments of metal centres M1 and M2 in an antiferromagnetically coupled homodimer with (right) and without (left) Dzyaloshinsky-Moriya (*DM*) interaction described by *G*.

Another type of magnetic exchange interaction especially relevant for conjugated π-electron systems is the so-called spin-polarisation mechanism. It is based on an unpaired electron with a certain spin polarising the spin density distribution of its neighbouring, chemically bound atoms. For example an organic radical with an α spin induces an increased β spin density at the neighbouring atom and again an alpha spin density in the next neighbour. This polarisation is significantly mediated via conjugated π systems leading to exchange interaction in organic polyradicals, which is ferromagnetic in case of an odd and antiferromagnetic in case of an even number of bridging carbon atoms.[31] It was proven, that this concept can be adopted to metal complexes bridged by aromatic systems. Accordingly, *ortho* or *para* bridging of metals via a benzenoid system leads to antiferromagnetic exchange, while *meta* bridging gives rise to ferromagnetic interaction.[32,33]

There are more special kinds of magnetic interaction, e.g. in metals mediated by itinerant electrons, however, those mechanisms are scarcely relevant for molecular magnets and therefore not further detailed here. Hereinafter, the use of coordination chemistry to first of all understand and subsequently exploit the magnetic interactions within molecules is portrayed.

1.2.2 Polynuclear Molecular Magnets Based on 3d Transition Metals

Molecular magnets were elucidated to be materials, whose bulk magnetic properties can mainly be assigned to the expected behaviour of one individual molecule the material consists of. So

intramolecular magnetic interactions will by far predominate possible intermolecular magnetic interactions. Keeping in mind the possible exchange interaction pathways, this can be ensured in coordination compounds by the use of bulky organic ligands, which feature several coordination sites in combination with appropriate bridging moieties.

Following this very general design idea, first structural correlations to the observed magnetic exchange interactions were established. The work of Hodgson, Hatfield *et al.* describing the dependence of magnetic coupling in dihydroxo-bridged planar dinuclear Cu(II) complexes on the Cu−O−Cu angle is an elegant example worth mentioning here.[34] The impressive work of Kahn *et al.* utilised mostly extended "salen" and oxalate-derived ligands (see fig. 1.4) to generate homo- and heterodinuclear transition metal complexes. The investigation of effects of structural and chemical features on the nature of the magnetic coupling lead to understanding and a certain predictability.[35–37] With these prerequisites at hand, the route was paved towards the deliberate design of molecular magnets aiming towards application perspectives.
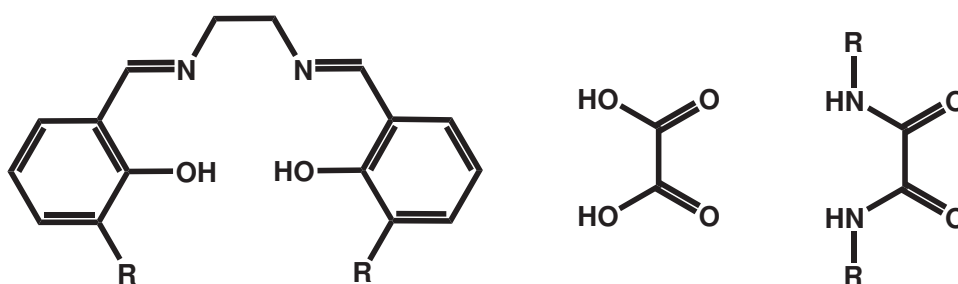

Figure 1.4: Some ligand core structures (in their protonated forms), which were extensively used by Kahn *et al.* for the systematic studies on magnetic exchange in homo- and heterodinuclear 3d metal complexes.[35–37] From left to right: *N,N'*-(2-hydroxybenzylidene)-1,2-diaminoethane ("salen"), oxalic acid, oxalic acid diamide.

One aim still relevant today is the creation of molecules with a high spin ground state. Such molecules offer application perspectives especially in the area of magnetic cooling.[38–40] The mentioned rationalisation and predictability of magnetic interactions allow for a goal-oriented choice of bridging ligands and so-called blocking ligands, which are designed to prevent the formation of coordination polymers. However, it has to be admitted, that most high spin molecular clusters in literature are product of serendipitous self assembly rather than a tailored stepwise build up of ferromagnetically coupled building blocks. Despite this, remarkable successes could be achieved in this field. Some bridging ligands very extensively used for high spin molecular clusters are oxo and carboxylate moieties,[41,42] fluoride,[43] azide[44] and cyanide[45] ions, due to their short bridging distances and thereby mediation of stronger magnetic interactions.

The record result by numbers in this area featuring a spin ground state of $S = \frac{83}{2}$ is an oxo-bridged manganese cluster incorporating seven Mn(II) and twelve Mn(III) ions as spin carriers. Out of this class of molecular clusters, also the first compound with reported single molecule magnet (SMM) behaviour $[Mn_{12}O_{12}(CH_3COO)_{16}(H_2O)_4] \cdot 2\,Ch_3COOH \cdot 4\,H_2O$ ($[Mn_{12}]$) arose.[46,47] Section 1.3 is dedicated to this special class of molecular magnets, thus the topic is not further discussed here.

A special highlight will be brought upon efforts to create high spin molecules via the spin polarisation approach, first because it is one example with the ferromagnetic interaction being enforced by the ligand design and second for its topological similarity to the systems treated in this work. As already mentioned, the use of a benzenoid ligand backbone should inevitably provide a ferromagnetic contribution if the spin carriers are bridged via *meta* substituents or heteroatoms.[31] This approach can be utilised to build up triangular spin topologies with tritopic ligands based for example on phloroglucinol or triaminobenzene (see fig. 1.5). This design idea was successfully realised with trinuclear copper complexes resulting in an overall ferromagnetic exchange, *i.a.* by Glaser *et al.*[33,48,49] with a phloroglucinol based ligand system and in our group by Plaul[50] with a triaminobenzene based ligand system. It was also elucidated, that a metallacyclophane formation with two ligands of the respective type enhances the spin polarisation mechanism.[50–52] Unfortunately, the exploitation of this mechanism with transition metal ions bearing higher spins is more challenging. Nevertheless, these molecules remain valuable building blocks for the construction of higher aggregates to yield higher spin states.
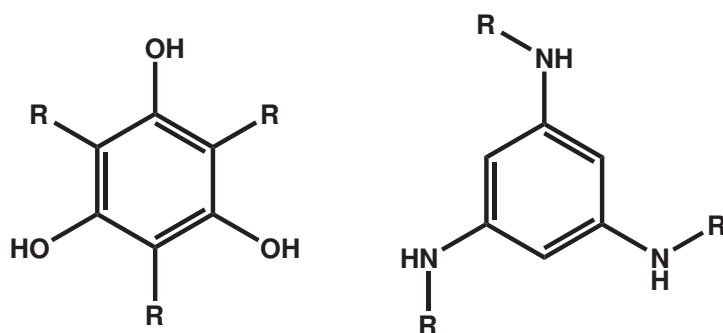
Figure 1.5: Two kinds of ligand backbones, which are utilised to build up triangular spin topologies ferromagnetically coupled via spin polarisation: Phloroglucinol (left)[33,48,49] and triaminobenzene (right).[50–52]

1.2.3 Transition Metal Complexes as Spin Qubits

A distinctly more recent topic within molecular magnetism is the design of molecular components for quantum technologies. The frame of this work is by far insufficient to adequately introduce the wide field of quantum technologies, so only the very basics of one particular branch, namely quantum computing will be discussed briefly. Subsequently, some state of the art molecular realisations of components for quantum computing based on 3d transition metals are presented.

Quantum computation means the performing of computational processes utilising quantum mechanical phenomena. A nomenclature of components derived from that one of classical computing is applied, so the quantum mechanical equivalent to a classic bit is called quantum bit or qubit. The manipulation of them by means of quantum logic gates is the analogon to classical logic gates. The unique qubits' requirements for a physical realisation of "hardware" for a general purpose quantum computer were developed by diVincenzo[53] and are called the "DiVincenzo criteria". Condensed to a minimum, these are (i) a scalable physical system

with well-characterised qubits, (ii) the ability to initialise the state of the qubits to a common state, (iii) decoherence times significantly longer than the gate operation times (at least by a factor of 10^4), (iv) a "universal" set of quantum gates is feasible and (v) a qubit-specific measurement capability for readout. Although there are already some announcements of machines performing specific quantum operations,[54,55] to the best of my knowledge there is no physical realisation satisfactorily fulfilling all criteria. Therefore, recent research has focused on developing dedicated quantum computers as for example quantum simulators,[56] because only then are the strict necessities of the DiVincenzo criteria are partially lifted.[6]

Now, what does all this mean to a chemist trying to make a contribution using the tools of molecular magnetism? First of all, the most fundamental ingredient of a quantum computer, the qubit, can be realised by electronic spins, which intrinsically feature an $s = +\frac{1}{2}$ and an $s = -\frac{1}{2}$ state usable as computational states $| 0 \rangle$ and $| 1 \rangle$, respectively. This concept is pursued in some promising solid state approaches, *e.g.* few electron quantum dots[57,58] or nitrogen vacancies in diamond.[59,60] However, purely electronic spins are hard to tailor by chemical means and scalability of such systems is very challenging. Thus, the use of coupled (especially anti-ferromagnetically) electronic spins accommodated within molecular magnets promises several advantages. Addressing—this means initialisation, manipulation and readout of computational states in the qubit—can be accomplished via magnetic pulses resonating with the respective g-value of the spin qubit (the principle of pulsed ESR spectroscopy), which can be engineered chemically. Also the sheer size of a molecular magnet in comparison to electronic spins in solids facilitates the control of qubit–qubit interactions.[61] States of the molecule, which are not encoding $| 0 \rangle$ or $| 1 \rangle$ (so-called non-computational states) can be exploited for specific gates or global manipulations, which even should allow quantum computation without individual addressing of the qubits.[62,63]

Mononuclear molecular magnets can be deliberately engineered, *e.g.* towards large spin decoherence times (T_2),[64] which are essential for performing quantum operations. This is usually achieved by obstruction of decoherence pathways via neighbouring nuclear spins or easily rotatable functional groups. The current record holder is $[V^{IV}(C_8S_8)_3]^{2-}$ [65] (fig. 1.6 left), with $T_2 = 700\,\mu s$. But also polynuclear molecular magnets like the antiferromagnetically coupled ring $Me_2NH_2[Cr_7Ni(O_2CMe_3)_{16}]$ (Cr_7Ni)[66] (fig. 1.6, right) feature remarkable decoherence times of several μs[67,68] and have been extensively studied for their suitability as qubits. The nearly ideal isotropic nature of its doublet ground state makes this molecule a particularly suitable candidate.[69–71]

However, the use of coupled polynuclear molecular magnets implies even more benefits. In particular, the possibly smaller T_2 notwithstanding, the computational state can be encoded in collective degrees of freedom, such as spin chirality[73] which is a lot less vulnerable to decoherence than a single spin.[74] The particular feature of spin chirality becomes feasible in so-called geometrically spin-frustrated systems. That means topologies with uncompensated spin momentum in the magnetic ground state feature an additional degeneracy of this state resulting from competing magnetic interactions. The phenomenon was first described by Toulouse in spin glasses[75] and further evolved for molecular magnets by Kahn[76] and Dai.[77]
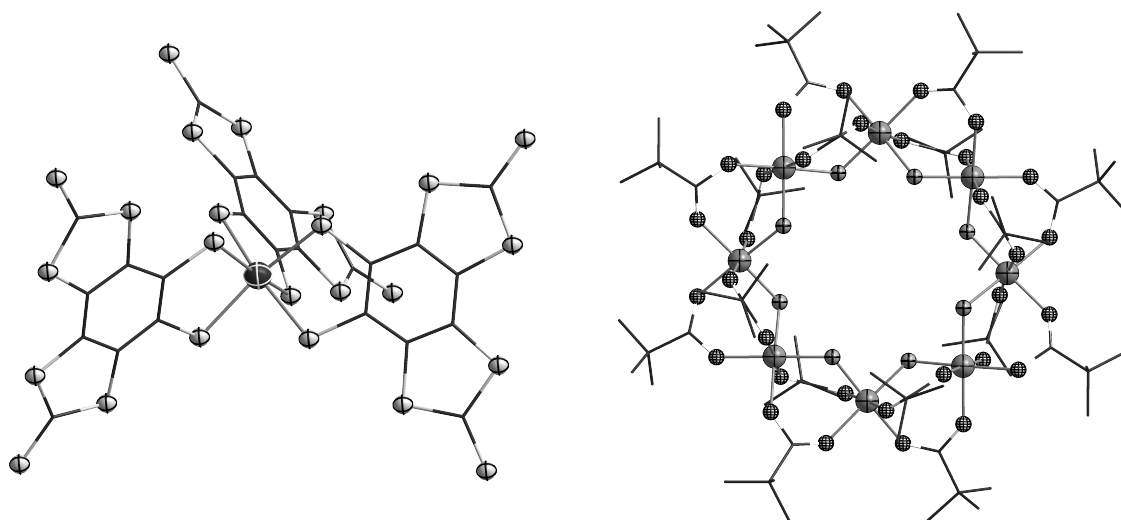
Figure 1.6: Molecular structures of a mononuclear (left) and a polynuclear (right) molecular magnet-based qubit candidate. **Left:** Molecular structure of $[V^{IV}(C_8S_8)_3]^{2-}$, C atoms are wire nodes, V: dark grey, S: light grey.[72] **Right:** Molecular structure of $Me_2NH_2[Cr_7Ni(O_2CMe_3)_{16}]$, H-atoms are omitted, C atoms are wire nodes, Cr/Ni: grey, F: light grey, O: chequered.[66]

This gives rise to various special properties of such systems,[78–81] spin chirality[73] being the most interesting one for the scope of this work. The simplest case for a purely molecular example of a frustrated spin system is an equilateral triangle of three half-integer, identical spin moments, which are coupled antiferromagnetically with identical coupling constants. This archetypal example of spin frustration in a molecular magnet and the resulting fourfold degeneracy with the corresponding spin projections is sketched in fig. 1.7. More complex topologies fulfilling the mentioned prerequisites such as the similar equilateral pentagon spin ring are predicted to show similar features with some restrictions.[82]

Spin-frustrated molecular magnets in general and antiferromagnetic equilateral spin triangles in particular were predicted to exhibit spin-electric coupling by Loss *et al.*,[82,83] since the spin chirality of the states (S_S) is sensitive to electric fields applied parallel to the triangular plane. If this happens in the presence of a static magnetic field also applied parallel to the triangular plane, the ramping of a sufficiently strong electric field manipulates spin states by anisotropic modulation of the exchange interaction J_{AF} or the spin–orbit interaction.[82] The former is proposed to occur in the absence of spin–orbit coupling-induced DM interaction. In principle, the electric field effect can even result in levels crossing[83] as is also illustrated in fig. 1.7. In conclusion, geometrically spin-frustrated molecular magnets cannot only protect their computational information from decoherence via spin-chiral states, but can also enable the manipulation of their spin states by means of electric fields. This is highly beneficial because in contrast to magnetic fields, strong electric fields can be focused to very small volumes and switched quickly when using Scanning Tunneling Microscopy (STM) tips as both source and manipulator.[84]

Consequently, there have been first approaches to make the electric field control of geometrically frustrated molecular magnets feasible. Canali *et al.*[87] performed some theoretical survey
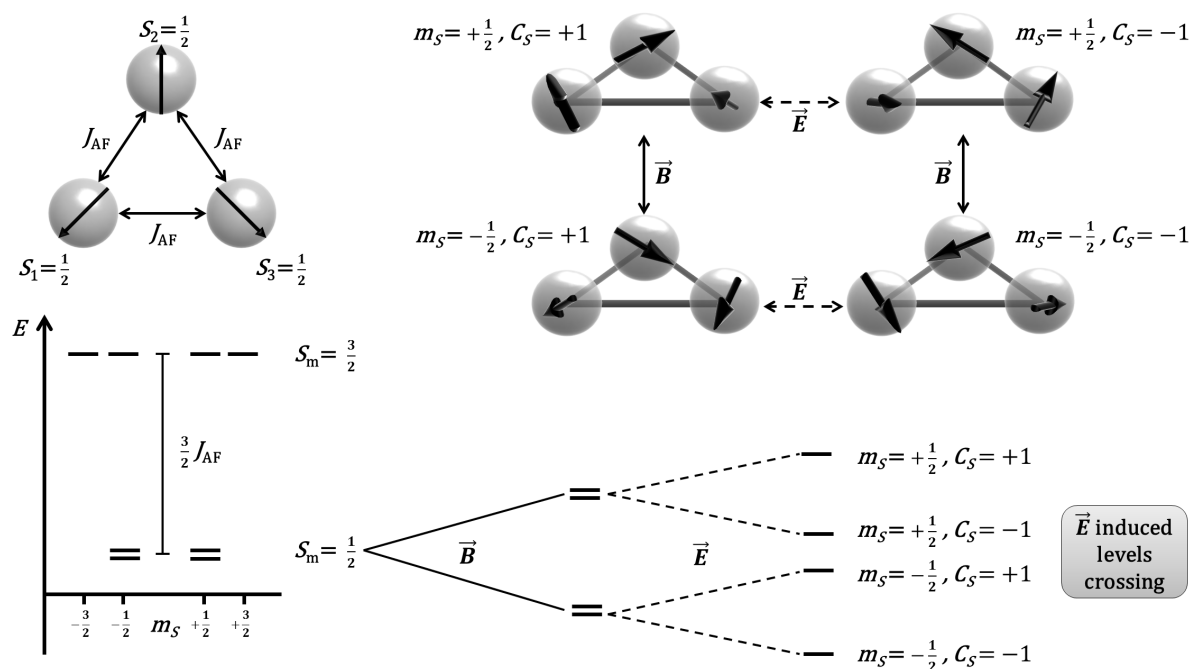
Figure 1.7: Left upper corner: spin topology of the archetypal example of a spin frustrated molecular magnet,[76] the equilateral triangle of antiferromagnetically coupled $S = \frac{1}{2}$ centres. Right upper side: spin projections of the microstates of the fourfold degenerate magnetic ground state also specifying which type of field (magnetic field $\vec{B}$: straight arrows, electric field $\vec{E}$: dashed arrows) can induce the transitions between them according to Loss *et al.*.[82] Left lower corner: energy splitting of spin states in this ideal molecule in absence of magnetic or electric fields. To its right this graph is extended for the fourfold degenerate $S_m = \frac{1}{2}$ spin ground state. First a magnetic field $\vec{B}$ is applied causing a Zeeman splitting between microstates with opposite sign of m_S. Second an electric field $\vec{E}$ is applied inducing energetic splitting between microstates with opposite sign of spin chirality C_S.[81,83] When $\vec{E}$ becomes sufficiently high a possible levels crossing is reached according to Loss *et al.*.[82,83]

on a [Cu(II)$_3$] spin triangle based on a polyoxometalate cage[88] to quantify the spin-electric effect in this particular example. Unfortunately, they used a very simplified computational model, which assumes D_{3h} symmetry of the spin system, whilst the molecule itself is rather an isosceles spin triangle according to crystallographic data. Up to now, numerous examples of antiferromagnetically coupled triangles of three equal half integer spins have been published and their magnetic properties at least fundamentally investigated.[89–96] However, none of them features a crystallographic C_3 symmetry in solid state, so none of them is actually an equilateral spin triangle and the ground state degeneracy is intrinsically lifted due to differences in the coupling constant. Furthermore, most of them carry a central oxo or hydroxo bridging ligand, which is not incorporated into a robust ligand backbone and therefore further reducing the local symmetry around the bridged metal centres. This often manifests in pronounced DM interaction,[97] whose role for the observation of spin-electric coupling remains to be clarified, at this stage there are reports predicting a detrimental effect.[98] Although there is a magnetic Jahn-Teller effect predicted for ideal equilateral spin triangles,[99] this is supposed to lead to a distortion of about 10 pm for the particular example of oxo-bridged triangles and expected to
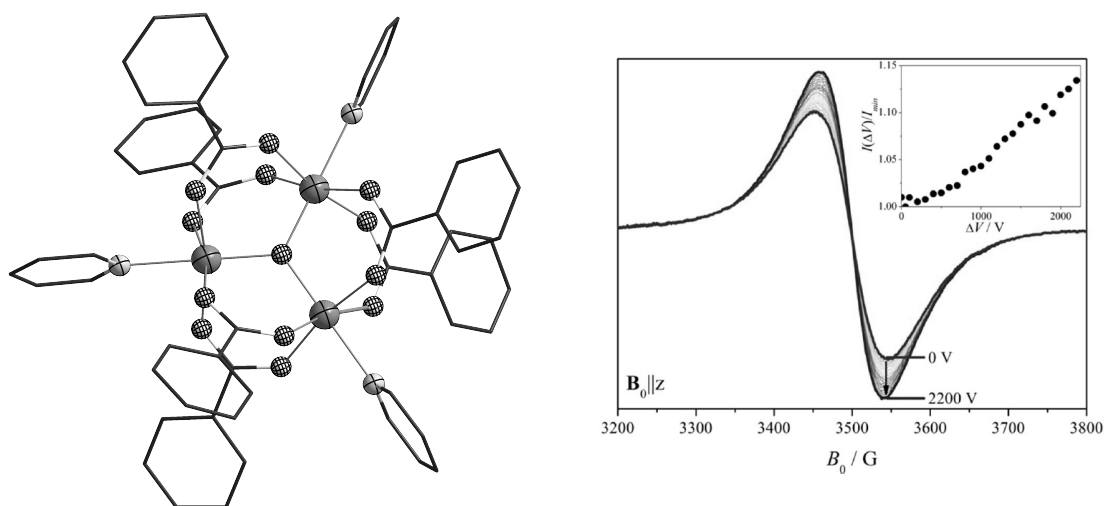
Figure 1.8: Left: Molecular structure of $[Fe_3O(O_2CPh)_6(py)_3]ClO_4 \cdot py$, H-atoms are omitted, C atoms are wire nodes, N: dark grey, F: light grey, O: chequered.[85] **Right:** X-band ESR spectrum of a single-crystal of $[Fe_3O(O_2CPh)_6(py)_3]ClO_4 \cdot py$ with $B_0 \parallel z$ and $E_0 \perp z$ under varying electric field strengths. The right upper inset shows the absolute integral of the spectrum related to the electric field. This shown increase is claimed to result from spin-electric coupling.[86] Figure taken and modified from[86] (with permission of Wiley-VCH).

be even lower for more robust ligand backbones.

Nevertheless, one example of such oxo-bridged triangular complex $[Fe_3O(O_2CPh)_6(py)_3]ClO_4 \cdot py$ indeed featuring crystallographic C_3 was studied for its low-temperature magnetism in much detail.[85] A low-temperature desymmetrisation was detected via inelastic neutron scattering. More detailed experimental work on detecting spin-electric effects on single-crystals by means of ESR spectroscopy with applied static electric fields was carried out by Boudalis *et al.*.[86] In there it is claimed to observe the effect as an increase in ESR signal intensity, but no microscopic explanation of the effect is given. In follow-up work on these systems the group relates observed phenomena mainly to DM interactions present in the compound based on comparisons with an isostructural Cr(III), which is argued to feature a smaller DM interaction.[100,101] One has to note critically at this point, that these experiments were carried out in frozen pyridine solution, which makes it hard to evaluate the local symmetry of the molecule and the states involved. The latter becomes an issue, since the coupling constant in the solid phase was determined to be lower than $30\,\mathrm{cm}^{-1}$ and decreases with the desymmetrisation at low temperatures.[85]

A different approach to probe spin-electric effects in single-crystals was recently presented by Fittipaldi *et al.*.[102] This electric field modulated (EFM) ESR setup uses alternating electric fields and their observations of a g-value modification on chiral Mn(II) radical chains could be deconvoluted properly. This might prove a powerful tool for the future detection and understanding of spin-electric effects in molecular magnets. Of course, on single-crystals, the anisotropy of effects can be studied. However, the final aim has to be a spin-frustrated molecular magnet showing spin-electric coupling on a functional surface, which allows for manipulation of single molecules via STM tips. The ideas followed within this work to enrich the field are

further expounded on in section 1.4.

1.3 Single-Molecule Magnets - A Story of Individualism

During magnetic investigations on high spin 3d metal clusters already described in section 1.2 in the early 1990s magnetic bistability was observed in $[Mn_{12}O_{12}(CH_3COO)_{16}(H_2O)_4]$ ($[Mn_{12}]$)[46,47] (see fig.1.9), which was first structurally and magnetically characterised in 1980[103] and originally synthesised by Weinland and Fischer in 1921.[104] The magnetic hysteresis found at cryogenic temperatures below 5 K could be related to the properties of a single isolated molecule without any intermolecular cooperativity or long range effects. Hence, this can be considered the cradle of single-molecule magnets (SMMs). It did not take long to let this finding fire the molecular magnetism community's imagination for marvelous application perspectives of such materials, the most obvious one being digital data storage and processing. Using a single molecule to store one bit of digital information would be a key innovation enabling to keep pace with Moore's law[105–107] and to overcome the superparamagnetic limit[108,109] for hard disk drives (HDDs). So the prospective usefulness of SMMs will be beyond doubt, if the condition of making them operable at higher temperatures with minor information loss can be fulfilled.

Before outlining the chemical development of SMMs, which can hopefully lead to meeting the prerequisites for application in information technology in the future, the theoretical background of their magnetic bistability and its relaxation shall be evolved briefly. First of all, SMMs are well-defined molecular magnets with neglectable intermolecular magnetic interactions and therefore a well-ordered magnetic structure with a fixed number of metal centres.[6] Magnetic anisotropy as well as a ground spin state larger than $S = \frac{1}{2}$ are essential ingredients for a molecular magnet to show SMM properties. Of course, magnetic anisotropy can be parametrised in various ways, the easiest case which is sufficient for the godfather SMM [Mn_{12}] and most 3d metals is the usage of an axial zero field splitting (ZFS) parameter D. D is half the energetic difference between the states with the highest and the lowest absolute spin value in absence of a magnetic field and is usually included as ZFS term $\hat{H}_{ZFS}$ into the spin Hamiltonian together with the rhombic ZFS parameter E according to eq. 1.15.[110]

$$\hat{H}_{ZFS} = D\left(S_z^2 - \frac{1}{3}S(S+1)\right) + E(S_x^2 - S_y^2) \tag{1.15}$$

If the sign of D is negative the state with the largest spin momentum is lowest in energy, which enables SMM behaviour. An energy barrier U_{eff} between the microstates m_S (in case of most 3d metal complexes) with positive and negative sign arises (see fig. 1.9) obeying the correlation given in eq. 1.16.

$$U_{\text{eff}} = |D|S^2 \text{ for non-integer total spins: } U_{\text{eff}} = |D|\left(S^2 - \frac{1}{4}\right) \tag{1.16}$$

This energy difference often called anisotropy barrier is one important measure for the temperature dependent SMM properties, the larger it is the higher the expected blocking temperature T_B can become. Below this temperature the SMM shows magnetic hysteresis, it is therefore the most important classification number for an SMM. Since the existence of magnetic hysteresis is

strongly dependent on the magnetic field sweep rate, it is widely agreed in the community to rather determine it as the uniting point of the zero field cooled and field cooled magnetisation curve as already described by Sessoli *et al.*,[47] therefore the concept will also be followed within this work.
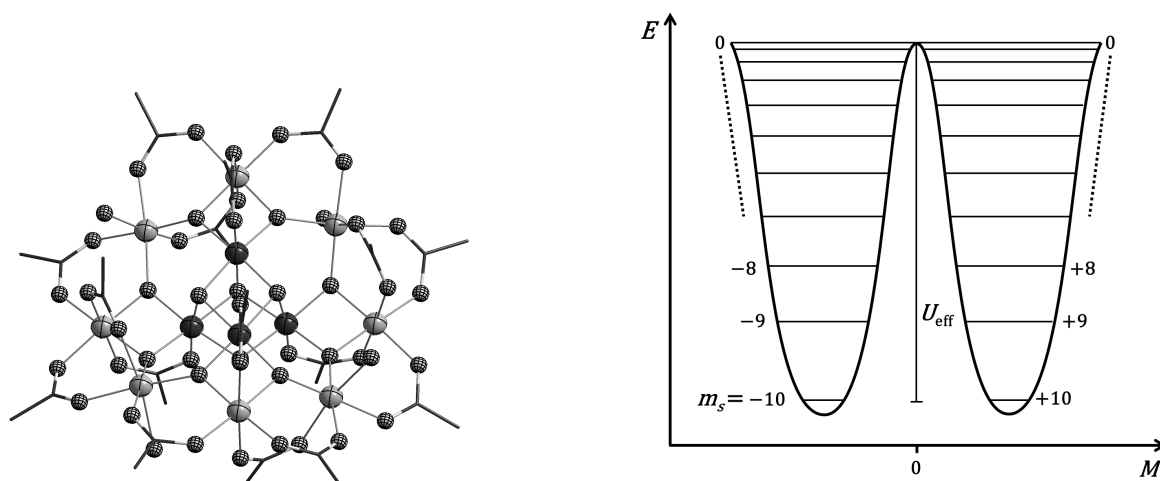
Figure 1.9: Left: Molecular structure of [Mn$_{12}$],[103] which is the first molecule SMM behaviour has been observed for.[47] Hydrogen atoms are omitted for clarity, C atoms are wire nodes, O: chequered, Mn(III) light grey, Mn(IV) dark grey. **Right:** Double well potential of [Mn$_{12}$] resulting from the anisotropy barrier U_{eff} between the microstates m_S with opposite sign.

The overall ZFS parameter D of a molecular magnet consisting of coupled 3d metal ions (for which the D formalism is applicable)[110] is strongly correlated to the single-ion anisotropy D_i, which itself is limited by the condition $S_i D_i S_i < 15\,\mathrm{cm}^{-1}$.[111] This results in the necessity for large numbers of ferromagnetically coupled ions to generate anisotropy barriers of some hundred wavenumbers, which is a challenge in itself. Unfortunately, the additional condition arises, that the single-ion anisotropy axes have to be aligned collinear, otherwise the overall D of the molecular magnet is reduced drastically. To deliberately tailor both of those conditions by means of coordination chemistry is a tough challenge. This is illustrated by the fact that the record anisotropy barrier Mn(III) cluster consists of only six Mn(III) centres,[111–113] while many clusters with more metal centres feature only neglectable anisotropy barriers.[114–117]

Consequently an alternative is needed to achieve the ambitious goal of making SMMs feasible for applications. One approach suggested and followed is the use of 3d metals with significant unquenched orbital angular momenta as well as ligand fields low in symmetry and coordination number.[118,119] Of course, the deliberate design of such chemical environments is a lot easier to realise for mononuclear complexes and the need for collinear alignment of magnetic anisotropy axes of multiple centres within the molecule becomes obsolete. Therefore, this approach is mainly followed by means of so-called single-ion magnets (SIMs, term first introduced by Ishikawa *et al.*[120]) containing only one 3d metal centre and has brought considerable progress into the field.[118,119,121,122] However, this branch shall not be further detailed here, since it has no bearing upon the content of this work.

1.3.1 Origin of Single-Ion Anisotropy in Lanthanoids and its Optimisation

Another class of metal ions featuring large total angular momenta and high single-ion magnetic anisotropies are lanthanoid ions. Hence, their use for SMM design is self-evident, but accompanied by some crucial differences in electronic structure and magnetism in comparison to 3d metals. First of all, the evolution of the states being responsible for the magnetic behaviour of the ions shall be developed. The interaction causing the highest differences in energy of electronic states is the electron–electron repulsion defining also the spin moment S of the ground state. The further energetic splitting is sketched for the example of the Dy^{3+} ion in figure 1.10 also depicting some approximate energy dimensions of the respective splittings. Subsequent in energy a splitting of electronic states is caused by spin–orbit coupling of the spin momentum S with the orbital angular momentum L, which is much stronger than for most 3d metals and resulting in spin–orbit coupled states J. Ultimately, the ligand field splits the spin–orbit coupled states J into the microstates m_J. As compared to 3d transition metals, the ligand field splitting is weaker due to the shielding of the f-orbitals, yet it is the contribution one can tailor by chemical means to evoke SMM properties.[117,123,124]

The anisotropic electron density distributions for the respective microstates were calculated and visualised by Sievers[126] and Rinehart *et al.*.[125] One can learn there, that for the late lanthanoids especially relevant for SMM design the electron density of the m_J states with the maximum total angular momentum is oblate (Tb^{3+}, Dy^{3+}, Ho^{3+}) or prolate (Er^{3+}, Tm^{3+}, Yb^{3+}) in shape (see fig. 1.10). Hence, to selectively stabilise these states and consequently maximise the anisotropy barrier by increasing the separation of the m_J states these geometries have to be enforced by the ligand environment. For oblate ions an axial ligand field is needed, whilst the SMM properties of prolate ions benefit from an equatorial ligand field.[125] Despite this knowledge the chemical implementation of these concepts remains challenging, because lanthanoid ions do not feature preferred coordination numbers or geometries. Instead their coordination behaviour is variable and governed by their Lewis acidity as well as steric demand and pre-organisation of the ligands. Hard and highly charged donors are preferred by Ln^{3+} ions and usually form the shortest bonds, which then determine the magnetic anisotropy axes and crystal field splitting.[117,124,127,128] Nevertheless, compounds scratching the limit[129] of imaginable chemical realisation of axial[130,131] and equatorial[132] ligand fields were synthesized also using organometallic tools.

1.3.2 Magnetic Relaxation in Ln³⁺ SMMs and its Investigation

Eventually taking a closer look at the magnetic relaxation of SMMs it can quickly be captured, that the maximisation of local magnetic anisotropy is not the only ingredient necessary to increase T_B. In contrast to spin qubits, where the spin–spin relaxation times T_2 are most relevant, the spin–lattice relaxation governs the slow relaxation of magnetisation in SMMs.[117,128,133] So the theory developed for spin–lattice relaxation in inorganic solids[134,135] in principle also applies here. However, there are some differences between relaxation behaviour in 3d transition metal
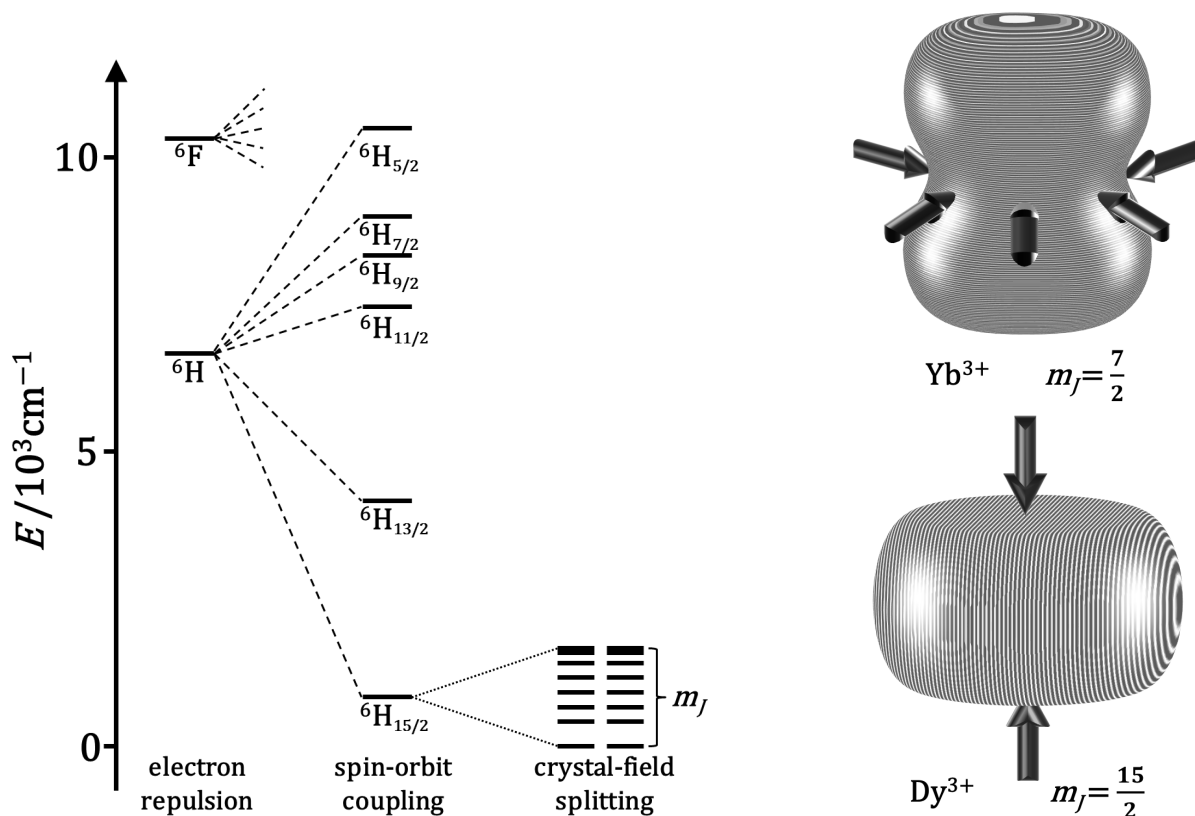
Figure 1.10: Left: Schematic illustration of the low energy electronic structure of the Dy(III) ion with sequential perturbations of electron-electron repulsions, spin–orbit coupling, and the crystal field. The energies for crystal field splitting into eight Kramers doublets (m_J) are arbitrary. Energy is measured relative to the ground m_J state. Crystal field splitting of higher ^{6}H terms and further splitting of ^{6}F term as well as all terms higher in energy and possible mixing of states are not depicted for the sake of clarity.[125] **Right:** Approximations of the angular dependence of the total 4f charge density for the maximum total angular momentum m_J states for the prolate Yb(III) ion (top) and the oblate Dy(III) ion (bottom). The black arrows sketch ideal electron donor approaching directions to stabilise these states (equatorial for Yb(III), axial for Dy(III)) and thereby optimise the magnetic anisotropy for SMM behaviour.[125,126]

ion complexes and that based on lanthanoid ions as well as between Kramers (non-integer m_J) and non-Kramers (integer m_J) ions. The following discussion is focused on lanthanoid Kramers ions due to their major relevance in this work and frequent usage for SMM design in general.[136–138]

One relaxation process that might occur is the so-called direct process. It describes a direct transition from one crystal field microstate m_J to another one m_J'. The energy difference is transferred to the lattice as an acoustic phonon, which is a single quantum of a long-wavelength lattice vibration, hence it is a one-phonon process. This process is forbidden for Kramers ions, if the two states involved are mirror images ($m_J' = -m_J$). Therefore, it only becomes relevant with large magnetic fields applied, when different m_J states get closer in energy. Also the energy differences are very small ($\sim 1\,\mathrm{cm}^{-1}$), where there are hardly any phonon states available in this energy range.[128,135]

More relevant spin–lattice relaxation processes, especially at temperatures above 5 K are two-phonon processes involving phonons of higher frequencies, where the density of states increases. In the first-order Raman process, the released energy from the relaxing spin system is taken up into a superposition of two phonons matching the energy difference, which can be seen as a virtual intermediate state of the lattice. In case of a second-order Raman process, also the spin system is subject to a transition *via* a virtual intermediate state. The latter can in theory lead to relaxation with an apparent thermal barrier smaller than the gap to the first excited m_J state, which was observed for several complexes.[139–141] However, these observations can also be explained by correlations between the spin-system and off-resonance normal modes of the individual molecules without second-order effects involved following the same Arrhenius like temperature dependence.[142,143] Such phenomena will be related to as vibrational mode correlated relaxation of magnetisation (VMCRM) in all further discussion within this work.
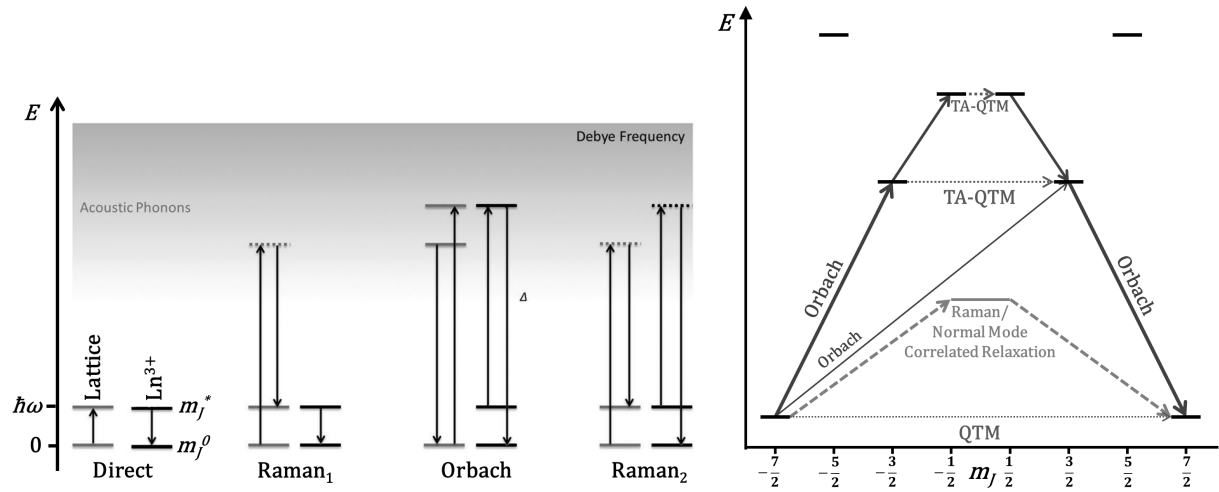
The last spin–lattice based relaxation process discussed here is the Orbach process. An excited state m_J' is actually populated by absorption of one phonon and subsequently relaxed to the m_J^0 ground state. This does not necessarily lead to a loss of the magnetic information, meaning a population equilibration between m_J and $-m_J$. It is the only process featuring the essential need to overcome the energy gap between m_J^0 and m_J', which can be chemically tailored *via* the local crystal field.[128,135]

Another relaxation mechanism of high importance for lanthanoid based SMMs not being a spin–lattice relaxation process is quantum tunneling of magnetisation (QTM). Tunneling of magnetisation is a quantum phenomenon, which was first observed for small ferromagnetic particles.[144] Little later it was measured as defined steps in hysteresis curves of $[Mn_{12}]$[145,146] at discrete magnetic fields causing two different m_S states to be nearly equal in energy and therefore have a finite tunneling probability. It especially occurs at low temperatures, when all temperature-dependent (spin–lattice) relaxation pathways are effectively blocked. Quantum tunneling itself is temperature-independent, but relies on transversal elements coupling the involved m_J states.[128,147] These can be caused by hyperfine interactions with nuclear spins,[148] effective transverse magnetic fields, *e.g.* non-collinear anisotropic magnetic ions in the environment and transversal (perpendicular in case of axial systems) components in the g-tensor of the ground state m_J^0. If these criteria are fulfilled in an excited state m_J' a prominent thermally assisted (TA-)QTM is expected and often observed in lanthanoid based SMMs.[148,149] One should mention here that magnetic fields regardless of their origin can as well reduce the tunneling rate due to an energetic shift of the involved m_J states.[128,150]

All the described relaxation processes are illustrated in fig. 1.11. Their respective contributions to the overall magnetic relaxation of the molecular system can be gathered in equation (1.17) also illustrating the temperature dependence of the processes.[128,153]

$$\tau_T^{-1} = A \cdot \exp\left(\frac{-\Delta_{\text{rev}}}{k_{\text{B}T}}\right) + BT^n + \frac{C_1}{1 + C_2H^2} + DH^mT \tag{1.17}$$

This very equation is used to parameterise the temperature (T) and for some cases also

Figure 1.11: Left: Schematic depiction of spin-lattice relaxation processes occurring in lanthanoid-based SMMs. Grey bars are acoustic phonons of the lattice, black bars are m_J states of the lanthanoid ion, dashed bars are virtual states. The grey shade intensifying with higher energy illustrates the increasing density of lattice states (acoustic phonons) up to the Debye limit. Scheme adapted from [128]. **Right:** Relaxation scheme of an arbitrary Yb^{3+} complex with an equatorial ligand field [125] including all m_J states (especially excited states undergo significant mixing, [151,152] which is neglected here). The thickness of the arrows represents a qualitative discrimination of the transition probabilities. TA-QTM means thermally assisted quantum tunneling of magnetisation, direct processes are not depicted due to their low probability for Kramers ions in the absence of large magnetic fields.

magnetic field strength (H) dependent magnetic relaxation of an SMM. In order of appearance the summands account for the Orbach, Raman, QTM and direct processes, where A, B, C_1, C_2 and D are the respective rate determining constants. In the absence of a magnetic field, the term for the tunneling process can be summed to a single rate constant C_{QTM}. The exponents n and m characterise the temperature dependence of the Raman and the magnetic field dependence of the direct process. According to theory, $m = 2$, $n = 9$ for a Kramers ion, $n = 5$ in the presence of low lying states of the spin system, [128,135] however, in fittings of experimental data especially of polynuclear Ln(III) ion based SMMs often minor deviations from these values are found and discussed. [154,155] The parameter Δ_{rev} appearing in the Orbach term can be the energy gap to the excited crystal field state, which is an intermediate state for the particular relaxation process (Δ_{CF}), analogous to U_{eff} in transition metal cluster SMMs. It can also describe the apparent thermal barrier of vibrational mode correlated relaxation of magnetisation (VMCRM) (Δ_{vib}), which also has an Arrhenius-like temperature dependence. [143]

The experimental determination of the magnetic relaxation time τ_T in dependence of temperature can in principle be carried out by measuring the time-dependent decay of magnetisation (M) on a previously magnetised sample by means of a SQUID magnetometer and subsequent fitting of the curve with an exponential decay law given in eq. (1.18), where t is time and α is the dispersion coefficient. The theoretical borders of the latter are $\alpha = 0$, which means a single relaxation process and $\alpha = 1$ which means an infinite number of relaxation processes, so it contains hints about different relaxation regimes at different temperatures.

$$M(t) = \exp\left(\frac{t}{\tau_T}\right)^{1-\alpha} \tag{1.18}$$

Admittedly, SQUID magnetometry is a very slow method in comparison to spectroscopy, therefore this method is only successful for molecular magnets with $T_{\mathrm{B}} > 2\,\mathrm{K}$ at very low temperatures.[130,131,156] For a broader temperature range characterisation frequency (ν) dependent AC magnetic susceptibility measurements are performed. In this case, the AC magnetic susceptibility χ splits up into a real (χ', in-phase) and an imaginary part (χ'', out-of-phase) (see eq. (1.19), $\omega = 2\pi\nu$).

$$\chi(\omega) = \chi'(\omega) - i\chi''(\omega) \tag{1.19}$$

The distribution of the components characterises the interplay of magnetic response and energy dissipation. A phase delay occurs due to the slow relaxation processes, so τ_T is the time required to restore a thermal equilibrium χ. An isothermal susceptibility χ_T, which is identical with χ for $\omega\tau_T \ll 1$, and an adiabatic susceptibility χ_s observed when $\omega\tau_T \gg 1$, because of the delayed response of the magnetic susceptibility, can be derived.[157,158] The AC data can be fitted to eq. (1.20) applying a generalised Debye model to extract χ_T, χ_S, τ_T and α.[6,159]

$$\chi(\omega) = \chi_s + \frac{\chi_T - \chi_s}{1 + (i\omega\tau_T)^{1-\alpha}} \tag{1.20}$$

The obtained temperature dependence of τ_T is usually plotted as $\ln(\tau_T)$ vs. T^{-1}, so that processes with an Arrhenius-like temperature dependence as well as pure QTM appear as linear areas and the curve can be fitted to variations of eq. (1.17) to describe the relaxation behaviour over the whole available temperature range.[157,158] The energy barrier(s) for spin reversal extracted from these fits will generally be named Δ_{rev} within this work, because it is not always clear whether it corresponds to an energetic gap between crystal field states m_J (and if yes, which states are involved) or VMCRM.[143] To shed additional light on the nature of the relaxation processes featuring thermal barriers, *ab-initio* calculations revealing the energies of the crystal field states are of high value. Furthermore, very recently a Mößbauer-spectroscopy related method to measure vibrational modes potentially relevant for magnetic relaxation was reported by Schünemann *et al.*,[160] but is not exploited in this work.

1.3.3 Recent Highlights and Improvement Approaches

Since the nature of the different relaxation processes is described, design criteria should be developed and cast into chemical realisations, which then approach the ideal lanthanoid-based SMM. During the last decade nearly all published SMMs with "record breaking" T_B or Δ_{rev} were based on Dy(III).[130,131,156,161–164] So one can most probably accept this very ion as the most

suitable candidate to create the "ideal SMM", being the oblate Kramers Ln^{3+} ion with the largest J and the most linear evolution from axial to equatorial electron density distribution of the free-ion m_J states.[125,165] Hence, a strictly axial ligand field cannot only maximise local magnetic anisotropy but also provide a high purity of the m_J ground state as well as the first few excited states.[165]
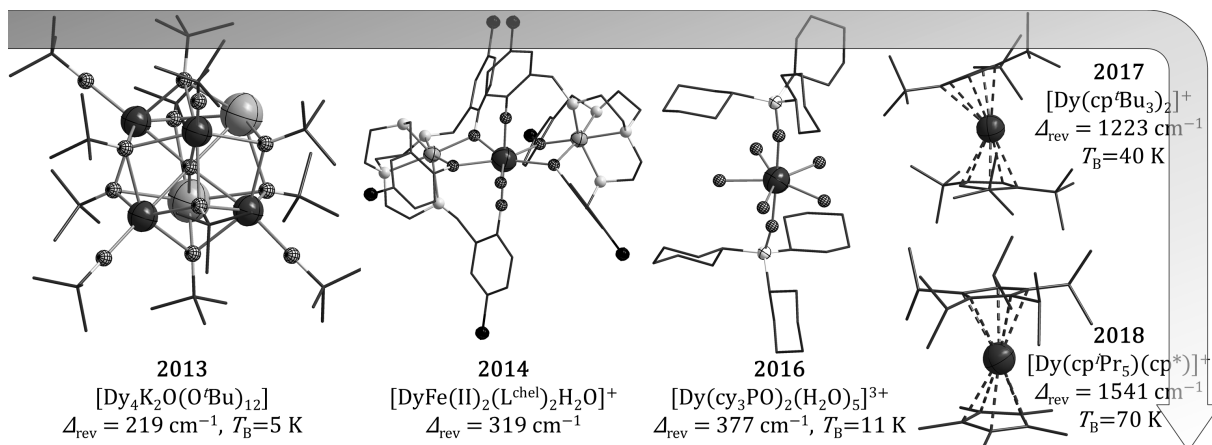
Figure 1.12: Some highlights of SMM development published during the last decade, the arrow marks progress in time. H atoms and counterions are omitted for clarity, wire nodes are carbon, dark grey large ball: Dy, grey giant ball: K, grey ellipsed: Fe, chequered: O, light grey: N, white ellipsed: P. Structures and data reported in [130,161,162,164,165] (from left to right).

A deeper sight into the mentioned record complexes (see figure 1.12) in chronological order reveals that 2013's champion is a tetranuclear Dy(III) cluster with T_B=5 K.[161] In 2014 a heterometallic [Fe(II)$_2$Dy][162] complex took over the reversal barrier record for d-f SMMs. Mononuclear pentagonal bipyramidal Dy(III) complexes[163,164] in 2016 approached areas of T_B >10 K. Then mononuclear organometallic dysprosocenium compounds set the pace in 2017 and 2018 and still occupy the highest reported T_B.[130,131,156] This suggests, that progress in SMM indeed is a story of individualism with respect to nuclearity, a claim that yet needs to be probed. The high T_B dysprosocenium compounds are also extremely sensitive to air and water. So the need for further optimisation and exploitation of different concepts has not at all diminished.

One point already raised is heterometallic 3d-4f complexes, which is a fascinating playing field for sophisticated coordination chemistry design approaches due to the different coordination behaviour of 3d and 4f metals. A huge variety of compounds has been reported till today.[137,166–170] Meanwhile, it can be concluded, that especially magnetically isotropic paramagnetic[169,171] or diamagnetic[168,170,172] 3d metal ions can be beneficial for enhancing SMM properties. For magnetically anisotropic 3d ions, it is hard to achieve collinearity of local anisotropy axes and suppress adverse mixing of microstates.[150] Although it is promising, this area will not be further detailed here for it is not within the scope of this work.

A design criterion inherently influencing nearly all possible relaxation pathways is local symmetry around the lanthanoid ion. Most obvious, the coordination geometry governs the local magnetic anisotropy and, as we already have found out, strictly linear coordination is optimum for oblate ions, which would correspond to a local C_∞ symmetry. Since this situation
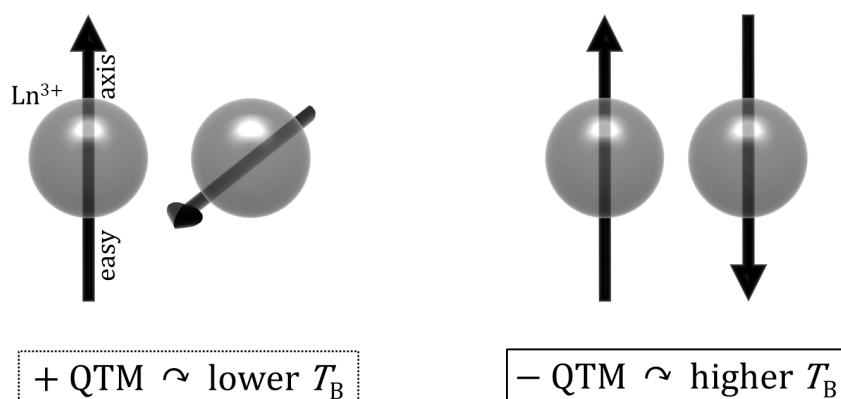
is hard to achieve due to chemical limitations, taking a closer look is not in vain. With respect to vibrational mode correlated relaxation processes driven by spin–phonon coupling,[143,173] which are the limiting factor in recent high-temperature SMMs,[174] high molecular symmetry is expected to be beneficial. Because the total number of vibrational modes is reduced with increasing molecular symmetry—as follows from group theory—the available pathways are reduced and the vibrational structure is more discrete. However, research on spin-phonon coupling in molecular magnets is in progress and latest results also mention a high molecular rigidity and weak intermolecular interactions to suppress respective relaxation pathways.[175] Eventually, also suppression of QTM can effectively be tackled by symmetry considerations, as it relies on transversal crystal field components.[147] For certain coordination geometries with point symmetries C_n ($n \geq 7$), C_{5h}/D_{5h}, S_8/D_{4d} and S_{12}/D_{6d} all transverse crystal field parameters vanish, so QTM should be minimised.[165] Unfortunately, any kind of true C_5 symmetry contradicts the laws of crystallography, so that the examples of pentagonal bipyramidal Dy(III) SMMs can only feature a D_{5h} pseudo symmetry.[163,164,176–180] However, the effect was impressively demonstrated for D_{4d} symmetry in comparison to C_4 on an otherwise chemically identical structure.[172,181]

Another non-neglectable influence especially enhancing QTM are hyperfine interactions of the spin system with nuclear spins.[182,183] In that respect, designing donor environments lacking nuclear spins should be constructive, but the strongest effect originates from the nuclear spin of the lanthanoid ion itself. Hence, its removal by isotopic enrichment yields the largest improvements of SMM behaviour.[184] In rare cases the interaction with the nuclear spin can even lead to suppression of QTM due to effective coupling of a non-Kramers ion as Ho(III) to a Kramers-like ground state.[185] Nevertheless, a removal of nuclear spins is beneficial for the demanded magnetic properties in most cases.

1.3.4 Coupling Lanthanoids in Dinuclear Complexes

One more aspect shall be brought up here, namely the magnetic interactions between lanthanoids. These interactions are generally weak due to the shielding of the f electrons, which prevents effective superexchange mechanisms.[13] Therefore, the dipolar interaction usually delivers the main contribution, which is strongly anisotropic and distance-dependent as was pointed out in section 1.2. Other components of apparent coupling are usually hard to characterise, however theoretical approaches made good progress in the appropriate description of magnetic exchange in lanthanoids.[186,187]

Already for the coupled manganese cluster SMMs, it was observed that exchange coupling can effectively suppress QTM relaxation if the anisotropy of the single centres is aligned in a suitable way.[188] In the case of lanthanoids, the ideal case for QTM suppression is an exactly collinear alignment of the easy axes of magnetisation (a coplanar alignment for easy plane cases).[189] This effect can be explained by a local magnetic field caused by the neighbouring spin leading to an energetic shift between the two otherwise degenerate microstates $+m_J$ and $-m_J$ making QTM less probable. As follows from (1.13) the higher the proximity of the involved ions is the larger the effect becomes. Numerous Dy(III) dimers tackling this goal were reported[136,190–192]

Ln^{3+} axis easy

$\boxed{+ \; \text{QTM} \; \curvearrowright \; \text{lower} \; T_\text{B}}$ $\boxed{- \; \text{QTM} \; \curvearrowright \; \text{higher} \; T_\text{B}}$

Figure 1.13: Schematic representation of two possible alignments of the single-ion magnetic ground state's easy axes of magnetisation in a dinuclear arrangement of Ln^{3+} ions with easy axis magnetic anisotropy. The skew alignment of easy axes shown on the left hand side gives rise to transversal spin components enhancing QTM, whilst the collinear (antiparallel) alignment on the right hand side effectively suppresses magnetic relaxation *via* QTM due to local magnetic fields energetically splitting $+m_J$ and $-m_J$.

but an exactly collinear arrangement of the easy axes remains rare in literature and often the Dy centres feature a poor local anisotropy.[189,193–196] An exploitation of this effect has recently been aspired for dysprosocenium building blocks, but an improvement in comparison to the single-ion congeners could not yet be achieved.[197–200] The trouble about the approach is, that as soon as the single-ion anisotropy axes of the ground state or even of excited states relevant for the magnetic relaxation deviate from collinearity, transversal spin components arise which then increase the QTM rate and degrade the SMM behaviour (see also fig. 1.13).

A further boost of magnetic interaction can be obtained by bridging via radical ligands as was shown in many examples,[155,201,202] which also led to respectable SMM properties.[203–206] Again the transversal spin component introduced into the coupled spin system of the molecule in most cases makes the approach a double-edged sword. However, with lanthanoids caged in fullerenes this drawback could obviously be overcome because the radical bridging and even lanthanoid-lanthanoid bonding was achieved in line with the anisotropy axes, which leads to a large T_B of 22 K.[207,208]

In summary, the design criteria for lanthanoid SMMs that can outperform the remarkable successes, which have already been achieved comprise a rigid molecular compound with minimum intermolecular interactions and high molecular symmetry. The lanthanoid centre is ideally Dy(III) and demands a stiff coordination environment with preferential point symmetries C_{5h}/D_{5h}, S_8/D_{4d} or C_n ($n \geq 7$) providing maximum axiality especially of charged donor atoms. The environment should lack nuclear spins and at least two of such centres should be in close proximity with a collinear alignment of their axial ligand fields.

1.3.5 Boon and Bane of the Triangle

If we imagine the situation of three such anisotropic lanthanoid centres designed for good SMM behaviour (*vide supra*) arranged in an equilateral triangle in analogy to what was discussed in

section 1.2, some cases of particular interest emerge.
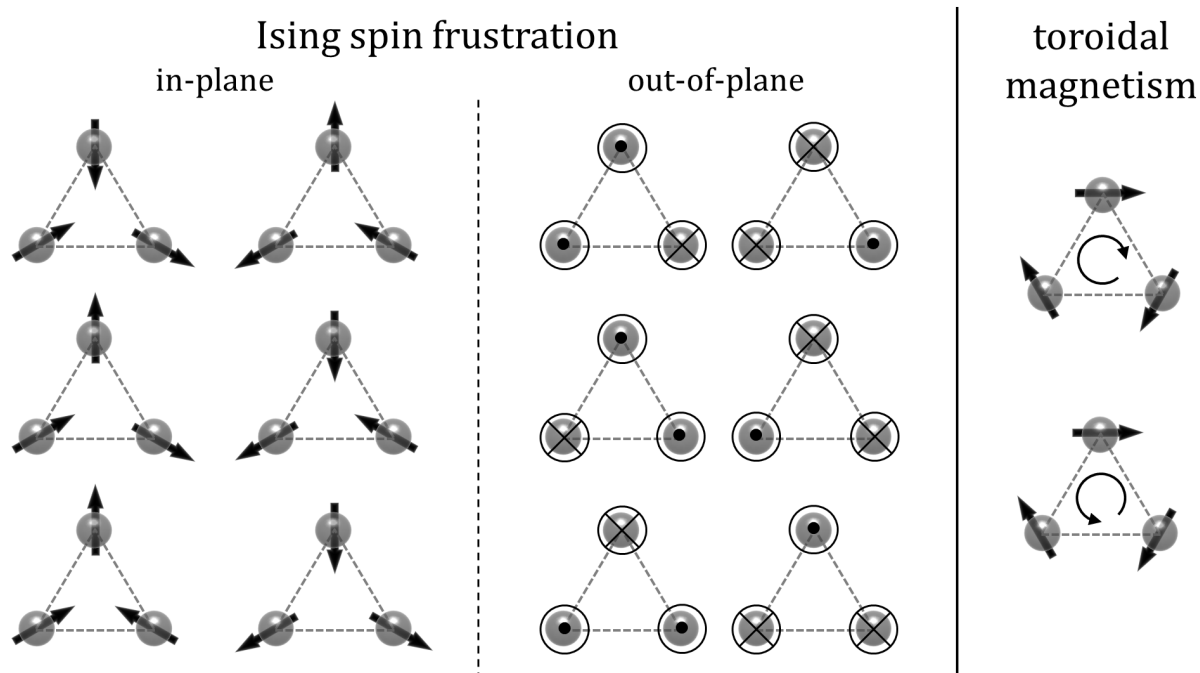
Figure 1.14: Representation of the three special scenarios of equilateral triangle arrangements of lanthanoid ions with easy axis magnetic anisotropy approximated as Ising spins and their respective ground state degeneracy, which are described in this subsection. Namely those are (from left to right) in-plane Ising spin frustration,[209] out-of-plane Ising spin frustration[210] and toroidal magnetism.[211,212]

The first case would be the easy axes of all three metal centres pointing into the centre of the triangle, resulting in intersecting angles for the anisotropy axes of 120° each, so obeying eq. (1.13) α becomes 30°, thus the dipolar interaction leads to a ferromagnetic sixfold degenerate ground state (see fig. 1.14). For this case, theoretical surveys predict that magnetisation reversal in such a triangle of three Ising spins (a valid approximation for highly axial Dy(III) centres) is facilitated in comparison to a similar system containing only two spin centres. This is mainly because for loss of magnetisation only one Ising spin has to be reversed leading to an in-(triangular)-plane spin-frustrated excited molecular state, whilst for the dinuclear case both spins have to be reverted to extinguish magnetisation.[209] Subsequent experimental results could prove this prediction right so this very situation is not a desirable design target, at least with respect to SMM properties.[213]

The next ideal scenario of interest is an all-collinear (parallel or antiparallel) alignment of the anisotropy axes of the three spin centres, hence $\alpha = 90°$ and the dipolar interaction becomes antiferromagnetic. Consequently, the molecular ground state is indeed an out-of-plane frustrated triangle of Ising spins (see fig. 1.14), nevertheless the blocking of QTM should still apply. Very recently a system nearly ideally realising this situation featuring a CO_3^{2-} ion as C_3-symmetric bridging unit was reported showing a T_B of 5 K.[210] Unfortunately it does not provide any local pseudosymmetry, so the single-ion environment still offers potential for improvement, but anyhow it is the best performing SMM among the limited number of Dy

triangles in literature also aiming for this goal.[214–218]

A third ideal arrangement of anisotropy axes is an in-plane canting, so that the magnetic moment of each individual centre is aligned along an imaginary circle connecting all corners of the triangle (see fig. 1.14). This leads to a so called toroidal ground state, which apparently does not feature a measurable magnetic moment, but only a so-called toroidal moment arising from the vortex arrangement of all spin moments with direction perpendicular to the spin plane.[211] Molecules featuring such a toroidal moment are called single-molecule toroics (SMTs) and are predicted to also show magnetoelectric effects on a molecular level, which amongst others makes them valuable targets for molecular spintronics.[219,220]
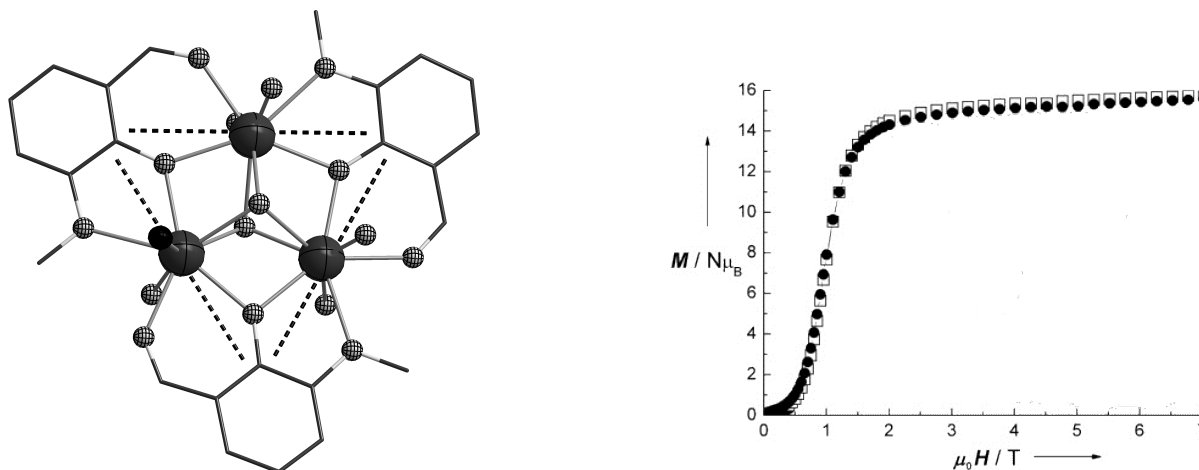
Figure 1.15: Left: Molecular structure of $[Dy_3(\mu_3\text{-}OH)_2(L^{o-van})_3Cl(H_2O)_5]Cl_3$, H atoms are omitted, C are dark grey wire nodes, Cl: black, Dy: dark grey, O: chequered.[221] The black dashed lines show the approximate orientations of easy axes of magnetisation of the single ion ground state determined *via ab-initio* calculations.[222] **Right:** Magnetic field dependence of magnetisation for $[Dy_3(\mu_3\text{-}OH)_2(L^{o-van})_3Cl(H_2O)_5]Cl_3$ (black dots) and a chemically related compound (white squares) at 2 K showing a sigmoidal shape, which is indicative for a toroidal ground state (figure adopted and modified).[221]

To the best of my knowledge, no ideal molecular realisation of an SMT has been reported yet, however, some mixed moment SMTs, where symmetry lowering with respect to the ideal case leads to incomplete cancellation of the magnetic moment are known.[211,212,223–226] The first and to date best understood example of an SMT is a Dy triangle based on *o*-vanillin (L^{o-van}) ligands $[Dy_3(\mu_3\text{-}OH)_2(L^{o-van})_3Cl(H_2O)_5]Cl_3$.[221,222] There the presence of the toroidal state could be proven in bulk by the characteristic of magnetisation to remain close to zero for low magnetic fields (sigmoidal shape, see fig. 1.15).

Due to the cancellation of net magnetic moment, SMTs, of course, can never be good SMMs, but as already mentioned they are a promising class of molecules themselves. Furthermore, the design criteria for the single lanthanoid centre within the triangular arrangement are similar to the ones for SMMs. A maximisation of local anisotropy and exclusion of transversal spin components is crucial to approach an Ising spin, which is ideal to create toroidal states.

In summary, of the three different triangular arrangements of Ising spins based on Ln^{3+} ions, only one is beneficial for SMM behaviour in comparison to a mononuclear analogue. Namely, this is a collinear alignment of all three spins perpendicular to the triangular plane.

Nevertheless, all three described scenarios are interesting targets for molecular realisations due to their ground state degeneracy as is illustrated in figure 1.14. Especially the vortex arrangement of the Ising spins within the triangular plane giving rise to toroidal moments is of particular interest for the investigation of spin-electric effects and development of molecular spintronics.[211,219,220]

1.4 Intramolecular Cooperativity via C_3-Symmetric Ligands - Universal Remedy?

In the two previous sections, various targets that could bring forward molecular spintronics and pave the way towards technological applications of molecular magnets have been devised. Central subject of this work is to create molecular realisations pointing towards these targets by means of C_3-symmetric ligands based on the carbonic acid derivative triaminoguanidine as core fragment. Here, previous works with such ligands are briefly reflected and subsequently the directions of impact conceived for this work to fulfil the design criteria sketched beforehand are elucidated.

Triaminoguanidine itself is a C_3-symmetric building block formally providing six nitrogen donor sites distributed into three coordination pockets, however, to the best of my knowledge there are no polynuclear molecular coordination compounds of pure triaminoguanidine known. The family of derived ligands mainly used in this work are Schiff-bases of triaminoguanidine and aromatic aldehydes (see fig. 1.16). The resulting compounds enable a trinucleating ligation behaviour forming N–N diazine bridges upon the now facilitated deprotonation of the core fragment. The aldehyde component is usually equipped with further donor sites, so that trinucleating ligands with three or four donor sites per pocket are readily available. This component also allows for widespread chemical modifications in terms of donor sites and geometries, polarity, bulkiness and so on. Furthermore, the free ligand as well as its deprotonated complexing form features a conjugated π-electron system spanning the whole ligand system. This provides a high extent of rigidity and preorganisation. The described ligand family will be named with the suffix "tag" in the following parts.
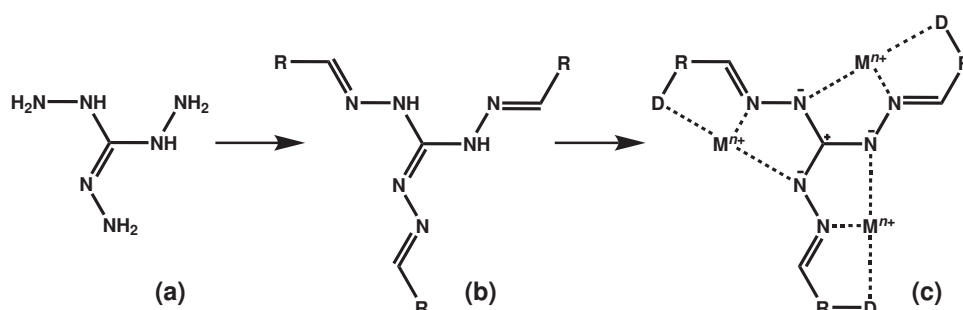
Figure 1.16: The evolution of the "tag" family of C_3-symmetric ligands from the core fragment triaminoguanidine (a) to triple Schiff-bases using aldehydes with aromatic backbones R (b) carrying additional donor atoms D, which enable a symmetric coordination of up to three metal ions M^{n+} (c). Scheme (c) also illustrates the C_3 symmetry, the N–N diazine bridging of the metal centres M^{n+} as well as the conjugated and therefore planar nature of the deprotonated ligand core.

The use of the "tag" ligand family, namely triple salicylaldehyde derivatives, as trinucleating agents was first demonstrated by Müller *et al.* in the early 2000s to build up supramolecular assemblies of diamagnetic transition metals.[227,228] Along this line the creation of various supramolecular objects like tetrahedrons and octahedrons was reported.[229–233] They also described a first discrete molecular triangle,[234] but this concept was not further pursued by them.

Jiang *et al.* investigated a "tag" ligand with 8-hydroxyquinoline-1-carbaldehyde as fluorescent probe for Cd(II) also isolating a trinuclear complex.[235] Synthetic efforts on the build-up of coupled paramagnetic systems and a profound investigation of their magnetic properties were only established over the past years in the workgroup of Prof. Plass.

First results in that field include coordination polymers based on Cu(II), which are formed in the absence of suitable capping coligands and exhibit three dimensional network structures.[236–239] Though being an interesting topic themselves paramagnetic coordination polymers are no suitable candidates for the targets outlined in sections 1.2 and 1.3 due to their "infinite" nature and therefore not further illuminated here.

Initial successes in generating discrete molecular species based on "tag" ligands were achieved by Ion for trinuclear Ni(II) complexes[240,241] and by Zharkouskaya[242] for trinuclear Cu(II) complexes. Then, major contributions to the development and understanding of the coordination chemistry of "tag" ligands with 3d metals were made by Plaul[50] and Schuch.[239] Spielberg compiled deeper insights into the spectroscopic and magnetic properties of the trinuclear Cu(II) complexes.[243]

Trinuclear Ni(II) complexes based on "tag" show antiferromagnetic coupling between the three Heisenberg-like $S = 1$ Ni(II) centres leading to a diamagnetic ground state not exhibiting geometric spin frustration.[50,239–241] Therefore, they are not suitable candidates for spin qubits or exploration of spin-electric effects. However, the investigation and interplay of local magnetic anisotropies of the Ni(II) centres[244] as well as their capability of forming pentanuclear aggregates[245] (also with heterometals in the central position)[50] remain pulsating topics.

A different story can be told for the Cu(II) case. Large antiferromagnetic coupling ($\approx 300\,\mathrm{cm}^{-1}$) is detected for trinuclear Cu(II) complexes based on "tag" ligands leading to an energetically well isolated $S = \frac{1}{2}$ ground state manifold (see section 1.2). So these systems indeed fulfill the criteria for coupled spin triangle qubits and the predicted spin-electric coupling in spin triangles discussed in section 1.2. One archetypal congener with a ligand derived from salicylaldehyde and triaminoguanidine (H_5saltag) is [Cu_3(saltag)(bpy)$_3$]$ClO_4 \cdot 3\,$dmf[246] (see fig. 1.17), which also features molecular C_3 symmetry given by the crystal structure. Modelling of magnetic susceptibility and X-band ESR spectra suggest only a neglectable contribution of Dzyaloshinski-Moriya interaction, which further emphasises its adequacy for these purposes.[98]

Unfortunately, in crystalline bulk material the compound forms closely associated dimers of triangles via π-stacking interactions resulting in significant intermolecular magnetic interaction. This represents a perturbation to the low-temperature energy structure, so synthetic efforts were undertaken to separate the molecules in bulk material. The latter include the introduction of bulky substituents such as *tert*-butyl[239] and adamantyl[247] groups to the ligand backbone, but none of these attained the desired effects. Contrariwise, the modification of the salicylaldehyde backbone often led to a loss of the crystallographic C_3 symmetry. Thus, the separation of [Cu_3(saltag)] complexes in crystalline phases, while retaining the ideal molecular C_3 symmetry remains a viable target. Furthermore, a deposition of such molecules on suitable surfaces could intrinsically solve the dimerisation problem.
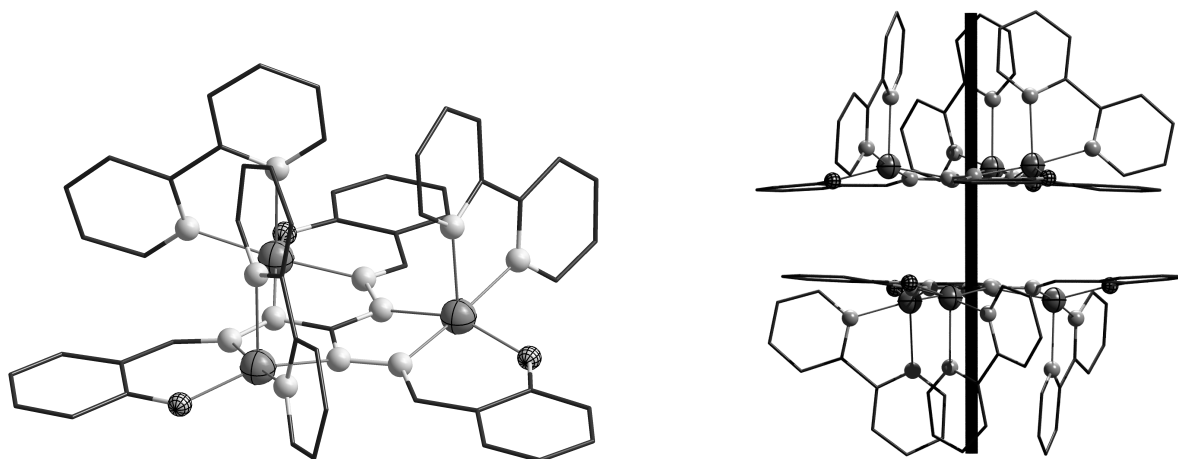
Figure 1.17: Left: Molecular structure of the spin triangle [Cu$_3$(saltag)(bpy)$_3$]$^+$, C atoms are wire nodes, O: chequered, Cu: grey, N: light grey, H atoms, cocrystallised solvent and counteranion are omitted for clarity. **Right:** Crystal packing of two [Cu$_3$(saltag)(bpy)$_3$]$^+$ complex cations illustrating dimerisation and the crystallographic C_3 axis (black line).[246]

Encouraged by these findings, the further development of spin triangles on the basis of 3d transition metals and "tag" ligands paving their way to adequate spin qubits and probes for spin-electric coupling is one key aspect of this work.

Pioneering works by Schuch revealed the feasibility of mononuclear lanthanoid complexes based on "tag" ligands (see fig. 1.18).[239] Especially the respective Dy(III) complexes show high single-ion anisotropy, as could be shown by *ab-initio* calculations[248] and noteworthy single-ion magnet behaviour. In these structures a lanthanoid is coordinated by two "tag" ligands, so that each ligand formally preserves two more coordination pockets.
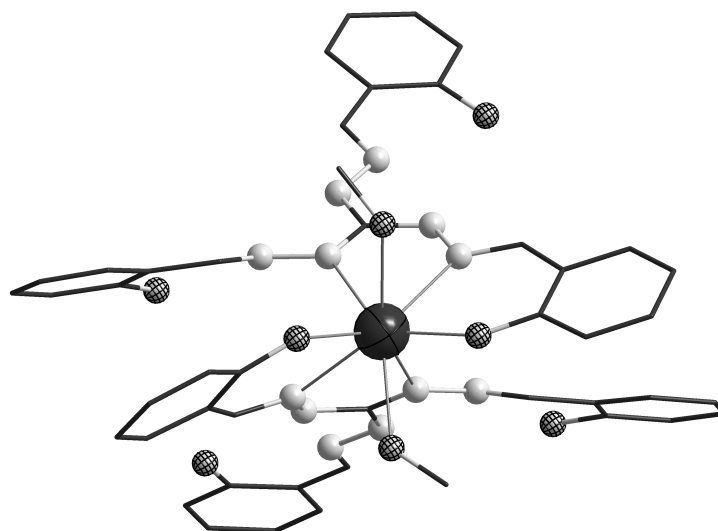
Figure 1.18: Molecular structure of [Dy(saltag)$_2$(MeOH)$_2$]$^+$, a typical congener of the mononuclear lanthanoid complexes established by Schuch.[239] C atoms are wire nodes, O: chequered, Cu(II) grey, N light grey, H atoms, cocrystallised solvent and counteranion are omitted for clarity.

Taking into consideration the discussion in section 1.3, by extending such structures to dinuclear systems a tremendous enhancement of single-molecule magnet behaviour might be achieved. The spatial proximity enables an effective blocking of quantum tunneling of magnetisation by dipolar interaction depending on the alignment of the respective anisotropy axes. The high rigidity of the ligand should ensure the conservation of the beneficial local coordination environment upon further coordination. Introducing a third lanthanoid ion gives rise to the exciting triangular setup. Thanks to the expected high local anisotropy of the single centres, compounds finding themselves in the hypersurface between geometrically frustrated Ising spins, cooperative polynuclear SMMs and single molecule toroics can be postulated.

Because of that, exploring the chemistry of polynuclear lanthanoid complexes of "tag" ligands and evaluating their potential for enriching the field of molecular magnets for quantum technologies is the second focal point of this work.

In summary, this means that "tag" ligands with their inherent properties of tritopicity, C_3 symmetry, rigidity, capability to mediate magnetic interactions and chemical versatility shall indeed be exploited as universal remedies to tackle the various hot topics in molecular magnetism introduced in the two prior sections.

C_3-Symmetric Ligands Based on Triaminoguanidine

In this short chapter, all ligands synthesised and used for complexation in the frame of this work are introduced and described. A summary of structures and corresponding abbreviations is presented, so as to facilitate comprehension of the succeeding chapters.

As was already explained in section 1.4, the triaminoguanidine core is a C_3-symmetric building block, which provides entirely planar conjugated molecules after a triple Schiff-base condensation with aromatic aldehydes. Especially if the aromatic aldehyde bears additional donor functions, tritopic ligands evolve, meaning ligands featuring three equivalent coordination pockets, which cannot chelate the same metal ion and are inherently bridged via N–N diazine bridges. All of these ligands retain the triaminoguanidine core consisting of one carbon and six nitrogen atoms forming a plane, which is referred to as "tag plane" (least squares approximation if not an ideal plane) henceforth. The tag-based ligands are categorised by the type of aldehyde they are condensed with.

Synthesis works similar for all ligands presented in this section by reacting somewhat more than three equivalents of the aromatic aldehyde in MeOH with an aqueous solution of one equivalent triaminoguanidine hydrochloride yielding the respective hydrochloride form. Therefore, synthetic strategies are not further detailed for the individual tag-based ligands.

2.0.1 saltag Ligands

The family of tag-based ligands known for the longest time[227] and most extensively studied are the triple Schiff-bases of triaminoguanidine and salicylaldehyde (saltag). By the phenolic hydroxo group, one additional protonated donor moiety is introduced, so that each pocket bears a tridentate [N_2O] donor set. By coordination of a metal ion, one five-membered and one six-membered chelate ring is formed within one pocket.

The free ligand is best described as H_5saltag, indicating that it can provide up to five negative charges by deprotonation under common synthetic conditions. For synthetic reasons the saltag
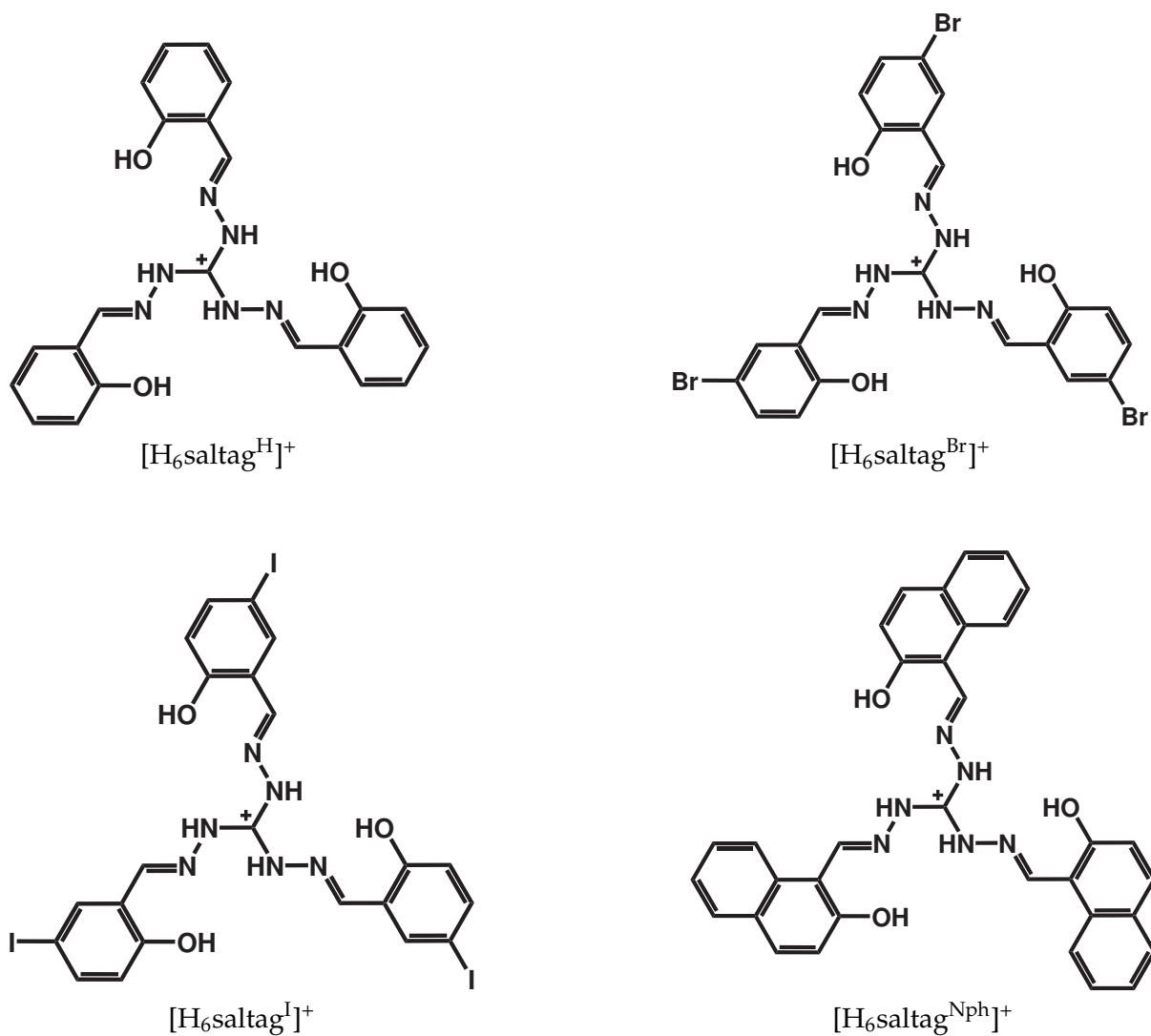
Figure 2.1: Structure schemes of the saltag-based ligands used in this work. Chloride counteranions are omitted, so that the cationic forms illustrating the C_3 symmetry are depicted. All Schiff-base moieties are in *trans*-configuration. The ligands are drawn in the conformation most appropriate for tridentate coordination of the three identical pockets.
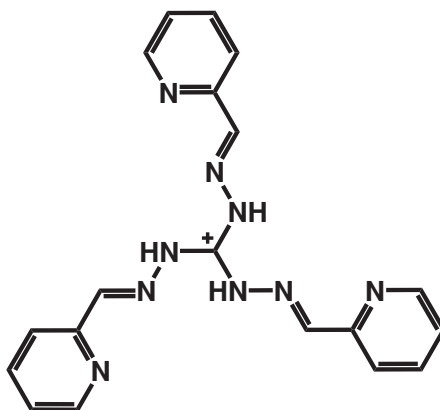
Figure 2.2: Structure scheme of H_2pytag $\cdot$ HCl. The chloride counteranion is omitted. All Schiff-base moieties are in *trans*-configuration. The ligand is drawn in the conformation, in which it was reported to undergo tridentate coordination of the three identical pockets.[50,249]

ligands as well as all other tag-based ligands mentioned in this work are isolated and used as their hydrochloride salts, extending the abbreviation to H_5saltag $\cdot$ HCl and increasing the demand for base addition for full deprotonation up to six equivalents. Finally there are four different derivatives of saltag ligands used in the frame of this work, which are distinguished by specifiers in superscript, so that the full denomination of the unsubstituted homologue is H_5saltag$^H \cdot$ HCl.

Beside the ligand derived from unsubstituted salicylaldehyde, H_5saltag$^H \cdot$ HCl,[227] two ligands derived from salicylaldehyde carrying a halogen substituent in 4-position H_5saltag$^{Br} \cdot$ HCl[229] and H_5saltag$^I \cdot$ HCl (first reported in this work) as well as one ligand derived from a 3,4-benzo anellated salicylaldehyde H_5saltag$^{Nph} \cdot$ HCl[239] are relevant for this work. These ligands' structures are sketched in fig. 2.1.

In comparison to H_5saltag$^H \cdot$ HCl, the acidity of the phenolic OH group is increased in H_5saltag$^{Br} \cdot$ HCl. The heavy atom in the periphery of the ligand raises the tendency of the system to crystallise, but also the solubility is lowered. In contrast, H_5saltag$^I \cdot$ HCl has a smaller impact on the acidity of the phenol, instead its crystallising predisposition and solubility is even higher. The extended π-system of H_5saltag$^{Nph} \cdot$ HCl enables effective π-stacking interactions, which is often beneficial for crystallisation. However, its solubility is significantly decreased with respect to H_5saltag$^H \cdot$ HCl and it is a lot more susceptible to redox chemistry, mostly meaning decomposition.

2.0.2 pytag Ligand

Condensation of triaminoguanidine hydrochloride with pyridine-2-carboxaldehyde analogously yields the ligand H_2pytag $\cdot$ HCl[249] (see fig. 2.2), which can provide only two negative charges in its deprotonated form. The pyridine-2-carboxaldehyde carries an additional N-donor site, so that each pocket is equipped with an [N$_3$] donor set and forms two five-membered chelate rings upon coordination of a metal ion. Overall, the pocket is less tight than that of saltag ligands, which alleviates complexation of larger 3d metal ions such as Co(II)[249] or Mn(II).[50]

Theoretically, a tridentate coordination forming one six-membered and one five-membered chelate ring with all-*cis* configured Schiff-base groups is imaginable for pytag. However, no such example has been reported until now. The reactivity of H_2pytag·HCl towards lanthanoid ions is not investigated at all.

2.0.3 quintag Ligand

H_5quintag·HCl, the last tag-based ligand relevant for this work, is derived from aromatic aldehyde 8-hydroxyquinoline-2-carboxaldehyde. It was first utilised in[235], however, the synthesis procedure reported there turned out to be impractical. This is why the protocol used for synthesis of H_5quintag·HCl in the frame of this work is given in the experimental part.
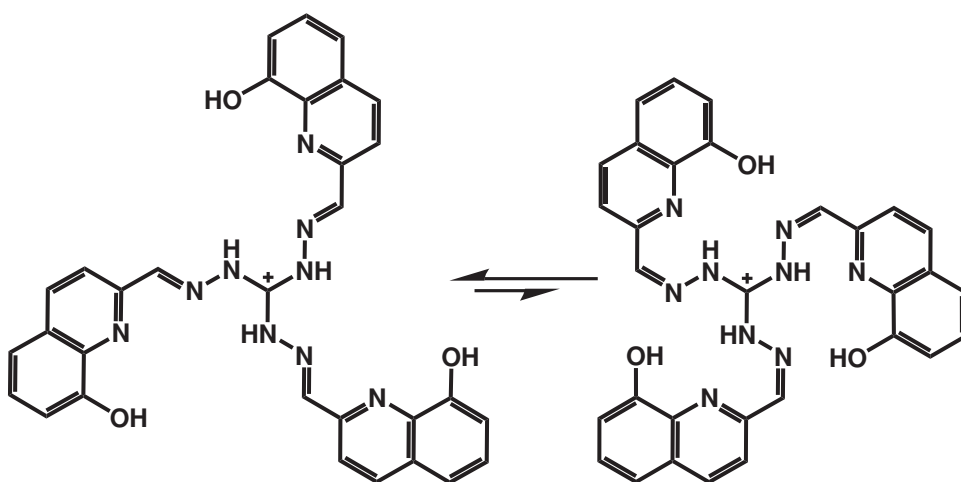
Figure 2.3: Structure scheme of H_5quintag·HCl. The chloride counteranion is omitted. Both, the all-*trans*-configuration and the all-*cis*-configuration of the Schiff-base moiety are depicted. The ligand is drawn in the conformation most appropriate for tridentate coordination of the three identical pockets.

The aldehyde component carries two additional donor functions leading to a tetradentate [N_3O] donor set for each pocket. As for the saltag ligands, five negative charges can be provided upon full deprotonation of the ligand. Two possible configurations of the quintag ligand are sketched in fig. 2.3. An in-ligand-plane chelation with Schiff-base moieties in the preferred *trans*-configuration leads to the formation of three five-membered chelate rings. This coordination mode appears suitable for large metal ions such as lanthanoids and is also the one found for a Cd(II) complex reported in literature.[235]

In contrast, an all-*cis*-configured coordinating quintag ligand forms two five-membered and one six-membered chelate rings per pocket. The donor set of each pocket forms a square plane, which is ideal for binding small 3d metal ions. Of course, to form the energetically unfavoured *cis*-configuration, additional energy input during possible syntheses might be necessary. Since the ligand features an extended π-system like H_5saltag^{Nph}·HCl, redox processes can become problematic. Therefore, the accessibility of the all-*cis* coordination mode has yet to be proven.

Magnetically Coupled 3d Metal Complexes

3.1 Geometrically Spin-Frustrated Cu(II) Complexes

3.1.1 Synthesis and Characterisation

For various reasons expounded in section 1.2 the synthesis of novel trinuclear Cu(II) complexes of tag-based ligands was desirable. One new synthesis strategy (see fig 3.1) proved very successful, namely the isolation of a presumably polymeric precursor material. This is done by combining three equivalents of the favoured Cu(II) salt, one equivalent of a tag-based ligand and the stoichiometric amount of NEt$_3$ to deprotonate the chelate ligand in DMF and enforcing precipitation of the precursor material by transferring the mixture into MeOH. Without further analysis of the precursor, its redissolution succeeds in good donor solvents. In the present work only pyridine is reported, but preliminary experiments also disclose 2,6-lutidine, 2,6-lutidine-N-oxide or morpholine and its derivatives as promising candidates, which could offer intriguing structural variations. Following this very path with pyridine followed by layering with MeOH and, if necessary, suitable weakly coordinating anions yielded five of the six compounds presented in this section.

The first complex, which was synthesised and isolated following the route described above is [Cu$_3$(saltag^H)(py)$_6$]ClO$_4$ (**1**), which is already reported.[250] Due to its high relevance, as will be further explained in upcoming subsections, an isostructural Zn(II) complex arose as synthetic target to enable diamagnetic dilution of **1** by doping single Cu(II) centres into the Zn(II) matrix. This opens access to probing single ion magnetic properties of **1**, e.g. by ESR experiments, and generally allows the deconvolution of single-ion properties from properties of the coupled spin system. To reach this aim of high importance the complex [Zn$_3$(saltag^H)(py)$_6$]ClO$_4$ (**2**) could be synthesised and crystallised by directly layering the H$_5$saltag$^H \cdot$HCl ligand above a Zn(ClO$_4$)$_2$ solution. The aptitude of the compound's structure as diamagnetic dilution matrix for **1** is discussed in the forthcoming subsection. Unfortunately, up to now all attempts to
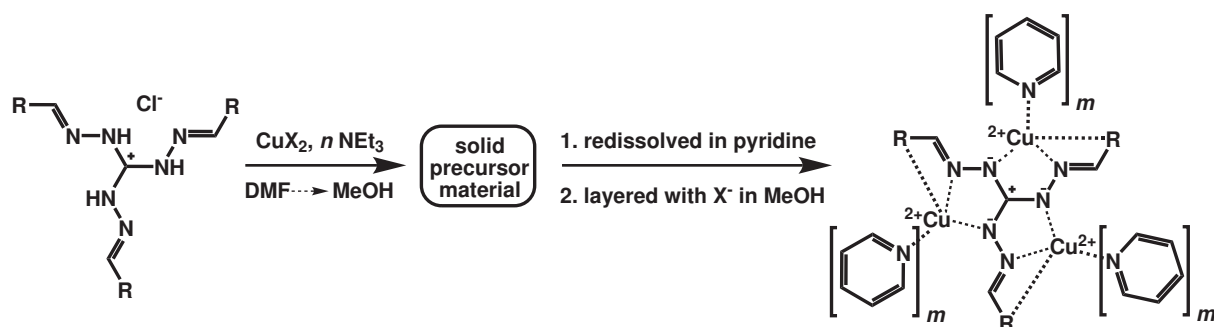
Figure 3.1: Scheme of the general synthesis route yielding five of the seven complexes presented in this section. R is the respective donor bearing aromatic aldehyde component of the tag-based ligand, X^- is a weakly coordinating monoanion, n is the stoichiometric number of protons of the tag-based ligand and m varies between 1 and 2.

synthesise diamagnetically diluted samples of **1** based on a matrix of **2** remained without success. This originates mainly from the incompatibility of unchelated Cu(II) ions with pyridine in the presence of weakly coordinating anions (immediate precipitation of pyridine adducts).

By varying the weakly coordinating counteranion in the synthesis route schemed in 3.1 the compounds $[Cu_3(saltag^H)(py)_6]NO_3$ (**3**) and $[Cu_3(saltag^H)(py)_3OTf]$ (**4**) are feasible. Encouraged by the tremendous effect of the counteranion on the complex structure, the concept was transferred to the synthetic path used by Spielberg *et al.*,[246] namely admixing $H_5saltag^H \cdot HCl$ ligand, Cu(II) salt and NEt$_3$ in stoichiometric ratio 1:3:6 in DMF and layering with a MeOH solution of 2,2′-bipyridine. This approach yielded complex $[Cu_3(saltag^H)(bpy)_3]OTf$ (**5**). However, since **5** shows very similar molecular structure and magnetic properties to the compound treated in[246] the idea was not pursued onward.

Eventually, using the novel H$_5$quintag ligand, which provides an additional donor site per pocket, two Cu(II) complexes were synthesised, isolated and structurally characterised. In both cases the path schemed in fig. 3.1 was followed. If in the synthesis Cu(ClO$_4$)$_2$ is employed as Cu(II) source and the reaction is kept at room temperature the expected trinuclear compound $[Cu_3(quintag)(py)_3]ClO_4$ (**6**) is isolated. In contrast, taking CuCl$_2$ as starting material and the application of heat during the synthesis yields the hexanuclear neutral complex $[Cu_6(quintag^{ox})_2(py)_4]$ (**7**). In this complex two Cu(II) triangles are fused by coordinative bonds (detailed explanation in the next subsection) and each ligand molecule became oxygenated at one of its three Schiff-base carbonyl C atoms. Hence, one Schiff-base moiety of each ligand is now a carboxylic acid amide, which is deprotonated in its ligating form. Therefore, the monoanionic charge needed to counterbalance the complex cation in all other complexes reported in this section is now borne by the formal chelate ligand H$_6$quintag^{ox}.

For all mentioned complexes CHN elemental analyses confirmed the chemical composition. Partially, minor changes in the content of non-coordinating solvent with respect to the X-ray single-crystal structure analysis are revealed. ESI-MS experiments succeed for the saltag^H based complexes **1**, **3**, **4** and **5** mainly showing signals of the complex cation with pyridine or 2,2′-bipyridine coligands partly removed or replaced by MeOH. ESI-MS spectra of **2**, **6** and **7** recorded under comparable conditions did not exhibit signals related to the trinuclear complex

fragments, which is most probably due to their very poor solubility in polar protic solvents.

3.1.2 Crystal Structures

[Cu$_3$(saltag^H)(py)$_6$]ClO$_4$ (1)

A detailed structure description of **1** has already been reported.[250] Crystals of **1** exhibit the polar trigonal space group $P31c$ (#159). The asymmetric unit contains two crystallographically independent Cu centres (Cu1 and Cu2), each encircled by one third of a saltag^H ligand and two pyridine coligands, respectively. One third of a pyridinium cation, one third of two water molecules and one third of three perchlorate counteranions, respectively, are also incorporated in the asymmetric unit, so that a C_3 operation yields the chemical composition [Cu$_3$(saltag^H)(py)$_6$]$_2$Hpy(ClO$_4$)$_3 \cdot$ 2 H$_2$O. Both complex cations formed by Cu1 and Cu2 (see fig. 3.2), respectively, are centered on a crystallographic C_3 axis, so that within the fragments all Cu centres are equivalent. The general arrangement of the individual components along the two crystallographic C_3 axes is depicted in fig. 3.3.

The copper centres of the two fragments (Cu1 and Cu2) are coordinated in a compressed trigonal bipyramidal fashion by an [N$_4$O] donor set, where an [N$_2$O] pocket is provided by the central saltag^H ligand and two pyridine molecules saturate the remaining coordination sites (fig. 3.2). For corresponding bond lengths and angles see table 3.1. The donor atoms O11 (O21) and N11 (N21) are at the apical positions of the bipyramid featuring the shortest bond lengths among the coordinative bonds (Cu1–O11: 190.7(3), Cu2–O21: 190.0(2); Cu1–N11: 197.4(3), Cu2–N21: 197.9(3) pm). The Cu–N bonds of the two pyridine ligands in the trigonal plane are rather elongated and vary between 211.9(3) and 218.5(3) pm for both complex molecules. The distorted trigonal bipyramidal coordination environment is confirmed by continuous shape measures,[251–253] which give the lowest deviation parameters for a trigonal bipyramid (Cu1: 1.694; Cu2: 1.705), and a τ parameter[254] of 0.60 for Cu1 and 0.57 for Cu2. In summary the Cu(II) coordination in both complex cations in **1** can be evaluated as very similar.

Neither the intramolecular Cu$\cdots$Cu distances of 484.23(8) pm (Cu1) and 484.06(8) pm (Cu2), nor the diazine bridging dihedral angles Cu–N–N–Cu of 176.6(2)° (Cu1) and 179.4(2)° (Cu2), which are remarkably close to 180° for an ideal in-plane position of the Cu centres, reveal significant differences between the two complex cations.

However, one crucial difference between both complex cations is their exposure to the perchlorate counteranions. Cu1 complex cation is symmetrically enclosed by two perchlorate anions (PC1 and PC2 in fig. 3.3) intruding into the "propeller"-like arrangement of the pyridine coligands above and below the tag plane. Contrarily, only one perchlorate anion (PC3 in fig. 3.3) approaches the Cu2 complex cation in an analogous manner and its opposite "propeller" site is occupied by a disordered water molecule (W2 in fig. 3.3). Significant directed electrostatic attractions with the positively charged triaminoguanidine centre of the saltag^H ligand can be assumed, because the Cl–O bond lengths in all three perchlorates are no longer equal. The one pointing towards the ligand centre is elongated with respect to the three remaining ones, which are equivalent by symmetry (see table 3.2). This observation can be interpreted as an enhanced
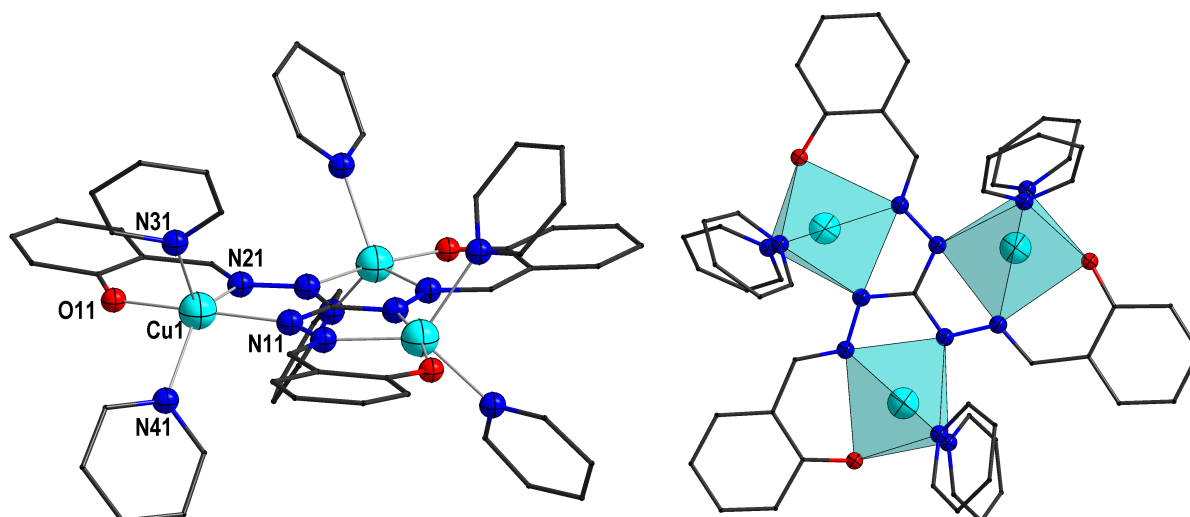
Figure 3.2: Left: Molecular structure of Cu1 complex cation $[Cu_3(saltag^H)(py)_6]^+$ of (**1**) with atom labels, C atoms are wire nodes, Cu: light blue, N: blue, O: red. H atoms and counteranion are omitted for clarity. Numbering scheme is similar but carrying a "2" as second digit for Cu2 complex cation. **Right:** Illustration of the distorted trigonal bipyramidal coordination polyhedra of Cu1 complex cation in **1**. View along crystallographic c-axis, colour code is identical.

Table 3.1: Selected bond lengths (pm) and angles (°) from the coordination environment of both complex cations $[Cu_3(saltag^H)(py)_6]^+$ in **1**. The corresponding numbering scheme is depicted in fig. 3.2.

	$n = 1$	$n = 2$
Cun–O1n	190.7(3)	190.0(2)
Cun–N1n	197.4(3)	197.9(3)
Cun–N2n	198.6(3)	198.8(3)
Cun–N3n	218.5(3)	211.9(3)
Cun–N4n	212.9(3)	217.4(3)
O1n–Cun–N1n	171.39(11)	170.77(11)
O1n–Cun–N2n	92.51(11)	92.02(10)
O1n–Cun–N3n	91.21(11)	87.96(11)
O1n–Cun–N4n	88.13(12)	92.15(11)
N1n–Cun–N2n	79.38(11)	79.78(11)
N1n–Cun–N3n	95.67(11)	95.07(11)
N1n–Cun–N4n	95.55(12)	95.71(11)
N2n–Cun–N3n	123.39(12)	136.53(11)
N2n–Cun–N4n	135.11(12)	121.20(11)
N4n–Cun–N3n	101.46(11)	102.22(11)
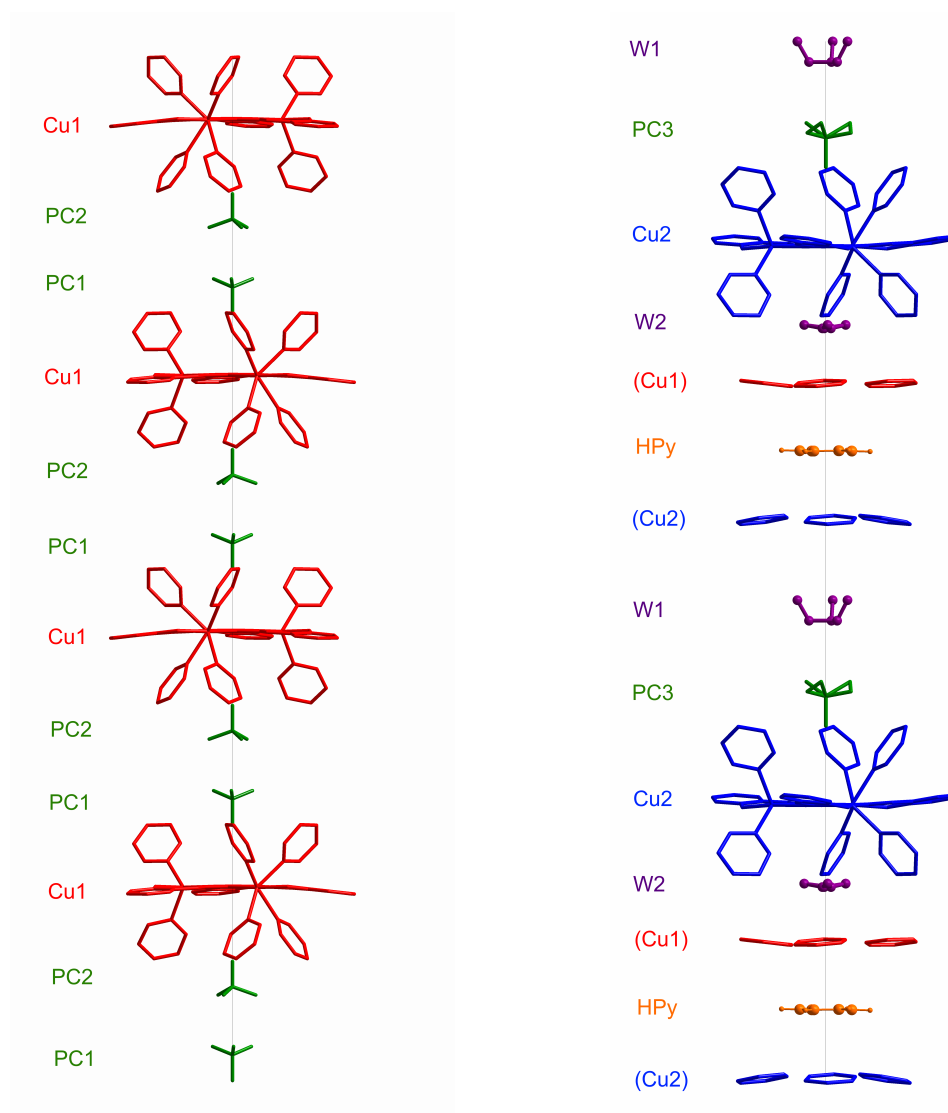
Figure 3.3: The unit cell of **1** contains two different crystallographic C_3 axes, along which the complex cations with Cu1 (left, red) and Cu2 (B, right, blue) are aligned. Depicted is the side view on both axes along the crystallographic b-axis. In case of Cu1 (left, red) two perchlorate anions (PC1 and PC2, green) are alternating with the complex cation along the axis. For Cu2 (right, blue) an alternating stacked arrangement is observed with the remaining perchlorate anion (PC3, green), the first water molecule (W1, violet, disordered), a symmetrically shifted Cu2 complex cation, the pyridinium cation (HPy, orange), a symmetrically shifted Cu1 complex cation (red), and the second water molecule (W2, violet, disordered). Hydrogen atoms are omitted for clarity. Figure taken from [250] (published by The Royal Society of Chemistry).

localisation of the negative charge at the O forming the longest bond. Considering that the effect is most pronounced for PC3, which lacks a negative charge on the opposing side of the ligand plane as well as the corresponding distances to the central C1 of the ligand support this interpretation. These very interactions were also investigated by means of DFT calculational methods, even allowing for their quantification and uncovering a significant $ClO_4 \cdots$ pyridine contribution to this interaction.[250]

Table 3.2: Selected bond lengths (pm) and angles (°) from the coordination environment of both complex cations $[Cu_3(saltag^H)(py)_6]^+$ in **1**. The corresponding numbering scheme is depicted in fig. 3.2.

	PC1	PC2	PC3
Cl–O^{tag}	146.7(14)	143.3(8)	153.5(11)
Cl–O^{C_3}	135.4(8)	141.3(5)	137.1(7)
O–C1^{tag}	349.4(13)	426.6(10)	411.84(13)

A layer structure with alternating arrangements of both Cu1 and Cu2 complex cations can be recognised in fig. 3.4. Complex cations are linked via $\pi \cdots \pi$-interactions between the pyridine coligands bearing N31 and the pyrdine coligands with donor atom N42 in crystallographic c direction, as is illustrated in fig. 3.4. Hence, along the crystallographic c-axis periodically two layers of complex cations are linked, followed by a lack of $\pi \cdots \pi$-interaction.

In summary, compound **1** is the first reported tag-based Cu(II) triangle featuring a trigonal bipyramidal coordination of the Cu centres. The alternative coordination geometry appears to be partially enforced by the special interacting arrangement of the perchlorate counteranions. Related to that, it is the first of this series not exhibiting a dimer formation, which is usually associated with a perturbation of the low energy spectrum of spin states of the individual triangle.

$[Zn_3(saltag^H)(py)_6]ClO_4$ (2)

Keeping in mind the purpose of this compound as explained in the synthesis part, this compound seemingly not fitting into this chapter at all will be briefly discussed against the background of its structural similarity to **1**. A first obvious difference is the hexagonal space group of **2** being $P6_3/m$ (# 176). Hence, the asymmetric unit contains not one third but rather one sixth of the molecular sum formula. There is one crystallographically independent Zn centre (Zn1) in the structure, the trinuclear complex cation $[Zn_3(saltag^H)(py)_6]^+$ is formed by an S_6 symmetry operation on the asymmetric unit. Bond lengths and angles of the coordination environment of the metal ion are listed in table 3.3.

A five-fold coordination with an $[N_4O]$ donor set provided by one pocket of the saltag^H and two pyridine coligands is present at Zn1, which is the same coordination motif as found in **1**. However, the distribution of coordinative bond lengths is rather narrow ranging from 198.7 pm to 209.2 pm, which is in contrast to **1**, where the pyridine donor sites are explicitly elongated in the frame of a Jahn-Teller elongation of the trigonal plane. The resulting coordination polyhedron is a slightly distorted trigonal bipyramid characterised by the corresponding shape
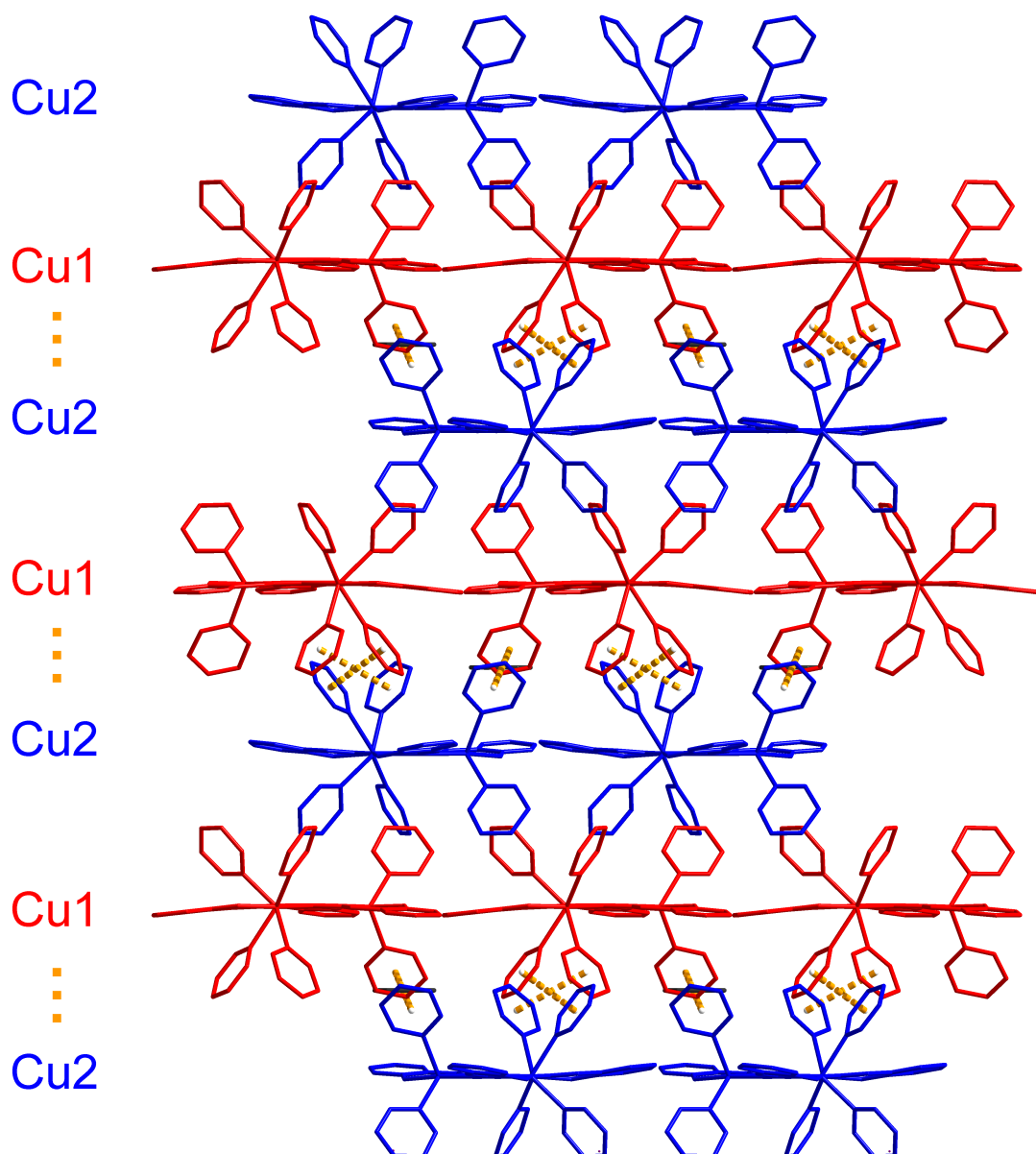
Figure 3.4: Packing diagram of **1** with a view along the crystallographic b-axis. The color code repre-
sents the two different cationic trinuclear Cu(II) complexes based on Cu1 (red) and Cu2
(blue). The intermolecular $\pi \cdots \pi$-interactions are shown as dashed orange bonds. Hydro-
gen atoms, cocrystallised solvent molecules and counteranions are omitted for clarity. Fig-
ure taken from [250] (published by The Royal Society of Chemistry).

Table 3.3: Selected bond lengths (pm) and angles (°) from the coordination environment of Zn1 in
$[\text{Zn}_3(\text{saltag}^{\text{H}})(\text{py})_6]\text{ClO}_4$ (**2**). The corresponding numbering scheme is depicted in fig. 3.5,
N3' is created by the mirror plane, which is the chelate ligand plane $(x, y, -z + \frac{1}{2})$.

Zn1–N1	209.2(5)	Zn1–N2	206.7(5)
Zn1–N3	208.5(4)	Zn1–O1	198.7(5)
N1–Zn1–N2	76.5(2)	N1–Zn1–N3	97.43(14)
N1–Zn1–O1	165.2(2)	N2–Zn1–N3	125.99(12)
N2–Zn1–O1	88.7(2)	N3–Zn1–O1	91.23(14)
N3–Zn1–N3'	108.0(2)		

parameter[251–253] 1.304 and a τ parameter[254] of 0.65.

The perchlorate counteranion is equally distributed among two positions on the crystallographic C_3 axis, above and below the ligand plane, in the centre of the "propeller" formed by the three pyridine coligands on each side of the ligand plane. The elemental analysis of bulk material of **2** suggests the presence of water, which could fill the unoccupied perchlorate positions, respectively. This "interactive" arrangement of the perchlorate counterions is similarly found in **1**. Also the $\pi \cdots \pi$-interactions to neighbouring complex cations mediated by the pyridine coligands illustrated for **1** in fig. 3.4 are similarly found in **2** (see fig. 3.6). No further cocrystallised solvent molecules or cations are found in the structure.

In conclusion, the structure of **2** can be utilised as a suitable diamagnetic matrix for possible doping with Cu(II) ions to determine single-ion magnetic properties of **1**. Despite the different space group and minor deviations in the coordination environment of the metal centre, the structural features of the individual molecules are sufficiently congruent. The major discrepancies between the structures pertain the lack of cocrystallised solvent molecules and cations, which should not impair the single-ion magnetic properties of doped Cu(II) ions.

[Cu₃(saltag^H)(py)₆]NO₃ (3)

At this point, a preliminary structure motif of **3** is presented and discussed. Harsh disorders and insufficient description of the counteranion, as well as large thermal ellipsoids with elongations especially in the crystallographic c-direction are indicative of large uncertainties in the actual atomic positions. Even the correctness of the found hexagonal space group $P6_3/m$ (# 176) is still in question. Nevertheless, the structure motif reveals some essential features of **3** and hence is discussed here, albeit with all due cautiousness. For a final solution and evaluation of the crystal structure, additional synchrotron diffraction data might be necessary.

The asymmetric unit—with the assumed space group—consists of half of one third of the saltag^H ligand, half a Cu atom, one sixth of the nitrate counteranion, one pyridine coligand and some partition of a cocrystallised MeOH molecule, so **3** is built by applying an S_6 symmetry operation leading the composition [Cu₃(saltag^H)(py)₆]NO₃ · 0.75 MeOH (see fig. 3.7). Consequently, the saltag^H ligand forms a mirror plane. Some preliminary numbers describing bond lengths and angles of Cu1's coordination sphere are given in table 3.4.

Notwithstanding the uncertainties of the structure, the fundamental coordination environment of Cu1 appears reasonably determined. An [N₄O] donor set provided by one pocket of the chelate ligand and two pyridine coligands (N3 and N3') reveals a distorted trigonal bipyramidal coordination polyhedron (see fig. 3.7 with a shape deviation parameter[251–253] of 1.482 and a geometry parameter $\tau = 0.72$[254]). In accordance with an expected Jahn-Teller distortion, the axial bonds of Cu1 with O1 and N1 are somewhat shorter than the ones in the trigonal plane with N2 (not significant), N3 and N3'. Intramolecular Cu$\cdots$Cu distances measure about 483 pm.

No dimer formation occurs, but the complex cations are well isolated. Presumably, there is an intermolecular connection of adjacent complex cations via $\pi \cdots \pi$-interactions of the pyridine
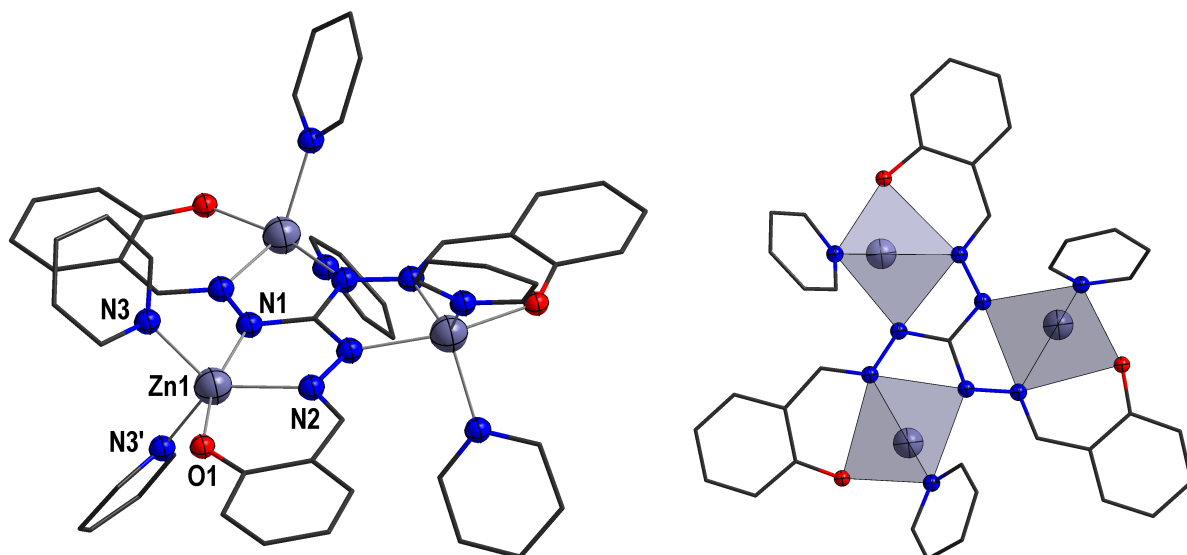
Figure 3.5: Left: Molecular structure of complex cation $[Zn_3(saltag^H)(py)_6]^+$ of (**2**) with atom labels, C atoms are wire nodes, Zn: blueish-grey, N: blue, O: red. H atoms and counteranion are omitted for clarity. **Right:** Illustration of the distorted trigonal bipyramidal coordination polyhedra of **2**. View along crystallographic c-axis, colour code is identical.
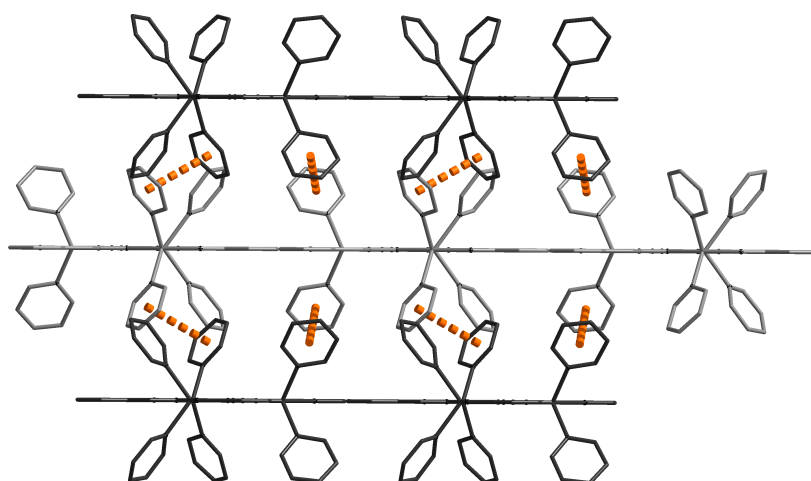
Figure 3.6: Illustration of intermolecular $\pi\cdots\pi$-interactions to adjacent complex molecules in **2** via the pyridine coligands as orange dashed bonds. View along crystallographic a-axis.

Table 3.4: Selected bond lengths (pm) and angles (°) from the coordination environment of Cu1 in $[Cu_3(saltag^H)(py)_6]^+$ in **3**. The corresponding numbering scheme is depicted in fig. 3.7, N3' is created by the mirror plane, which is the chelate ligand plane $(x, y, --z + \frac{1}{2})$. Due to the structure of **3** being a motif, no errors are given and the values must be considered preliminary.

Cu1–N1	196.9	Cu1–N2	197.7
Cu1–N3	214.1	Cu1–O1	189.8
N1–Cu1–N2	79.9	N1–Cu1–N3	96.8
N1–Cu1–O1	171.6	N2–Cu1–N3	128.7
N2–Cu1–O1	91.7	N3–Cu1–O1	88.4
N3–Cu1–N3′	102.6		

coligands present. In contrast to **1**,[250] in this motif the nitrate counteranion is not positioned in the centre of the "propeller" formed by three pyridine coligands above and below the triangular plane. Hence, it cannot have the structure directing effect, which was discovered for the perchlorate ion in **1**.[250] Instead this key position appears to be occupied by the cocrystallised MeOH molecule. However, as was explained afore, the information needs to be taken with caution.
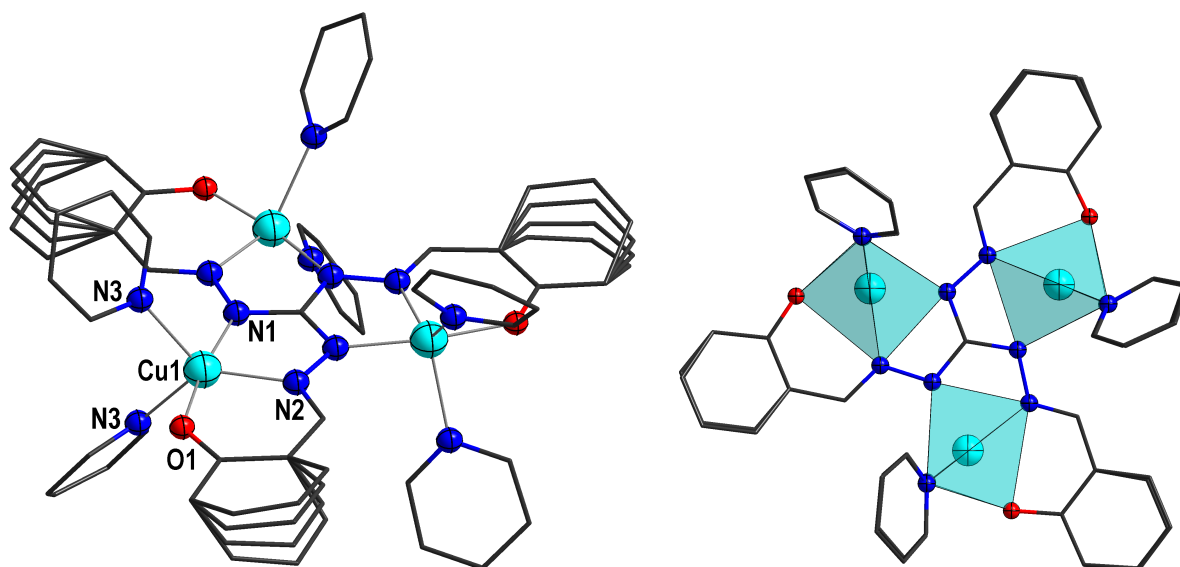
[Cu₃(saltag^H)(py)₃OTf]   (4)

Compound **4** forms crystals with the trigonal space group $R\bar{3}$ (#148), whose asymmetric unit is built up by one Cu(II) ion embedded in one third of a saltag^H ligand, one third of a triflate anion and one pyridine coligand. Performing the C_3 symmetry operation yields the whole trinuclear complex molecule with the composition [Cu₃(saltag^H)(py)₃OTf] (see fig. 3.8). Its bond lengths and angles within the coordination sphere of the Cu(II) ion are listed in table 3.5.

Cu1 is coordinated by an [N₃O] donor set provided by one pocket of the chelate ligand and the pyridine coligand with bond lengths ranging from 188.8 pm (O1) to 199.0 pm (N3). While the three saltag^H donor sites form a plane identical to the tag plane, the pyridine donor N3 is heavily bent out of this very plane (distance to plane is 128 pm) and consequently, the Cu centre is lifted above this ligand plane by 40 pm. Overall this would result in a distorted square planar coordination with a shape deviation parameter[251–253] of 2.669. However, the triflate anion, which formally counterbalances the complex cation described so far, also shows a close contact between its potential oxygen donor site O2 and Cu1 (294.7 pm). Although triflate is of course a weak donor, especially when trivalently bound to three Cu(II) centres, a coordinative interaction can be assumed here. This increases the donor environment to [N₃O₂] featuring a strong Jahn-Teller elongation of the putative axial donor O2. Continuous shape measures indicate, that the coordination geometry is severely distorted between ideal square pyramid (5.048) and trigonal bipyramid (4.614) reference polyhedra, with a slight preference for the latter. In contrast, the τ-parameter[254] of 0.11 points towards a square pyramid, because it does not consider bond lengths and thus neglects elongation. Regardless of the particular geometry, due to the trivalent coordination of the triflate counteranion **4** can be considered the first neutral complex of the tag-based Cu(II) triangle family, which features a crystallographic C_3 symmetry.

The displacement of Cu1 from the chelate ligand plane is also reflected in a low diazine bridging dihedral angle Cu–N–N–Cu of 149°. The corresponding intramolecular Cu···Cu distance amounts 469.8 pm. In the crystal structure of **4**, the formation of dimers by two complex molecules becomes apparent once again (see fig. 3.9). Interestingly, the intramolecular Cu···Cu distance is nearly identical to the interdimer one (475.6 pm), so that the trigonal antiprism formed by the six Cu centres is close to an ideal octahedron. Both tag planes of the dimer are 311 pm apart.

An interconnection of the dimers to neighbouring complex molecules via $\pi\cdots\pi$-interactions of the pyridine coligands is illustrated in fig. 3.9. However, the distance of 414 pm between the π-planes involved suggests, if at all, a weak interaction.

Figure 3.7: Left: Molecular structure of complex cation $[Cu_3(saltag^H)(py)_6]^+$ of (**3**) with atom labels, C atoms are wire nodes, Cu: light blue, N: blue, O: red. H atoms, counteranion and cocrystallised solvent are omitted for clarity. The pronounced disorder of the saltag^H ligand's aromatic ring is schemed. **Right:** Illustration of the distorted trigonal bipyramidal coordination polyhedra of **8**. View along crystallographic c-axis, colour code is identical.
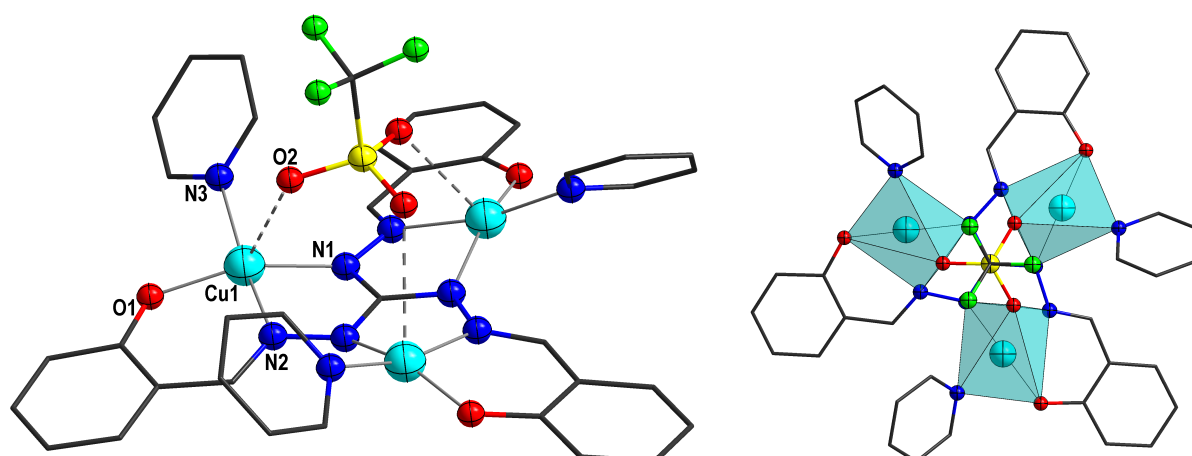
Figure 3.8: Left: Molecular structure of complex cation $[Cu_3(saltag^H)(py)_3OTf]$ of (**4**) with atom labels, C atoms are wire nodes, Cu: light blue, N: blue, O: red, S: yellow, F: light green. H atoms are omitted for clarity. **Right:** Illustration of the distorted five-cornered coordination polyhedra of **4**. View along crystallographic c-axis, colour code is identical.

Table 3.5: Selected bond lengths (pm) and angles (°) from the coordination environment of Cu1 in $[Cu_3(saltag^H)(py)_3OTf]$(**4**). The corresponding numbering scheme is depicted in fig. 3.8.

Cu1–N1	195.5(2)	Cu1–N2	194.4(2)
Cu1–N3	199.0(2)	Cu1–O1	188.8(2)
Cu1–O2	294.7(2)		
N1–Cu1–N2	80.38(7)	N1–Cu1–N3	99.61(7)
N1–Cu1–O1	158.62(7)	N1–Cu1–O2	81.19(7)
N2–Cu1–N3	165.20(7)	N2–Cu1–O1	93.49(7)
N2–Cu1–O2	76.51(7)	N3–Cu1–O1	91.49(7)
N3–Cu1–O2	88.83(7)	O1–Cu1–O2	117.51(7)
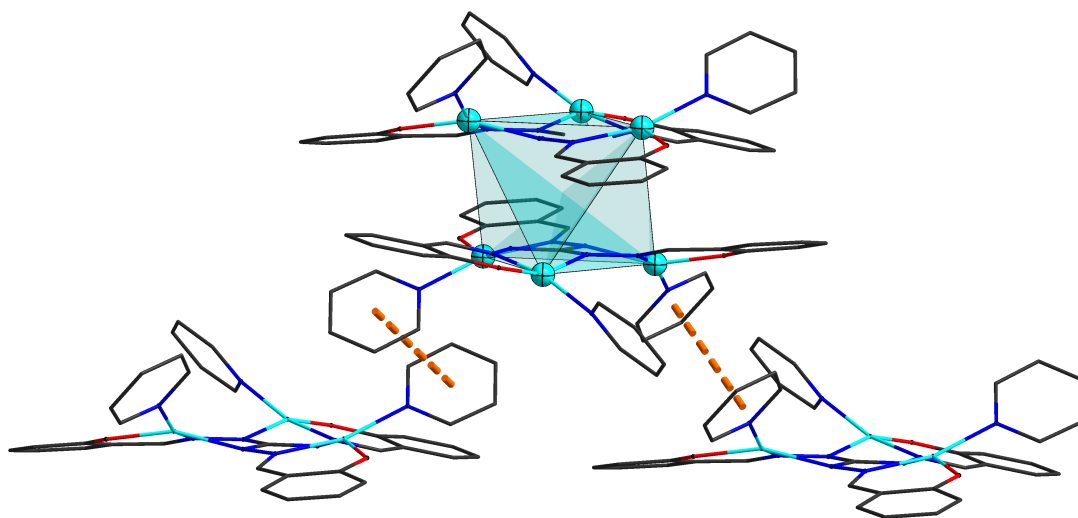
Figure 3.9: Illustration of dimer formation by two complex molecules in **4** resulting in the schemed trigonal antiprismatic arrangement of six Cu centres, H atoms and axially coordinating triflate anions are omitted for clarity. Weak intermolecular $\pi \cdots \pi$-interactions to adjacent complex molecules via the pyridine coligands are marked as orange dashed bonds.

[Cu$_3$(saltag^H)(bpy)$_3$]OTf (5)

Due to the high similarity not only of the molecular structure, but also of the unit cell properties of **5** with the trinuclear complex [Cu$_3$(saltag^H)bpy$_3$]ClO$_4$ already published,[246] this part is kept brief. The trigonal space group $R\bar{3}$ (#148) allows for the present C_3 symmetry of the complex cation, resulting in only one crystallographically independent Cu centre (Cu1) forming the asymmetric unit together with one third of the saltag^H ligand, one 2,2'-bipyridine coligand and one third of the triflate counteranion. The latter is the major difference between **5** and [Cu$_3$(saltag^H)(bpy)$_3$]ClO$_4 \cdot$ 3 DMF,[246] which has a perchlorate counteranion. A depiction of the whole complex cation is shown in fig. 3.10. Bond lengths and angles of the [N$_4$O] donor environment of Cu1 provided by one pocket of the tritopic chelate ligand and one 2,2'-bpy coligand are listed in table 3.6.

The Cu(II) ion is coordinated in a distorted square planar fashion, whereat the [N$_2$O] saltag^H ligand pocket forms the square plane together with N3 of the 2,2'-bpy coligand. A more distant (224 pm) axial position of N4 is indicative for an axial Jahn-Teller elongation. Continuous shape measures[251–253] reveal nearly equal deviation parameters for ideal square pyramid (2.762) and vacant octahedron (2.845) geometry and demonstrate a rather rough distortion. A τ-parameter[254] of 0.32 can be determined, which is identical to the one found in [Cu$_3$(saltag^H)(bpy)$_3$]ClO$_4 \cdot$ 3 DMF[246] and further emphasises the high congruency of the structures. The dihedral bridging angle Cu–N–N–Cu of the diazine moiety is 149.7° (152° in[246]) resulting in an intramolecular Cu$\cdots$Cu distance of 479.9 pm. An intersecting angle between the Cu ion's coordination plane and the tag plane of 14.5° (14° in[246]) is found.

As is habitual for distorted square pyramidal coordinated saltag-based Cu(II) triangles,[239,246]
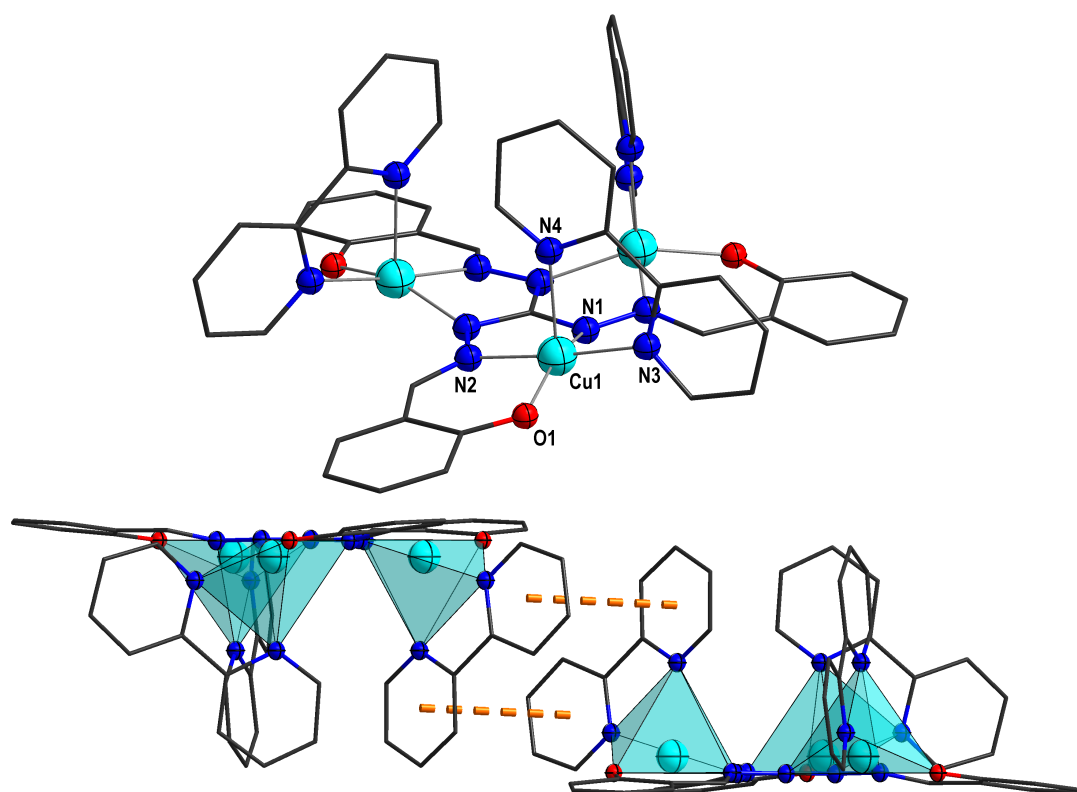
Figure 3.10: Top: Molecular structure of complex cation [Cu$_3$(saltag^H)(bpy)$_3$]$^+$ of (**5**) with atom labels, C atoms are wire nodes, Cu: light blue, N: blue, O: red. H atoms and counteranion are omitted for clarity. **Bottom:** Illustration of the distorted square pyramidal coordination polyhedra of **5** and the $\pi\cdots\pi$-interactions between 2,2'-bipyridine coligands (orange dashed bonds) of adjacent complex cations. View along crystallographic b-axis, colour code is identical.

Table 3.6: Selected bond lengths (pm) and angles (°) from the coordination environment of Cu1 in [Cu$_3$(saltag^H)(bpy)$_3$]OTf (**5**). The corresponding numbering scheme is depicted in fig. 3.10.

Cu1–N1	201.6(2)	Cu1–N2	196.1(2)
Cu1–N3	204.6(2)	Cu1–N4	224.1(2)
Cu1–O1	192.7(2)		
N1–Cu1–N2	78.69(9)	N1–Cu1–N3	102.69(8)
N1–Cu1–N4	99.83(8)	N1–Cu1–O1	156.13(3)
N2–Cu1–N3	175.20(9)	N2–Cu1–N4	98.85(8)
N2–Cu1–O1	92.97(8)	N3–Cu1–N4	76.41(8)
N3–Cu1–O1	87.48(8)	N4–Cu1–O1	103.56(8)

a supramolecular dimerisation of the hemispherical complex cations occurs with the six Cu centres forming a trigonal antiprism. The distance between the tag planes amounts to 356.9 pm (356 pm in [246]). Also, the intermolecular $\pi\cdots\pi$-interaction depicted in fig. 3.10 has already been described in detail. [246]
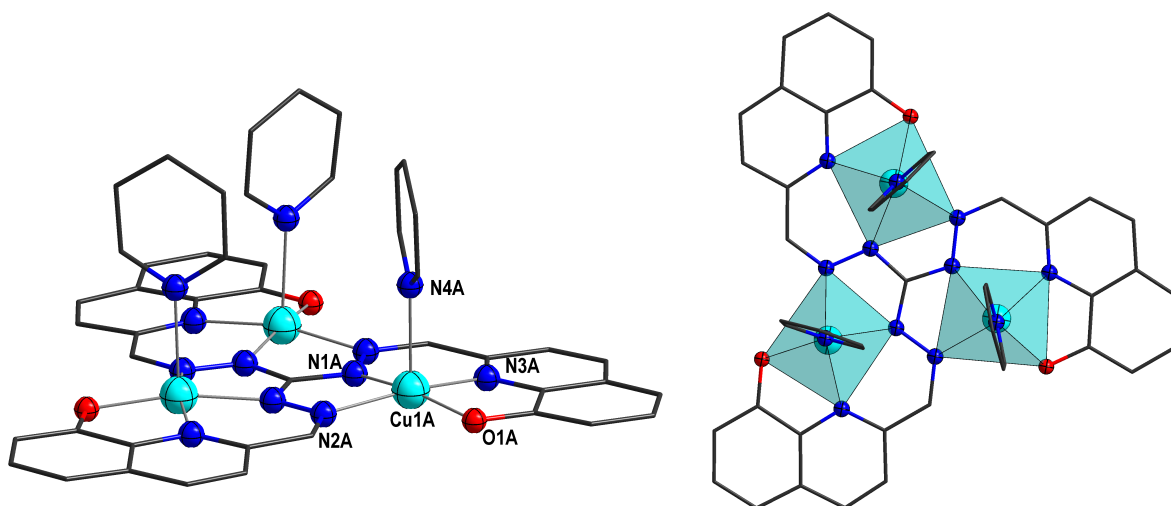
[Cu$_3$(quintag)(py)$_3$]ClO$_4$ (6)

The compound crystallises in the trigonal Sohncke space group $R3$ (#146). One third of each of two crystallographically independent monocationic complex molecules A and B as well as one third of the perchlorate counteranions are embodied in the asymmetric unit. The main threefold rotational axis generates the two trinuclear complex cations A and B. Both, A and B, have the same chemical composition [Cu$_3$(quintag)(py)$_3$]$^+$. Hence, all three N$_3$O pockets of the ligand each chelate a Cu(II) ion, whose coordination sphere is saturated by one pyridine coligand leading to an N$_4$O overall donor set. Bond lengths and angles related to the coordination sphere of both Cu(II) centres are listed in table 3.7. As becomes evident there, the differences between both complex cations are minor and they are therefore mainly discussed together. Representatively, A is depicted in fig. 3.11.

In the ligand plane, all four donor atoms (O1, N1–N3) feature a narrow distribution of bond lengths from 193 to 202 pm, however the bite angles deviate significantly from 90° (ideal square) due to the rigid ligand scaffold. In contrast, the N-donor of the pyridine coligand (N4) is farther away (A: 230 pm, B: 232 pm) and thus forms the Jahn-Teller axis of the distorted square-pyramidal coordination environment, as one would expect for Cu(II). This pyridine N-donor is positioned nearly normal to the tag plane (deviation A: 2.4°; B: 6.6°). Generally, there is no relevant out-of-plane bending of the ligand observable and also the Cu(II) ions' protrusion from the square plane (A: 19 pm, B: 14 pm) is barely perceivable. Consequently, the shape deviation parameters [251–253] are comparatively low for square pyramid (A: 1.002, B: 1.301) and vacant octahedron (A: 1.559, B: 1.749), although the former shows better congruence. Overall, the Cu centres in molecule B show a higher degree of distortion according to the continuous shape measures.

Dihedral angles Cu–N–N–Cu along the diazine bridge of 166.2° (A) and 171.3° (B) are found. These are the closest values to 180° (in-plane bridging) reported for triaminoguanidine-based Cu(II) triangles with distorted square planar coordination geometry. [50,239,246,247] Two neighbouring Cu(II) ions in the triangle are 473.1 (A) and 475.2 pm (B) apart, respectively. To the best of my knowledge, this is the first reported example of a triaminoguanidine-based ligand coordinating in its *cis*-rotamer form with respect to the Schiff-base double bond, and therefore the proof of feasibility of this very configuration for coordination chemistry under suitable conditions.

Zooming further out, the well-known formation of dimers of triangles, here complex cations A and B, becomes also obvious in **6**. The corresponding distance of the two tag planes is 330.4 pm, the shortest intradimer Cu$\cdots$Cu span amounts to 422.2 pm. A remarkable feature is the arrangement of the six Cu centres in the dimer, taking an intermediate position between ideal triangular prism and antiprism geometries (see fig. 3.12). For all other tag-based Cu triangles

Figure 3.11: Left: Molecular structure of complex cation [Cu₃(quintag)(py)₃]⁺ (**6**) with atom labels, C atoms are wire nodes, Cu: light blue, N: blue, O: red, H atoms and counteranion are omitted for clarity. **Right:** Illustration of the distorted square pyramidal coordination polyhedra of **6**. View along crystallographic *c*-axis, colour code is identical.

Table 3.7: Selected bond lengths (pm) and angles (°) from the coordination environment of the two crystallographically independent Cu(II) centres within the asymmetric unit of [Cu₃(quintag)(py)₃]ClO₄ (**6**). The corresponding numbering scheme is depicted in fig. 3.11.

Cu1A–N1A	193.1(7)	Cu1A–N2A	202.1(8)
Cu1A–N3A	195.8(7)	Cu1A–N4A	230.0(8)
Cu1A–O1A	193.0(7)		
Cu1B–N1B	192.5(8)	Cu1B–N2B	205.2(9)
Cu1B–N3B	194.3(9)	Cu1B–N4B	231.9(8)
Cu1B–O1B	194.3(7)		
N1A–Cu1A–N2A	80.9(3)	N1A–Cu1A–N3A	88.7(3)
N1A–Cu1A–N4A	97.5(3)	N1A–Cu1A–O1A	168.9(3)
N2A–Cu1A–N4A	93.9(3)	N2A–Cu1A–N3A	166.2(3)
N2A–Cu1A–O1A	103.8(3)	N3A–Cu1A–N4A	96.5(3)
N3A–Cu1A–O1A	84.8(3)	N4A–Cu1A–O1A	93.2(3)
N1B–Cu1B–N2B	80.2(3)	N1B–Cu1B–N3B	88.1(4)
N1B–Cu1B–N4B	99.3(3)	N1B–Cu1B–O1B	169.6(3)
N2B–Cu1B–N4B	92.3(3)	N2B–Cu1B–N3B	165.8(4)
N2B–Cu1B–O1B	104.6(3)	N3B–Cu1B–N4B	97.6(3)
N3B–Cu1B–O1B	85.7(4)	N4B–Cu1B–O1B	89.8(3)
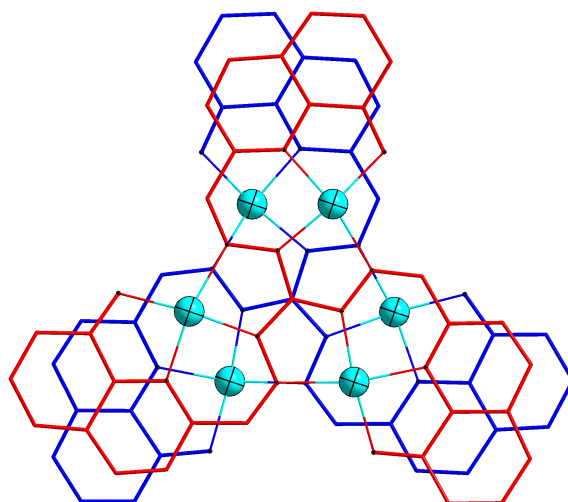
Figure 3.12: Illustration of dimer formation by two complex cations A (blue) and B (red) in **6** along crystallographic c-axis, Cu: light blue, H atoms, axial pyridines and counteranions are omitted for clarity.
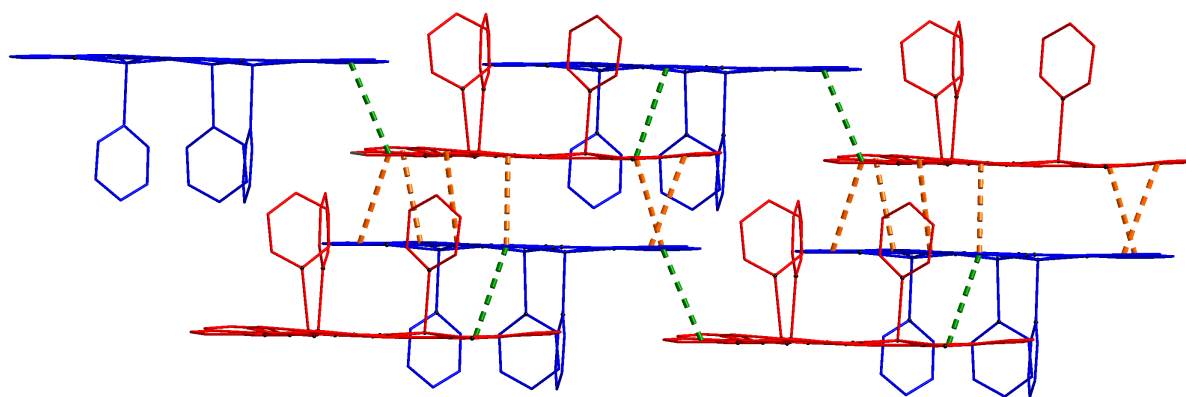
Figure 3.13: Illustration of different $\pi\cdots\pi$-interactions in the crystal structure of **6**. The intradimer $\pi\cdots\pi$-interactions (orange dashed bond) connect the dimers formed by cationic complex molecule A (blue) and cationic complex molecule B (red) in a multivalent fashion. Interdimer $\pi\cdots\pi$-interactions connecting these dimers to its next neighbours are presented as green dashed bonds. View along crystallographic a-axis.

those dimers formed nearly ideal trigonal prisms or antiprisms depending on the presence or absence of bulky substituents. This particular observation in **6** can be explained by the overlap of the quinoline backbones of A and B suggesting effective trivalent $\pi \cdots \pi$-interactions (orange dashed bonds in fig. 3.13), which is also in accordance with the planes' distance of about 330 pm mentioned earlier.

Those π-stacked dimers exhibit another interdimer $\pi \cdots \pi$-interaction to neighbouring dimers, which runs along the crystallographic c-axis (green dashed bonds in fig. 3.13). A separation of the involved π-planes of around 335 pm can be determined.

$[Cu_6(quintag^{ox})_2(py)_4]$ (7)

Crystals of the hexanuclear neutral Cu(II) complex of two monooxygenated quintag ligands (quintag^{ox}) **7** possess the monoclinic space group $P2_1/c$ (#14). Hence, there is no crystallographic C_3 symmetry present in the molecule as one would expect due to the broken symmetry of the ligand. In the asymmetric unit, half a neutral complex molecule, two cocrystallised MeOH molecules and one cocrystallised pyridine are found. The entire hexanuclear neutral complex is created by inversion of the asymmetric unit. Besides the the two chelate ligands it contains four pyridine coligands saturating the coordination spheres of two of the three crystallographically independent Cu(II) centres (Cu1 and Cu3), respectively. A chemical connection between the two formal trinuclear units is built via Cu2, which is coordinated by two nitrogen donors from the tag core of one quintag^{ox} ligand and the [NO] donor set of the hydroxquinoline moiety of the other chelate ligand. This leads to a metallacyclophane-like arrangement as is illustrated in fig. 3.14. Bond lengths and angles of all three coordination environments are summarised in table 3.8.

While Cu1 and Cu3 exhibit distorted square pyramidal coordination geometry, the donor sphere around Cu2 will be subject to further discussion. A distorted square basal plane is provided by an [N$_3$O] donor set of the chelate ligand pockets for all three Cu centres. Corresponding bond lengths range from 192 to 207 pm. In contrast, an axial position occupied by the pyridine coligands for Cu1 and Cu3 is significantly elongated (228 and 225 pm, respectively), which is in accordance with a Jahn-Teller distortion expected for Cu(II). Continuous shape measures[251–253] reveal deviation parameters of 2.892 for Cu1 and 1.060 for Cu3, hence, the environment of Cu3 is closer to the ideal square pyramid.

Since Cu2 links both chelate ligands in a metallacyclophane-like fashion, this causes a rough out-of-plane distortion of one hydroxyquinoline moiety (bearing N6 and O2) of the fully π-conjugated quintag^{ox} ligand (36.9° intersecting angle with tag plane). Thus, also the coordination environment of Cu2 is farther away from ideal polyhedra. Considering only the four donor atoms of the two chelate ligand pockets involved, which show narrow distribution of bond lengths (N1, N6', N8, O2'), yields a shape parameter of 4.674 for a square plane as highest proximity. At a distance of 292 pm the atom O3' takes up an axial position with respect to the distorted square, which suggests a coordination, albeit a weak one. Extending the donor sphere for this very atom results in a shape parameter of 4.438 for a trigonal bipyramid as closest
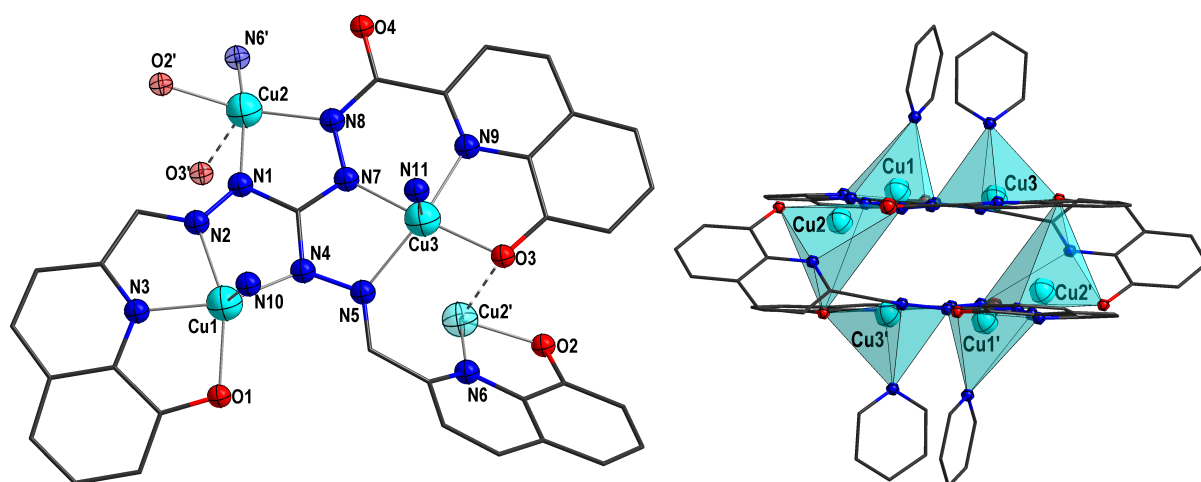
Figure 3.14: Left: Molecular structure of half a molecule of [Cu$_6$(quintag^{OX})$_4$(py)$_4$] (**7**) with atom labels, C atoms are wire nodes, Cu: light blue, N: blue, O: red, H atoms, cocrystallised solvent and pyridine residues of donors N10 and N11 are omitted for clarity. Transparent atoms are part of the mirror image completing the molecule, which is created by inversion symmetry ($-x+1, -y+1, -z$). **Right:** Illustration of the distorted square pyramidal coordination polyhedra of Cu(II) centres in **7** (whole molecule) also demonstrating the metallacyclophane character of the compound. Colour code is identical.

Table 3.8: Selected bond lengths (pm) and angles (°) from the coordination environment of the three crystallographically independent Cu(II) centres within the hexanuclear neutral complex [Cu$_6$(quintag^{OX})$_2$(py)$_4$](**7**). The corresponding numbering scheme is depicted in fig. 3.14.

Cu1–N2	201.3(2)	Cu1–N3	192.2(2)
Cu1–N4	196.8(2)	Cu1–N10	227.6(2)
Cu1–O1	205.7(2)		
Cu2–N1	196.9(2)	Cu2–N6′	201.3(2)
Cu2–N8	196.4(2)	Cu2–O2′	191.8(2)
Cu2–O3′	291.6(2)		
Cu3–N5	207.2(2)	Cu3–N7	191.5(2)
Cu3–N9	197.1(2)	Cu3–N11	224.7(2)
Cu3–O3	193.1(2)		
N2–Cu1–N3	77.84(9)	N2–Cu1–N4	79.05(8)
N2–Cu1–N10	106.68(8)	N2–Cu1–O1	155.57(8)
N3–Cu1–N10	102.60(8)	N3–Cu1–N4	154.31(9)
N3–Cu1–O1	81.39(8)	N4–Cu1–N10	94.64(8)
N4–Cu1–O1	117.81(8)	N10–Cu1–O1	90.24(8)
N1–Cu2–N6′	157.98(8)	N1–Cu2–N8	80.17(8)
N1–Cu2–O2′	95.78(8)	N1–Cu2–O3′	93.79(8)
N6′–Cu2–O2′	84.68(8)	N6′–Cu2–N8	107.92(8)
N6′–Cu2–O3′	64.19(8)	N8–Cu2–O2′	155.93(8)
N8–Cu2–O3′	115.16(8)	O2′–Cu2–O3′	88.69(8)
N5–Cu3–N7	80.62(8)	N5–Cu3–N9	164.65(8)
N5–Cu3–N11	92.69(8)	N5–Cu3–O3	103.27(7)
N7–Cu3–N11	93.50(8)	N7–Cu3–N9	88.88(8)
N7–Cu3–O3	170.61(8)	N9–Cu3–N11	99.15(8)
N9–Cu3–O3	85.53(8)	N11–Cu3–O3	94.83(8)

agreement (6.688 for square pyramid). This view gives rise to an oxo-bridging between Cu2 and Cu3 at an angle of 80.73°. Eventually, the oxo moiety formed during the complex synthesis, in here atom O4, is 313.9 pm away from Cu2. Therefore, a donor contribution from this atom remains questionable, especially its alignment with respect to the other donor atoms is hardly integrable into common coordination chemistry concepts.

Metal$\cdots$metal distances within the hexanuclear complex and dihedral angles of the three distinct diazine bridges are listed in table 3.9. A noteworthy finding is the proximity of Cu2 and Cu3 with a separation of 323 pm, which is unusually short for tag-based Cu(II) complexes. Accordingly, this is the metal ion couple with the already mentioned oxo-bridge occuring.

Table 3.9: Metal$\cdots$metal distances (pm) and dihedral angles of diazine bridges (°) in the hexanuclear neutral complex [Cu_6($quintag^{ox}$)$_2$(py)$_4$](**7**). Atoms marked with an apostrophe are part of the mirror image completing the molecule, which is created by inversion symmetry ($-x + 1, -y + 1, -z$).

Cu1–Cu2	484.0	Cu1–Cu3	478.1
Cu1–Cu1′	879.4	Cu1–Cu2′	607.2
Cu1–Cu3′	519.2	Cu2–Cu3	472.7
Cu2–Cu2′	657.7	Cu2–Cu3′	323.0
Cu3–Cu3′	472.1		
Cu1–N2–N1–Cu2	167.4	Cu1–N4–N5–Cu3	159.7
Cu2–N8–N7–Cu3	175.5		

Another remarkable feature of the molecular structure is the observation, that two of three ligand pockets have their Schiff-base double bond in *trans*-configuration and hence form exclusively five-membered chelate rings. One remaining pocket carries the serendipitously introduced oxo group making the Schiff-base an amide, which is *cis*-configured assuming a double bond between N8 and its neighbouring C-atom with respect to the hydroxyquinoline moiety (the higher priority of the O according to CIP-rules is neglected for the sake of clarity). This leads to the formation of two five-membered and one six-membered chelate ring around Cu3, which is also the one centre with the highest congruency to ideal square pyramidal coordination geometry according to continuous shape measures. The shortest intermolecular metal$\cdots$metal distance amounts to 837.3 pm. No hints for intermolecular interactions could be found in the crystal structure.

Comparative Remarks

An overview of some crucial structural parameters for all six Cu(II) complexes reported in this work is compiled in table 3.10. Among them, two compounds feature distorted trigonal bipyramidal coordination of the Cu centres (**1** and **3**), **4** is an intermediate case hard to categorise here and three of them show the well-known distorted square pyramidal coordination motif (**5**, **6** and **8**). The complexes of the novel quintag ligand unveil a proximity to an ideal square ligand plane when *cis*-configured with respect to the Schiff-base moiety, which has not been observed for any other tag-based Cu complex, yet.

Table 3.10: Comparison of structural parameters obtained from crystal structures of the triaminoguanidine-derived ligand-based Cu(II) complexes reported in this work. The deviation parameters for ideal trigonal bipyramidal (Sh-TBP) and square pyramidal (Sh-SPY) coordination polyhedra determined via continuous shape measures[251–253] as well as the geometry parameter τ[254] are given in the upper half of the table. The lower half lists the intratriangular Cu$\cdots$Cu distance d_{Cu}, the diazine bridging dihedral angles Cu–N–N–Cu δ_{Cu} and the shortest distances between triaminoguanidine planes d_{tag}.

	1		3	4	5	6		7		
Centre	Cu1	Cu2	Cu1	Cu1	Cu1	Cu1A	Cu1B	Cu1	Cu2	Cu3
Sh-TBP	1.694	1.705	1.482	4.614	3.346	6.170	6.589	7.985	4.438	5.947
Sh-SPY	3.074	2.655	4.377	5.084	2.762	1.002	1.301	2.892	6.688	1.060
τ	0.60	0.57	0.72	0.11	0.32	0.05	0.06	0.02	0.03	0.10
d_{Cu}/ pm	484.2	484.1	483	469.8	479.9	473.1	475.2	484.0		478.1
δ_{Cu}/ °	176.6	179.4	180	149.0	149.7	166.2	171.3	159.7, 167.4, 175.5		
d_{tag}/ pm	766.3		736	310.8	356.9	328.5		291.0		

The distorted trigonal bipyramidal complexes **1** and **3** are not only the first of their kind, but also realise a nearly ideal in-plane bridging via the N–N-diazine groups with dihedral angles close to 180°. Eventually the problem of dimer formation is overcome in these complexes, as becomes obvious from the shortest tag plane distances of 766.3 and 736 pm. At the same time the obverse extreme is found in **4**, which exhibits the closest arrangement of the tag planes in the dimer reported so far. This property is outmatched by **7**, where two Cu triangles are chemically entwined leading to an even smaller span between the tag planes of 291 pm.

3.1.3 Magnetic Properties

For all mentioned Cu(II) complexes temperature-dependent susceptibility measurements were undertaken. A detailed discussion of **1**'s magnetic behaviour has already been reported.[250] Overall, the high-temperature regime is very similar for all compounds and characterised by the decrease of $\chi_{mol}T$ from a room temperature value lying significantly below the expected spin-only value for three independent Cu(II) centres ($1.125\,\mathrm{cm^3 K\,mol^{-1}}$ for $g = 2$). A well-developed plateau corresponding to the geometrically frustrated $S = \frac{1}{2}$ is reached at about $100\,\mathrm{K}$ in all cases. Significant distinctions between the individual compounds arise in the low-temperature region, which are therefore discussed separately.

Compounds **1**, **3**, **4** and **5** form one group, whose low-temperature magnetic behaviour is characterised by a further decline of $\chi_{mol}T$ below $20\,\mathrm{K}$ (see fig. 3.15). Among this group, the low-temperature drop is significantly lower for **1** and **3**, which feature trigonal bipyramidal Cu(II) coordination and lack dimerisation of triangles. In contrast, $\chi_{mol}T$ of **6** (fig. 3.16) and **7** (fig. 3.16)—the complexes based on the quintag ligand—begin to ascend from $25\,\mathrm{K}$ downwards.

The magnetic susceptibility curves of all mentioned Cu(II) compounds were fitted by full matrix diagonalisation approaches using only one isotropic g_{iso}-value for the entire coupled trinuclear complex to avoid overparametrisation. For the four complexes with decreasing low-temperature susceptibility an equilateral triangle spin topology with one unitary isotropic magnetic exchange coupling constant J_1 for all three possible exchange pathways was applied, resulting in the following spin Hamiltonian:

$$\widehat{H} = -J_1 \left(\widehat{S}_1\widehat{S}_2 + \widehat{S}_1\widehat{S}_3 + \widehat{S}_2\widehat{S}_3 \right) + g_{iso}\mu_B B \sum_{i=1}^{3} \widehat{S}_i \tag{3.1}$$

For a good agreement with the experimental data, in all four cases intermolecular interactions needed to be considered via a mean field parameter zJ as it is implemented in PHI program,[255] which was used for the fittings.

Parameters obtained from the fittings are collated in table 3.11. Coupling constants J_1 amount to scarcely $-300\,\mathrm{cm^{-1}}$ for **1**, **3** and **5**, which is very similar to the ones reported before.[239,246] **4** exhibits a somewhat larger coupling of $-369\,\mathrm{cm^{-1}}$. This cannot be explained by structural parameters related to the diazine bridging (compare table 3.10), but rather be interpreted as an increase of spin density in the ligand plane, because the coordination environment of the Cu(II) ions is closer to square planar than in all the other cases. In a simplified crystal field theory picture this leads to an energetic increase of the $d_{x^2-y^2}$ orbital bearing the unpaired electron, hence a more well-defined "magnetic orbital" and more effective antiferromagnetic exchange. The mean field parameters zJ accounting for intermolecular magnetic interactions are considerably smaller for the complexes **1** and **3**. This is in line with the expectation arising from the crystal structure, because the distorted trigonal bipyramidal coordination of the Cu centres suppresses dimer formation. Thus, the goal of preventing the perturbation of the molecular low energy spectrum of the spin triangle by intermolecular magnetic interactions can be regarded a big step forward with these compounds.
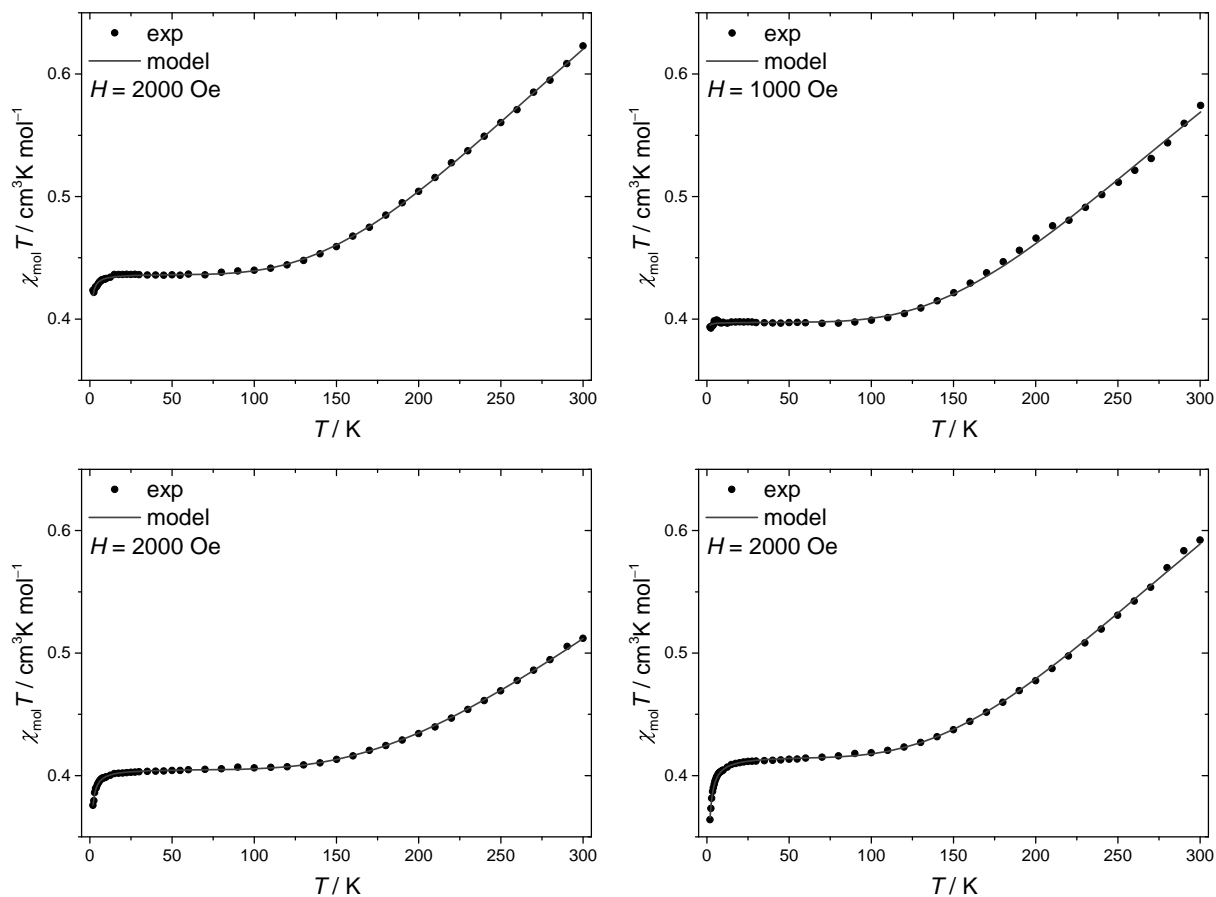
Figure 3.15: Temperature dependence of magnetic susceptibility ($\chi_{mol}T$) of powdered crystalline samples of **1** (**left top**), **3** (**right top**), **4** (**left bottom**) and **5** (**right bottom**) depicted as black dots, respectively. Corresponding parameters used for the fitted curves (grey lines) are given in table 3.11, the underlying model is an equilateral triangle spin topology with the Hamiltonian given in eq. (3.1).
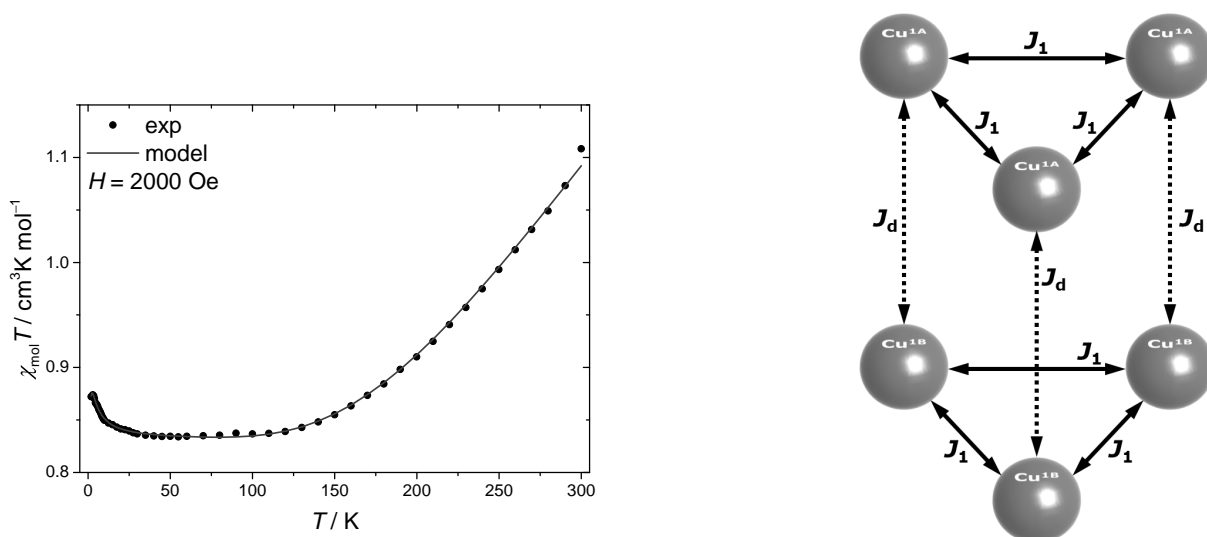
Figure 3.16: Left: Temperature dependence of magnetic susceptibility ($\chi_{mol}T$) of powdered crystalline sample of **6** taking a dimer of triangles as reference system (black dots) and the corresponding fitted curve (grey line) utilising parameters given in table 3.11 in the Hamiltonian in eq. (3.2). **Right:** Scheme of the trigonal prism spin topology and coupling scheme applied to fit the magnetic susceptibility of **6**.

Regarding the two compounds with increasing low-temperature $\chi_{mol}T$, different spin topologies are necessary to reproduce the experimental data. In the first instance, **6** was modelled as a dimer of two identical equilateral triangles with an intratriangle magnetic exchange J_1, respectively. Then, Cu(II) centres opposing each other along a stretched edge of the trigonal prism formed by the triangles are coupled by an additional intradimer exchange interaction J_d. This can be justified by dint of the crystal structure, which is the first to uncover effective $\pi\cdots\pi$ stacking between chelate ligands' aromatic rings (compare fig. 3.12). The resulting topology is depicted in fig. 3.16, mind that the molecular reference system for the $\chi_{mol}T$ curve is now a dimer of triangles. A corresponding spin Hamiltonian is derived as follows:

$$\widehat{H} = -J_1\left(\widehat{S}_1\widehat{S}_2 + \widehat{S}_1\widehat{S}_3 + \widehat{S}_2\widehat{S}_3 + \widehat{S}_4\widehat{S}_5 + \widehat{S}_4\widehat{S}_6 + \widehat{S}_5\widehat{S}_6\right) - J_d\left(\widehat{S}_1\widehat{S}_4 + \widehat{S}_2\widehat{S}_5 + \widehat{S}_3\widehat{S}_6\right) + g_{iso}\mu_B B\sum_{i=1}^{6}\widehat{S}_i \quad (3.2)$$

A molecular field parameter zJ was added to yield a good fit of the experimental data, disclosing a J_1 of $-342\,\text{cm}^{-1}$. This increased coupling constant can be explained—akin to the case of **4**—by the proximity to a square planar coordination environment of the Cu centres in comparison to other saltag-based Cu(II) triangles. However, the augmentation of J_1 is less pronounced than for **4**, because **6** features stronger pyridine donors and shorter bond lengths in the elongated axial ligand positions. For the first time amidst the tag-based Cu(II) triangles, a ferromagnetic intradimer exchange interaction J_d could be detected, which scales two orders of magnitude below J_1, namely $+1.97\,\text{cm}^{-1}$. These are exciting findings, since the weak entanglement of states of two geometrically frustrated spin triangles while retaining their magnetic moment is an interesting property with respect to their possible spin-qubit application,[62,63] which is also demanded by the diVincenzo criteria[53] (see section 1.2). Finally, the weak and
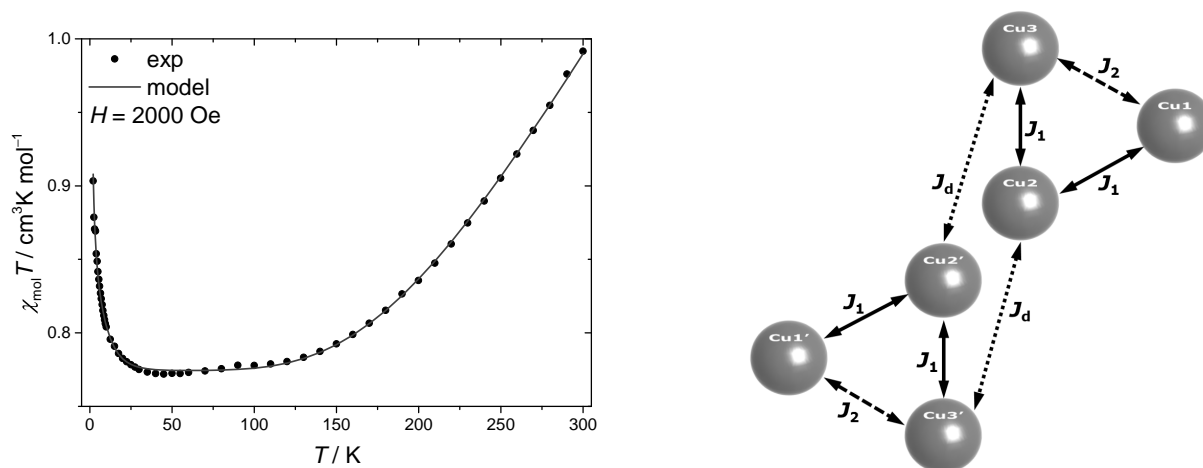
Figure 3.17: Left: Temperature dependence of magnetic susceptibility ($\chi_{mol}T$) of powdered crystalline sample of **7** (black dots) and the corresponding fitted curve (grey line) utilising parameters given in table 3.11 in the Hamiltonian in eq. (3.3). **Right:** Scheme of the armchair conformation-like spin topology and coupling scheme applied to fit the magnetic susceptibility of **7**.

also ferromagnetic zJ of +0.021 can be interpreted as minor intradimer magnetic exchange contributions running along the diagonals of the rectangular planes of the spin trigonal antiprism or weak interdimer exchange, e.g. via the π-stacking to adjacent molecular dimers (green dashed bonds in fig. 3.13). A slightly higher overall residual of the fit is obtained with respect to the other Cu(II) triangles most probably owing to the neglect of the structurally resolved differences between the two complex cations participating in the dimer (see subsection 3.1.2). Notwithstanding, the consideration of two different spin triangles would clearly overparametrise the available data.

Fitting experimental $\chi_{mol}T$-curves of **7**, the last member of tag-based Cu(II) complexes presented in this work, requires an even more complex spin topology, which approaches the circumstances given by its crystal structure. Due to the significant differences in the coordination environment and alignment within the triangle of Cu1 and Cu3 on the one hand and Cu2 on the other hand, two different magnetic exchange coupling constants J_1 and J_2 are operative within the two formal triangles building up the molecule. The cyclophane-like structure of the molecule entails Cu2 to subtend Cu3' of the second triangle and *vice versa* Cu2' faces Cu3, which is accounted for with the intertriangle coupling constant J_d. Collectively, this constructs a spin topology like a cyclohexane in armchair conformation as is illustrated in fig. 3.17. Translated into a spin Hamiltonian this yields:

$$\widehat{H} = -J_1\left(\widehat{S}_1\widehat{S}_2 + \widehat{S}_2\widehat{S}_3 + \widehat{S}_{1'}\widehat{S}_{2'} + \widehat{S}_{2'}\widehat{S}_{3'}\right) - J_2\left(\widehat{S}_1\widehat{S}_3 + \widehat{S}_{1'}\widehat{S}_{3'}\right) - J_d\left(\widehat{S}_2\widehat{S}_{3'} + \widehat{S}_{2'}\widehat{S}_3\right) + g_{iso}\mu_B B \sum_{i=1}^{6}\widehat{S}_i \quad (3.3)$$

Within the triangles the two distinct coupling constants J_1 and J_2 reflect the two cases of coordination present in the symmetric congeners **4** and **6** approximated as square plane with a distant weak O-donor (Cu2) and a somewhat closer N-donor (Cu1 and Cu3) in the apical

positions, respectively. Accordingly J_1 shows the larger modulus of $-370\,\text{cm}^{-1}$ as it includes Cu2, while J_2 is quite similar to the coupling in **4** amounting to $-344\,\text{cm}^{-1}$. The divalent intertriangle coupling J_d of $-1.4\,\text{cm}^{-1}$ is antiferromagnetic, too. This very interaction is mediated via a μ-phenoxy bridge with the bridging angle of 80.73°. Magneto-structural correlations are only reported for bis-μ-phenoxy bridged Cu dimers, so their prediction of an exchange coupling of $59\,\text{cm}^{-1}$ for this angle finds only limited applicability.[256] Nevertheless, the present ratio of exchange interactions in the frame of the armchair spin topology surprisingly leads to an $S = 1$ spin ground state of the molecule as is revealed from energy level simulations in PHI.[255] For a good fitting, no mean field parameter is necessary, which is in accordance with the absence of intermolecular interactions in **7** and additionally prevents overparametrisation against the background of the augmented number of coupling constants included. Like for the fitting of **6**, a slightly higher residual could be ascribed to the neglect of differences in the local anisotropy of the individual Cu(II) centres.

In the course of the whole discussion a treatment of the obtained values for g_{iso} has so far been left out. For some compounds low-temperature ESR spectroscopic studies reveal a set of g-values of the spin ground state, which are in good agreement with the average values from the susceptibility fits as will be detailed in the forthcoming subsection. Apart from that, all obtained g_{iso}-values are slightly above two and thus in a reasonable range for Cu(II) ions. Interpreting minor variations in these very values is scarcely meaningful, since they are very sensitive to marginal deviations in the actual molar mass of the sample caused, for instance, by partial loss of cocrystallised solvent molecules.

Table 3.11: Parameters obtained from fittings of the temperature dependence of the magnetic susceptibility $\chi_{mol}T$ for the the Cu(II) complexes described in this chapter.

	1	**3**	**4**	**5**	**6**	**7**
g_{iso}	2.155	2.06	2.08	2.107	2.103	2.034
$J_1/\,\text{cm}^{-1}$	−297.8	−295.3	−369.1	−298.9	−342.2	−370.2
$J_2/\,\text{cm}^{-1}$	-	-	-	-	-	−344.22
$J_d/\,\text{cm}^{-1}$	-	-	-	-	+1.97	−1.41
$zJ/\,\text{cm}^{-1}$	−0.048	−0.006	−0.101	−0.172	+0.021	-
Residual	$0.67 \cdot 10^{-4}$	$0.17 \cdot 10^{-4}$	$0.23 \cdot 10^{-4}$	$0.99 \cdot 10^{-4}$	$3.61 \cdot 10^{-4}$	$3.18 \cdot 10^{-4}$

Recapitulating the intratriangle coupling constants found for the Cu systems reported in this work (table 3.11), it must be stated that possible influences of the diazine bridging angle Cu–N–N–Cu (table 3.10) are clearly overridden by variations of the coordination environment and therewith the spin density distribution. Hence, reported magneto-structural correlations[257,258] are scarcely applicable.

In summary, for all discussed Cu(II) compounds strong antiferromagnetic intratriangle couplings could be detected and quantified, which lead to energetically well-isolated geometrically spin-frustrated ground states of the spin triangles, although the ideal C_3 symmetry of the triangle is lifted in case of **7**. Low temperature intertriangle magnetic interactions are minimised in congeners with trigonal bipyramidal coordination of the Cu(II) ions (**1** and **3**), while **6** is the

first example featuring such interactions of ferromagnetic nature. The unusual spin topology in **7** results in an $S = 1$ spin ground state of two anellated spin triangles, withal exclusively antiferromagnetic interactions present.

3.1.4 ESR Spectroscopy

Low temperature X-band ESR spectroscopy was carried out on powdered samples of **1**, **6** and **7**, because they represent novel structures of tag-based Cu(II) triangles. For **1** and **6**, frozen pyridine solutions were additionally examined, with pulsed ESR experiments performed on the former by Junjie Liu, which have already been reported.[250] Unfortunately, comparable frozen solution studies were not feasible for **7** due to its low solubility. Besides, for all samples similar spectra were recorded at 10, 20 and 150 K and these show only broadening of the same signals with decreasing intensities and are therefore not treated further.

A depiction of the experimental spectra can be found in figures 3.18 and 3.19. For all spectra full matrix diagonalisation simulations were performed to approach the experimental data. First, a reproduction of the spectrum based on a single $S = \frac{1}{2}$ possessing an axial set of g-values was targeted. These very g-values were then transferred into the following spin Hamiltonian representing the equilateral triangle spin topology:

$$\widehat{H} = -J_{\text{ex}}\left(\widehat{S}_1\widehat{S}_2 + \widehat{S}_1\widehat{S}_3 + \widehat{S}_2\widehat{S}_3\right) \;+\; g_{x,y,z}\mu_{\text{B}}B\sum_{i=1}^{3}\widehat{S}_i \tag{3.4}$$

This allowed to survey the influence of the exchange coupling on the simulated spectrum. The three g-tensors of the individual spin centres were rotated by 120° with respect to each other to account for the molecular C_3 symmetry. Of course, this procedure neglects possible rhombicity of the single ion g-tensors of the individual Cu(II) centres, which can be expected according to *ab-initio* calculations done by Michael Böhme for **1**.[250] However, since the experiments exclusively probe the coupled spin ground state of the molecules the triangular plane remains magnetically isotropic and the apparent g-tensor is always an axial one, thus only two different g-values can be extracted from the spectra. For a better understanding of the single ion magnetic anisotropy the pursued diamagnetically diluted samples are essential. Since the presented equilateral triangle spin topology is inappropriate for **7**, here a modification of the Hamiltonian onto two distinct coupling constants (isosceles triangle) in analogy to the treatment of the susceptibility data was included.

In this manner, all three powder spectra could be simulated in good agreement with the experimental data applying the approximate isotropic exchange couplings resulting from the corresponding susceptibility. Anisotropic linewidth was included as a g-strain parameter necessary for the respective g_z values. Entire parameter sets used for the simulations are collated in table 3.12.

To acquire information about the possible contribution of Dzyaloshinski-Moriya antisymmetric exchange interaction, the Hamiltonian was extended for a z-component antisymmetric
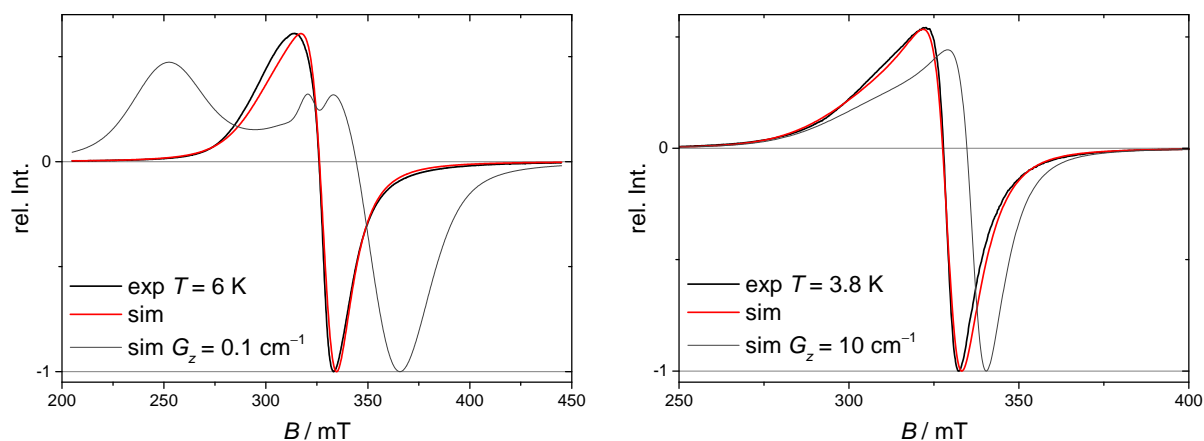
Figure 3.18: Left: X-band ESR spectrum of powdered crystalline **1** recorded at 6 K (black line). **Right:** X-band ESR spectrum of powdered crystalline **7** recorded at 3.8 K (black line). For both spectra corresponding simulations utilising the parameters given in table 3.12 are drawn in red, the thin dark grey line is a simulation with the same parameters adding an antisymmetric exchange G_z as given in the figure.
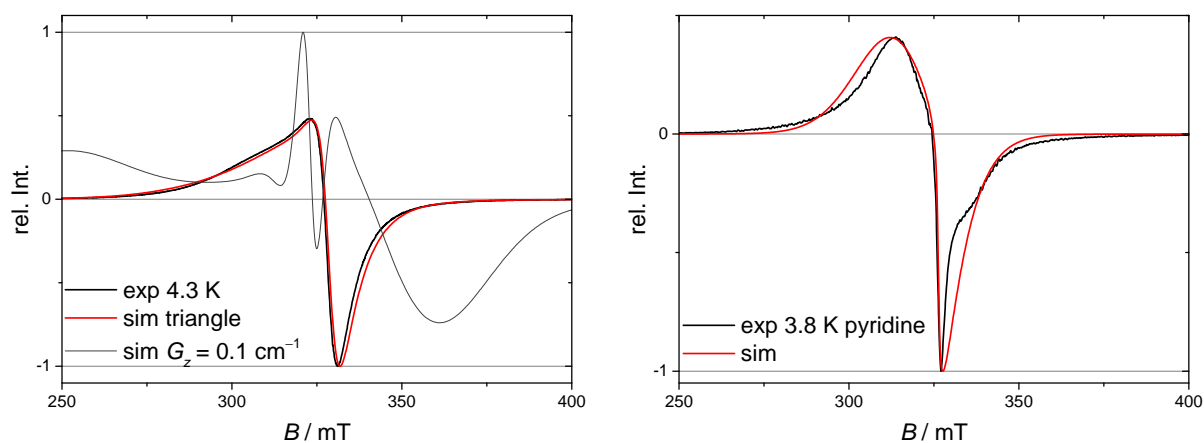
Figure 3.19: Left: X-band ESR spectrum of powdered crystalline **6** recorded at 4.3 K (black line). **Right:** Frozen pyridine solution X-band ESR spectrum of **6** recorded at 3.8 K (black line). For both spectra corresponding simulations utilising the parameters given in table 3.12 are drawn in red. The thin dark grey line in the left spectrum is a simulation with the same parameters adding an antisymmetric exchange G_z as given in the figure.

exchange term with the parameter G_z:

$$\widehat{H} = -G_z \left[(\widehat{S}_{1,x}\widehat{S}_{2,y} - \widehat{S}_{1,y}\widehat{S}_{2,x}) + (\widehat{S}_{2,x}\widehat{S}_{3,y} - \widehat{S}_{2,y}\widehat{S}_{3,x}) + (\widehat{S}_{3,x}\widehat{S}_{1,y} - \widehat{S}_{3,y}\widehat{S}_{1,x}) \right] \qquad (3.5)$$

Setting this parameter to $0.1\,\mathrm{cm}^{-1}$ has a tremendous influence on the simulated low-temperature ESR spectra for **1** and **6** (compare fig. 3.18 and 3.19) and lead to entirely different spectra, whereas a cutback of the parameter about one order of magnitude has no apparent effect on the simulation of **6** but leads to a minor improvement of congruency for **1**. It can therefore be concluded, that antisymmetric exchange contributions are far below $0.1\,\mathrm{cm}^{-1}$ in these two compounds. Consequently, the model used for fitting the susceptibility, in which antisymmetric exchange components are neglected, is confirmed to be adequate.

Table 3.12: Parameters utilised in simulations of low-temperature ESR spectra of **1**, **6**, **7**. LW(L) is purely Lorentzian isotropic linewidth, g-strain is an anisotropic line broadening pertaining the named g-components.

	1		**6**	**7**
	pwd 6 K	pwd 4.3 K	pyridine 3.8 K	pwd 3.8 K
$g_{x,y}$	2.040	2.044	2.120	2.040
g_z	2.189	2.210	2.055	2.180
$J_{ex}/\,\mathrm{cm}^{-1}$	−300	−300	−300 −300 −300.1	−370 −370 −344
LW (L) / mT	12	5	0.7	7
g-strain$_z$	0.2	0.28	0.17(x,y)	0.2

In contrast, in the case of **7** such small antisymmetric exchange has no visible effect on the simulated spectra, it becomes significant only at about $10\,\mathrm{cm}^{-1}$ (compare fig. 3.18). Because of the different coupling constants present, the ground state degeneracy is lifted and thereby the sensitivity of resonances accessible in X-band experiments to antisymmetric exchange components vanishes. Hence, no statement about the dimension of possible Dzyaloshinski-Moriya exchange is possible for **7** based on this data.

Finally, the X-band spectrum of **6** in frozen pyridine solution at 3.8 K could only be simulated by an inversion of the single ion g-components assuming larger $g_{x,y}$ than g_z and also applying the g-strain to the x,y components. This somehow opposes the findings from the frozen pyridine solution X-band ESR studies on **1**[250] and suggests significant changes of the coordination environment of the individual Cu(II) ions in pyridine solution. Interestingly, the congruence of the simulation with the experimental curve could be improved perceptibly by a minor change in one coupling constant (from 300 to $300.1\,\mathrm{cm}^{-1}$), which lifts the ground state degeneracy and indicates a lowering of the molecular symmetry in solution. However, the agreement between the experimental and the simulated spectrum is still rather poor in comparison to the powder spectra, which leaves open space for different interpretations. For this very reason analogous approaches to determine possible antisymmetric exchange were renounced in this case.

In conclusion the low-temperature X-band ESR surveys revealed an axial g-value for the ground spin states of compounds **1**, **6** and **7**, which are in agreement with the averaged g-values

obtained from the susceptibility fits. For **1** and **6** possible antisymmetric exchange G_z could be shown to be much smaller than $0.1\,cm^{-1}$, which validates the model utilised for susceptibility fits lacking such contribution. Due to the lower symmetry of **7** its X-band ESR spectrum is less sensitive to Dzyaloshinski-Moriya exchange-based influences. Frozen pyridine solution spectra of **6** reveal noteworthy changes in the axial g-tensor of the spin ground state suggesting modifications of the coordination environment and a lowering of molecular symmetry, but the quality of its description remains developable.

3.1.5 Concluding Remarks

Six new Cu(II) complexes are added to the existing portfolio of tag-based Cu(II) antiferromagnetic triangles[50,239,242,246,247] in the frame of this work. For the first time, congeners with trigonal bipyramidal coordination of the individual Cu centres effectively blocking intermolecular magnetic exchange (**1**), formally neutral complexes (**4**) as well as ferromagnetically coupled dimers of triangles (**6**) and hexanuclear cyclophane-like assemblies (**7**) are reported.

Since the structural broadness of the available compounds can herewith tentatively be considered sufficient, the next logical steps to probe spin-electric coupling and thus suitability of the systems as electrically controllable spin qubits were tackled. This includes determination of T_2 spin coherence times of **1** in solution[250] in cooperation with Arzhang Ardavan's group in Oxford, which emerged to be indeed suitable for a classical qubit addressing according to DiVincenzo's criteria.[53] Also, in the frame of this cooperation first traces of spin-electric coupling mechanisms could be detected by Hahn-echo ESR experiments with electric fields in a solution of **1**.[259]

Single crystals of the same compound were investigated in electric field modulated ESR experiments[102,260] in cooperation with Roberta Sessoli's group in Florence. A signal clearly indicating spin-electric effects could be detected in the triangular plane (manuscript in preparation), which is in accordance with the prediction of Loss *et al.*.[82,83] Against the background of these experiments, crystallising tag-based Cu(II) triangles in further non-centrosymmetric space groups, ideally lacking all mirror symmetry remains a desired synthetic target. This goal was partially achieved with **6**, however, the dimer formation accompanied by strong intradimer magnetic interaction leaves the suitability for these experiments in question.

The deposition of tag-based antiferromagnetic Cu(II) triangles on highly oriented pyrolithic graphite (HOPG) surfaces was successfully carried out (manuscript in preparation). The chemical integrity of the trinuclear unit on the surface could be proven by X-ray photoelectron spectroscopy (XPS) and desorption electrospray ionisation mass spectrometry (DESI-MS) measurements on the surface in cooperation with Maria Küllmer[261] and Ron Hermenau,[262] respectively. The retention of the magnetic properties on the surface was addressed via X-ray magnetic circular dichroism (XMCD) experiments in cooperation with Eugen Weschke[263] at beamline UE46 PGM-1 at BESSY II.[264] Although the surface deposition studies are not further detailed in the frame of this work, these investigations pave the way for scanning tunneling microscopy surveys allowing the probe of single molecules with high local electric fields at low temperatures. Such setups should be pursued as soon as possible, considering the overall very

promising results especially for **1**.

3.2 Bridged Spin-Frustrated Fe(III) Triangles

Growing the molecular entity of geometrically frustrated spin triangles to larger but still well-defined aggregates is an exciting aim. Taking into consideration, that possible molecular spin qubits need to be addressed as individual isolated molecules, *e.g.* on a surface or in a suitable matrix, the concept of "entanglement"[53] must be realised on a molecular level. Hence, coordinative linking of two tag-based antiferromagnetic spin triangles with adjustable magnetic interaction might be an ideal molecular realisation of two entangled spin-qubits.

For first synthetic approaches, hexacyanoferrates were chosen as bridging units. They are highly charged, well characterised and structurally stable but at the same time redox-active and thereby variant in resulting spin momentum. As complementary tag-based triangular building blocks, respective Fe(III) complexes were chosen, because they combine high positive charge with good redox stability and kinetically labile coordination chemistry. Furthermore, in every known spin ground state of Fe(III), a non-integer spin leading to a geometrically frustrated molecular spin ground state is provided.

3.2.1 Synthesis and Characterisation

For the synthesis of heptanuclear iron complexes by hexacyanometalate bridging of trinuclear units based on saltag ligands, a one-pot multicomponent approach was developed. Successful isolation of crystalline material suitable for single-crystal X-ray diffraction was achieved with $H_5saltag^H \cdot HCl$ and $H_5saltag^{Br} \cdot HCl$ so far. Upon reaction with $FeCl_3 \cdot 6H_2O$ in pyridine as a mildly alkaline donor solvent, trinuclear complex species are to be formed *in situ* (see fig. 3.20, top). By addition of $NaClO_4$ and slow diffusion of MeOH to the solution containing $H_5saltag^{Br} \cdot HCl$ as ligand, crystalline $[Fe_3saltag^{Br}Cl_3(py)_6]ClO_4$ can be isolated as was first described by Plaul.[50] This very compound, though not directly used as a precursor, serves as a kind of reference for the more complex heptanuclear aggregates described in here.

The primarily described solution containing $H_5saltag^H \cdot HCl$ as tritopic ligand is subsequently exposed to $K_3[Fe(CN)_6]$ in the presence of 18-crown-6 to overcome solubility issues. Significant lowering of the solution's polarity by diffusion of toluene causes the formation of solid crystalline $[K(18\text{-crown-}6)][(Fe_3saltag^HCl_3(py)_6)_2\mu(Fe(CN)_6)]$ (**9**), which is a monoanionic heptairon complex with a complex $[K(18\text{-crown-}6)^+]$ countercation.

Analogously, if $H_5saltag^{Br} \cdot HCl$ is present in the reaction solution, the addition of NBz_3 enables an *in situ* reduction of $[Fe(CN)_6]^{3-}$ to $[Fe(CN)_6]^{4-}$. This allows the growth of crystals of the neutral heptairon-dipotassium complex $[(KFe_3saltag^{Br}Cl_3(py)_3)_2\mu(Fe(CN)_6)]$ (**10**).

Both complexes consist of two trinuclear iron complex-fragments of the tritopic tag-based ligand and one bridging hexacyanoferrate moiety. Vacant coordination sites at the Fe(III) centres are saturated by Cl^- and pyridine ligands. An overview of the synthetic routes to both complexes as well as a depiction of the chemical constitution and connectivity is given in fig. 3.20.

Elemental analyses of both materials reveal the presence of cocrystallised solvent molecules, namely one toluene in **9** and 1.5 pyridine in **10**. For the latter, three equivalents of cocrystallised
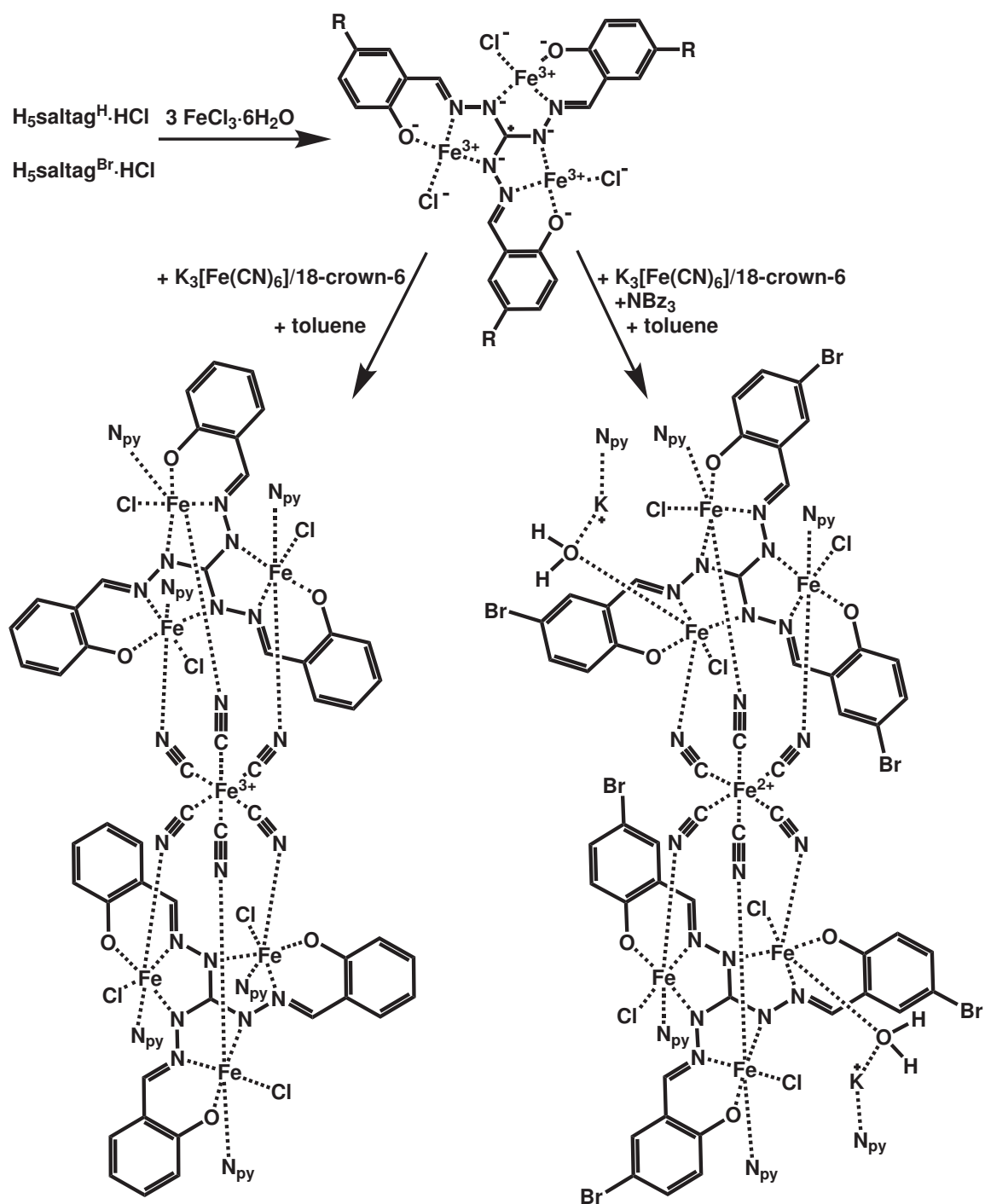
Figure 3.20: Synthesis scheme showcasing the synthetic routes to obtain [K(18-crown-6)][(Fe$_3$saltag^{H}Cl$_3$(py)$_6$)$_2\mu$(Fe(CN)$_6$)] (**9**, **left**) and [(KFe$_3$saltag^{Br}Cl$_3$(py)$_3$)$_2\mu$(Fe(CN)$_6$)] (**10**, **right**). Mind that in the lower sketches all formal charges except for the metal ions not included in the common precursor structure above are omitted and pyridine coligands are abstracted as 'N$_{py}$' for the sake of clarity, so they are meant to illustrate the chemical composition and connectivity of the complexes. Compound **9** on the bottom left side features a ferricyanide (Fe(III)ls) bridge and is overall monoanionic, the [K(18-crown-6)] countercation is omitted. Compound **10** on the bottom right side bears a ferrocyanide (Fe(II)ls) bridge and is a neutral complex as drawn.

pyridinium chloride also found in the crystal structure are confirmed. No ions related to intact complex molecules could be detected in ESI-MS experiments (positive and negative), which is probably due to low solubility of the compounds in polar protic solvents.

3.2.2 Crystal Structures

**[K(18-crown-6)][(Fe$_3$saltag^{H}Cl$_3$(py)$_6$)$_2\mu$(Fe(CN)$_6$)]** **(9)**

The heptanuclear iron complex crystallises in the trigonal space group $R\bar{3}$ (#148). The crystallographic C_3 axis goes through the central carbon atom of the triaminoguanidine moiety of the tritopic chelate ligand and the iron atom of a hexacyanoferrate moiety bridging two trinuclear fragments, so that all remaining iron atoms of the monoanionic complex are crystallographically equal. Half a complex anion of **9** is depicted in fig. 3.21. Furthermore the potassium atom of the [K(18-crown-6)$^+$] countercation is situated on this axis. The structure contains two crystallographically independent heptanuclear iron complex anions, referred to as A and B, whereat the latter superposes its enantiomers on the same crystallographic positions in a ratio of 1:1. Apart from that both complex anions are structurally very similar and therefore discussed together. Selected bond lengths and angles of both anions are listed in table 3.13. Moreover the cell contains three units of pyridinium chloride per complex anion, which are equivalent by crystal symmetry and form contact ion pairs (distance $N_{py} \cdots Cl = 308$ pm).

All Fe centres bound in the two chelate ligands have the same [N$_4$OCl] donor environment. One pyridine, one chloride and one bridging cyanide's N-terminus bind per iron centre as additional coligands forming a distorted octahedron (see fig. 3.21) together with the saltag ligand's [N$_2$O] donor pocket. Continuous shape measures[251–253] yield deviation parameters from the ideal octahedron geometry of 1.377 (A) and 1.241 (B). The corresponding bond lengths range from 181 pm to 243 pm, whereat the phenoxide forms the shortest and chloride shows the longest bonding distances. Interestingly, the second shortest coordinative bond is formed with the cyanide's N-terminus, despite its bridging nature and the rather unfavoured bridging angle Fe–N–C of 150° (for A, 151° for B).

The bridging hexacyanoferrate moiety shows slight deviations from its ideal octahedral coordination environment (shape parameter of 0.153 for A and 0.283 for B) caused by the tilt of the cyanide ions necessary to accomplish the trivalent bridging to each of the two triangles. This tilt is expressed by two distinct binding angles C–Fe–C of 86.8° (85.6°) between the ions pointing towards one triangle and 93.2° (94.4°) between the ions pointing towards opposite triangles. Although a decision on whether the bridge contains an Fe(II) or Fe(III) cannot be done on the basis of structural parameters,[265] the overall charge balance suggests it to be a ferricyanide (Fe(III)).

As in the trinuclear structure by Plaul[50] the Fe centres protrude from the tag plane by 50 pm (44 pm for B) in direction of the ferricyanide bridge, which is also reflected by the low diazine bridging dihedral angle Fe–N–N–Fe of 146° (148°). Intramolecular metal$\cdots$metal distances amount to 503 pm (501 pm) within the triangle, 489 pm (490 pm) to the bridging iron and 839 pm (842 pm) as shortest distance to the opposing triangle. An intersecting angle of 22° (27°)
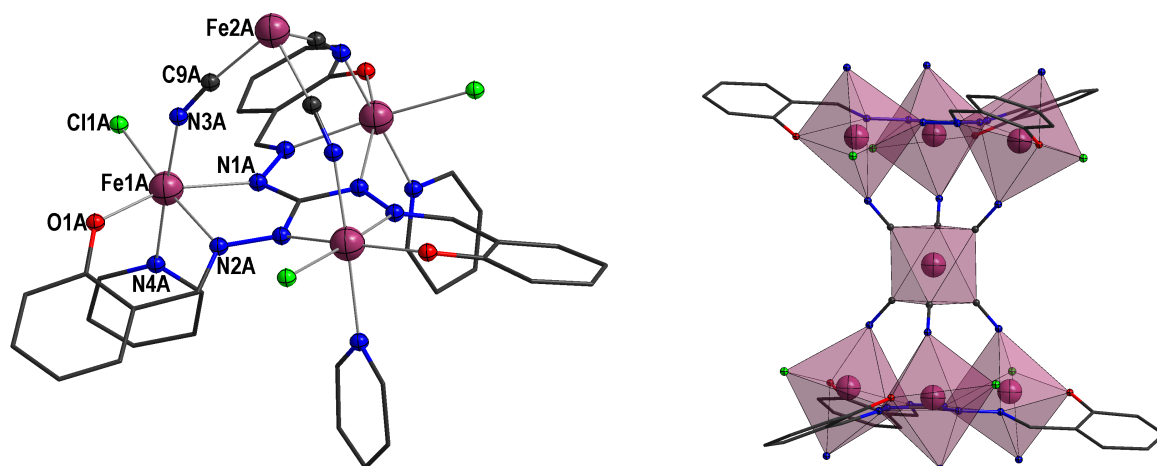
Figure 3.21: Left: Molecular structure of half a molecule of **9** with atom labels. C atoms are wire nodes, Fe: purple, N: blue, O: red, H atoms and cocrystallised solvent are omitted for clarity. **Right:** Illustration of the distorted octahedral coordination polyhedra of Fe(III) centres **9** (molecule A) also illustrating the hourglass topology. Pyridine residues of donors N4A are omitted for clarity. Colour code is identical.

Table 3.13: Selected bond lengths (pm) and angles (°) from the coordination environment of iron centres in the heptanuclear complex anions A and B of **9**. Symmetry generated equivalent atoms are marked with '$(-x + y, 1 - x, z)$", "$(-\frac{1}{3} + y, \frac{1}{3} - x + y, \frac{4}{3} - z)$", "'$(1 - x + y, 2 - x, z)$" and """$(y, 1 - x + y, 1 - z)$". The corresponding numbering scheme is depicted in fig. 3.21.

Molecule A		Molecule B	
Fe1A–O1A	190.9(5)	Fe1B–O1B	180.6(18)
Fe1A–N1A	211.1(5)	Fe1B–N1B	213.(2)
Fe1A–N2A	214.5(5)	Fe1B–N2B	203.4(17)
Fe1A–N3A	205.9(5)	Fe1B–N3B	204.8(8)
Fe1A–N4A	222.7(7)	Fe1B–N4B	224.8(9)
Fe1A–Cl1A	231.30(16)	Fe1B–Cl1B	242.7(7)
Fe2A–C9A	191.1(7)	Fe2B–C14B	189.3(11)
O1A–Fe1A–N1A	157.5(2)	O1B–Fe1B–N1B	165.0(7)
O1A–Fe1A–N2A	86.1(2)	O1B–Fe1B–N2B	90.3(8)
O1A–Fe1A–N3A	96.8(2)	O1B–Fe1B–N3B	94.7(6)
O1A–Fe1A–N4A	85.4(3)	O1B–Fe1B–N4B	89.1(6)
O1A–Fe1A–Cl1A	99.59(15)	O1B–Fe1B–Cl1B	96.9(7)
N2A–Fe1A–N1A	72.8(2)	N2B–Fe1B–N1B	74.9(6)
N2A–Fe1A–N3A	93.01(14)	N2B–Fe1B–N3B	90.6(5)
N2A–Fe1A–N4A	89.2(2)	N2B–Fe1B–N4B	87.6(4)
N2A–Fe1A–Cl1A	174.18(15)	N2B–Fe1B–Cl1B	172.7(5)
N3A–Fe1A–N1A	90.6(2)	N3B–Fe1B–N1B	87.9(4)
N3A–Fe1A–N4A	177.8(2)	N3B–Fe1B–N4B	175.8(4)
N3A–Fe1A–Cl1A	91.12(16)	N3B–Fe1B–Cl1B	90.3(3)
N4A–Fe1A–N1A	87.2(2)	N4B–Fe1B–N1B	87.9(4)
N4A–Fe1A–Cl1A	88.69(19)	N4B–Fe1B–Cl1B	91.0(3)
Cl1A–Fe1A–N1A	101.41(15)	Cl1B–Fe1B–N1B	97.9(4)
C9A–Fe2A–C9A'	86.8(3)	C14B–Fe2B–C14B'''	85.6(4)
C9A–Fe2A–C9A''	93.2(3)	C14B–Fe2B–C14B''''	94.4(4)

indicates the salicylic aldehyde arms of the chelate ligand to be heavily tilted from the tag plane. The arrangement of the metal centres can be considered as an hourglass-like topology (compare fig. 3.21) with the two bridged triangles in a staggered (trigonal antiprismatic) alignment. No hints for intermolecular interactions can be found in the structure.

## $[(KFe_3saltag^{Br}Cl_3(py)_3)_2\mu(Fe(CN)_6)]$ (10)

The neutral complex compound **10** crystallises in the monoclinic space group $P2_1/n$ (#14), where the asymmetric unit (see Figure 3.22) consists of half a neutral complex molecule and 4.75 cocrystallised non-coordinating pyridine molecules (not depicted) amongst which one is statistically disordered. The five-fold deprotonated saltag^{Br} ligand hosts three crystallographically independent iron nuclei, that are each chelated by the tridentate N_2O donor-set of the three equal coordination-pockets. Two of these triangles are hexavalently bridged by a hexacyanoferrate moiety, whose Fe centre is a crystallographic inversion centre. Selected bond lengths and angles of the coordination environments are listed in table 3.14.

All three iron centres are also coordinated by a chloro ligand situated in the plane of the chelate ligand. One remaining coordination site is occupied by the N-bottom of three bridging cyanide ions from the central hexacyanoferrate moiety at all three iron centres. The coordination sphere is saturated by a pyridine donor in case of Fe1 and Fe3 and a water ligand in case of Fe2. Coordination bond lengths range from 191 pm to 232 pm with phenolate donors forming the shortest and chloride donors forming the longest bonds. Again the bridging cyanide's N terminuses show the second shortest contact withal the unfavourable bridging angles Fe–N–C of 152° (all three centres). On the whole, a distorted octahedral coordination environment is found for these three iron centres (see fig. 3.23). The corresponding shape deviation parameters[251–253] for the ideal octahedron geometry are 1.408, 1.206 and 1.706 (Fe1, Fe2 and Fe3).

The aforementioned three cyanide ligands' C-terminuses bind the central bridging Fe4, which is the crystallographic inversion centre of the complex molecule. Together with the inverted counterpart the six cyanide ions surround Fe4 in a slightly distorted octahedral fashion (shape parameter 0.247). Per contra to the bridge in **9** no preferential directions of distortion can be detected. Also here, a determination of the oxidation state of the iron centre on the basis of structural features fails.[265] However, the overall charge balance of the structure necessitates it to be Fe(II) and hence, in contrast to the bridge in **9**, a ferrocyanide. This is in accordance with the addition of NBz$_3$ as a mild reducing agent during the synthesis.

Moreover, the water molecule coordinating Fe2 is a bridging ligand also coordinating a potassium ion. The latter is positioned above the tag plane and coordinated by one more pyridine molecule. Directly neighbouring the pyridine coligands of Fe1 and Fe2 the potassium ion has remarkably close contacts to the respective 2-H atoms of those pyridine molecules, namely K1–H = 269 pm and 263 pm, suggesting possible weak interactions.

Further structural properties of the triangular unit are comparable with those of **9**. However, the iron centre bearing the axial water ligand (Fe2) instead of the pyridine introduces some structural discrimination into the triangle also reflected in the following bridging parameters.
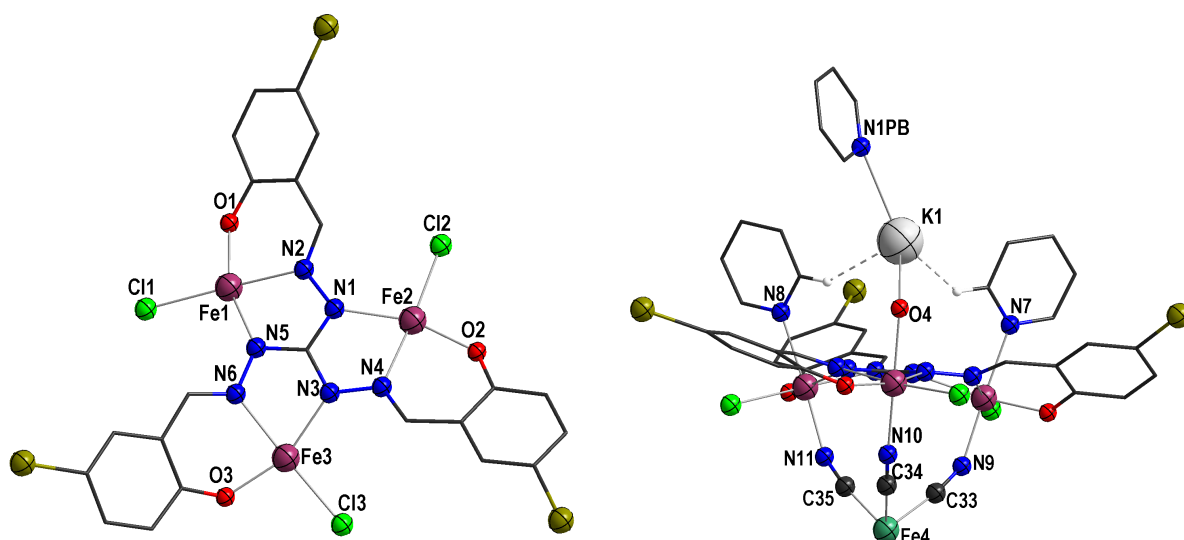
Figure 3.22: Left: View on one of the two bridged Fe(III) triangles of **10** with corresponding number-ing scheme, only the chelate ligand and chloride donor atoms in the ligand plane are shown. C atoms are wire nodes, Fe(III): purple, N: blue, O: red, Br: dark yellow H atoms and cocrystallised solvent are omitted for clarity. **Right:** View of the left figure rotated by 90° showing all parts of the asymmetric unit included in the neutral complex (shown half of it). Colour code is identical, additionally K: light grey, Fe(II): turquoise, H atoms are omitted for clarity except for the ones possibly involved in agostic interactions with the potassium ion (sketched as white dashed bonds).
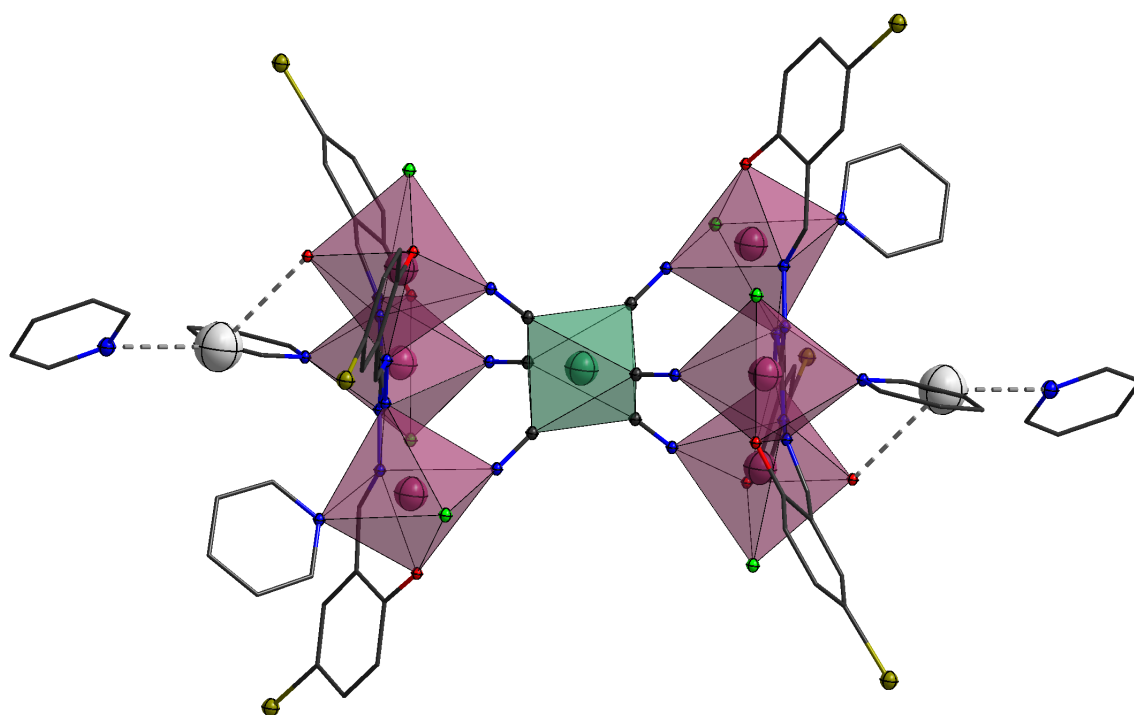
Figure 3.23: Illustration of the distorted octahedral coordination polyhedra of Fe(III) (purple) and Fe(II) (turquoise) centres in **10** also illustrating the hourglass topology.

Table 3.14: Selected bond lengths (pm) and angles (°) from the coordination environment of iron and potassium centres within the heptairon neutral complex **10**. The corresponding numbering scheme is depicted in fig. 3.22.

K1–N1PB	297.3(5)	K1–O4	305.9(4)	K1–H27A	269.4
K1–H32A	263.2				
Fe1–O1	193.4(3)	Fe1–N9	205.5(4)	Fe1–N5	213.1(4)
Fe1–N2	214.6(4)	Fe1–N7	221.9(4)	Fe1–Cl1	231.54(14)
Fe2–O2	191.8(4)	Fe2–N10	206.6(4)	Fe2–O4	210.9(4)
Fe2–N1	211.4(4)	Fe2–N4	214.7(4)	Fe2–Cl2	230.44(14)
Fe3–O3	191.4(3)	Fe3–N11	205.4(4)	Fe3–N3	209.3(4)
Fe3–N6	216.2(4)	Fe3–N8	222.9(4)	Fe3–Cl3	232.30(14)
Fe4–C33	189.7(5)	Fe4–C34	189.9(5)	Fe4–C35	189.9(5)
N1PB–K1–O4	108.83(12)				
N7–Fe1–Cl1	88.75(12)	O1–Fe1–N9	91.55(16)	O1–Fe1–N5	157.68(15)
N9–Fe1–N5	90.50(16)	O1–Fe1–N2	85.52(14)	N9–Fe1–N2	92.44(16)
N5–Fe1–N2	72.18(14)	O1–Fe1–N7	85.54(15)	N9–Fe1–N7	175.85(16)
N5–Fe1–N7	91.07(15)	N2–Fe1–N7	84.40(15)	O1–Fe1–Cl1	100.20(11)
N9–Fe1–Cl1	94.69(13)	N5–Fe1–Cl1	101.78(11)	N2–Fe1–Cl1	170.72(11)
N4–Fe2–Cl2	174.88(13)	O2–Fe2–N10	94.85(17)	O2–Fe2–O4	89.63(15)
N10–Fe2–O4	173.49(15)	O2–Fe2–N1	159.31(15)	N10–Fe2–N1	87.55(16)
O4–Fe2–N1	86.60(15)	O2–Fe2–N4	86.39(15)	N10–Fe2–N4	88.96(16)
O4–Fe2–N4	86.62(15)	N1–Fe2–N4	73.08(15)	O2–Fe2–Cl2	97.14(11)
N10–Fe2–Cl2	94.41(12)	O4–Fe2–Cl2	89.70(11)	N1–Fe2–Cl2	103.17(11)
N11–Fe3–N3	89.89(16)	O3–Fe3–N6	84.91(15)	N11–Fe3–N6	89.68(16)
N3–Fe3–N6	72.09(14)	O3–Fe3–N8	86.65(15)	N11–Fe3–N8	176.44(17)
N3–Fe3–N8	89.73(15)	N6–Fe3–N8	93.57(15)	O3–Fe3–Cl3	97.26(11)
N11–Fe3–Cl3	89.43(12)	N3–Fe3–Cl3	105.81(11)	N6–Fe3–Cl3	177.72(11)
N8–Fe3–Cl3	87.26(12)	O3–Fe3–N11	95.10(16)	O3–Fe3–N3	156.45(15)
C34–Fe4–C35	86.6(2)	C33–Fe4–C34	93.6(2)	C33–Fe4–C35	95.1(2)

Distances of the iron centres from the tag plane are 59, 37 and 57 pm (Fe1, Fe2 and Fe3, respectively) and the dihedral angles of the diazine bridges are determined to 148°, 141° and 149° (Fe1–N2–N1–Fe2, Fe1–N5–N6–Fe3 and Fe2–N4–N3–Fe3, respectively). Fe2 also shows the longest span to the bridging cyanometalates Fe4 of 494 pm in contrast to those of Fe1 and Fe3, which are both 490 pm. Intratriangle Fe···Fe distances are again homogeneous around 505 pm, while the shortest intramolecular intertriangle Fe···Fe distances are 840, 844 and 840 pm (for Fe1, Fe2 and Fe3, respectively). No hints for intermolecular interactions were detected in the structure.

3.2.3 Mößbauer Spectroscopy

Mößbauer spectra of both compounds **9** and **10** were recorded at 80 K in the absence of a magnetic field and fitted by Eckhard Bill.[266] They are therefore described only very briefly, because the results are essential for the further investigation of the compounds. Both spectra with the corresponding fits are depicted in fig. 3.24.
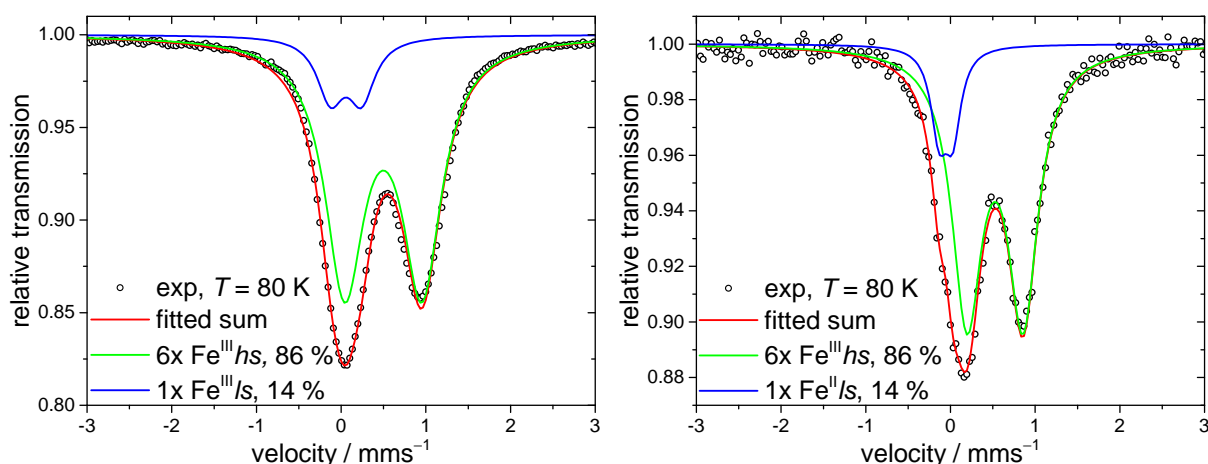
Figure 3.24: Left: Experimental Mößbauer spectrum (black spheres) of **9** with corresponding fit. Red line represents the sum fitted spectrum consisting of two subspectra for six high-spin Fe(III) centres (green) and one low-spin Fe(III) centre (blue) in the ratio 6:1. **Right:** Mößbauer spectrum of **10**, colour and symbol code is identical. Here the blue spectrum corresponds to a low-spin Fe(II) centre.

Both spectra could be fitted with two components (sub1 + sub2) in a ratio of 6:1, which perfectly concurs with the occurrence of the six Fe centres within the two triangles and the bridging hexacyanometalate unit of the complexes. A collection of the used fitting parameters is given in table 3.15. The six iron centres within the triangular unit are described with a rather equal isomeric shift δ_{rel} (relative to sodium nitroprussiate dihydrate) in the typical range for Fe(III) high-spin centres.[267] Somewhat surprising is the deviation of the quadrupole splitting ΔE_Q, however, this is hard to rationalise for arbitrarily distorted coordination environments. Linewidths are again comparable for sub1 in both compounds.

The components sub2 accounting for the bridging hexacyanoferrates only show minor differences in the isomeric shift. This is no hint for the oxidation state of the iron centre, since on the basis of the isomeric shift a discrimination of ferricyanides and ferrocyanides is not possi-

Table 3.15: Parameters obtained from fittings of the Mößbauer spectra of **9** and **10**.

parameter	9		10	
	sub 1	sub 2	sub 1	sub 2
δ_{rel}/ mms^{-1}	0.50	0.06	0.53	−0.05
ΔE_Q/ mms^{-1}	0.91	0.37	0.66	0.16
linewidth/ mms^{-1}	0.56	0.38	0.43	0.23
weighting/ %	86	14	86	14

ble.[268–270] Nevertheless, the values are in a reasonable range for hexacyanometalates bridging to Fe(III) centres coordinated by donors of comparable strength.[271] Eventually, the quadrupole splitting is significantly larger in **9**, which is a clear hint for the bridge to be Fe(III). For symmetric ferrocyanides no ΔE_Q is detected,[268] however, desymmetrisation of the coordination environment gives rise to small quadrupole splittings.[268,269] Interestingly, the exact parameters of **10** are also reported for a ferrocyanide moiety bridging two triangles of high spin Fe(III) centres at 80 K by Glaser *et al.*.[271]

Merging the hints from the crystal structure analysis with the findings from Mößbauer spectroscopy, the oxidation and spin states of the distinct Fe centres in **9** and **10** can be determined beyond doubt. In both compounds the Fe centres bound in the saltag ligand based triangular units are Fe(III) high spin. In contrast the bridging hexacyanoferrate moiety is a ferricyanide (Fe(III) low spin) in **9** and a ferrocyanide (Fe(II) low spin) in **10**.

3.2.4 Magnetic Properties

Magnetic susceptibility measurements of the compounds **9** and **10** were carried out in the temperature range from 2 K to 300 K. The resulting $\chi_{mol}T$ curves are depicted in Figure 3.25, mind that the right curve belonging to **10** refers to only half a molecule (for reasons expounded later). High temperature values at 300 K are below the expected values for the respective uncoupled electronic spins assuming $g = 2$ (26.625 for **9** and 13.125 for **10**). Both compounds show a continuous decrease of $\chi_{mol}T$ upon lowering the temperature, which indicates antiferromagnetic coupling mechanisms operative. At 7 K **9** reaches a minimum of $\chi T = 2.43\,\text{cm}^3\text{Kmol}^{-1}$ and grows upon further cooling. Contrarily, **10**'s magnetic susceptibility reaches a very narrow plateau at 5 K ($\chi T = 1\,\text{cm}^3\text{Kmol}^{-1}$) and continues to drop below 3.5 K.

According to the crystal structure and the spin states of the individual Fe centres confirmed by Mößbauer spectroscopy, the spin topologies sketched in fig. 3.26 were developed. An hourglass spin topology necessary to adequately describe the molecular magnetic properties of **9** results in a very high dimensionality (>93000) of the spin system, which is not accessible via full matrix diagonalisation approaches by common computers.

Instead, broken-symmetry density functional theory calculations provided by Böhme[272] were carried out on the molecular structures of **9**. A simulation of $\chi_{mol}T$ based on these theoretical results reproduces the general trends of the experimental curve (see fig. 3.25). The corresponding parameter set (see table 3.16) includes the intratriangle magnetic exchange cou-
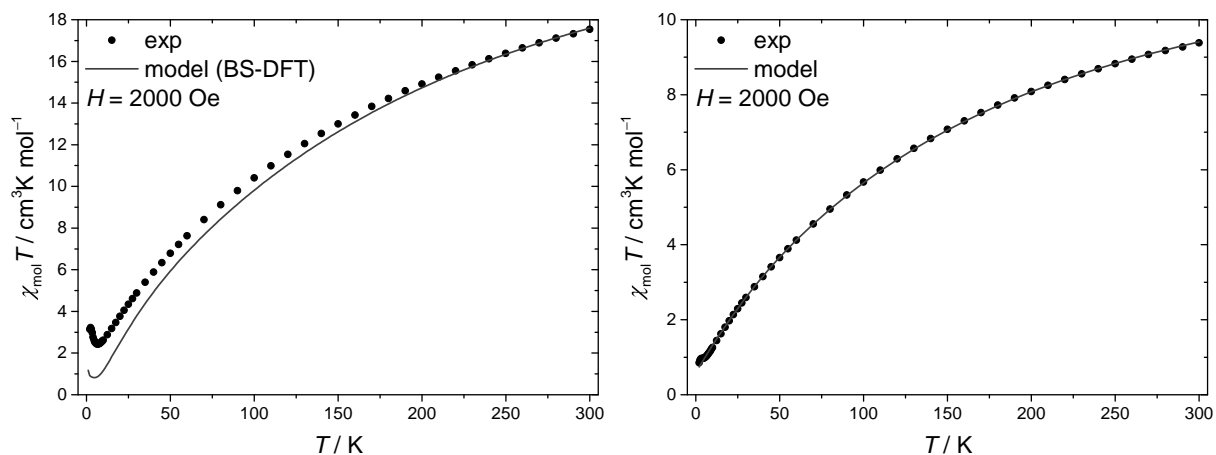
Figure 3.25: Temperature dependence of magnetic susceptibility ($\chi_{mol}T$) of powdered crystalline samples of **9** (**left**) and **10** (**right**) depicted as black dots, respectively. In the left graph, the grey line is a simulation of $\chi_{mol}T$ based on BS-DFT calculated parameters.[272] The right graph contains the best fit of experimental values to Hamiltonian (3.6). All corresponding parameters are given in table 3.16.
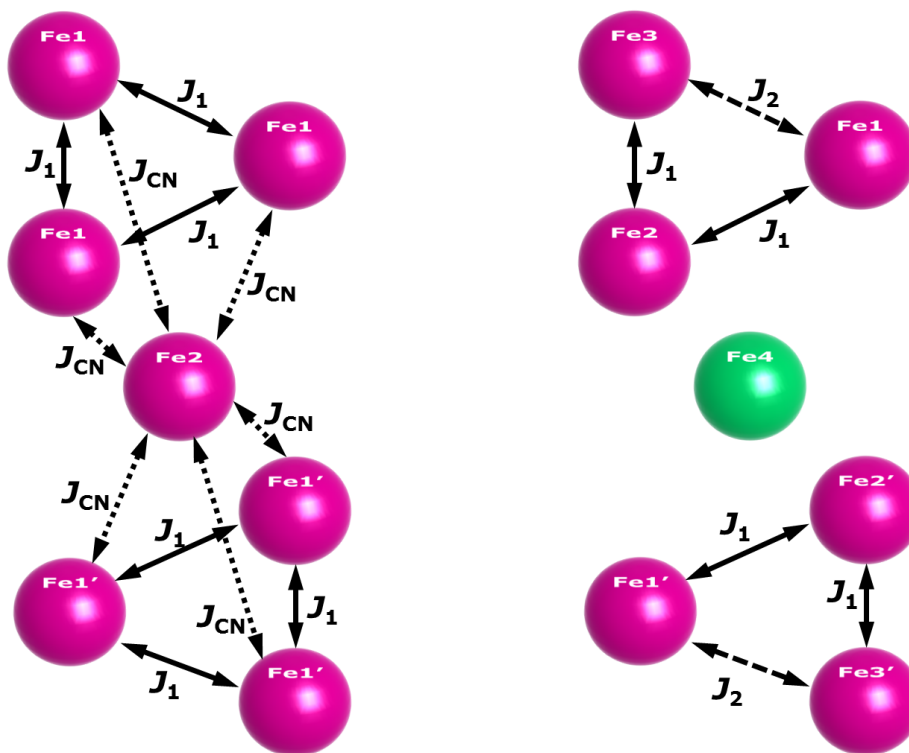
Figure 3.26: Spin topologies developed for **9** (**left**, hourglass) and **10** (**right**, two independent isosceles triangles).

pling J_1 amounting to $-14.3\,\text{cm}^{-1}$ and an exchange of the Fe(III)*hs* centres in the triangle with the Fe(III)*ls* centre via the bridging cyanides J_{CN} of $+7.8\,\text{cm}^{-1}$. However, the calculation appears to overestimate at least the antiferromagnetic coupling constant J_1. This presumption is supported by the discrepancy between experimental curve and model as well as a comparison with the J_1 value determined for the compound [Fe$_3$saltag^{Br}Cl$_3$(py)$_6$]ClO$_4$,[50] which forms a structurally and electronically comparable discrete triangle. Nevertheless, the antiferromagnetic intratriangle interaction is within the expected range and a ferromagnetic interaction of both triangles with the central ferricyanide moiety is clearly uncovered.

Considering the geometrically frustrated spin ground state of the triangular unit, this compound after **6** forms a second example of two ideal equilateral triangle spin qubits[62,63] "entangled" by weak ferromagnetic interactions as demanded by the DiVincenzo criteria.[53] Admittedly, the ferromagnetic coupling is in the same order of magnitude as the intratriangle antiferromagnetic coupling, so the actual suitability of this very candidate as molecular realisation of two entangled qubits has yet to be proven, e.g. by pulsed ESR experiments.

An entirely different situation is present in **10**. Since the diamagnetic ferrocyanide bridge does not mediate significant magnetic exchange, the two triangles are virtually independent (see fig. 3.26). At the same time, the ferrocyanide iron Fe4 is a crystallographic inversion centre, so that the effective spin system necessary to describe the molecular magnetic properties of **10** can be reduced to one coupled triangle. The experimental magnetic susceptibility was therefore related to half a molecule, which can now be fitted to the following Hamiltonian:

$$\widehat{H} = -J_1\left(\widehat{S}_1\widehat{S}_2 + \widehat{S}_2\widehat{S}_3\right) - J_2\left(\widehat{S}_1\widehat{S}_3\right) + g_{iso}\mu_B B\sum_{i=1}^{3}\widehat{S}_i \tag{3.6}$$

Mind that two different coupling constants are used to account for the significant structural difference of Fe2 with respect to the other two iron centres. This leads to an isosceles triangle spin topology for **10**.

To achieve a satisfying agreement with the experimental data, the applied model has to be extended for the z-component of an antisymmetric Dzyaloshinsky-Moriya exchange with the Hamiltonian given below.

$$\widehat{H} = -G_z\left[(\widehat{S}_{1,x}\widehat{S}_{2,y} - \widehat{S}_{1,y}\widehat{S}_{2,x}) + (\widehat{S}_{2,x}\widehat{S}_{3,y} - \widehat{S}_{2,y}\widehat{S}_{3,x}) + (\widehat{S}_{3,x}\widehat{S}_{1,y} - \widehat{S}_{3,y}\widehat{S}_{1,x})\right] \tag{3.7}$$

Although the isotropic exchange is divided into two coupling constants J_1 and J_2, the antisymmetric exchange was considered equal for all three exchange pathways. A splitting into two antisymmetric exchange coupling constants did not significantly improve the fitting results, hence, the embedding of an additional parameter is scarcely justified.

The resulting isotropic coupling constants (see table 3.16) of this fit, $J_1 = -13.28\,\text{cm}^{-1}$ and $J_2 = -11.69\,\text{cm}^{-1}$, average to a value agreeing with the coupling constant found for the reference C_3-symmetric triangle [Fe$_3$saltag^{Br}Cl$_3$(py)$_6$]ClO$_4$.[50] A g_{iso} value of 2.01 is reasonable for the very isotropic Fe(III)*hs* without orbital contribution expected. The occurrence of moderate antisymmetric exchange $G_z = 2.57\,\text{cm}^{-1}$ agrees with the lifted C_3 symmetry in the triangle.

However, its presence needs further confirmation by low-temperature ESR studies[100,101] not undertaken within the frame of this work. In either case, the fourfold degeneracy expected for an ideal equilateral spin triangle is lifted, as can be retraced by simulations of the spin states applying the parameters from the fit. In the absence of antisymmetric exchange, the first two Kramers doublets are split by $4.8 \, \text{cm}^{-1}$. This gap increases to $16.1 \, \text{cm}^{-1}$, when the antisymmetric exchange is included.

A further diminution of the fitting residual to a quarter accompanies the introduction of a mean field parameter $zJ = +0.287 \, \text{cm}^{-1}$ (listed in the row J_{CN} in table 3.16), which can be interpreted as a weak coupling of the two triangles via the diamagnetic ferrocyanide bridge. However, the high overall number of parameters definitely bears the risk of overparametrisation, so that these results have to be evaluated cautiously. Nevertheless, the change in the other parameters as compared to the first fit is neglectable. As a result, in **10** the possible weak ferromagnetic coupling between the triangles is two orders of magnitude lower than the antiferromagnetic intratriangle interaction resulting in a different extent of entanglement in comparison to **9**.

Table 3.16: Parameters obtained from fittings of the temperature dependence of the magnetic susceptibility $\chi_{\text{mol}}T$ for the compounds **10** and $[\text{Fe}_3\text{saltag}^{\text{Br}}\text{Cl}_3(\text{py})_6]\text{ClO}_4$ (data of the latter taken from [50] for comparison). For **9** parameters extracted from BS-DFT calculations by Böhme[272] are listed.

parameter	9	10		$[\text{Fe}_3\text{saltag}^{\text{Br}}\text{Cl}_3(\text{py})_6]\text{ClO}_4$ [50]
g_{iso}	2.00	2.01	2.01	2.00
$J_1 / \, \text{cm}^{-1}$	−14.3	−13.28	−13.28	−12.35
$J_2 / \, \text{cm}^{-1}$	-	−11.69	−11.93	-
$J_{\text{CN}} / \, \text{cm}^{-1}$	+7.8	-	$zJ = +0.287$	-
$G_z / \, \text{cm}^{-1}$	-	2.57	2.08	-
Residual	-	0.10836	0.02465	0.00667

3.2.5 Concluding Remarks

Two hexacyanometalate bridged heptanuclear iron complexes **9** and **10** are the first members of the entirely new class of metallo-bridged dimers of tag-based triangles. Already these two examples presage the extraordinary potential to build up exciting spin topologies and access various molecular magnetic features. A structurally related class of compounds was investigated by Glaser *et al.*,[33,271,273] however the triangular building block is only weakly coupled via spin-polarisation mechanism in those systems. In contrast, tag-based ligands promote stronger superexchange via the diazine bridges. Deliberate synthesis allows selective introduction of either a paramagnetic ferricyanide mediating ferromagnetic exchange between both triangles or a diamagnetic ferrocyanide bridge transmitting, if at all, only very weak magnetic interaction between the triangles. Mößbauer spectroscopy is an essential tool to handle the redox and spin state variant nature of iron in these complex aggregates. For proper description of molecular magnetic properties assistance of *ab-initio* calculations is crucial, because common methods fail

in these very high dimensional spin systems. Furthermore, profound ESR investigations of the two compounds presented here are of high interest and have yet to be carried out.

In perspective, not only an exchange of metal ions in the triangular building block should be surveyed, but also screening hexacyanochromates, hexacyanomanganates and hexacyanocobaltates as bridging units unlocks a whole new synthetic playing field. Hexacyanochromate(III) is a bridging candidate of exceptional interest, because it combines the large $S = \frac{3}{2}$ spin momentum with good redox stability.[274,275] For the triangular building block, a bowl-like distortion of the ligand plane—as it is found in $[Fe_3saltag^{Br}Cl_3(py)_6]ClO_4$[50] and $[Cr_3saltag^{Br}Cl_3(py)_6]ClO_4$ (see next section 3.3)—appears to be beneficial for successful synthesis of such complexes from structural considerations.

3.3 Ferromagnetically Coupled Cr(III) Complexes

As was discovered by Dirk Schuch afore, complexation of chromium(III) ions with tag-based ligands is possible.[239] The presence of ferromagnetic interactions, which are uncommon for these ligand systems, were shown by SQUID magnetometry and reproduced by corresponding BS-DFT calculations.[248] The latter revealed very minor overlap integrals of the magnetic orbitals leading to a ferromagnetic superexchange interaction.[239,248] At the same time, the d^3 configuration of the Cr(III) ion in an expected octahedral ligand field features no orbital angular momentum or magnetic anisotropy. This makes them interesting for the sake of their large spin ground state, e.g. as magnetic refrigerants. Unfortunately, before the present work no trinuclear compound of this class could be crystallised, hence no structural information was available. Due to the high ligand field splitting energies for chromium(III) in complexes and the resulting chemical inertness, also compounds with lower nuclearity are interesting targets for the stepwise build-up of heteronuclear compounds. In this work, further effort was put into synthesis and crystallisation of Cr(III) complexes with tag-based ligands.

3.3.1 Synthesis and Characterisation

The deliberate synthesis of polynuclear Cr(III) complexes with triaminoguanidine based ligands demands for different procedures than most of the other syntheses reported in this work. This is mainly due to the chemical inertness of octahedral Cr(III) complexes, which is caused by the large ligand field stabilisation energy of the d^3 configuration in octahedral ligand fields. Therefore, the kinetics of complexation reactions is more similar to 4d metals than to most other 3d metals. So the fact, that Schuch could isolate and characterise crystals of an unfortunately unreproducible heptanuclear "intermediate" Cr(III) complex of the saltag^H ligand[239] is symptomatic. The challenging thing about driving such a reaction to a thermodynamic minimum product quantitatively is treading the fine line between sufficient application of energy and possible ligand decomposition.

The reaction of three equivalents $CrCl_3 \cdot 6\,H_2O$ with one equivalent $H_5saltag^{Br} \cdot HCl$ in pyridine by the application of heat below reflux conditions for a certain time of 30 min led to the formation of a dinuclear neutral complex $[Cr_2(Hsaltag^{Br})Cl_2(py)_4]$ (**11**), which could be isolated as crystalline material by very slow evaporation of the solvent over 4 months.

In contrast, under similar conditions using a slightly overstoichiometric amount of $CrCl_3 \cdot 6\,H_2O$ and prolonging the reaction time by ten minutes enables the formation of $[Cr_3(saltag^{Br})Cl_3(py)_6]^+$. A crystallisation of this fragment to isolate crystalline **12** is achieved by slow diffusion of MeOH and large amounts of weakly coordinating perchlorate anions into the reaction solution. However, yields are poor (<25 % calculated based on the chelate ligand) for both reactions and despite meticulous control of reaction time and temperature reproducibility avowedly remains an issue.

3.3.2 Crystal Structures

[Cr$_2$(Hsaltag^{Br})Cl$_2$(py)$_4$] (11)

Compound **11** crystallises in the monoclinic space group $P2_1/c$ (#14). The asymmetric unit contains the neutral complex molecule [Cr$_2$(Hsaltag^{Br})Cl$_2$(py)$_4$] (see fig. 3.27) as well as three non-coordinating pyridine and three water molecules. There are no hints for intermolecular interactions in the crystal structure, merely an intramolecular hydrogen bridge in the vacant coordination pocket of the saltag^{Br}, which still bears a proton, is evident. The two remaining coordination pockets coordinate one Cr(III) ion each and together with one chlorido and two pyridine coligands per ion a distorted octahedron with an N$_4$OCl donor set, respectively, is formed. While the chlorido donor lies in the plane formed by the chelate ligand in first approximation, the pyridine molecules take the out of plane donor positions. Both Cr(III) centres are crystallographically independent, their bond lengths and angles are listed in table 3.17.

Still, their coordination environment is rather similar and therefore described jointly. Bond lengths of the coordinative bonds range from 191.5 to 233.2 pm, whereat the phenolate oxygen donor forms the shortest and the chlorido forms the longest bond, respectively. The Cr–N distances of the nitrogen donors of the Hsaltag^{Br} ligand (N2, N3, N4, N5) formally sharing two negative charges are around 200 pm. Hence, the neutral pyridine donors form longer bond lengths about 210 pm. Deviations of the bite angles from the ideal octahedral occur in the chelate ligand plane in relation to the five membered chelate ring formed by N2, N3 and N4, N5. The numbering scheme as well as a depiction of the coordination polyhedra can be found in fig. 3.27. Continuous shape measures [251–253] also reveal a slight distortion from the ideal octahedron (0.992 for Cr1 and 0.817 for Cr2). The intramolecular metal $\cdots$ metal distance (Cr1 $\cdots$ Cr2) is 497 pm and the diazine bridging moiety shows a torsion angle Cr–N–N–Cr of 171.1°. The closest intermolecular span amounts to 865 pm (Cr1 $\cdots$ Cr2′).

Interestingly, the bromophenol moiety of the vacant coordination pocket is the one, which is most bent with respect to the triaminoguanidine ligand plane. The intersecting angle equals 20° measured as tag plane versus aromatic plane of the vacant bromophenol, while this angle is 14° for the two moieties involved in the coordination.

[Cr$_3$saltag^{Br}Cl$_3$(py)$_6$]ClO$_4$ (12)

The crystals formed by compound **12** are isostructural to the ones of the Fe(III) triangle with the saltag^{Br} ligand originally synthesised by Plaul.[50] The trigonal space group $P\bar{3}$ (#147) allows for crystallographic C_3 symmetry. Indeed the asymmetric unit consists of one third of the trinuclear Cr(III) cationic complex and one third of the ClO$_4{}^-$ counteranion, so that the entire molecule is built by rotation symmetry operations (see fig. 3.28). Its three crystallographically equivalent Cr(III) centres are coordinated in a distorted octahedral fashion by an N$_4$OCl donor set provided by one N$_2$O pocket of the saltag^{Br} chelate ligand, two pyridine molecules and one chlorido ligand. Like in **11**, the chlorido donor is in the chelate ligand plane, while the two pyridine donors are roughly perpendicular to this plane. The bond lengths and angles of the
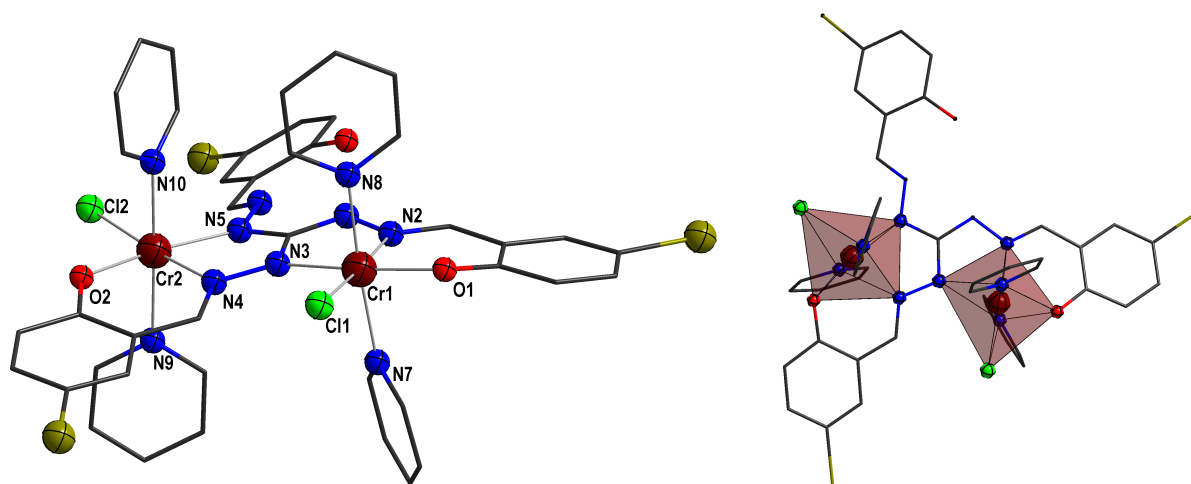
Figure 3.27: Left: Molecular structure of neutral complex [Cr$_2$(Hsaltag^{Br})Cl$_2$(py)$_4$] (**11**) with atom labels, C atoms are wire nodes, Cr: reddish brown, N: blue, O: red, Cl: green, Br: dark yellow, H atoms and cocrystallised solvent are omitted for clarity. **Right:** Illustration of the distorted octahedral coordination polyhedra of **11**, colour code is identical.

Table 3.17: Selected bond lengths (pm) and angles (°) from the coordination environment of the two crystallographically independent chromium(III) centres within the dinuclear neutral complex [Cr$_2$(Hsaltag^{Br})Cl$_2$(py)$_4$](**11**). The corresponding numbering scheme is depicted in fig. 3.27.

Cr1–N2	200.86(5)	Cr1–N3	206.17(3)
Cr1–N7	209.49(4)	Cr1–N8	210.31(4)
Cr1–O1	191.51(3)	Cr1–Cl1	233.23(6)
Cr2–N4	201.91(4)	Cr2–N5	201.91(3)
Cr2–N9	210.88(5)	Cr2–N10	209.78(5)
Cr2–O2	192.79(3)	Cr2–Cl2	230.38(5)
N2–Cr1–N3	77.12(1)	N2–Cr1–N7	90.29(1)
N2–Cr1–N8	88.42(1)	N2–Cr1–O1	90.71(1)
N2–Cr1–Cl1	176.73(1)	N3–Cr1–N7	91.27(1)
N3–Cr1–N8	91.87(1)	N3–Cr1–O1	167.72(1)
N3–Cr1–Cl1	101.92(1)	N7–Cr1–N8	176.25(1)
N7–Cr1–O1	87.12(1)	N7–Cr1–Cl1	92.87(1)
N8–Cr1–O1	89.38(1)	N8–Cr1–Cl1	88.49(1)
O1–Cr1–Cl1	90.32(1)		
N4–Cr2–N5	77.63(1)	N4–Cr2–N9	91.35(1)
N4–Cr2–N10	88.67(1)	N4–Cr2–O2	90.87(1)
N4–Cr2–Cl2	176.02(1)	N5–Cr2–N9	92.05(1)
N5–Cr2–N10	89.87(1)	N5–Cr2–O2	168.50(1)
N5–Cr2–Cl2	99.79(1)	N9–Cr2–N10	178.04(1)
N9–Cr2–O2	87.97(1)	N9–Cr2–Cl2	91.78(1)
N10–Cr2–O2	90.07(1)	N10–Cr2–Cl2	88.29(1)
O2–Cr2–Cl2	91.71(1)		

coordination environment of the Cr(III) ion are shown in table 3.18.

The shortest coordinative bond to the Cr(III) centre is formed by the phenolate oxygen donor (191.3 pm). N1 and N2, the nitrogen donors of the chelate ligand, show distances of 205.6 and 202.7 pm. This is slightly longer than the corresponding sites in **11**, which is reasonable, since the two negative charges delocalised within the triaminoguanidine core are now distributed among all three occupied coordination pockets. The distortion of the coordination polyhedra is comparable to the ones in **11**, continuous shape measures[251–253] determine a deviation parameter of 0.943 from the ideal octahedron. In the triangle the Cr centres are separated by 496 pm, their corresponding dihedral angle with the bridging diazine Cr–N–N–Cr amounts to 167.0°. The shortest intermolecular metal$\cdots$metal distance is 793 pm. The aberration of the saltag^{Br} ligand from planarity is more pronounced than in the dinuclear complex, the intersecting angle between the tag plane and the aromatic plane of the bromophenol is increased to 27.6°.

A weak intermolecular $\pi \cdots \pi$-interaction with an aromatic plane distance of approximately 350 pm can be assumed by the coplanar and overlapping arrangement of the two ligating pyridine molecules (see fig. 3.29). The ones bearing the donor atom N3 exhibit more overlap the ones containing N4. Nevertheless, this leads to a three-dimensional network of $\pi \cdots \pi$-interactions weakly interconnecting each complex cation to its next neighbours.

3.3.3 Magnetic Properties

Temperature dependent magnetic susceptibility measurements on polycrystalline samples of **11** and **12** were undertaken and their experimental results are shown in fig. 3.30. For the dinuclear compound **11** the $\chi_{mol}T$ value at 300 K is slightly below 4 cm^{3}K mol^{-1}, which is a bit higher than the theoretical spin-only value for two independent electronic spins of $S = \frac{3}{2}$ (3.75 cm^{3}K mol^{-1} for $g = 2$). This deviation might be due to the ferromagnetic exchange interaction suggested by the continuous increase of $\chi_{mol}T$ upon lowering of the temperature down to 10 K. There a maximum of 5.6 cm^{3}K mol^{-1} is traversed, which is a bit lower than the value for a possible ferromagnetically coupled electronic spin ground state of $S = 3$ (6 cm^{3}K mol^{-1}).

The trinuclear complex **12** shows a similar general trend of the curve, only the increase appears less steep. The high-temperature minimum at 300 K amounts to 5.7 cm^{3}K mol^{-1}, so again it is somewhat larger than expected for three isolated electronic spins of $S = \frac{3}{2}$ (5.625 cm^{3}K mol^{-1}) already indicating possible ferromagnetic interaction. A maximum $\chi_{mol}T$ of 11.5 cm^{3}K mol^{-1} is reached around 3 K, whereupon a subsequent drop of $\chi_{mol}T$ is hardly visible within the experimental range. Nevertheless, the detected maximum is below the one of a ferromagnetically coupled purely electronic $S = \frac{9}{2}$ ground state (12.375 cm^{3}K mol^{-1}).

An appropriate model to describe the spin systems of both complexes and eventually reproduce the temperature dependence of the magnetic susceptibility was aspired. Since no orbital contribution or magnetic anisotropy is expected for octahedrally coordinated Cr(III), simplified spin Hamiltonians including exchange and Zeeman terms were applied. Thus, for **11** a classic
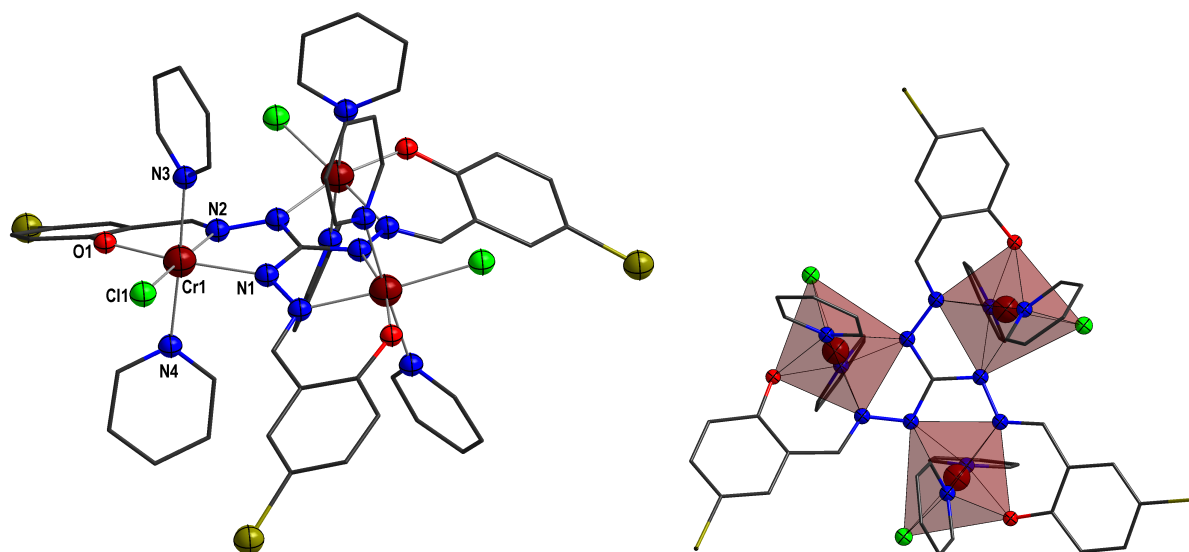
Figure 3.28: Left: Molecular structure of cationic complex [Cr$_3$saltag^{Br}Cl$_3$(py)$_6$]ClO$_4$ in **12** with atom labels, C atoms are wire nodes, Cr: reddish brown, N: blue, O: red, Cl: green, Br: dark yellow, H atoms and counteranion are omitted for clarity. **Right:** Illustration of the distorted octahedral coordination polyhedra of **12**, view along crystallographic c-axis, colour code is identical.

Table 3.18: Selected bond lengths (pm) and angles (°) from the coordination environment of the chromium(III) centres within the trinuclear complex cation of [Cr$_3$saltag^{Br}Cl$_3$(py)$_6$]ClO$_4$ (**12**). The corresponding numbering scheme is depicted in fig. 3.28.

Cr1–N1	205.6(2)	Cr1–N2	202.7(3)
Cr1–N3	208.3(3)	Cr1–N4	210.5(3)
Cr1–O1	191.3(2)	Cr1–Cl1	230.4(1)
N1–Cr1–N2	76.76(10)	N1–Cr1–N3	91.65(10)
N1–Cr1–N4	90.83(10)	N1–Cr1–O1	166.21(10)
N1–Cr1–Cl1	99.55(7)	N2–Cr1–N3	87.96(10)
N2–Cr1–N4	94.02(10)	N2–Cr1–O1	89.52(10)
N2–Cr1–Cl1	175.59(8)	N3–Cr1–N4	177.13(10)
N3–Cr1–O1	89.26(10)	N3–Cr1–Cl1	89.74(8)
N4–Cr1–O1	88.67(10)	N4–Cr1–Cl1	88.42(8)
O1–Cr1–Cl1	94.21(7)		
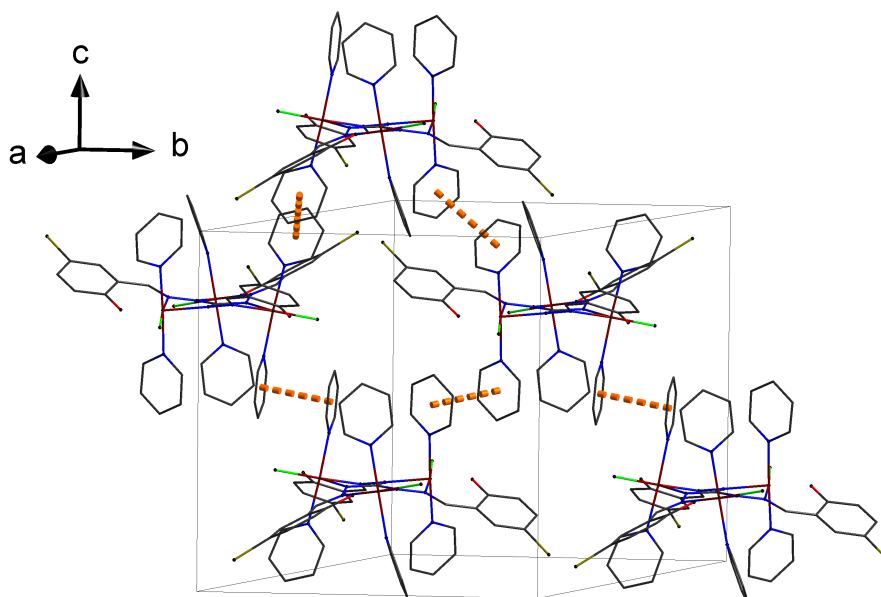
Figure 3.29: Illustration of the three-dimensional network of $\pi\cdots\pi$-interactions (orange dashed bonds) in the crystal structure of **12** interconnecting the cationic complexes to their next neighbours. Black straight lines mark the unit cell edges.

spin dimer topology results in:

$$\widehat{H} = -J_{ex}\left(\widehat{S}_1\widehat{S}_2\right) + g_{iso}\mu_B B \sum_{i=1}^{2}\widehat{S}_i \tag{3.8}$$

A fit using this very Hamiltonian resulted in the parameters given in table 3.19 as "fit-Cr2", whereat the isotropic g_{iso}-value was fixed to 1.98 since this is common sense in literature for octahedral Cr(III) ions and avoids overparametrisation. To achieve a good description of the experimental data a small mean field parameter zJ had to be included, which accounts for intermolecular magnetic interactions.[255] An isotropic exchange of J_{ex} = +8.13 cm^{-1} is obtained.

This can be considered a rather extraordinary result, because ferromagnetically coupled Cr(III) homodimers are rare in literature and usually coupling constants are significantly smaller.[276–281] Correlations between bridging angles/distances and magnetic exchange coupling are reported for oxo-bridged Cr(III) dimers, exclusively.[282] Thus, it is hard to classify the compound in such a manner. However, to the best of my knowledge **11** is not only the first reported ferromagnetically coupled homodinuclear Cr(III) complex with a diazine bridge, but also the homopolynuclear Cr(III) complex with the largest ferromagnetic coupling constant ever found.

For the trinuclear complex **12** the Hamiltonian had to be extended for an equilateral triangle spin topology:

$$\widehat{H} = -J\left(\widehat{S}_1\widehat{S}_2 + \widehat{S}_1\widehat{S}_3 + \widehat{S}_2\widehat{S}_3\right) + g_{iso}\mu_B B \sum_{i=1}^{3}\widehat{S}_i \tag{3.9}$$
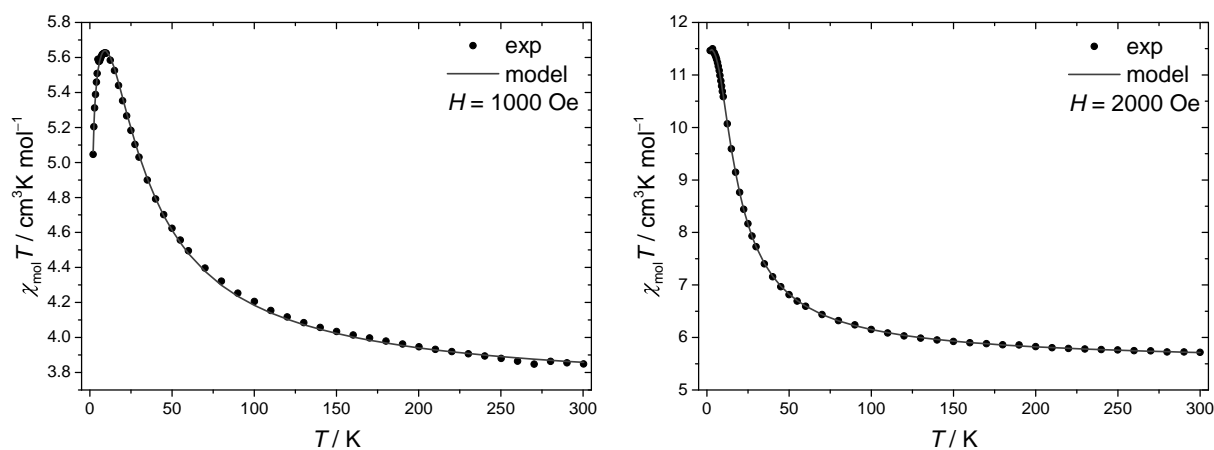
Figure 3.30: Temperature dependence of magnetic susceptibility ($\chi_{mol}T$) of powdered crystalline samples of **11** (**left**) and **12** (**right**) depicted as black dots, respectively. Corresponding parameters used for the fitted curves (grey lines) are given in table 3.19, the underlying Hamiltonians are given in eqs. (3.8) and (3.9).

Table 3.19: Parameters obtained from fittings of the temperature dependence of the magnetic susceptibility $\chi_{mol}T$ for the compounds **11** and **12**. The bold fits are the ones depicted in fig. 3.30. Asterisks mark values, which were fixed for the fit.

	$[Cr_2(Hsaltag^{Br})Cl_2(py)_4]$ **11**	$[Cr_3saltag^{Br}Cl_3(py)_6]ClO_4$ **12**	
parameter	**fit-Cr2**	fit 1	**fit 2**
g_{iso}	1.98*	1.92	1.98*
$J_{ex}/\ cm^{-1}$	+8.13	+3.62	+3.06
$zJ/\ cm^{-1}$	−0.014	0.0009	0.005
$G_z/\ cm^{-1}$	-	-	+1.11
Residual	0.01270	0.29025	0.00528

Fitting the experimental values to this Hamiltonian requires setting the g_{iso}-value as a parameter open to variation to get any reasonable fit ("fit 1" in table 3.19). Still the experimental data is not well reproduced (residual of 0.29). So in a next extension of the spin Hamiltonian a term for antisymmetric exchange in z-direction as is dictated by the strict triangular symmetry was included:

$$\widehat{H} = -G_z \left[\left(\widehat{S}_{1,x}\widehat{S}_{2,y} - \widehat{S}_{1,y}\widehat{S}_{2,x}\right) + \left(\widehat{S}_{2,x}\widehat{S}_{3,y} - \widehat{S}_{2,y}\widehat{S}_{3,x}\right) + \left(\widehat{S}_{3,x}\widehat{S}_{1,y} - \widehat{S}_{3,y}\widehat{S}_{1,x}\right) \right] \tag{3.10}$$

This is parametrised by the antisymmetric coupling constant G_z. In the corresponding fit ("fit 2" in table 3.19) the residual is reduced by two orders of magnitude in comparison to "fit 1", while keeping the total number of parameters constant, because g_{iso} can again be fixed to 1.98. An isotropic exchange of $+3.06\ cm^{-1}$ is obtained, which is comparable to the one in "fit 1" and roughly half the value determined for **11**. It is slightly higher than what Schuch found for his trinuclear $[Cr_3saltag^X(bpy)_3Cl_3]$ complexes, which are not structurally characterised.[239] Those complexes bear 2,2′-bipyridine coligands instead of pyridine, which enforces a different coordination environment, so the aberrations are reasonable. To retrace the underlying coupling

pathways and explain the decrease in the interaction from **11** to **12** theoretical calculations appear desirable.

G_z is quantified to $+1.11\,\mathrm{cm}^{-1}$, which is one order of magnitude above a value determined for an antiferromagnetically coupled spin triangle based on Cr(III).[283] Of course, the presence of an antisymmetric interaction needs further approval by ESR spectroscopic studies. This was exemplarily shown for the already mentioned antiferromagnetic Cr(III) triangle.[283] Although the role of Dzyaloshinski-Moriya interactions for magnetoelectric effects in antiferromagnetically coupled systems is broadly discussed,[100,101,284] similar considerations are non-existent for ferromagnetically coupled molecular magnets to the best of my knowledge. Merely, an extensive study of a ferromagnetically coupled Cu(II) triangle featuring antisymmetric exchange has been reported recently.[285] So if the antisymmetric exchange can be confirmed, it will make **12** an exciting subject to further investigations.

3.3.4 ESR Spectroscopy

A low-temperature X-band ESR study on powdered crystalline **12** was undertaken. As becomes obvious in fig. 3.31 the spectrum recorded at 3.7 K, which was the lowest accessible temperature in the survey, features a developed fine structure with various different resonances contributing. This stands in contradiction to exclusively isotropically coupled Cr(III) ions in an ideal C_3-symmetric arrangement (simulated spectrum as narrow grey line in fig. 3.31). While at 5 K the fine structure can still be vaguely discerned, at higher temperatures it is entirely swallowed by the increasing linewidth.
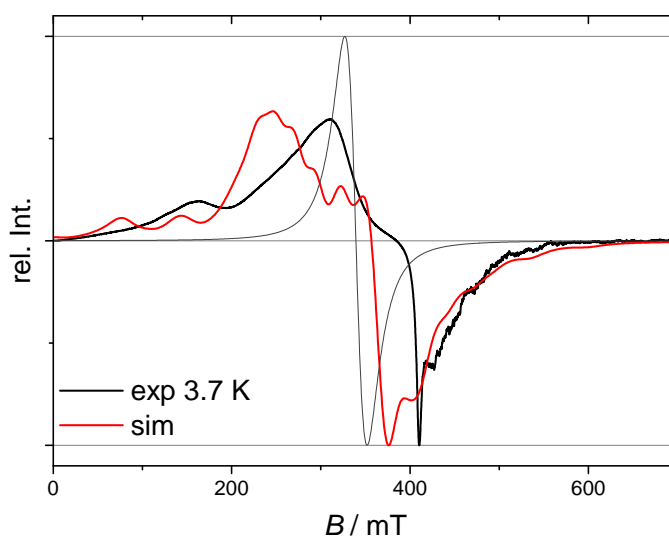
Figure 3.31: Left: X-band ESR spectrum of powdered crystalline **12** recorded at 3.7 K (black line). A corresponding simulation utilising parameters given in the text is drawn in red. Despite the poor congruency with the experimental spectrum, the necessary presence of anti-symmetric exchange is illustrated. In contrast a spectrum of three purely isotropically coupled Cr(III) centres is drawn as a narrow grey line.

Simulating the spectrum was aspired, but turned out to be challenging, because the spectrum is extremely sensitive to the interplay between isotropic exchange J_ex and the antisymmetric

exchange G_z (Hamiltonian as given in eqs. (3.9) and (3.10)). Common fitting routines fail, due to the complexity of the spectrum. Approaching the spectrum by manual iterative simulations is complicated, because considerable time is needed for a single simulation as soon as antisymmetric exchange is included.

Therefore in this work only a preliminary simulation can be presented (see fig. 3.31), which shows rather poor agreement with the experimental data. For the shown simulation an isotropic $g_{iso} = 1.98$, an isotropic ferromagnetic exchange coupling $J_{ex} = +2.67\,\text{cm}^{-1}$, an antisymmetric exchange $G_z = +0.70\,\text{cm}^{-1}$ and an isotropic, purely Lorentzian line broadening of 25 mT were used. Based on these results, it can already be stated, that the magnetic susceptibility fitting slightly overestimates the antisymmetric exchange. For a satisfying simulation, a broad computational survey of parameters J_{ex} and G_z, *ab-initio* calculations and CW-ESR spectra at lower temperatures to further sharpen the individual resonances contributing might be constructive. It should be added, that the high complexity ESR spectrum at the same time encrypts both coupling constants in a very precise manner.

3.3.5 Concluding Remarks

Two Cr(III) complexes **11** and **12** based on the saltag^{Br} ligand were structurally and magnetically characterised. They form a further step towards an exploitation of the extremely exciting field of Cr(III) complexes of tag-based ligands. Both complexes show remarkable ferromagnetic couplings, **11** even exhibits the largest ferromagnetic coupling reported for Cr(III) homodimers so far. Against this background, the systematic investigation of more N–N diazine bridged Cr(III) complexes is a worthwhile target. As a dinuclear complex with one vacant binding pocket of the saltag^{Br} ligand, **11** forms an interesting building block for possible heteronuclear 3d-metal triangles. Also, the coordination of lanthanoid ions in a bridging manner by means of two vacant ligand pockets to create mixed 3d-4f SMMs is imaginable.

The trinuclear complex **12** features an $S = \frac{9}{2}$ spin ground state. Furthermore, the presence of significant Dzyaloshinski-Moriya antisymmetric exchange could be indicated by low-temperature ESR spectroscopy, which is an entirely unexplored phenomenon for ferromagnetically coupled homometallic Cr(III) complexes. A bridging of two such complex molecules with hexacyanometalates analogous to what is described in section 3.2 should be feasible, especially since **12** is isostructural to the formal precursor of **10**. Any kind of paramagnetic bridge leads to a large spin ground state, because even an antiferromagnetic exchange between bridge and triangle leads to a ferrimagnetic spin ground state. Such clusters are designated candidates for magnetic refrigeration applications.

Besides synthetic perspectives, profound investigation of both compounds via theoretical calculations and ESR spectroscopy is essential for a better description of the magnetic exchange pathways and understanding of the underlying mechanisms and energetic structure.

Polynuclear 4f Metal Complexes

4.1 Alkali Metal Ion Containing Monodysprosium Complexes

A first monodysprosium complex of a tag-based ligand containing additional alkali metal ions and showing slow relaxation of magnetisation was reported by Schuch.[239] In this very compound the sodium ions occupy two vacant pockets, so that a distorted trinuclear sandwich complex of two tritopic ligands is formed, whereat the ligand planes are rigorously tilted from coplanarity due to different coordination demands of the different metal ions.

In the present work this approach was further followed, because the selective binding of different alkali metal ions should affect the spreading angle of the ligand planes and hence coordination angles at the Dy centre while leaving the electronic situation of the ligand system almost unchanged. The effects of this structural tuning on the magnetic behaviour can then be evaluated.

4.1.1 Synthesis and Characterisation

Synthesis of mononuclear Dy complexes bearing additional alkali metal ions in the remaining pockets of the tag-based ligand could be successfully carried out using the saltag^{Nph} ligand. The reaction of one equivalent $Dy(NO_3)_3$ with two equivalents of the ligand and four equivalents of NEt_3 in a mixture of DMF and MeOH leads to the crystallisation of such compounds in the presence of the weakly coordinating BPh_4^- anion. Depending on whether $KBPh_4$ or $NaBPh_4$ is added to the reaction, $[DyK_2(H_3saltag^{Nph})_2(dmf)_3(MeOH)_3]BPh_4$ (**13**) or $[DyNa_2(H_3saltag^{Nph})_2(dmf)_3(MeOH)_3]BPh_4$ (**14**) is isolated. Unfortunately, in face of synthetic efforts, no analogous compounds with Li^+, Rb^+ or Cs^+ ions incorporated could be isolated.

Elemental analysis confirms the chemical composition of both complexes, but also indicates partial loss of the coordinating MeOH molecules upon storage under air. At the same time, the reaction solution turns from orange into black within some weeks, which is apparently due to ligand oxidation processes, also affecting the crystalline material in the mother liquor.

Using nujol oil it was possible to store the intact crystalline material for somewhat longer time periods. ESI-MS spectra of both compounds exclusively show signals for mononuclear monocationic complex fragments without alkali metal ions bound, so the identity of the second metal ion present in the structure could not be further confirmed by this method. Also the IR spectra of both complexes do not reveal significant differences in the vibrational structure of both compounds.

4.1.2 Crystal Structures

Compounds **13** and **14** isostructurally crystallise in the trigonal space group $P\bar{3}$ (#147). The C_3 rotational axis runs through the central triaminoguanidine carbon atom of both saltag$^{\mathrm{Nph}}$ ligands forming the complex. This goes along with the necessity for the Dy and the alkali metal ions to be statistically distributed among all three coordination pockets, since these three positions are symmetry related and the only metal sites present in the structure. Refinement of elements as different as Dy and K/Na on the same positions leads to large uncertainties and very high displacement factors, so that the crystal structures should rather be considered structural motifs. Both structures are therefore treated as one and the same, because a meticulous discussion of minor distinctions is scarcely appropriate against the background of indeterminateness in the structures.

The only crystallographically independent mixed metal site is henceforth referred to as M1. It is environed by two [N$_2$O] donor pockets provided by each saltag$^{\mathrm{Nph}}$ ligand, respectively, as well as one coordinating DMF and one coordinating MeOH, which results in an [N$_4$O$_4$] overall donor set (see fig. 4.1). The four O-donors as well as the the four N-donors form rhombic planes, respectively, so that the coordination geometry can in easy words be described as on the path between rhombic prism and rhombic antiprism. In more geometric terms it can best be described as distorted triangular dodecahedron (point symmetry D_{2d}), which is also the ideal polyhedron with the smallest deviation parameter (2.317) obtained by continuous shape measures.[251–253] The phenolate O-donors form the shortest and the O-donor of the DMF molecule forms the longest bond with M1. However, the discrete values as listed in table 4.1 need to be taken with great caution due to the low precision of the structure, especially the value M1–O2 of 188 pm appears questionable, since comparable systems feature lanthanoid–phenolate-O bonding distances, which are way above 200 pm.[163,210]

The angle between the two phenolate donors, which feature the shortest bond lengths to M1 and hence are presumably also the ones bearing the highest negative charge density, is approximately 120°. Intramolecular $\pi \cdots \pi$-interactions of the naphthyl moieties are indicated in fig. 4.1, which stabilise the triangular triple-sandwich structure formed by the two chelate ligands involved. The distance of the two parallel tag planes is about 310 pm and an intramolecular metal$\cdots$metal span of 512 pm can be approximated. All three metal centres within the triangular complex cation are double bridged via one N–N diazine moiety of each saltag$^{\mathrm{Nph}}$ ligand, respectively.

Analysis of the supramolecular arrangement in the crystal structure provides no hints for intermolecular interactions between the complex cations. This is a crucial difference of mononu-
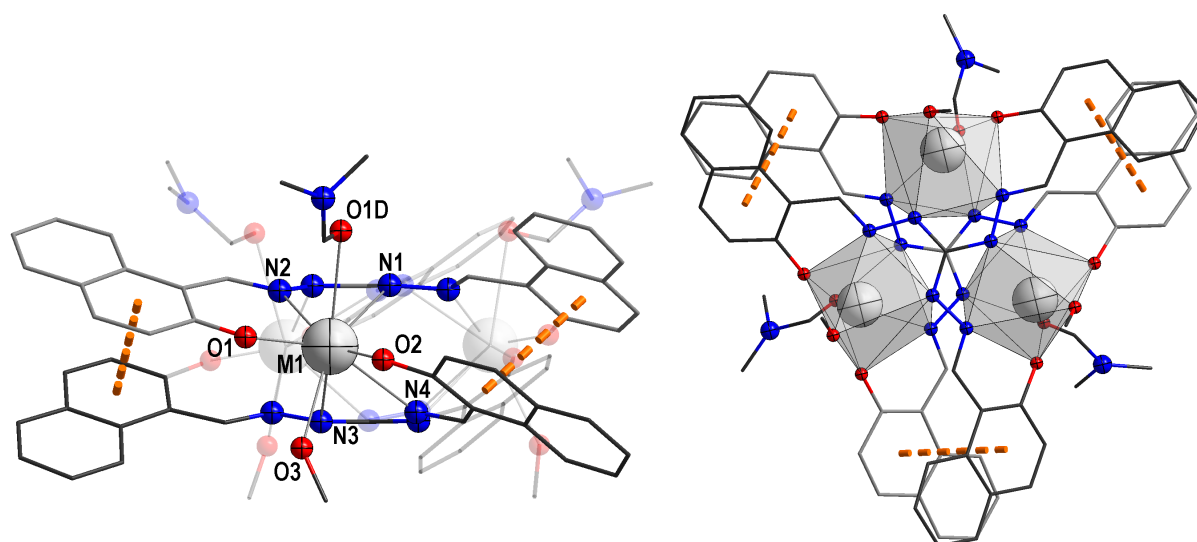
Figure 4.1: Left: Molecular structure of complex cation $[M_3(saltag^{Nph})_2(dmf)_3(MeOH)_3]^+$ in **13** and **14** with atom labels, C atoms are wire nodes, Dy/K/Na: light grey, N: blue, O: red. H atoms and counteranion are omitted for clarity. Intramolecular $\pi \cdots \pi$-interactions are schemed as orange dashed lines. Parts of the molecule not involved in the coordination of the labelled metal centre have been rendered transparent for clarity. View along crystallographic a-axis. **Right:** Illustration of the distorted triangular dodecahedron coordination polyhedra of **13** and **14**. Orange dashed bonds indicate the intramolecular $\pi \cdots \pi$-interactions of the naphthyl moieties. View along crystallographic c-axis, colour code is identical.

Table 4.1: Selected bond lengths (pm) and angles (°) from the coordination environment of Dy/K/Na1 referred to as M1 in $[M_3(saltag^{Nph})_2(dmf)_3(MeOH)_3]^+$ in **13** and **14**. The corresponding numbering scheme is depicted in fig. 4.1. Due to the structures of **13** and **14** being isostructural motifs, the one crystallographically independent metal centre is named M1, no errors are given and the values must be considered preliminary.

|			
M1–N1	256	M1–N2	256
M1–N3	279	M1–N4	268
M1–O1	204	M1–O2	188
M1–O3	265	M1–O1D	282
N1–M1–N2	61.6	N1–M1–N3	86.4
N1–M1–N4	74.3	N1–M1–O1	127.0
N1–M1–O2	99.9	N1–M1–O3	149.8
N1–M1–O1D	63.4	N2–M1–N3	75.0
N2–M1–N4	116.2	N2–M1–O1	69.0
N2–M1–O2	156.8	N2–M1–O3	127.0
N2–M1–O1D	73.8	N3–M1–N4	57.6
N3–M1–O1	98.8	N3–M1–O2	120.3
N3–M1–O3	71.0	N3–M1–O1D	144.2
N4–M1–O1	149.7	N4–M1–O2	67.2
N4–M1–O3	76.7	N4–M1–O1D	124.2
O1–M1–O2	120.8	O1–M1–O3	77.4
O1–M1–O1D	86.2	O2–M1–O3	76.1
O2–M1–O1D	85.4	O3–M1–O1D	143.8

clear Dy complexes **13** and **14** in comparison to all other monodysprosium complexes based on tag ligands reported,[239] which feature dimerisation of complex cations via hydrogen bonds of the MeOH coligands.

4.1.3 Magnetic Properties

For both compounds DC and AC magnetic susceptibility measurements, the latter with static magnetic fields H_{DC} of 0, 400 and 1000 Oe applied, as well as magnetic hysteresis studies were carried out, whose results are comparatively discussed hereinafter.

The temperature dependence of the static DC magnetic susceptibility $\chi_{mol}T$ is very similar for **13** and **14** and no significant differences can be detected. Corresponding curves are depicted in fig. B.1 of appendix B.1. High temperature values are in good agreement with the expected value for one isolated Dy(III) ion ($14.172\,\mathrm{cm^3Kmol^{-1}}$). Upon lowering of the temperature, $\chi_{mol}T$ decreases, as it is typically observed for highly anisotropic lanthanoid ions.

However, significant distinctions are revealed by the dynamic AC magnetic susceptibility measurements. Qualitatively, the out-of-phase susceptibility χ'' of **13** exhibits local maxima at higher temperatures (10–30 K) indicative for slow relaxation of magnetisation even without a static field H_{DC} applied, while for **14** only the increase at very low temperatures caused by QTM is recognisable at $H_{DC} = 0\,\mathrm{Oe}$ (compare table B.1 in appendix B.1). Upon determination of the relaxation times τ_T via a generalised Debye model (eq. (1.20)) it stands out, that the relaxation broadness as represented by the dispersion parameter α is larger for **14**, which also reduces the temperature range available for the fit of τ_T (see table 4.2 and tables B.1, B.2 and B.3 in appendix B.1).
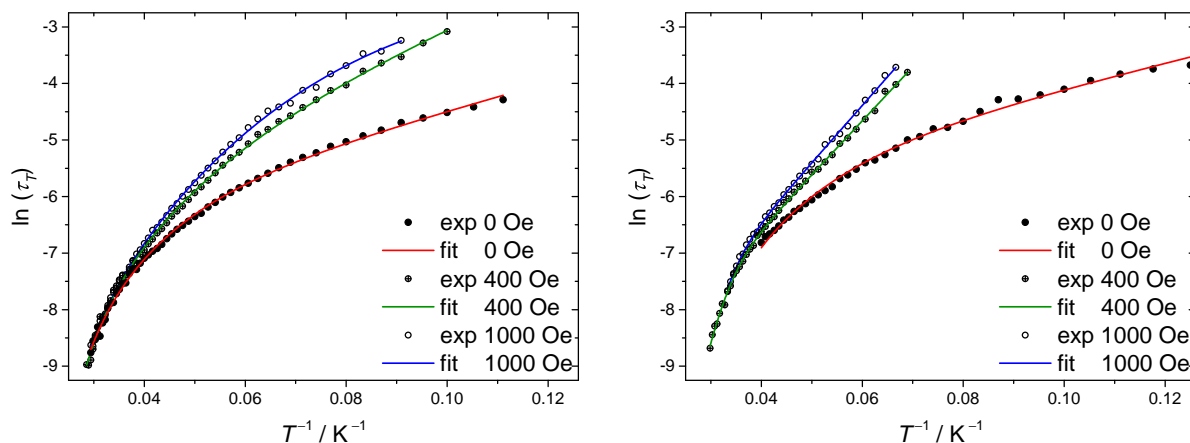
Figure 4.2: Logarithmic plot of the relaxation time τ_T of **13** (**left**) and **14** (**right**) at different static magnetic fields H_{DC} against T^{-1}. The corresponding fits of the relaxation behaviour to the multiprocess relaxation law given in eq. 4.1 yielded the parameters given in table 4.2 and are drawn as solid lines.

After the extraction of relaxation times in the temperature ranges given in table 4.2, a fitting of the relaxation behaviour for each static magnetic field to a modification of eq. 1.17 was pursued. Fortunately, THz-ESR investigations,[286,287] which in principle allow for the determination of the energetic gap between ground state and first excited Kramers doublet,[288] on compound **14**

Table 4.2: Collection of Debye model fittable temperature ranges and alpha parameters from the AC magnetic susceptibility measurements on **13** and **14** at different static magnetic fields H_{DC} applied as well as parameters extracted from fits of the temperature dependence of the corresponding magnetic relaxation times τ_T to the multiprocess relaxation law given in eq. 4.1. Fixed parameters are marked with an asterisk.

H_{DC}	value	[DyK$_2$] (**13**)	[DyNa$_2$] (**14**)
0 Oe	fittable T-range	$9\cdots 34$ K	$8\cdots 25$ K
	α-range	$0.313(3)\cdots 0.17(2)$	$0.466(9)\cdots 0.24(1)$
	$\Delta_{CF}/$ cm^{-1}	306*	306*
	$A_{CF}/$ s^{-1}	$6.4(9)\cdot 10^8$	$1.9\cdot 10^9$*
	$\Delta_{vib}/$ cm^{-1}	16.7(7)	14.7(8)
	$A_{vib}/$ s^{-1}	$9.0(8)\cdot 10^2$	$4.4(5)\cdot 10^2$
	$B/$ s^{-1}K^{-n}	$8.9(3)\cdot 10^{-5}$	$7.8(3)\cdot 10^{-5}$
	n	5*	5*
400 Oe	fittable T-range	$10\cdots 35$ K	$14.5\cdots 33$ K
	α-range	$0.392(8)\cdots 0.15(2)$	$0.432(12)\cdots 0.232(14)$
	$\Delta_{CF}/$ cm^{-1}	306*	306*
	$A_{CF}/$ s^{-1}	$9.2(9)\cdot 10^8$	$1.92(6)\cdot 10^9$
	$\Delta_{vib}/$ cm^{-1}	27(2)	66.3(6)
	$A_{vib}/$ s^{-1}	$6.5(2)\cdot 10^2$	$3.23(14)\cdot 10^4$
	$B/$ s^{-1}K^{-n}	$8.6(3)\cdot 10^{-5}$	-
	n	5*	-
1000 Oe	fittable T-range	$11\cdots 34$ K	$15\cdots 30$ K
	α-range	$0.356(9)\cdots 0.19(2)$	$0.411(11)\cdots 0.26(2)$
	$\Delta_{CF}/$ cm^{-1}	306*	306*
	$A_{CF}/$ s^{-1}	$7.0(6)\cdot 10^8$	$1.97(13)\cdot 10^9$
	$\Delta_{vib}/$ cm^{-1}	5(5)	70.4(7)
	$A_{vib}/$ s^{-1}	20(11)	$3.51(18)\cdot 10^4$
	$B/$ s^{-1}K^{-n}	$9.19(14)\cdot 10^{-5}$	-
	n	5*	-

revealed a signal at $306\,\text{cm}^{-1}$.[289] This is interpreted as the energy gap between the two lowest lying KDs and hence fixed as Δ_{CF} value for all fits on **14** and **13**. The latter is justified by the putative isostructurality of both compounds and the fact, that the corresponding Orbach process has only marginal influence on the overall fit, because it becomes the predominant relaxation process only above $25\,\text{K}$ (see fig. 4.2). This regime is only partially covered by the available data points.

As was already adumbrated, one equation was used to fit the relaxation curve for both compounds at all three static magnetic fields. This includes in the order of appearance of terms in the equation given subsequently, one thermal Orbach process, one VMCRM process and one Raman process.

$$\tau_T^{-1} = A_{\text{CF}} \cdot \exp\left(\frac{-\Delta_{\text{CF}}}{k_{\text{B}T}}\right) + A_{\text{vib}} \cdot \exp\left(\frac{-\Delta_{\text{vib}}}{k_{\text{B}T}}\right) + BT^n \tag{4.1}$$

For the Raman exponent n a value of 5 was fixed, leaving a reasonable number of variable parameters. Furthermore, for **14** the Raman process was entirely excluded for applied static fields of $400\,\text{Oe}$ and $1000\,\text{Oe}$, because its temperature regime (below $15\,\text{K}$) is not covered by the data. For the same reason, no QTM was included, although definitely present. Direct relaxation measurements to cover the tunneling regime failed due to probably too low relaxation times. The fits are depicted in fig. 4.2 and the obtained parameters collated in table 4.2.

The zero field relaxation behaviour of both compounds is similar in first approximation, but with increasing H_{DC}, for **13** the Raman process becomes more relevant, while the VMCRM nearly vanishes at $1000\,\text{Oe}$. In contrast, VMCRM grows more predominant with higher H_{DC}, and even the formal barrier Δ_{vib} is significantly increased in **14**. These findings are hard to rationalise, because although not implemented in their respective terms, magnetic field dependence of VMCRM and Raman processes against the background of spin-phonon coupling are subject to ongoing discussion and not finally solved.[143,173] Nevertheless, it can be concluded that differences in the vibrational structure of **13** and **14** are reflected in the magnetic field dependence of their relaxation behaviour.

It has to be further stated, that the strongest field dependence is expected for the QTM operative, which can unfortunately not be resolved with the present data. Merely, the higher dispersion coefficient α over the whole accessible temperature range suggests a larger contribution of QTM in case of **14** as compared to **13**. Even so, it impacts the magnetic relaxation at higher temperatures, so that the presented parametrisation needs to be taken with caution.

Magnetic hysteresis curves of both compounds at $2\,\text{K}$ are shown in fig. 4.3. A butterfly shape is found meaning that the hysteresis entirely collapses already at $250\,\text{Oe}$, which is indicative of strong QTM present at low magnetic fields. For **13** the hysteretic spreading is twice as large as in **14** featuring a maximum at $1000\,\text{Oe}$ in both cases. The difference shows, that either QTM is weaker or suppressed more effectively by magnetic fields in **13**.

A correlation of the different magnetic behaviour with structural features is not possible due to the putative isostructurality and low quality of the crystal structures. Since the main abundant isotopes of Na and K both feature a nuclear spin of $\frac{3}{2}$, interactions with nuclear spins
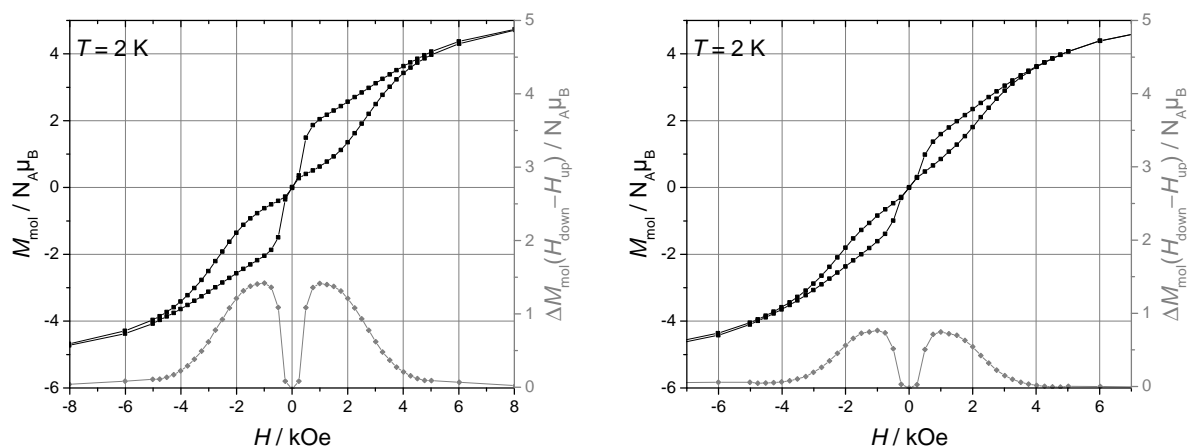
Figure 4.3: Hysteresis curves of **13** (**left**) and **14** (**right**) at 2 K, the grey curve illustrates the difference between the curve with decreasing magnetic field and the curve with increasing magnetic field.

can also be excluded as origin of distinctions. Hence, slight structural differences not resolved in the available crystal structures or dissimilar strain created by the different ionic radii of K^+ and Na^+ remain possible sources for the suspected discrepancies in their vibrational structure.

4.1.4 Concluding Remarks

The two presented compounds **13** and **14** are the first tag-based mononuclear Dy(III) complexes lacking intermolecular hydrogen bonding in close proximity to the Dy centre and hence can be considered a magnetically uncoupled reference for the multinuclear systems presented later on. The magnetic isolation of the Dy centres in **13** and **14** is indicated by the butterfly-shape of their hysteresis curves, which stands in contrast to the exchange-bias promoted open hysteresis observed for the alleged mononuclear saltag based Dy complexes reported by Schuch.[239]

Unfortunately, the exact molecular structure of **13** and **14** is insufficiently resolved so far. For a precise correlation of evident differences in their magnetic behaviour with structural features, a structure determination *e.g.* by diffraction of synchrotron radiation is desirable and would also allow for constructive support by *ab-initio* calculational methods.

In spite of the discussed drawbacks, incorporation of alkali metal ions into mononuclear Dy(III) complexes as structural tuners, simultaneously retaining the electronic situation of the ligands remains a great concept to study purely structural and possibly also vibrational influences on the SMM-behaviour of the system. It should therefore be further pursued and might also be extended to other diamagnetic cations being electronically almost innocent like late alkaline earth metal ions.

4.2 Dinuclear Lanthanoid Complexes

4.2.1 Synthesis and Characterisation

For the targeted synthesis of dinuclear lanthanoid complexes with tag-based ligands two different strategies proved successful. First, the absence of protic solvents in the reaction mixture prevents the formation of higher nuclearity aggregates, regardless of the excess of lanthanoid precursor present and the base equivalents added as long as the base strength remains in the aqueous window. This might have different reasons, on the one hand stabilisation of unbound anions is much worse in aprotic solvents as compared to protic solvents, so that the formation of negatively charged anion complexes occurs. Hence, the actual availability of lanthanoid ions is reduced. On the other hand, also the stabilisation of a fully deprotonated and thus highly anionic ligand as possible transient species is poor. The usage of stronger, non-aqueous bases to generate higher nuclearities also in aprotic solvents was attempted, but led to ligand decomposition, especially in the presence of lanthanoid ions.

These observations have been exploited to synthesise the dinuclear Dy complexes $[Dy_2(H_2saltag^{Br})_2(dmf)_4] \cdot 1.75 H_2O$ (**15**) from a DMF/MeCN mixture, $[Dy_2(H_2saltag^{Br})_2(dmf)_4] \cdot 2 DMF$ (**16**) from solely DMF and $[Dy_2(H_2saltag^{Br})_2(py)_4] \cdot H_2O \cdot py$ (**17**) from pyridine/MeCN. In all cases two equivalents of the chelate ligand were reacted with somewhat more than three equivalents of a Dy precursor. For **15** and **16**, triethylamine was added as a base.

The second approach comprises the synthesis in the presence of protic solvents, but deliberately limits the actual availability of lanthanoid ions. One possible way to do that is a careful adjustment of stoichiometry, which is not trivial because mononuclear and trinuclear complexes are omnipresent competing products. Using two equivalents of $H_5saltag^{Br} \cdot HCl$ and 2.5 equivalents $DyCl_3 \cdot 6 H_2O$ with 12 equivalents of NEt_3 in MeOH enabled the isolation of $[Dy_2(H_2saltag^{Br})_2(MeOH)_4]$ (**18**).

Another realisation of this strategy was also followed within the synthesis of **16**, because the final step for the isolation is a diffusion of water into the reaction solution. Thereby, the availability of Dy(III) ions is slowly increased, because the unbound counteranions become stabilised with growing water content. In general, the crystallisation of dinuclear tag-based lanthanoid complexes from very polar solvents is favoured by the fact, that they form neutral complexes in contrast to mononuclear and trinuclear analogues.

For all mentioned compounds, the chemical composition as presented is confirmed by elemental analysis, merely for **18** an exchange of the MeOH coligands by water is indicated. In case of **15** and **17**, molecule ions of the complexes were detected via ESI-MS experiments, whereat the former loses its MeOH coligands upon ionisation in MeOH and the latter retains its pyridine coligands after ionisation in a MeOH/THF mixture. Interestingly, for both compounds the molecule anions in negative mode were better detectable than the molecule cations in positive mode.

A chemically similar compound to **17** using the $H_5saltag^{I} \cdot HCl$ has already been reported and characterised by Wünscher,[290] however, the synthesis described there is rather cumbersome.

The procedure given in this work for **17** can also be adapted to synthesise Wünscher's compound in a more straightforward manner.

Utilising the synthetic procedures of **15** and **16** isostructural Y, Gd, Tb, Er and Yb complexes were synthesised, but due to their negligible relevance for the scope of this work they are not further treated. In principle, similar complexes of all other lanthanoids should be feasible with minor adjustments of the synthesis. The Y and Gd analogues of **15** are resumed in the magnetic properties subsection. An Y complex isostructural to **15** with statistically doped Dy ions is henceforth referred to as **15@Y**.

4.2.2 Crystal Structures

For all tag ligand-based dinuclear Dy complexes reported in this work, a sandwich-like arrangement of the two tag ligands involved is found, whereat the tag planes are tilted by a certain angle ϑ_{SW} against each other, because the third pocket of the sandwich remains unoccupied. Moreover, the tag ligands are oriented contracyclical. Both Dy centres are coordinated by one [N_2O] binding pocket of each chelate ligand, leading to an [N_4O_2] component of the overall donor set, which all compounds have in common. This coordination mode also includes the double diazine bridging of the two metal centres by one arm of each ligand. The donor set is completed by two donor solvent molecules varying among the different compounds, so that an overall eightfold coordination is found in all cases. The shortest coordinative bonds are always formed by the phenolate O-donors, thus they are presumably the donors with the highest negative charge density and their alignment is essential for the evaluation of magnetic properties (compare section 1.3) later on.

Since the crystal structures of **15**, **16**, **17** and **18** are similar in the mentioned aspects, only **15**'s structure is discussed in profound detail. For **16**, **17** and **18** crucial differences are highlighted and eventually relevant structural parameters are gathered and compared.

[Dy$_2$(H$_2$saltag^{Br})$_2$(dmf)$_4$] · 1.75 H$_2$O   (15)

The compound crystallises in the orthorhombic space group *Fdd*2 (#43) as the neutral complex molecule [Dy$_2$(H$_2$saltag^{Br})$_2$(dmf)$_4$] together with 1.75 cocrystallised water molecules, which are bound by multivalent hydrogen bonds in the vacant coordination pocket (see fig. 4.4). Both Dy(III) centres are crystallographically independent, however, their coordination environment is very similar and therefore discussed together. Bond lengths and angles within the coordination sphere of the Dy(III) ions are listed in table 4.3.

Besides the [N_4O_2] donors provided by the two saltag^{Br} ligands the coordination sphere of the Dy centres in **15** is completed by the carbonyl-O of two DMF molecules yielding an [N_4O_4] overall donor set (fig. 4.4). The corresponding bond lengths can be categorised pairwise, the shortest bonds formed by the phenolate-O (O1, O1A, O3, O3A) average to 223 pm followed by the bonds with the DMF-based donors (O1L, O2L, O3L, O4L), which are 240 pm on average. For the N-donors the differences are apparently more related to steric strain, than electronics, because nitrogen donors in the double diazine bridge (N1, N2, N5A, N6A) consistently form
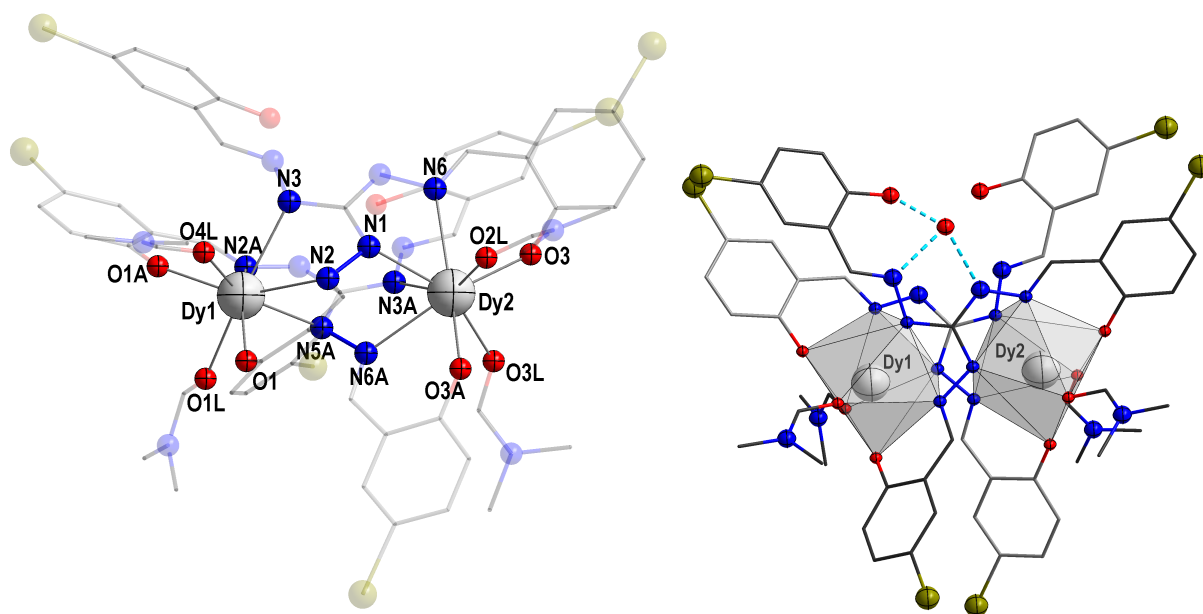
Figure 4.4: Left: Molecular structure of neutral complex $[Dy_2(H_2saltag^{Br})_2(dmf)_4] \cdot 1.75H_2O$ (**15**) with atom labels, C atoms are wire nodes, Dy: light grey, N: blue, O: red, Br: dark yellow. H atoms and cocrystallised water molecule are omitted for clarity. Parts of the molecule not involved in the coordination of the labelled metal centres have been rendered transparent for clarity. **Right:** Illustration of the distorted square antiprism coordination polyhedra of **15**. Multivalent hydrogen bonding interactions of one cocrystallised water molecule are drawn as light blue dashed bonds. View along the normal to the tag planes. Colour code is identical.

Table 4.3: Selected bond lengths (pm) and angles (°) from the coordination environment of Dy1 and Dy2 in **15**. The corresponding numbering scheme is depicted in fig. 4.4.

Dy1–N2	248.7(5)	Dy2–N1	247.3(5)
Dy1–N2A	257.9(5)	Dy2–N3A	255.7(5)
Dy1–N3	254.4(5)	Dy2–N6	258.6(5)
Dy1–N5A	248.5(5)	Dy2–N6A	252.9(5)
Dy1–O1	223.6(5)	Dy2–O2L	240.0(5)
Dy1–O1A	222.0(5)	Dy2–O3	222.1(4)
Dy1–O1L	238.8(5)	Dy2–O3A	224.1(5)
Dy1–O4L	238.6(5)	Dy2–O3L	243.6(5)
O1–Dy1–N2A	150.0(2)	O3–Dy2–N6A	153.9(2)
O1A–Dy1–N2	148.9(2)	O3A–Dy2–O3L	156.7(2)
O1–Dy1–O1A	118.8(2)	O3–Dy2–O3A	115.1(2)
O1L–Dy1–O4L	124.6(2)	O2L–Dy2–O3L	128.2(2)

the shorter bonds of 249 pm on average as compared to the non-bridging N-donors (N2A, N3, N3A, N6) with a mean bonding distance of 257 pm.

In table 4.3, a selection of bonding angles of the coordination sphere is given. The selection as such is given for all following dinuclear and also the trinuclear Dy complexes presented in this work. It includes the largest bonding angles of the two phenolate O-donors, the angle of these very donors with respect to each other and the angle of the two coordinating solvent molecules. This choice is motivated by its suitability to assume the agreement with an ideal axial coordination geometry promoting optimum magnetic anisotropy of the single Dy centre as described in section 1.3. The angle between the phenolate O-donors should approach 180° for an axial alignment of the strongest donors, while in an ideal scenario the angles with the remaining weaker donors, given here as the two largest so-called *trans*-angles, are 90° (equatorial arrangement). The angle between the coordinating solvents' donor atoms are given, because they are not bound within the ligand scaffold and hence vary a lot more among the different compounds than all the other donor angles. Of course, the fundamental arrangement of the chelate ligands' donors does not allow for this ideal situation and the phenolate-O donor angle is smaller than the two *trans*-angles with N-donors throughout all Dy complexes reported in this work. However, observable trends within the individual congeners will be discussed and resumed in the "Magnetic Properties" subsection.

In case of **15** the coordination sphere shows closest agreement with a triangular dodeca-hedron (point symmetry D_{2d}) as is indicated by continuous shape measures[251–253] yielding a corresponding deviation parameter of 1.249 (for Dy1, 1.264 for Dy2). The two rhombic planes of this polyhedron are formed by the four O-donors and the four N-donors, respectively. A distance of the Dy centres from these planes can be determined to 112 pm (113 pm) for $[O_4]$ and 163 pm (165 pm) for $[N_4]$, once more reflecting the clear preference of the lanthanoid ions for the harder O-donors.

A sandwich tilting angle between the two tag planes of the molecule $\vartheta_{SW} = 6.4°$ is found for **15**. Both Dy centres within the molecule are 507 pm apart, while the shortest intermolec-ular Dy$\cdots$Dy span is 798 pm, the corresponding contact is along the crystallographic *c*-axis. The neutral complex molecules align on this very axis in alternating sequence between the asymmetric unit and its inversion symmetry generated equivalent.

$[Dy_2(H_2saltag^{Br})_2(dmf)_4] \cdot 2\,DMF$ (16)

The chemical composition of the neutral complex in **16** is identical to the one of **15**, only the cocrystallised solvent molecule is DMF instead of water. It can therefore be considered a solvomorph of **15** crystallising in the monoclinic space group $C2/c$ (#15). The most essential feature is the asymmetric unit consisting of only half a complex molecule, so that only one crystallographically independent Dy centre is present, while the second one within the molecule is generated by a $C2$ operation along the crystallographic *b*-axis.

Bond lengths an angles of the only crystallographically independent Dy centre are given in table 4.4. The higher crystallographic symmetry of the system is accompanied by a better
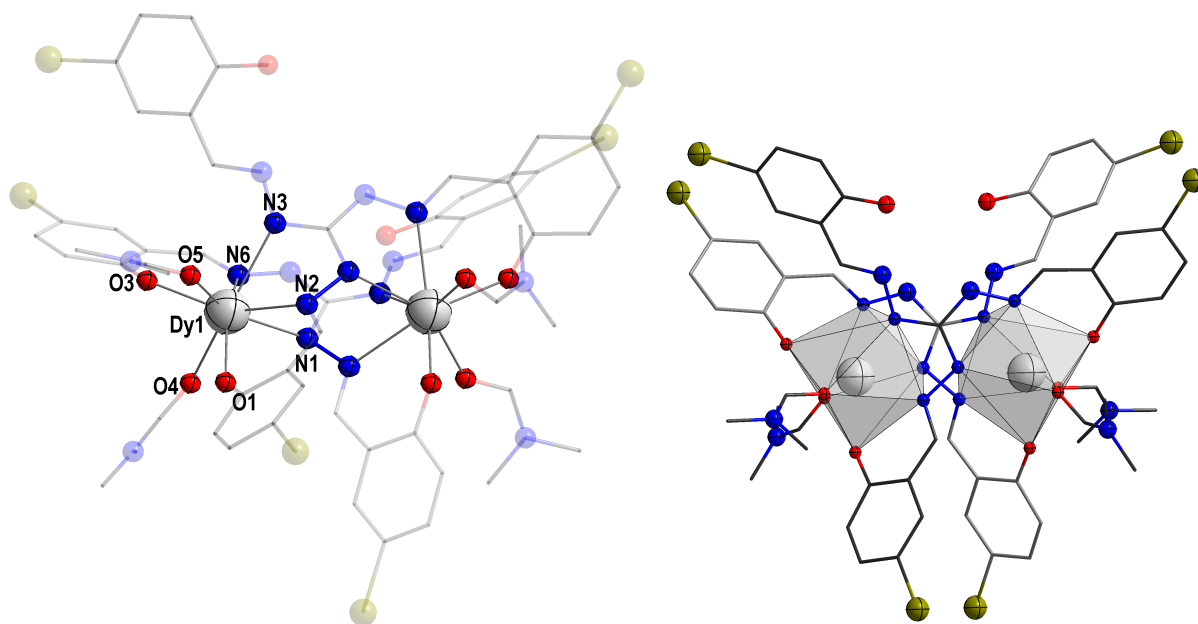
Figure 4.5: Left: Molecular structure of neutral complex [Dy$_2$(H$_2$saltag^{Br})$_2$(dmf)$_4$]·DMF (**16**) with atom labels, C atoms are wire nodes, Dy: light grey, N: blue, O: red, Br: dark yellow. H atoms and cocrystallised DMF molecules are omitted for clarity. Parts of the molecule not involved in the coordination of the labelled metal centres have been rendered transparent for clarity. **Right:** Illustration of the distorted triangular dodecahedron coordination polyhedra of **16**. View along the normal to the tag planes. Colour code is identical.

Table 4.4: Selected bond lengths (pm) and angles (°) from the coordination environment of Dy1 in **16**. The corresponding numbering scheme is depicted in fig. 4.5.

Dy1–N1	245.5(7)	Dy1–N2	247.9(9)
Dy1–N3	252.5(9)	Dy1–N6	251.2(9)
Dy1–O1	222.2(7)	Dy1–O3	224.2(7)
Dy1–O4	243.1(9)	Dy1–O5	238.8(8)
O1–Dy1–N6	148.5(3)	O3–Dy1–N2	149.1(3)
O1–Dy1–O3	115.4(3)	O4–Dy1–O5	127.3(3)

agreement of the metal centres' donor environment with the ideal triangular dodecahedron geometry revealed by the lower shape deviation parameter[251–253] of 0.907. Very similar distances of the metal centre from the O$_4$ donor plane and the N$_4$ donor plane of 113 pm and 160 pm as compared to **15** are found.

However, the intersecting angle of the two tag planes ϑ_{SW} = 12.5° is twice as large as in **15** and the metal···metal distance of 504 pm is somewhat shorter. Complementarily, the next intermolecularly neighbouring Dy atom is significantly farther away (862 pm).
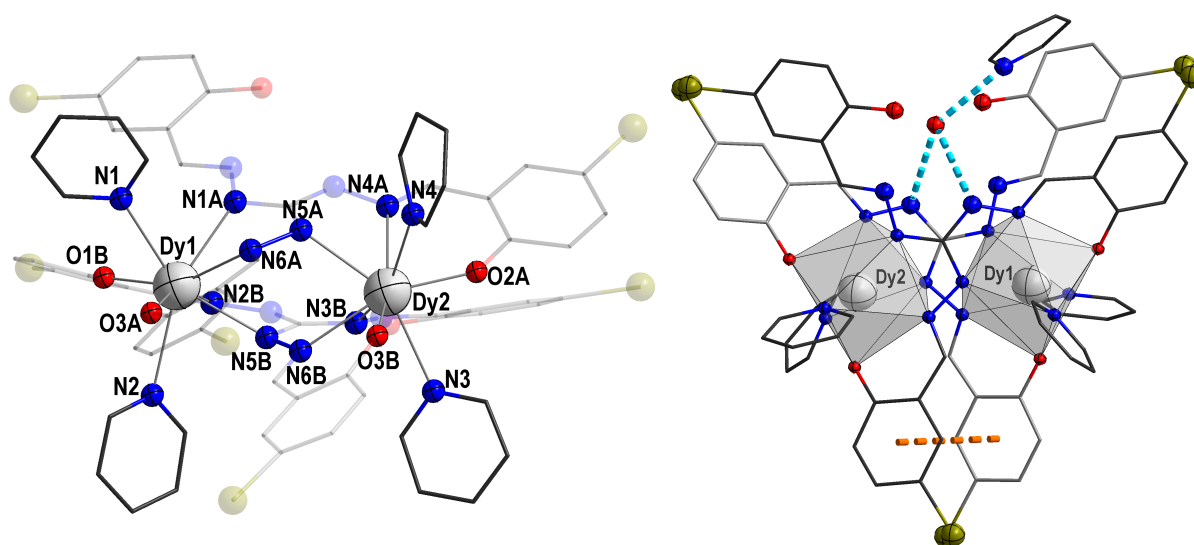
[Dy$_2$(H$_2$saltag^{Br})$_2$(py)$_4$]·H$_2$O·py (17)

Triclinic space group $P\bar{1}$ (#2) is found in crystals of **17**, which contain two crystallographically independent Dy centres in the neutral complex [Dy$_2$(H$_2$saltag^{Br})$_2$(py)$_4$]. Besides, a cocrys-

tallised water molecule is bound by multivalent hydrogen bonds in the vacant coordination pocket of the chelate ligands (see fig. 4.6). A further cocrystallised pyridine molecule is attached to this water molecule via hydrogen bond.

Most singular property of the compound is the coordinative saturation of the Dy centres by N-donor pyridine coligands leading to an $[N_6O_2]$ overall donor set. In contrast to all other polynuclear lanthanoid complexes reported in this work, the bonding distance of the solvent coligands to the metal centre is significantly longer (average: 262 pm) than the ones of the N-donors provided by the tag-based chelate ligands (average: 251 pm). Consequently, the bonds with the phenolate O-donors are somewhat shorter averaging to 220 pm. Again, a distorted triangular dodecahedron coordination geometry is revealed by continuous shape measures[251–253] yielding a corresponding deviation parameter of 1.294 (for Dy1, 1.185 for Dy2). Metal centres' distances of 113 pm (117 pm) from the $[O_2N_2]$ and 160 pm (161 pm) from the $[N_4]$ donor planes are found, which is similar to the precedent compounds despite the differences in the donor set.

An intramolecular $\pi \cdots \pi$-interaction (centroid–plane = 346 pm) is detected between the aromatic rings of the chelate ligand arms bearing the bridging diazine moieties (see fig. 4.6). This interaction being present only at one side of the triangular ligands promotes the tilting of the tag planes to an intersecting angle of ϑ_{SW} = 13.1°. The span between the metal centres within the molecule is 508 pm, their closest intermolecular neighbouring metals are 828 pm afar.
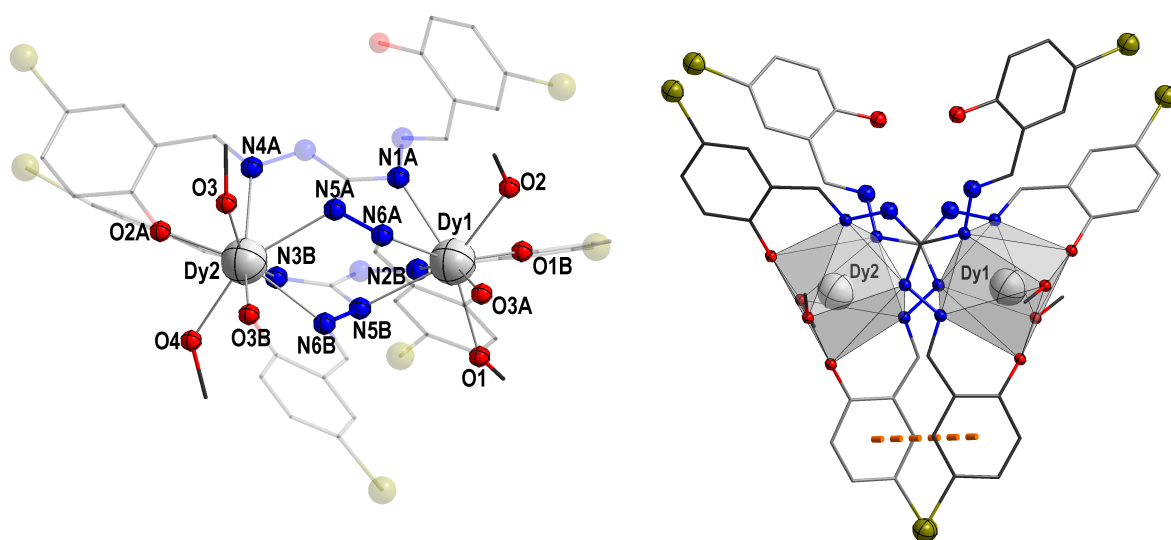
Figure 4.6: Left: Molecular structure of neutral complex [Dy$_2$(H$_2$saltag^{Br})$_2$(py)$_4$]·H$_2$O·py (**17**) with atom labels, C atoms are wire nodes, Dy: light grey, N: blue, O: red, Br: dark yellow. H atoms and cocrystallised DMF molecule are omitted for clarity. Parts of the molecule not involved in the coordination of the labelled metal centres have been rendered transparent for clarity. **Right:** Illustration of the distorted triangular dodecahedron coordination polyhedra of **17**. View along the normal to the bottom tag plane (lighter grey). The light blue dashed lines show hydrogen bonds of the cocrystallised water and pyridine molecules. The orange dashed line illustrates the intramolecular $\pi\cdots\pi$-interaction. Colour code is identical.

Table 4.5: Selected bond lengths (pm) and angles (°) from the coordination environment of Dy1 and Dy2 in **17**. The corresponding numbering scheme is depicted in fig. 4.6.

Dy1–N1	262.5(4)	Dy2–N3	259.5(4)
Dy1–N1A	249.6(3)	Dy2–N3B	250.2(3)
Dy1–N2	265.3(4)	Dy2–N4	261.2(4)
Dy1–N2B	254.3(3)	Dy2–N4A	255.6(3)
Dy1–N5B	245.9(3)	Dy2–N5A	251.8(3)
Dy1–N6A	252.1(3)	Dy2–N6B	248.8(3)
Dy1–O1B	221.5(3)	Dy2–O3B	219.8(3)
Dy1–O3A	218.2(3)	Dy2–O2A	220.4(3)
O1B–Dy1–N6A	155.06(11)	O2A–Dy2–N6B	153.37(11)
O3A–Dy1–N2B	153.82(11)	O3B–Dy2–N4A	154.94(11)
O1B–Dy1–O3A	112.38(10)	O2A–Dy2–O3B	113.45(11)
N1–Dy1–N2	133.53(11)	N3–Dy2–N4	128.45(12)

[Dy₂(H₂saltag^Br)₂(MeOH)₄] (18)

In triclinic crystals of **18** featuring the space group $P\bar{1}$ (#2), exclusively the neutral complex molecule [Dy₂(H₂saltag^Br)₂(MeOH)₄] is found. The solvent based coligands are protic MeOH molecules in this compound. Both Dy centres in the neutral complex molecule are crystallographically independent (see fig. 4.7), their environing bond lengths and angles are given in table 4.6.

Figure 4.7: Left: Molecular structure of neutral complex [Dy₂(H₂saltag^Br)₂(MeOH)₄] (**18**) with atom labels, C atoms are wire nodes, Dy: light grey, N: blue, O: red, Br: dark yellow. H atoms are omitted for clarity. Parts of the molecule not involved in the coordination of the labelled metal centres have been rendered transparent for clarity. **Right:** Illustration of the distorted triangular dodecahedron coordination polyhedra of **18**. View along the normal to the bottom tag plane (lighter grey). The orange dashed line illustrates the intramolecular $\pi\cdots\pi$-interaction. Colour code is identical.

The distribution of coordinative bond lengths is again similar to **15**, even the solvent donors' averaged bonding distance of 243 pm is only marginally longer. Likewise, the spacing between the Dy centres and the donor planes has comparable values of 117 pm (for Dy1, 115 pm for Dy2) from the [O₄] and 162 pm (162 pm) from the [N₄] plane. Accordingly, the coordination polyhedron with the largest agreement as obtained by continuous shape measures[251–253] is again the triangular dodecahedron with deviation parameters of 1.423 (Dy1) and 1.111 (Dy2).

However, a significantly lower symmetry is unveiled for Dy1. This discrimination is further illustrated by the somewhat larger bonding distance Dy1–O3A of 225 pm. These observations can be related to the occurrence of two hydrogen bonds between phenolate donors O3A and MeOH donors O2 (d = 283 pm) of a neighbouring complex molecule (fig. 4.8), thereby forming a dimer of two complex molecules. The resulting tetranuclear supramolecule shows a linear arrangement of the Dy nuclei with a downthrow at the hydrogen bridge. Correspondingly, an intramolecular Dy1$\cdots$Dy2 distance of 518 pm and an intradimer distance Dy1$\cdots$Dy1 of 593 pm is found.

Table 4.6: Selected bond lengths (pm) and angles (°) from the coordination environment of Dy1 and Dy2 in **18**. The corresponding numbering scheme is depicted in fig. 4.7.

Dy1–N1A	248.2(4)	Dy2–N3B	248.9(5)
Dy1–N2B	254.4(5)	Dy2–N4A	256.4(5)
Dy1–N5B	256.6(4)	Dy2–N5A	255.4(4)
Dy1–N6A	251.2(5)	Dy2–N6B	249.9(5)
Dy1–O1	244.7(4)	Dy2–O2A	222.6(4)
Dy1–O1B	221.3(4)	Dy2–O3	242.5(4)
Dy1–O2	244.6(4)	Dy2–O3B	220.6(4)
Dy1–O3A	224.8(3)	Dy2–O4	243.8(4)
O1B–Dy1–N6A	157.84(15)	O2A–Dy2–N6B	153.24(16)
O3A–Dy1–N2B	155.30(15)	O3B–Dy2–N4A	151.53(16)
O1B–Dy1–O3A	111.09(13)	O2A–Dy2–O3B	114.33(14)
O1–Dy1–O2	128.04(13)	O3–Dy2–O4	126.78(15)

As in **17**, an intramolecular $\pi \cdots \pi$-interaction between the aromatic rings of the chelate ligand arms bearing the bridging diazine moieties is found. Abetted by this interaction, the largest intersecting angle of the tag planes $\vartheta_{SW} = 14.7°$ among the dinuclear complexes discussed in this work is present in **18**. Though, the tag planes are distorted quite roughly, so that the definition of their least squares plane has to be taken with equitable caution.
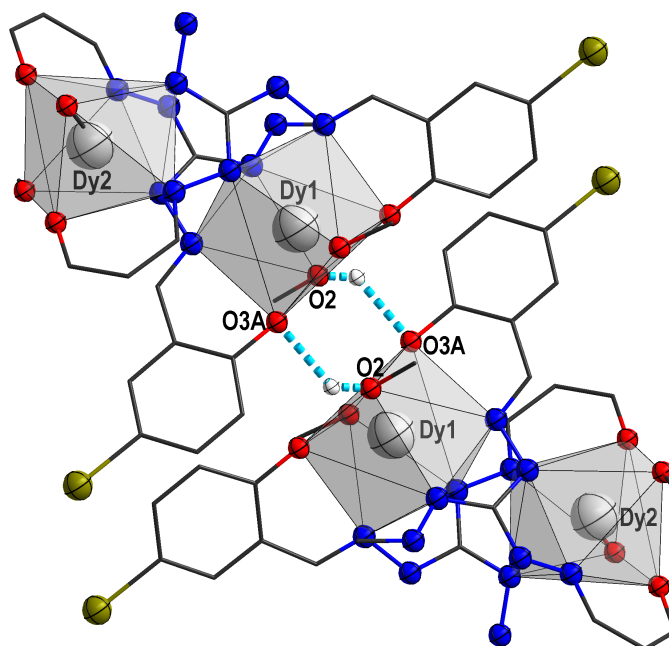
Figure 4.8: Depiction of hydrogen bonds between atoms O2 and O3A leading to dimer formation in **18** with atom labels, C atoms are wire nodes, Dy: light grey, N: blue, O: red, Br: dark yellow. H atoms and wide parts of the two complex molecules involved are omitted for clarity.

Comparative Remarks

Analysis of the dinuclear Dy(III) complexes' crystal structures suggests an overall large similarity among them. However, already minor structural changes can have significant effects on magnetic anisotropy, magnetic interactions, vibrational structure and hence SMM properties. Therefore, some structural parameters, which affect these properties were chosen and collated in table 4.7. Backgrounds of the influence of structural features on the magnetic properties are explicated in more detail in sections 1.2 and 1.3.

Table 4.7: Comparison of structural parameters obtained from crystal structures of the dinuclear Dy(III) complexes reported in this work. The deviation parameters from ideal triangular dodecahedron (Sh-TDD) coordination polyhedra determined via continuous shape measures[251–253] are given in the upper part of the table. The lower half lists averaged bond lengths d_{av}[O$_{Ph}$–Dy], the bonding angle of the phenolate O-donors $\angle$O$_{Ph}$–Dy–O$_{Ph}$, which form the shortest coordinative bonds with the metal centres, the intersecting angle between the lines through the phenolate-O donors of each Dy centre $\angle$O–O$_{Dy}$ - O–O$_{Dy'}$ as well as the intramolecular metal distance d[Dy$\cdots$Dy$_{intra}$].

	15		**16**	**17**		**18**	
Centre	Dy1	Dy2	Dy1	Dy1	Dy2	Dy1	Dy2
Sh-TDD	1.249	1.264	0.907	1.294	1.185	1.423	1.111
d_{av}[O$_{Ph}$–Dy]/ pm	222.8	223.1	223.2	219.9	220.1	223.1	221.6
$\angle$O$_{Ph}$–Dy–O$_{Ph}$/°	118.8	115.1	115.4	112.4	113.5	111.1	114.3
$\angle$O–O$_{Dy}$ - O–O$_{Dy'}$/°	60.9		62.3	59.9		56.2	
d[Dy$\cdots$Dy$_{intra}$]/ pm	507		504	508		518	

First, the shape deviation parameter from the closest ideal coordination polyhedron, the triangular dodecahedron, Sh-TDD is a measure for the proximity to an ideal point symmetry of the ligand field, which is of outstanding importance for magnetic relaxation.[165] Howbeit the approached polyhedron does not feature $D4_d$ point symmetry, which would be ideal for the suppression of magnetic relaxation in an eight-coordinate case,[165] but only $D2_d$. Nevertheless, every kind of higher point symmetry should reduce available relaxation pathways.[143,173] With respect to this measure, complex **16** clearly shows the highest congruency with the triangular dodecahedron case and shows the further advantageous property of two symmetry related and hence identically coordinated metal centres.

Second, the averaged bonding distances of the phenolate O-donors of each Dy centre d_{av}[O_{Ph}–Dy] are indicative for them to be the most influential donor sites in terms of determination of magnetic anisotropy axes.[149–151] Namely, the shorter these bonds are, the minor is the effect of all remaining donor atoms, which perturb the axial symmetry and hence the ideal magnetic anisotropy for SMM behaviour. Here, compound **17** exhibits a slight preference, however, the differences must be evaluated as negligible, so that the effect of this parameter should be minor in the present selection.

As it is known for the saltag-based Dy(III) complexes, that their easy axis of magnetisation is determined by the phenolate O-donors[248,272] their binding angle $\angle O_{Ph}$–Dy–O_{Ph} is another structural parameter with tremendous influence on the local magnetic anisotropy. For maximum energetic separation and high purity of the ligand field split microstates the angle should approach $180°$.[129] Notwithstanding that the presented compounds are far off this value, **15** features the most beneficial situation.

Considering the same rational for the approximation of easy axes of magnetisation, the intersecting angle between the lines through the phenolate-O donors of each Dy centre $\angle O$–O_{Dy1} - O–O_{Dy2} should roughly agree with the intersecting angle between the easy axes of both Dy centres. This angle determines, whether and to what extent the dipolar magnetic interaction (which is predominant in magnetically anisotropic lanthanoids, see sections 1.2 and 1.3) is beneficial for the suppression of QTM. A parallel arrangement is ideal,[189] thus the angle should be minimised. The smallest such angle is found in **18**, however the mentioned dimer formation brings further interactions into play for this complex, which might not be advantageous. Since the strength of these dipolar magnetic interactions are highly distance dependent (compare eq. (1.13)), the intramolecular metal$\cdots$metal distance d[Dy$\cdots$Dy$_{intra}$] indicates the expectable strength of this interaction. Contrarily, this parameter suggests weakest interactions for **18**, while it is comparable for the other complexes. Overall, no clear preference for the beneficialness of dipolar magnetic interaction for SMM properties among the four dinuclear Dy complexes can be estimated based on structural parameters.

Against the background of these comparing considerations, the interpretation of magnetic properties presented hereinafter could allow for an evaluation on which parameter is most influential on the SMM properties of the dinuclear tag-based Dy complexes.

4.2.3 Magnetic Properties

Temperature-dependent DC magnetic susceptibility measurements carried out on all compounds presented in this section can be found in appendix B.2. Due to the complex energy spectrum of the Dy(III) ion, no fitting of the data was attempted. Hence, very little information can be extracted from them.

In contrast, magnetic relaxation behaviour was probed via AC magnetic susceptibility measurements at static magnetic fields H_{DC} of 0, 400 and 1000 Oe. If feasible, direct measurement of relaxation of magnetisation was used to examine magnetic relaxation at very low temperatures. It is discussed in detail for each compound hereinafter. The temperature dependence of in-phase (χ') and out-of-phase (χ'') magnetic susceptibility components as well as the Cole-Cole plots illustrating their fit to a generalised Debye model (eq. (1.20)) to extract the relaxation times τ_T are shown in appendix B.2 for all compounds.

Furthermore, the compounds were checked for magnetic hysteresis and discrepancies in the magnetic behaviour upon slow warm-up in weak magnetic fields under field-cooled and zero field-cooled conditions (ZFC measurements). For the compounds exhibiting such phenomena, these are explicated in the following discussions.

[Dy$_2$(H$_2$saltag^{Br})$_2$(dmf)$_4$] · 1.75 H$_2$O   (**15** and **15@Y**)

Although a fit of the DC magnetic susceptibility curve is not feasible for the dinuclear Dy complexes, a full matrix diagonalisation fit to the Hamiltonian for a spin-dimer given below was undertaken for an isostructural Gd$_2$ analogue of **15** to approximate the superexchange contribution to the magnetic interaction for the dinuclear Dy complexes presented in this section.

$$\widehat{H} = -J_{ex}\left(\widehat{S}_1\widehat{S}_2\right) \; + \; g_{iso}\mu_B B \sum_{i=1}^{2} \widehat{S}_i \tag{4.2}$$

The Gd(III) ions were treated as magnetically isotropic $S = \frac{7}{2}$ centres, which is justified by the quenching of orbital angular momentum in its f^7 electron configuration. Fit parameters $g = 2.08$ and $J_{ex} = -0.044\,\mathrm{cm}^{-1}$ were obtained, the corresponding curve together with the experimental data is shown in fig. 4.9. J_{ex} found in this Gd(III) compound is a valid estimate for the superexchange contribution in all Dy(III) complexes presented in this and the following section, because the bridging mode and interionic distances are equal in first approximation.

Furthermore, the result is in good agreement with the estimation based on CAS-SCF calculations with subsequent POLY-ANISO[222,291] simulation of the temperature-dependent magnetic susceptibility of **15** provided by Böhme,[272] which suggests a value of $-0.5\,\mathrm{cm}^{-1}$ (see fig. B.3). The dipolar interaction mentioned there should preponderantly vanish in case of the Gd$_2$ analogue due to its magnetically isotropic nature. Other results from these calculations relevant for this section are the relative energies of the individual Dy centres' Kramers doublets (table B.4) as well as the alignment of the easy axes of magnetisation of the magnetic ground state with
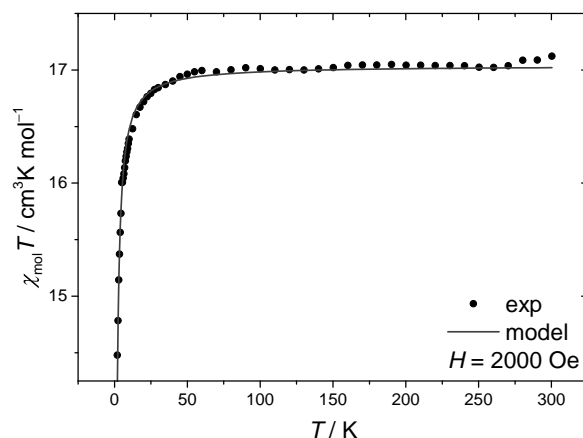
Figure 4.9: Temperature dependence of molar magnetic susceptibility $\chi_{mol}T$ of the isostructural Gd$_2$ analogue of **15** at an applied magnetic field of H = 2000 Oe. The fit to the Hamiltonian given in eq. (4.2) is drawn as solid grey line.

respect to each other (fig. B.2). The latter uncovers an intersecting angle of 77.3° (compare $\angle$O–O$_{Dy1}$ - O–O$_{Dy2}$ = 60.9°) and a dihedral angle with the Dy centres of 37.7°. This is far from the parallel alignment, which is ideal for the suppression of QTM, nevertheless, significant magnetic interaction is evident and has to be considered for the evaluation of the magnetic behaviour.

Compound **15** is the only one presented in this work, whose AC susceptibility was recorded on a Physical Property Measurement System (PPMS), therefore larger measurement frequencies are available and the fittable range was extended to somewhat higher temperatures or rather faster relaxation times τ_T as compared to the magnetically diluted isostructural **15@Y** (see table 4.8) and all other compounds in this chapter. Nonetheless, it is discussed in direct comparison with its magnetically diluted isostructural derivative **15@Y**. The factual ratio Dy:Y in the investigated material was determined to be 1:3.5 via comparison of their saturation magnetisation normalised to the sample mass. Accordingly, in case of statistic distribution of Dy among structural positions, the molecule bearing two Dy(III) ions should not contribute significantly to the magnetic properties of the material **15@Y**.

A first drastic difference between the AC magnetic behaviour of both compounds is the temperature trend of the out-of-phase susceptibility χ'' (see tables B.5, B.6 and B.6). Without a static magnetic field, it is close to zero at very low temperatures around 2 K for **15**, while it is maximises for **15@Y**. Upon increase of the static magnetic field, χ'' grows at very low temperatures in case of **15** (especially at 1000 Oe) and, in contrast, drops to almost zero for **15@Y**. Large χ'' at very low temperatures is indicative for high relaxation rates of magnetisation mostly due to QTM, since it is the only process without temperature dependence. Consequently, the QTM rate appears to be low in the absence of a static magnetic field and increases upon application of such for **15** and *vice versa* for **15@Y**. The α-range of the fittable AC susceptibility data (see table 4.8) further supports that assumption, given the fact that large QTM rates tremendously increase the dispersion parameter α due to their low directionality. Eventually, the feasibility of direct relaxation measurements from 2 to 3.5 K for **15** at zero field, which were
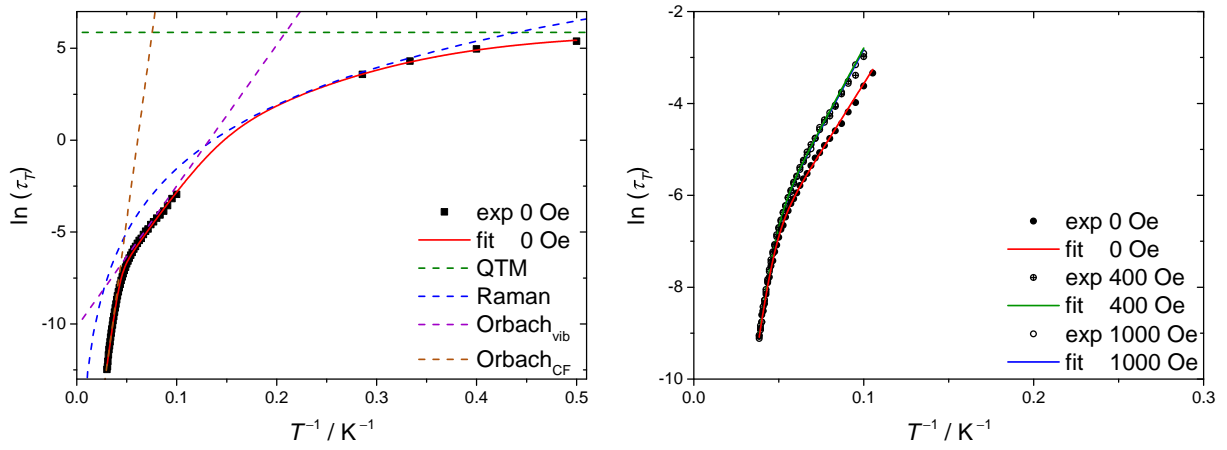
Figure 4.10: Logarithmic plot of the relaxation time τ_T of **15** (**left**) and **15@Y** (**right**) at different static magnetic fields H_{DC} against T^{-1}. The corresponding fits of the relaxation behaviour to the multiprocess relaxation law given in eq. 4.3 yielded the parameters given in table 4.8 and are drawn as solid lines. The dashed lines in the left graph illustrate the discrete relaxation processes also revealing the temperature range, in which they are dominant, respectively.

Table 4.8: Collection of Debye model fittable temperature ranges and alpha parameters from the AC magnetic susceptibility measurements on **15** and **15@Y** at different static magnetic fields H_{DC} applied as well as parameters extracted from fits of the temperature dependence of the corresponding magnetic relaxation times τ_T to the multiprocess relaxation law given in eq. 4.3. Fixed parameters are marked with an asterisk.

H_{DC}	value	[Dy$_2$] (**15**)	[Dy@Y$_2$] (**15@Y**)
0 Oe	fittable T-range (AC sus.)	$10 \cdots 33\,\mathrm{K}$	$9.5 \cdots 26\,\mathrm{K}$
	fittable T-range (direct rel.)	$2 \cdots 3.5\,\mathrm{K}$	-
	α-range (AC sus.)	$0.231(11) \cdots 0.158(3)$	$0.327(12) \cdots 0.12(2)$
	α-range (direct rel.)	$0.201(2) \cdots 0.064(2)$	-
	$\Delta_{CF}/\,\mathrm{cm}^{-1}$	$278(6)$	$190*$
	$A_{CF}/\,\mathrm{s}^{-1}$	$3.8(12)\cdot 10^{10}$	$2.77(7)\cdot 10^{8}$
	$\Delta_{vib}/\,\mathrm{cm}^{-1}$	$53.4(14)$	$40.9(6)$
	$A_{vib}/\,\mathrm{s}^{-1}$	$2.6(4)\cdot 10^{4}$	$1.28(7)\cdot 10^{4}$
	$B/\,\mathrm{s}^{-1}\mathrm{K}^{-n}$	$4.7(5)\cdot 10^{-5}$	-
	n	$5*$	-
	$C_{QTM}/\,\mathrm{s}^{-1}$	$0.0028(5)$	-
400 Oe	fittable T-range	$10 \cdots 30\,\mathrm{K}$	$10 \cdots 26\,\mathrm{K}$
	α-range	$0.210(9) \cdots 0.149(6)$	$0.221(13) \cdots 0.146(15)$
	$\Delta_{CF}/\,\mathrm{cm}^{-1}$	$275*$	$190*$
	$A_{CF}/\,\mathrm{s}^{-1}$	$3.22(12)\cdot 10^{10}$	$2.61(8)\cdot 10^{8}$
	$\Delta_{vib}/\,\mathrm{cm}^{-1}$	$62(2)$	$47.8(9)$
	$A_{vib}/\,\mathrm{s}^{-1}$	$7.0(13)\cdot 10^{4}$	$1.58(13)\cdot 10^{4}$
1000 Oe	fittable T-range	$11 \cdots 30\,\mathrm{K}$	$10 \cdots 26\,\mathrm{K}$
	α-range	$0.304(11) \cdots 0.142(4)$	$0.24(2) \cdots 0.131(16)$
	$\Delta_{CF}/\,\mathrm{cm}^{-1}$	$275*$	$190*$
	$A_{CF}/\,\mathrm{s}^{-1}$	$3.30(10)\cdot 10^{10}$	$2.67(5)\cdot 10^{8}$
	$\Delta_{vib}/\,\mathrm{cm}^{-1}$	$67.7(19)$	$47.7(6)$
	$A_{vib}/\,\mathrm{s}^{-1}$	$1.5(2)\cdot 10^{5}$	$1.63(9)\cdot 10^{4}$

not at all accessible on **15@Y**, are a necessary consequence of the large discrepancy of relaxation times τ_T at very low temperatures.

The temperature dependencies of the extracted relaxation times τ_T are shown in the logarithmic plot for both compounds in fig. 4.10. In case of **15** the high-temperature relaxation curves with applied static fields are virtually congruent and thus not shown for the sake of clarity. The zero field curve of **15** could successfully be fitted to the following relaxation law:

$$\tau_T^{-1} = A_{\mathrm{CF}} \cdot \exp\left(\frac{-\Delta_{\mathrm{CF}}}{k_{\mathrm{B}T}}\right) + A_{\mathrm{vib}} \cdot \exp\left(\frac{-\Delta_{\mathrm{vib}}}{k_{\mathrm{B}T}}\right) + BT^n + C_{\mathrm{QTM}} \tag{4.3}$$

For the remaining curves, only the first two (Orbach) processes of the law were included, because the characteristic temperature range (compare fig. 4.10, left) of the Raman process and the QTM is not covered by data points. The obtained best-fit parameters are gathered in table 4.8.

Thanks to the extended frequency range of the PPMS AC data of **15**, it is the only compound in this section for which the temperature regime of the first thermal Orbach process is well described. Hence, a thermal barrier Δ_{CF} of $278\,\mathrm{cm}^{-1}$ is obtained, which is in perfect agreement with the energetic gap between magnetic ground state (KD1) and second excited state (KD3) averaged for both Dy centres ($275\,\mathrm{cm}^{-1}$) revealed by the CAS-SCF calculations. Due to this accurate agreement, Δ_{CF} was fixed to $275\,\mathrm{cm}^{-1}$ for the fits of the curves with static magnetic fields applied and for all structurally related dinuclear Dy complexes presented in this section to avoid overparametrisation and compensate the poor degree of determinateness of this process. The rate constants A_{CF} do not change at different static fields, which is in accordance with the expectation for an Orbach process via crystal field split states.

At the same time, the second Orbach process necessary to reproduce the experimental data features a thermal barrier Δ_{vib} of only $53\,\mathrm{cm}^{-1}$ ($H_{\mathrm{DC}}{=}0$), which is considerably below the smallest energetic gap between calculated Kramers doublets. Therefore, the process can be identified as vibrational mode correlated relaxation of magnetisation (VMCRM). The thermal barrier as well as the rate constants A_{vib} grow with increasing H_{DC}. Interestingly, this very trend does not occur in **15@Y**, so field dependence might be related to the interplay between the two magnetic centres. For the Raman process in the zero field curve of **15** n was fixed to 5, because its characteristic temperature range is only partially covered by data points. Aided by the direct relaxation-determined τ_T-values at very low temperatures, a minor QTM rate C_{QTM} of $0.003\,\mathrm{s}^{-1}$ was found.

Attempting to fit the curves of **15@Y** using $\Delta_{\mathrm{CF}} = 275\,\mathrm{cm}^{-1}$ entirely failed. However, when fixing the CAS-SCF calculated, averaged energetic gap between KD1 and KD2 ($190\,\mathrm{cm}^{-1}$), good fits were obtained. So obviously, the interplay between the two magnetic Dy centres enforces a thermal relaxation via the second excited KD, while an isostructural monodysprosium complex only needs to overcome the first excited KD for thermal relaxation. This can clearly be evaluated as a cooperative effect, which is beneficial for SMM behaviour. The VMCRM-related Orbach process is comparable to the one found for **15** in zero field and shows much less field dependence, as was already mentioned. Although, Raman process and QTM cannot be determined for **15@Y**, the inaccessibility of direct relaxation measurement at very low temperatures hints, that their

rate constants are significantly higher as compared to the ones of **15**.
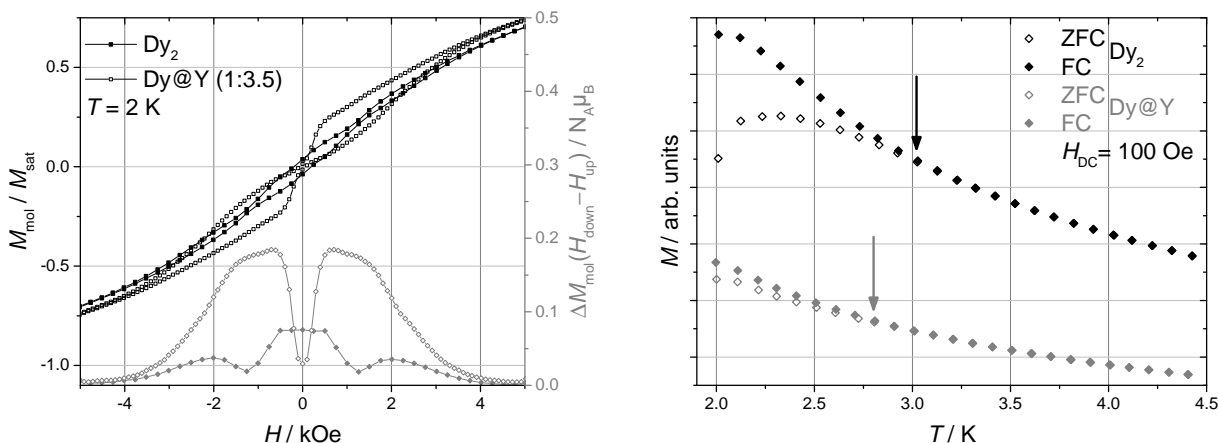
Figure 4.11: Left: Hysteresis curves of **15** and **15@Y** at 2 K, the grey curves illustrate the difference between the curve with decreasing magnetic field and the curve with increasing magnetic field. **Right:** Zero field-cooled and field-cooled temperature dependence of the magnetisation of **15** (black) and **15@Y** (grey) upon slow warm-up with a static magnetic field H_{DC}=100 Oe applied.

This presumption is further evidenced by magnetic hysteresis and ZFC measurements shown in fig. 4.11. In the ZFC at $H_{DC} = 100$ Oe the coalescence of the curves occurs clearly below 3 K for **15@Y** and somewhat above 3 K for **15**, while the spreading of both curves is much broader for the latter. Hence, a blocking temperature T_B of about 3 K can be proclaimed for **15**. It shows open hysteresis at 2 K and zero magnetic field. In contrast, the 2 K hysteresis curve of **15@Y** nearly entirely collapses at zero field, although its opening is wider at weak fields approaching zero (maximum at 500 Oe). This collapse is caused by QTM in the absence of magnetic fields, which is obviously effectively blocked in the exchange-coupled dinuclear complex **15**, which instead shows a minimum at 1250 Oe.

Such an effect was described for several dinuclear Dy complexes and is sometimes called exchange-biasing.[186,188,191,192,292] However, due to the complex nature of magnetic exchange in case of lanthanoid ions this effect cannot easily be quantified but requires complex multimethod investigations.[186,292] A magnetic field of about 1000 Oe effectively disrupts the exchange-bias caused blocking of QTM. A first step towards deeper insight into the interconnection between magnetic exchange and relaxation has already been made by single-crystal micro-SQUID hysteresis measurements at various temperatures (also below 2 K) and magnetic field sweep rates (see fig. B.4) carried out by Marko Damjanović.[293] Further investigations, like multiband ESR experiments are desirable to clarify this mechanism.

Against the background of this well characterised and performing SMM **15** as archetypal congener, the magnetism of the structurally related dinuclear Dy complexes is subsequently discussed, before possible chemical and structural correlations to the magnetic behaviour are concluded.

[Dy$_2$(H$_2$saltag^{Br})$_2$(dmf)$_4$]·2 DMF   (**16**)

As was already detailed, the main features distinguishing **16** from **15** are the higher local symmetry around the Dy centres and the crystallographic C_2 axis in the molecule making both Dy ions symmetry equivalent. Hence, possible differences in magnetic behaviour should mainly arise from these findings. Unfortunately, for **16** no *ab-initio* calculations are available yet, so that from the temperature dependence of the DC susceptibility (fig. B.5) no further insight can be obtained.

At first sight, the AC magnetic susceptibility data of **16** (fig. B.6) looks similar to **15**, χ'' at very low temperatures is close to zero in the absence of static magnetic fields and at $H_{DC} = 400$ Oe, which is indicative of low QTM operative. Again, a static field of 1000 Oe gives rise to increased relaxation in this very temperature regime. This trend is also reflected by the significantly larger α-parameters for $H_{DC} = 1000$ Oe at temperatures below 10 K (see 4.9) obtained from the fits of τ_T. Notwithstanding, the overall fittable range starts at lower temperatures and the α-parameters are much smaller as compared to the results for **15**. This finding appears reasonable, because relaxation should be more uniform in the two symmetry-related Dy centres. Direct relaxation measurement was successful at zero field from 2 to 3 K.
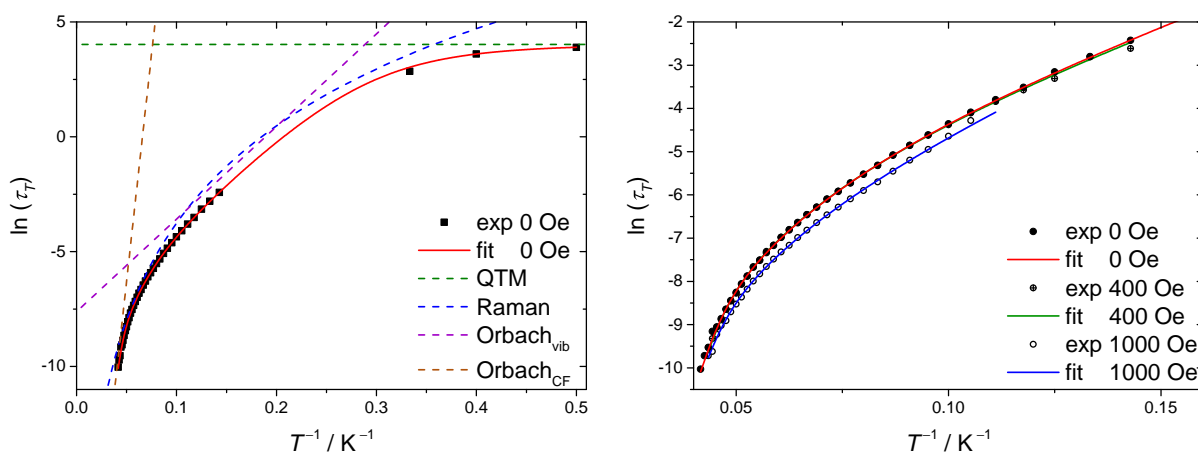
Figure 4.12: Logarithmic plot of the relaxation time τ_T of **16** at zero static field (**left**) and at different static magnetic fields H_{DC} (**right**) against T^{-1}. The corresponding fits of the relaxation behaviour to the multiprocess relaxation law given in eq. 4.3 yielded the parameters given in table 4.9 and are drawn as solid lines. The dashed lines in the left graph illustrate the discrete relaxation processes also revealing the temperature range, in which they are dominant, respectively.

A logarithmic plot of the temperature dependence of τ_T given in fig. 4.12 illustrates the best fits of the relaxation curves to eq. 4.3, whose parameters are listed in table 4.9. For $H_{DC} = 0$ Oe, all processes could be parametrised, but the thermal Orbach process is only marginally determined, so that Δ_{CF} was fixed to 275 cm^{-1} (alike for the other fields). At applied static magnetic fields, no QTM was included and n of the Raman process was fixed to the value of 6.11 obtained from the zero field fit due to deficient coverage by data points. In comparison to **15**, the crystal field state-related Orbach process is somewhat more dominant in the relaxation, which is indicated by A_{CF} being one order of magnitude larger.

Table 4.9: Collection of Debye model fittable temperature ranges and alpha parameters from the AC magnetic susceptibility measurements on **16** at different static magnetic fields H_{DC} applied as well as parameters extracted from fits of the temperature dependence of the corresponding magnetic relaxation times τ_T to the multiprocess relaxation law given in eq. 4.3. Fixed parameters are marked with an asterisk.

H_{DC}	0 Oe	400 Oe	1000 Oe
fittable T-range (AC sus.)	$7 \cdots 23$ K	$7 \cdots 23$ K	$9 \cdots 23$ K
fittable T-range (dir. rel.)	$2 \cdots 3$ K	-	-
α-range (AC sus.)	$0.150(8) \cdots 0.056(13)$	$0.110(8) \cdots 0.06(11)$	$0.299(13) \cdots 0.04(10)$
α-range (dir. rel.)	$0.125(6) \cdots 0.064(5)$	-	-
$\Delta_{CF}/$ cm^{-1}	275*	275*	275*
$A_{CF}/$ s^{-1}	$2.12(12) \cdot 10^{11}$	$2.34(14) \cdot 10^{11}$	$2.3(2) \cdot 10^{11}$
$\Delta_{vib}/$ cm^{-1}	28.0(8)	27.3(8)	34(3)
$A_{vib}/$ s^{-1}	$2.0(2) \cdot 10^{3}$	$1.9(2) \cdot 10^{4}$	$8(2) \cdot 10^{4}$
$B/$ s^{-1}K^{-n}	$3.4(2) \cdot 10^{-5}$	$3.25(5) \cdot 10^{-5}$	$4.15(18) \cdot 10^{-5}$
n	6.11(2)	6.11*	6.11*
$C_{QTM}/$ s^{-1}	0.0180(3)	-	-

At the same time, the VMCRM-related Orbach process is subordinate with a rate constant A_{vib}, which is one order of magnitude lower and a minor thermal barrier Δ_{vib} around 30 cm^{-1}. While the barrier remains roughly the same, its rate constants mrkedly grows with increasing magnetic field. The rate constant B for the Raman process is a bit lower for **16** than in **15**, however these cannot be compared directly because of different temperature dependence n. Nevertheless the fit results suggest, that the relaxation pathways related to the vibrational structure of the material (VMCRM and Raman) are less influential in **16** compared to **15**. This is in accordance with the higher local and molecular symmetry of **16**, which should reduce available vibrational modes.

By contrast, the QTM rate C_{QTM} in **16**, which was only obtained for zero field, is one order of magnitude larger than in **15**. This result is further reflected by the ZFC measurement, which does not show opening between FC and ZFC above 2 K, as well as the absence of magnetic hysteresis at 2 K. Obviously the QTM suppression via exchange biasing is less effective in this compound.

This presumption is rather hard to rationalise, because detailed insight into the magnetic exchange is not at hand so far. Merely, the larger intersecting angle between the lines through the phenolate-O donors $\angle$O–O$_{Dy1}$ - O–O$_{Dy2}$ of 62.3° (60.9° in **15**) supplies a structural hint, that magnetic exchange might be less beneficial in **16**. However, easy axes of magnetisation calculated via *ab-initio* methods provide a more reliable basis for such estimations.

[Dy$_2$(H$_2$saltag^{Br})$_2$(py)$_4$] · H$_2$O · py (17)

For complex **17**, which contains N-donor pyridine coligands instead of DMF, the temperature dependence of the DC susceptibility of **17** is shown in fig. B.7, but again, no *ab-initio* calculations of the compound are available yet. Thus, no information about magnetic exchange can be

extracted.

The AC susceptibility curves (fig. B.6) look similar to the ones of **15** except for a slight shoulder at H_{DC} = 0 Oe and 400 Oe, which indicates that two separate relaxations are operative. These distinct relaxations also become visible in the Cole-Cole plots for the respective fields starting from 24.5 K (0 Oe) and 20 K (400 Oe), which are therefore shown separately in fig. B.8. Since a simultaneous fit of both processes was not successful, only the process shifted to higher χ'-values was fitted and the data points with χ' below the maximum of the semicircle were not considered from the mentioned temperature on.
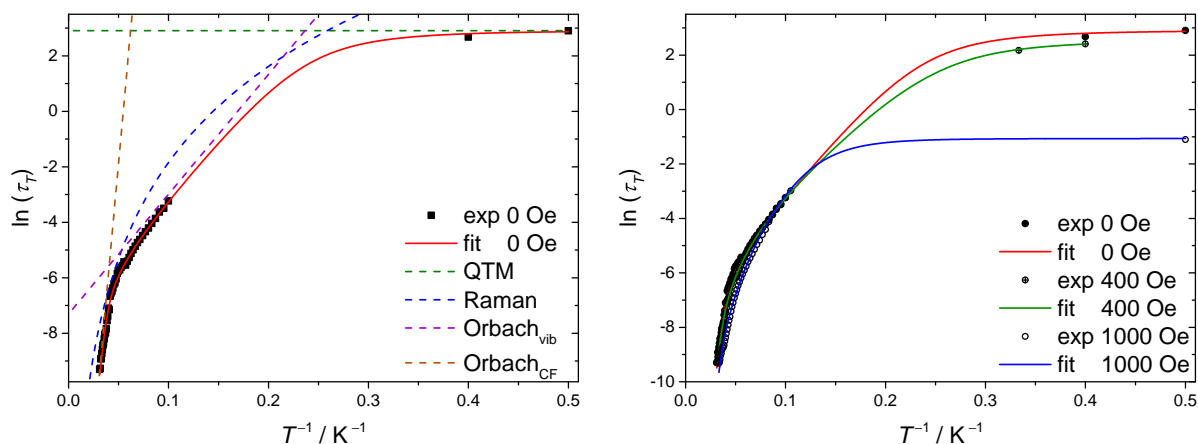
Figure 4.13: Logarithmic plot of the relaxation time τ_T of **17** at zero static field (**left**) and at different static magnetic fields H_{DC} (**right**) against T^{-1}. The corresponding fits of the relaxation behaviour to the multiprocess relaxation law given in eq. 4.3 yielded the parameters given in table 4.10 and are drawn as solid lines. The dashed lines in the left graph illustrate the discrete relaxation processes also revealing the temperature range, in which they are dominant, respectively.

Table 4.10: Collection of Debye model fittable temperature ranges and alpha parameters from the AC magnetic susceptibility measurements on **17** at different static magnetic fields H_{DC} applied as well as parameters extracted from fits of the temperature dependence of the corresponding magnetic relaxation times τ_T to the multiprocess relaxation law given in eq. 4.3. Fixed parameters are marked with an asterisk.

H_{DC}	0 Oe	400 Oe	1000 Oe
fittable T-range (AC sus.)	$10 \cdots 32$ K	$9.5 \cdots 31$ K	$12 \cdots 30$ K
fittable T-range (dir. rel.)	$2 \cdots 2.5$ K	$2.5 \cdots 3$ K	2 K
α-range (AC sus.)	$0.066(7) \cdots 0.176(8)$	$0.074(9) \cdots 0.204(9)$	$0.249(13) \cdots 0.104(15)$
α-range (dir. rel.)	$0.429(2) \cdots 0.389(5)$	$0.497(6) \cdots 0.41(2)$	$0.705(13)$
Δ_{CF} / cm^{-1}	275*	275*	275*
A_{CF} / s^{-1}	$2.5(2) \cdot 10^9$	$2.10(15) \cdot 10^9$	$4.0(8) \cdot 10^9$
Δ_{vib} / cm^{-1}	30(2)	25(3)	-
A_{vib} / s^{-1}	$1.4(5) \cdot 10^3$	$5(2) \cdot 10^2$	-
B / s^{-1}K^{-n}	$6.3(11) \cdot 10^{-5}$	$1.17(7) \cdot 10^{-4}$	$7(2) \cdot 10^{-5}$
n	5*	5*	5.44(10)
C_{QTM} / s^{-1}	0.055(3)	0.079(12)	2.9*

The occurrence of two separate relaxations appears reasonable for two aspects. First, the

structural difference between both Dy centres in **17** is somewhat larger as compared to **15** (compare table 4.16) and second, the α-parameters obtained over the whole fittable temperature range (see table 4.10) are a lot smaller than the ones in **15**. So the possible presence of two distinct relaxations may be swallowed by the broad dispersion of the AC data in **15**, while it is partially resolved in the more precise data of **17**. If these two relaxations are interpreted as separate relaxations of the two Dy centres, this means that above the split temperature for $H_{DC} = 0\,\text{Oe}$ and $400\,\text{Oe}$ only one Dy centre is described. Interestingly, at $H_{DC} = 1000\,\text{Oe}$ the splitting cannot be recognised, which is probably due to the increased α-values. Nevertheless, thanks to the overall low α-parameters for all three fields the fittable temperature range reaches above $30\,\text{K}$. Another peculiarity is the availability of direct relaxation data at around $2\,\text{K}$ for all three static fields.

The temperature dependence of τ_T as shown in fig. 4.13 was fitted to the relaxation law given in eq. (4.3) for all three static fields H_{DC}. Again, the thermal barrier Δ_{CF} for the crystal field related Orbach process was fixed to $275\,\text{cm}^{-1}$, which leads to very good agreement with the high-temperature linear area and its rate constant A_{CF}, as expected, shows no field dependence. Interestingly, it is one order of magnitude smaller than what is found for **15**.

In contrast, switching the static field from 0 to $400\,\text{Oe}$ shrinks the rate constant of the VMCRM-related Orbach process A_{vib} by one order of magnitude. Also the thermal barrier Δ_{vib} is reduced. For the curve at $H_{DC} = 1000\,\text{Oe}$ it is no longer necessary to include this process. This is an opposite trend to what is found for **15**, but has to be considered with caution, because under applied static fields, Raman and QTM process were not described for **15**. Notwithstanding, even at zero field and thus comparable nature of the fits, the rate constant A_{vib} in **17** is one order of magnitude smaller than in **15**. A structural explanation for this result might be the exchange of DMF coligands, which feature e.g. rotatable methyl groups, by pyridine coligands, which are two-dimensional rings with higher point symmetry and less vibrational degrees of freedom.

For $1000\,\text{Oe}$ it was necessary to fit the temperature coefficient n of the Raman process, which was fixed to 5 for the $0\,\text{Oe}$ and $400\,\text{Oe}$ due to poor data point coverage of its regime, to achieve a reasonable fit. The obtained corresponding rate constant B at zero field is comparable to the one in **15**.

Eventually, the rate constant for QTM C_{QTM} is alike for $0\,\text{Oe}$ and $400\,\text{Oe}$, but significantly larger at $1000\,\text{Oe}$ (where it was manually fixed to the value of the single direct relaxation data point at $2\,\text{K}$, which otherwise would have been discriminated by the fit routine). This is in accordance with the findings for the previous dinuclear Dy complexes. However, also at the lower fields C_{QTM} is one order of magnitude larger as compared to **15**, which this time cannot be explained with the intersecting angle $\angle\text{O–O}_{Dy1}$ - O–O_{Dy2} of $59.9°$, because this should be more beneficial for magnetic interaction (compare $60.9°$ for **15**). Instead, with the N-donor atoms additional nuclear spins are brought into the immediate environment of the Dy centre, which are known to enhance QTM.[182–184]

Higher QTM rates are once again confirmed by the absence of magnetic hysteresis at $2\,\text{K}$. The curve drawn in fig. 4.14 was recorded with a discontinuous measuring sequence directly jumping from $10\,\text{kOe}$ to $2\,\text{kOe}$ and can therefore not be compared with other hysteresis curves
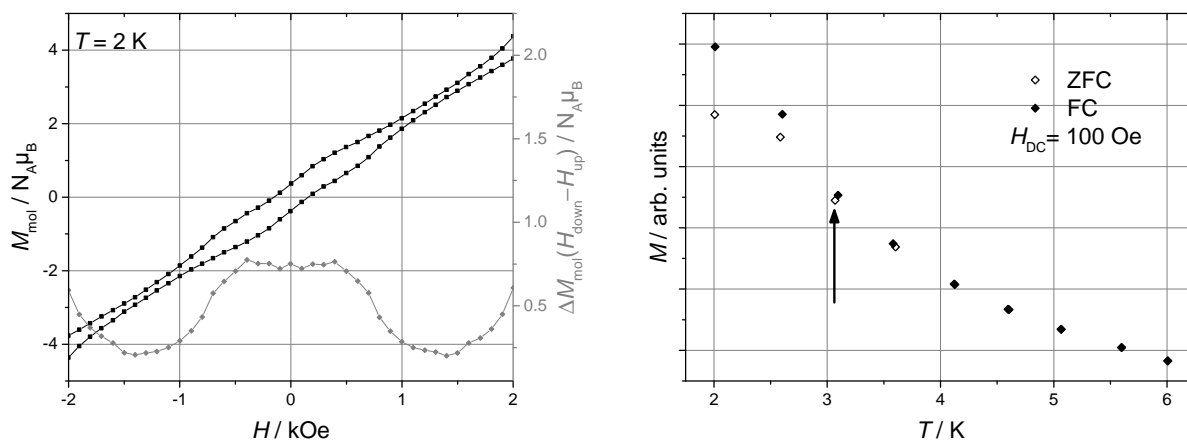
Figure 4.14: Left: Hysteresis curve of **17** at 2 K, the grey curves illustrate the difference between the curve with decreasing magnetic field and the curve with increasing magnetic field. Mind that this hysteresis curve is recorded with a very discontinuous measuring sequence directly jumping from 10 kOe to 2 kOe and can therefore not be compared with other hysteresis curves in this section. **Right:** Zero field-cooled and field-cooled temperature dependence of the magnetisation of **17** upon slow warm-up with a static magnetic field H_{DC}=100 Oe applied.

in this section. Withal, it nicely shows the magnetic field driven collapses in the hysteretic behaviour with a minimum at 1500 Oe, which is slightly higher than in **15** and therefore suggests, that exchange biasing is somewhat stronger in complex **17**.

The ZFC measurement, also shown in fig. 4.11, indeed exhibits a minor fission of the curves uniting at about 3 K, however, the density of data points is lower than in the corresponding measurement for **15**, so that the actual blocking temperature of **17** is probably below 3 K.

[Dy$_2$(H$_2$saltag^{Br})$_2$(MeOH)$_4$] (18)

For compound **18**, which bears MeOH coligands, the temperature dependence of the magnetic DC susceptibility is shown in fig. B.10 but not further processed in lack of *ab-initio* calculations.

AC susceptibility data of **18** (see fig. B.11) shows the same principal trends as the other dinuclear Dy complexes already discussed, but the temperature-shifted maxima of the different frequencies are rather flat. Especially the χ'' component at very low temperatures has significantly increased even at zero field H_{DC}, which is a hint that more QTM is operative than in the other dinuclear complexes.

Over the whole fittable temperature range (see table 4.11) the highest α-parameters among all dinuclear Dy complexes presented in this work are found. Consequently, no very low-temperature data via direct relaxation measurements is available. Furthermore, the extracted τ_T values have to be taken with caution, since α represents not only the dispersion broadness of the relaxation, but can also be interpreted as a measure for the preciseness of the fitted relaxation time.[294]

Fitting the extracted τ_T-values to the relaxation law given in eq. (4.3) yielded the relaxation
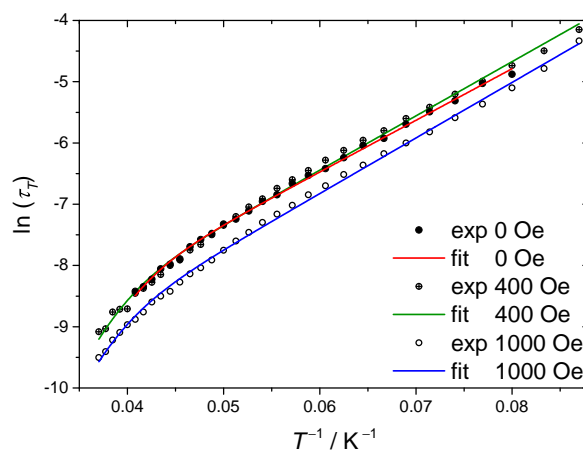
Figure 4.15: Logarithmic plot of the relaxation time τ_T of **18** at different static magnetic fields H_{DC} against T^{-1}. The corresponding fits of the relaxation behaviour to the multiprocess relaxation law given in eq. 4.3 yielded the parameters given in table 4.11 and are drawn as solid lines.

Table 4.11: Collection of Debye model fittable temperature ranges and alpha parameters from the AC magnetic susceptibility measurements on **18** at different static magnetic fields H_{DC} applied as well as parameters extracted from fits of the temperature dependence of the corresponding magnetic relaxation times τ_T to the multiprocess relaxation law given in eq. 4.3. Fixed parameters are marked with an asterisk.

H_{DC}	0 Oe	400 Oe	1000 Oe
fittable T-range (AC sus.)	$12.5 \cdots 24.5\,\mathrm{K}$	$11.5 \cdots 27\,\mathrm{K}$	$11.5 \cdots 27\,\mathrm{K}$
α-range (AC sus.)	$0.387(13) \cdots 0.24(2)$	$0.401(12) \cdots 0.181(18)$	$0.502(18) \cdots 0.194(15)$
$\Delta_{CF}/\,\mathrm{cm}^{-1}$	275*	275*	275*
$A_{CF}/\,\mathrm{s}^{-1}$	$1.66(18){\cdot}10^{10}$	$1.19(13){\cdot}10^{10}$	$1.61(13){\cdot}10^{10}$
$\Delta_{vib}/\,\mathrm{cm}^{-1}$	58.6(7)	61.6(10)	63.1(7)
$A_{vib}/\,\mathrm{s}^{-1}$	$1.02(6){\cdot}10^{5}$	$1.28(11){\cdot}10^{5}$	$2.13(13){\cdot}10^{5}$

curves drawn in fig. 4.15 and the parameters collected in table 4.11. Owing to the very limited range of data points QTM and Raman process are not described at all and thus left out. For the crystal field state-related Orbach process the thermal barrier Δ_{CF} was again fixed to $275\,\mathrm{cm}^{-1}$, although admittedly the temperature regime of this process is almost uncovered by data points. Nevertheless, rate constants A_{CF} comparable to the ones of **15** were obtained.

The VMCRM-related Orbach process in **18** exhibits similar thermal barriers Δ_{vib} as in **15** at all static fields H_{DC}, but the corresponding rate constants $A_{vib}/\,\mathrm{s}^{-1}$ are one order of magnitude higher. This might be related to the more flexible MeOH coligand, which, in comparison with DMF, brings a rotatable methyl group in closer proximity to the Dy centres.[143,173]

Despite the lack of relaxation data at very low temperatures, the absence of magnetic hysteresis and curve splitting in the ZFC measurements suggest large QTM rates. Considerations that the MeOH coligands approach additional protons bearing nuclear spins are one part of a possible explanation. However, also the supramolecular dimer formation via H bonds (compare fig. 4.8) leading to possible magnetic interaction with another Dy centre might perturb the exchange biasing, which suppresses QTM in the other dinuclear congeners. Overall, compound

18 must be evaluated as the worst performing SMM among the complexes presented in this section.

4.2.4 Concluding Remarks

Reviewing the results of this section it stands out, that for the actual performance of the discussed compounds as SMMs, the structural features governing the local anisotropy of the individual Dy centres are only one part of a very complex picture. The great advantage of this survey is the structural similarity of all four compounds presented, so that differences in the low energy spectrum of states are minor as compared to other aspects discussed hereinafter. This is supported by the viability of a fixation of the crystal field state-related thermal barrier Δ_{CF} to one and the same value for the description of all four compounds' magnetic relaxation.

The main influential differences among the congeners occur between molecular symmetry, chemical nature of the donor solvent based coligands and magnetic exchange interaction. Since the latter is hard to profoundly rationalise at the present state of investigations on the complexes, one simply has to accept for now, that magnetic exchange interaction is most beneficial for SMM behaviour in **15**, especially regarding the suppression of QTM via exchange biasing. It is therefore the best performing SMM among this series at very low temperatures and exhibits the highest blocking temperature.

However, when moving into higher temperature regimes, this picture changes. The relaxation mechanisms related to the vibrational structure of the material, namely Raman relaxation and VMCRM, are also important aspects of under-barrier relaxation, which can be considered the Achilles heel of lanthanoid-based SMMs.[143,174,175] These processes are significantly less developed in **16** and **17**, which can be attributed to higher molecular and possibly also local symmetry for the former and probably to more rigid pyridine coligand featuring higher point symmetry for the latter. When further comparing (e.g. **15@Y** for best comparability) with the results obtained for the mononuclear compounds described in section 4.1 (table 4.2) it obtrudes that the higher rigidity of the saltag^{Nph} ligand leads to a more effective suppression of these processes.

Eventually, from compound **18** one can learn, that MeOH is an unfavourable coligand due to its rotatable and protic nature and additional magnetic interactions beyond the dinuclear arrangement are disadvantageous with respect to SMM behaviour.

Now ranking these dinuclear exchange-coupled Dy complexes among comparable recent literature examples[191,292] they position in the upper third in terms of apparent thermal barriers, but feature extraordinarily low contributions of Raman and VMCRM processes especially as compared to the frontrunner compounds.[191,194,292] This is in agreement with the fact, that those compounds feature ligand backbones with various aliphatic groups incorporated, which are not present in the compounds of this work.

So tag-based ligands are in principle great building blocks for dinuclear, exchange-biased, lanthanoid-based SMMs, for their ability to mediate magnetic exchange, the possibility to provide high molecular symmetry and the suppression of vibrational structure related relaxation pathways. However, aiming for higher blocking temperatures, especially the local anisotropy

of the individual Dy centres has to be improved tremendously, which requires different design approaches than the ones realised in this section.

Notwithstanding, a brief vision on how to optimise the present systems in conclusion of this section be permitted. For better SMM behaviour, the complex molecule should have C_2 symmetry, which is the highest that can be provided in this structure motif, but, of course, can scarcely be enforced by chemical design. Ideally, the saltag^{Br} ligand is replaced by the saltag^{Nph} ligand and the solvent coligand is changed to an aprotic O-donor incorporated in a rigid cyclic system with high point symmetry. Of course, furan would immediately occur to one's mind, but given its neglectable donor strength it is no real candidate. Instead, with some clairvoyance of the forthcoming chapter, phthalan might be the perfect coligand for optimising SMM-behaviour in this system and can even be used as a component in a solvent mixture.

4.3 Trinuclear Lanthanoid Complexes

4.3.1 Synthesis and Characterisation

In general, the synthesis of trinuclear tag-based lanthanoid complexes requires two equivalents of the chelate ligand (L) and three equivalents of a suitable Ln(III) precursor to form complexes of the general composition $[Ln_3L_2]$. In spite of synthetic efforts with various tag-based ligands, in the frame of this work crystals of such complexes could exclusively be isolated with the halogen-substituted saltag ligands $H_5saltag^{Br} \cdot HCl$ and $H_5saltag^I \cdot HCl$. To bind three trivalent lanthanoid ions, full deprotonation of the saltag ligand is advantageous, thus for all syntheses presented in this section at least twelve equivalents of a base were used. Besides, it turned out to be practical to use a slight excess of the lanthanoid precursor.

Combining these concepts should lead to monoanionic complexes. However, corresponding reaction of $DyCl_3 \cdot 6 H_2O$ with $H_5saltag^{Br} \cdot HCl$ and NEt_3 in MeOH yields $[Dy_3(H_{0.5}saltag^{Br})_2(MeOH)_6] \cdot 3.5 MeOH$ (**19**). Elemental analysis, ESI mass spectrometry, IR spectroscopy and single-crystal x-ray diffractometry confirm this somewhat unexpected composition and contain no hint for the presence of a counteranion. Indeed, in the negative mode ESI-MS in MeOH the complex can be detected in its monoanionic form, but the spectrum in positive mode is silent. Hence, the counterbalancing positive charge has to be provided by one remaining proton statistically distributed among the two chelate ligands of the complex.

Eventually, modifying the synthesis by changing the chelate ligand to $H_5saltag^I \cdot HCl$, increasing the excess of NEt_3 and adding the spatial demanding, weakly coordinating bis-triphenylphosphine-iminium (PPN^+) cation leads to the formation of $PPN[Dy_3(saltag^I)_2(MeOH)_5] \cdot 5 MeOH$ (**20**). This compound clearly consists of a complex monoanion $[Dy_3(saltag^I)_2(MeOH)_5]^-$ and the PPN^+ cation, however, it is very sensitive to loss of the cocrystallised MeOH as well as the MeOH coligands and their exchange with water under air, which is also reflected by the elemental analysis. Attempts to follow this synthetic route with different weakly coordinating countercations providing a higher point symmetry such as tetraphenylphosphonium, methyltriphenylphosphonium and several methylated pyridinium derivatives were unsuccessful within the frame of this work.

Instead of separate addition of a countercation, switching the base to a molecule whose protonated form is more suitable for crystallisation than $HNEt_3^+$ is another synthetic approach followed. Along this line, the usage of 4-dimethylaminopyridine (DMAP) together with dysprosium trifluoromethanesulphonate ($DyOTf_3$) and $H_5saltag^I \cdot HCl$ in MeOH proved very successful, whereat the velocity of crystal growth and thus their final size can be controlled to some extent by means of the stoichiometry of DMAP added.

For the obtained compound $(H_{0.5}DMAP)_2[Dy_3(saltag^I)_2(MeOH)_6] \cdot 2 MeOH$ (**21**) again the nature of the counteranion remains somewhat in question. Although DMAP is present in the compound, there are two symmetry equivalent DMAP molecules per complex, as revealed by single-crystal X-ray diffractometry, among which the proton would have to be distributed statistically. So also the statistic protonation of the chelate ligands as found for **19** is an option, the question will be further discussed together with the crystal structure of **21**. Once more, the use

of bases potentially providing countercations with higher point symmetry like tribenzylamine and triphenylguanidine did not provide crystalline complexes so far.

The synthetic approaches presented hitherto all rely on MeOH as a solvent, which also acts as a coligand for the vacant coordination sites. As was explained in the introduction and also confirmed in the previous section 4.2, protic coligands in general and MeOH in particular are a rather disadvantageous with respect to magnetic relaxation. Unfortunately, complementary to the synthetic findings for dinuclear tag-based lanthanoid complexes, the presence of a protic solvent is prerequisite for the synthesis of trinuclear compounds derived from the synthetic studies in the frame of this work. This can most probably be related to better stabilisation of anions released by the lanthanoid precursors and possible anionic intermediate states of the saltag ligands as compared to aprotic solvents. The prior described syntheses are extremely sensitive to changes in the solvent system, comparable compounds could not be isolated using higher alcohols or even deuterated methanol. At the same time, the affinity of lanthanoid ions to alcohol O-donors is higher than to most common aprotic donor solvents, so the synthesis of a saltag-based trinuclear lanthanoid complex with aprotic coligands is challenging.

A fortiori the successful isolation of $[Dy_3(H_{0.5}saltag^I)_2(thf)_6]$ (**22**) from a solvent mixture of THF and 1,3-propanediol using DMAP as a base is a remarkable result. Here, 1,3-propanediol is a protic solvent very suitable for anion binding due to its ability to provide a chelate-like multivalent H bonding. At the same time, it appears that it cannot bind as a chelate coligand to the vacant coordination sites of the trinuclear $[Dy_3saltag^I)_2]^-$ unit, because the Dy centre demands large spreading angles between the two coligands (>125° for all compounds described in section 4.2), so that THF preferentially acts as a coligand.

This compound also features the somewhat problematic countercation question. Its composition represented as $[Dy_3(H_{0.5}saltag^I)_2(thf)_6]$ is what can be derived from the single-crystal X-ray diffractometry. However, the solved structure exhibits significant but disperse residual electron density in the periphery of the complex molecule. Besides, the elemental analysis strongly suggests the presence of $\frac{2}{3}$ of a $HDMAP^+$ countercation per complex molecule, which would necessitate a partial statistical occupation of certain crystallographic positions. A moderately sharp IR band at $3300\,cm^{-1}$ in the putative absence of hydroxyl groups can be interpreted as a corresponding N–H-valence vibration, which further supports the presence of the $HDMAP^+$ countercation, although similar bands can be caused by a proton bound to N-donors of the chelate ligand. Possibly, the picture can be clarified by means of higher resolution synchrotron X-ray diffraction data.

Against the background of their facile synthetic accessibility, isostructural complexes to **20** and **21** were synthesised for all late lanthanoid ions starting from Gd (except Tm). Due to their low relevance for the scope of this work they are not further discussed. However, isostructural Y and Lu complexes are resumed along with the discussion of magnetic properties, since they are exploited as a matrix for diamagnetic dilution of the Dy congeners.

4.3.2 Crystal Structures

For all compounds discussed in this section single-crystal X-ray diffractometry revealed crystal and molecular structures discussed in here. A sandwich-like arrangement of the two saltag ligands with all three Dy centres bound interjacently is equally found in the four compounds. The two tag planes are nearly parallel, but the phenol moieties are tilted out of these planes, so that the phenolate O-donors in first approximation form a third plane together with the three Dy centres lying almost parallel in between the two tag planes. Hence, all three Dy centres are bridged with both neighbouring ions via two N–N diazine moieties, respectively, forming a triangle. This alignment is stabilised by pairwise intramolecular $\pi \cdots \pi$-interactions between all six phenolate moieties, respectively, and very similarly found in the complex (anion) of all four compounds presented.

The local environment of the Dy sites is preponderantly analogous to what is described for the dinuclear lanthanoid complexes in section 4.2. The following discussion of the individual compounds is therefore limited to highlighting differences related to the coligands, the periphery of the complexes, the crystal symmetry and other unique features.

Particular attention is paid to the phenolate O-donors, which continuously exhibit the shortest bonds with the Dy centres and therefore in first approximation govern the orientation of the easy axis of magnetisation of the single ions in the magnetic ground state as was shown by *ab-initio* calculations.[272]

[Dy$_3$(H$_{0.5}$saltag^{Br})$_2$(MeOH)$_6$] · 3.5 MeOH   (19)

Crystals of **19** exhibit the triclinic space group $P\bar{1}$ (#2), accordingly the putative neutral complex [Dy$_3$(H$_{0.5}$saltag^{Br})$_2$(MeOH)$_6$] (depicted in fig 4.16) contains three crystallographically independent Dy centres, whose [N$_4$O$_4$] donor environments are described by means of bond lengths and characteristic angles in table 4.12. The closest congruency with an ideal coordination polyhedron as revealed by continuous shape measures[251–253] is found with the triangular dodecahedron for all three metal sites yielding deviation parameters of 1.330 (Dy1), 0.970 (Dy2) and 1.094 (Dy3).

In comparison with its most similar dinuclear relative **18**, **19** features somewhat larger discrepancies between the trans-angles of the two phenolate O-donors (see table 4.12) but otherwise a very analogous donor environment.

The two tag planes intersect at an angle of 1.0°, their intersecting angles with the plane spanned by the three Dy (further referred to as □Dy$_3$) centres are 3.6° and 3.4°, respectively, so the deviations from parallelism are minor. As was already mentioned, the phenolate O-donors forming the shortest bonds with the Dy centres lie almost perfectly within the □Dy$_3$ plane, the average protrusion is 25 pm with the largest value d[O$_{Ph}$–□Dy$_3$] being 42 pm (O3A).

One of each two MeOH coligands' O-donor atoms per Dy centre is involved in H bonding interactions with at least one of the cocrystallised MeOH molecules, namely O2M ($d_{O\text{-}O} = 272$ pm), O3M ($d_{O\text{-}O} = 265$ pm) and O6M ($d_{O\text{-}O} = 265$ pm). Apart from that, no intermolecular interactions are apparent from analysis of the crystal structure.
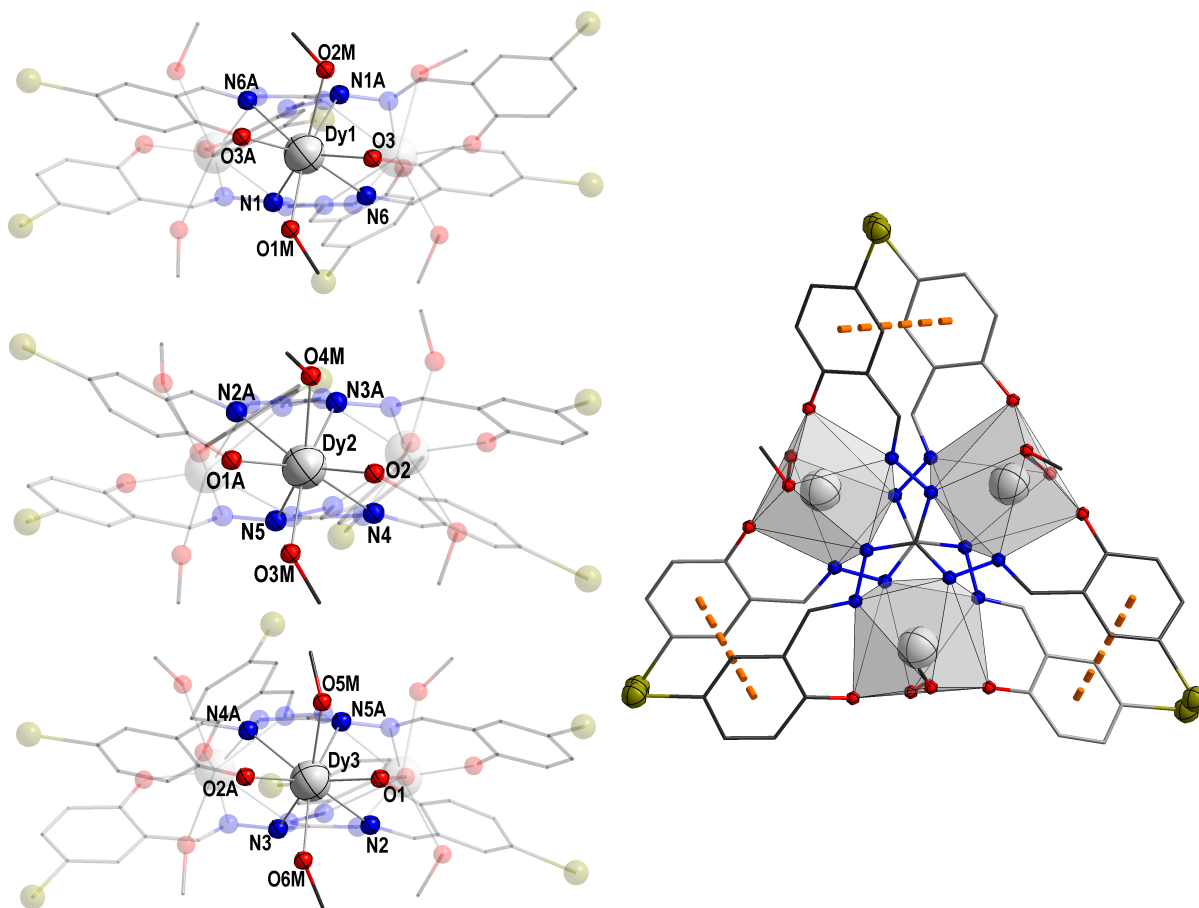
Figure 4.16: Left: Molecular structure of neutral complex [Dy$_3$(H$_{0.5}$saltag^{Br})$_2$(MeOH)$_6$] (**19**) with atom labels shown in three directions for the three crystallographically independent centres Dy1, Dy2 and Dy3. C atoms are wire nodes, Dy: light grey, N: blue, O: red, Br: dark yellow. H atoms and cocrystallised solvent molecules are omitted for clarity. Parts of the molecule not involved in the coordination of the labelled metal centres have been rendered transparent for clarity. **Right:** Illustration of the distorted square antiprism coordination polyhedra of **19**. View along the normal to the bottom tag plane (lighter grey). The orange dashed lines illustrate the intramolecular $\pi \cdots \pi$-interactions. Colour code is identical.

Table 4.12: Selected bond lengths (pm) and angles (°) from the coordination environment of Dy1, Dy2 and Dy3 in **19**. The corresponding numbering scheme is depicted in fig. 4.16.

Dy1–N1	242.93(10)	Dy2–N2A	252.58(8)	Dy3–N2	248.05(8)
Dy1–N1A	276.30(9)	Dy2–N3A	252.60(7)	Dy3–N3	245.87(7)
Dy1–N6	247.21(5)	Dy2–N4	249.82(6)	Dy3–N4A	248.38(7)
Dy1–N6A	256.04(7)	Dy2–N5	246.30(9)	Dy3–N5A	254.39(9)
Dy1–O1M	241.52(6)	Dy2–O1A	225.06(7)	Dy3–O1	219.78(6)
Dy1–O2M	247.87(7)	Dy2–O2	218.46(9)	Dy3–O2A	224.13(10)
Dy1–O3	225.93(8)	Dy2–O3M	242.86(6)	Dy3–O5M	250.25(6)
Dy1–O3A	215.58(6)	Dy2–O4M	249.08(6)	Dy3–O6M	240.74(6)
O3–Dy1–N6A	147.55(2)	O1A–Dy2–N4	156.49(2)	O1–Dy3–N4A	144.19(3)
O3A–Dy1–N6	164.43(3)	O2–Dy2–N2A	150.81(2)	O2A–Dy3–N2	153.98(2)
O3–Dy1–O3A	110.42(2)	O1A–Dy2–O3	109.23(2)	O1–Dy3–O2A	112.34(2)
O1M–Dy1–O2M	133.01(2)	O3M–Dy2–O4M	132.40(2)	O5M–Dy3–O6M	124.63(2)

PPN[Dy$_3$(saltag^I)$_2$(MeOH)$_5$] · 5 MeOH   (20)

Like the previously described compound, **20** also crystallises in triclinic space group $P\bar{1}$ (#2), therefore none of the three Dy sites in the complex anion [Dy$_3$(saltag^I)$_2$(MeOH)$_5$]$^-$ (drawn in fig. 4.17) are equivalent by symmetry. Contrariwise, in **20** one hepta-coordinated Dy centre (Dy2) significantly differs from the other two featuring coordination number eight. Corresponding bond lengths and selected angles are collected in table 4.13.

The [N$_4$O$_4$] environment of Dy1 and Dy3 is similar to what is found in **18**, however the bonding angles of the phenolate O-donors, which feature the shortest bond distances, are larger (averaged 115.9° vs. 112.7°), while the spreading angle of the O-donors of the MeOH coligands is lower (averaged 119.7° vs. 127.4°). Shape deviation parameters[251–253] of 1.655 (Dy1) and 1.180 (Dy2) are obtained for a triangular dodecahedron as ideal reference.

In case of Dy2, the [N$_4$O$_3$] donor set lacks one MeOH coligand in comparison to the other two Dy sites. A significant shortening especially of the phenolate O-donor bonding distances can be detected, which is accompanied by a rather small bonding angle O1A–Dy2–O3B of 99.3°. Presumably, this distinctly reduces the local magnetic anisotropy of Dy2. The capped octahedron was identified as closest reference polyhedron with a deviation parameter[251–253] of 1.737.

The two saltag planes as well as the □Dy$_3$ plane are nearly parallel exhibiting neglectable intersecting angles below 2°. Compared to **19** the phenolate O-donors coincide even better with the □Dy$_3$ plane. Their averaged protrusion amounts 19.3 pm, merely O1A is an outlier in that sense distanced from the plane by 70 pm.

H bonding interactions with cocrystallised MeOH molecules are present at both MeOH coligands' O-donors coordinating Dy3, being O4M ($d_{\text{O-O}} = 270$ pm) and O5M ($d_{\text{O-O}} = 285$ pm). In contrast, only one such interaction is found around Dy1 pertaining O3M ($d_{\text{O-O}} = 266$ pm) and none for the one MeOH coligand of Dy2.

An angle P–N–P of 146.0° is found in the PPN$^+$ cation, which underlines the non-allenoid nature of this moiety making it inappropriate for promoting C_3-symmetric space groups. Hence, it is not an auxiliary for inducing higher molecular symmetry, however, it is the only weakly coordinating countercation, which could successfully be incorporated in crystals of trinuclear tag-based lanthanoid complexes and thereby proves the complex to be a monoanion beyond doubt, as was already outlined in the prior subsection. At the same time, it stands out, that **20** is the most unsymmetric among the trinuclear lanthanoid complexes presented in this work. Since there is no special interaction of the PPN$^+$ countercation with the complex anion apparent from the structure, the question has to be raised whether the unsymmetric arrangement in the trinuclear complex is related to its anionic nature. Possibly, the removal of the last proton significantly varies the charge distribution in the whole [Ln$_3$L$_2$] arrangement. Anyhow, this question cannot be solved solely on the basis of structural data, but requires a targeted theoretical survey.
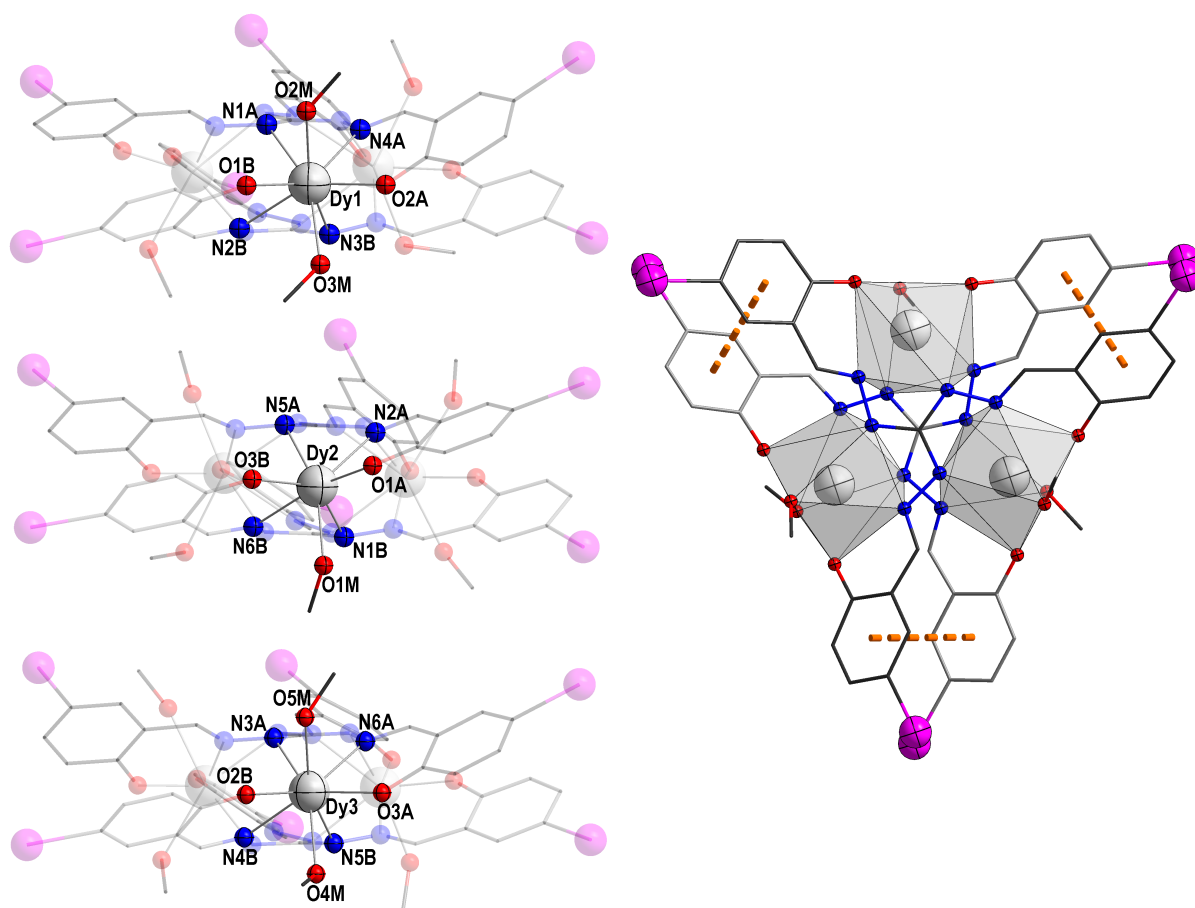
Figure 4.17: Left: Molecular structure of complex anion [Dy$_3$(saltag^I)$_2$(MeOH)$_5$]$^-$ in **20** with atom labels shown in three directions for the three crystallographically independent centres Dy1, Dy2 and Dy3. C atoms are wire nodes, Dy: light grey, N: blue, O: red, I: magenta. H atoms, countercation and cocrystallised solvent molecules are omitted for clarity. Parts of the molecule not involved in the coordination of the labelled metal centres have been rendered transparent for clarity. **Right:** Illustration of the distorted coordination polyhedra of **20**. View along the normal to the bottom tag plane (lighter grey). The orange dashed lines illustrate the intramolecular $\pi\cdots\pi$-interactions. Colour code is identical.

Table 4.13: Selected bond lengths (pm) and angles (°) from the coordination environment of Dy1, Dy2 and Dy3 in **20**. The corresponding numbering scheme is depicted in fig. 4.17.

Dy1–N1A	246.2(3)	Dy2–N1B	242.3(3)	Dy3–N3A	244.7(3)
Dy1–N2B	251.0(3)	Dy2–N2A	244.9(3)	Dy3–N4B	249.6(3)
Dy1–N3B	253.0(3)	Dy2–N5A	251.0(3)	Dy3–N5B	250.9(3)
Dy1–N4A	245.5(3)	Dy2–N6B	245.2(3)	Dy3–N6A	252.5(3)
Dy1–O1B	223.6(3)	Dy2–O1A	220.5(3)	Dy3–O2B	221.9(3)
Dy1–O2A	223.3(3)	Dy2–O3B	216.8(3)	Dy3–O3A	225.3(3)
Dy1–O2M	248.0(3)	Dy2–O1M	241.9(3)	Dy3–O4M	250.2(3)
Dy1–O3M	244.4(3)			Dy3–O5M	243.4(3)
O1B–Dy1–N4A	144.44(11)	O1A–Dy2–N6B	165.90(11)	O3A–Dy3–N4B	148.38(11)
O2A–Dy1–N2B	149.56(11)	O3B–Dy2–N2A	138.07(12)	O2B–Dy3–N6A	148.34(11)
O1B–Dy1–O2A	116.50(11)	O1A–Dy2–O3B	99.27(11)	O2B–Dy3–O3A	115.32(10)
O2M–Dy1–O3M	116.54(11)			O5M–Dy3–O4M	122.84(11)

(H$_{0.5}$DMAP)$_2$[Dy$_3$(saltag$^\text{I}$)$_2$(MeOH)$_6$] · 2 MeOH (21)

In compound **21** a higher crystal symmetry as compared to the previous trinuclear complexes, namely monoclinic space group $C2/c$ (#15), is found. The corresponding C_2 axis runs through one of the three Dy centres in the probable [Dy$_3$(saltag$^\text{I}$)$_2$(MeOH)$_6$]$^-$ complex anion making the two remaining Dy sites symmetry-equivalent, which is illustrated in fig. 4.18. Bond lengths and selected angles of the corresponding donor environments are listed in table 4.14.

Table 4.14: Selected bond lengths (pm) and angles (°) from the coordination environment of Dy1 and Dy2 in **21**. The corresponding numbering scheme is depicted in fig. 4.18. Symmetry generated equivalent atoms are marked with '$(1-x, y, \frac{3}{2}z)$.

Dy1–N2	251.4(2)	Dy2–N1	255.9(2)
Dy1–N5	253.1(2)	Dy2–N3	252.6(2)
Dy1–O1	219.3(2)	Dy2–N4	253.5(2)
Dy1–O4	243.4(2)	Dy2–N6	250.1(2)
		Dy2–O2	218.2(2)
		Dy2–O3	223.1(2)
		Dy2–O5	245.0(2)
		Dy2–O6	242.7(2)
O1–Dy1–N2'	150.87(8)	O2–Dy2–N6	152.49(8)
O1–Dy1–O1'	113.32(11)	O3–Dy2–N4	151.47(7)
O4–Dy1–O4'	131.79(12)	O2–Dy2–O3	113.80(7)
		O5–Dy2–O6	128.59(8)

Apart from the higher symmetry, the [N$_4$O$_4$] coordination of the Dy sites is very similar to what is found in **18**. However, the shape deviation parameters[251–253] for triangular dodecahedron symmetry of 0.789 (Dy1) and 0.999 (Dy2) are in sum the lowest found among all trinuclear lanthanoid complexes presented in this work. Even within the two different Dy centres the bonding angle of the two phenolate O-donors forming the shortest bonds is almost identic (113.32 vs. 113.8), so that very homogeneous single ion magnetic anisotropy can be expected.

An intersecting angle of the tag planes in the complex fragment of 0.8° indicates their quasi-parallelism. Also the intersecting angle of these very planes with the □Dy$_3$ plane shows the minor value of 1.2°. As governed by symmetry, the phenolate O-donors' distance from the □Dy$_3$ plane is narrowly distributed around the average value of 13.5 pm.

As was already raised, despite the presence of DMAP molecules in the structure, the nature of the countercation remains subject to discussion. Per complex unit, there are two DMAP molecules, which are symmetry equivalent. The more basic N atom of DMAP, which is incorporated in the aromatic ring, is included in an H bonding interaction with a MeOH coligand of Dy2 (O5, $d_{\text{N-O}} = 270$ pm, illustrated in fig. 4.18). Hence, if half a proton is statistically localised here, this will necessitate a rather unusual two-donor two-acceptor H bond. Another option is the statistical binding of half a proton at the less basic N atom of DMAP incorporated in the dimethylamino moiety. Since the corresponding lone-pair is part of the aromatic system such behaviour is unexpected but, if present, should lead to a lifting of the planarity at this N atom
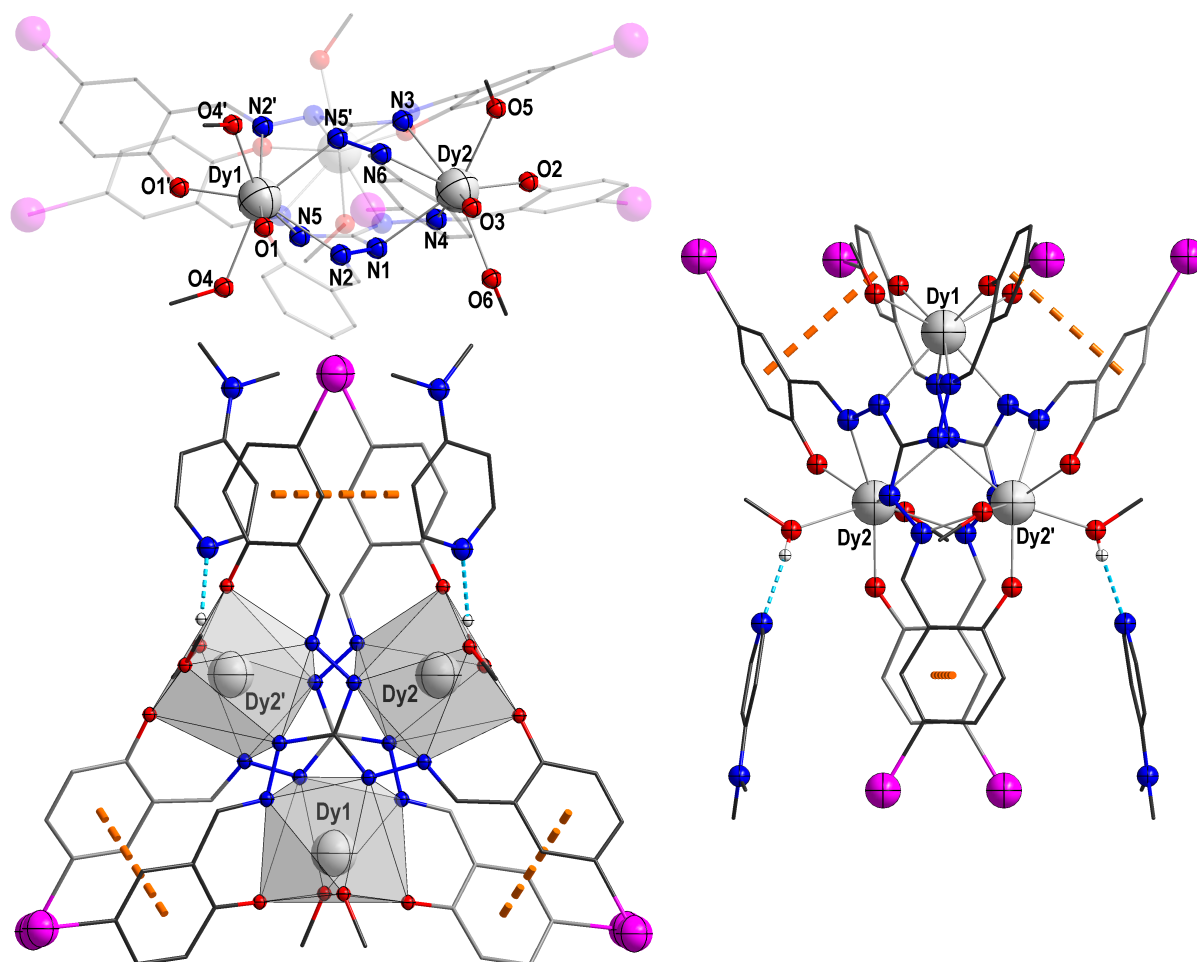
Figure 4.18: Left Top: Molecular structure of complex anion $[Dy_3(saltag^I)_2(MeOH)_6]^-$ in **21** with atom labels for the two crystallographically independent centres Dy1 and Dy2. C atoms are wire nodes, Dy: light grey, N: blue, O: red, I: magenta. H atoms, countercation and cocrystallised solvent molecules are omitted for clarity. Parts of the molecule not involved in the coordination of the labelled metal centres have been rendered transparent for clarity. **Left Bottom:** Illustration of the coordination polyhedra of **21**. View along the normal to the bottom tag plane (lighter grey). The orange dashed lines illustrate the intramolecular $\pi \cdots \pi$-interactions, light blue dashed lines are hydrogen bonds to possible HDMAP$^+$ countercations. **Right:** View along the crystallographic a-axis for recognition of C_2 symmetry and weak interactions in the complex **21**. Colour code is identical.

towards a tetrahedral arrangement. No hints into that direction such as residual electron density in proximity of the N atom or out-of-plane thermal ellipsoids of the methyl groups can be found in the structure, which is of good data quality and very well solved (see table A.20). Therefore, this option appears implausible. Eventually, a statistic distribution of the proton among the N-backbone of the chelate ligands as it is apparent in **19** is another option and, against the background of the prior discussion the preferential one, although the problem cannot be finally solved based on the available data.

The second MeOH coligand of Dy2 bearing the donor atom O6 shows an H bonding interaction with the cocrystallised MeOH molecule ($d_{O-O} = 264$ pm). In contrast, the MeOH coligands of Dy1 are otherwise unbound and no further intermolecular interactions are apparent in the structure.

[Dy$_3$(H$_{0.5}$saltag^I)$_2$(thf)$_6$] (22)

The last compound **22** in the series of trinuclear Dy complexes crystallises in monoclinic space group $P2_1/c$ (#14). However, in contrast to the previously described complex, none of the symmetry elements is reflected in the molecular symmetry of the alleged neutral complex [Dy$_3$(H$_{0.5}$saltag^I)$_2$(thf)$_6$] (depicted in fig. 4.19), so that it contains three crystallographically independent Dy centres whose bond lengths and selected angles of the coordination environment can be found in table 4.15.

Table 4.15: Selected bond lengths (pm) and angles (°) from the coordination environment of Dy1, Dy2 and Dy3 in **22**. The corresponding numbering scheme is depicted in fig. 4.19. No anisotropic displacement factors were determined for atoms O1–O6 included in the thf coligands, so no errors are given in connection with these atoms.

Dy1–N2A	256.2(12)	Dy2–N1A	254.6(12)	Dy3–N1B	260.6(13)
Dy1–N2B	256.7(11)	Dy2–N4A	255.9(11)	Dy3–N3A	253.9(12)
Dy1–N3B	251.3(11)	Dy2–N4B	255.8(11)	Dy3–N6A	258.2(12)
Dy1–N5A	254.4(11)	Dy2–N5B	251.5(13)	Dy3–N6B	262.2(13)
Dy1–O1A	218.9(10)	Dy2–O2A	216.7(10)	Dy3–O3A	215.1(10)
Dy1–O1B	218.2(10)	Dy2–O2B	217.3(10)	Dy3–O3B	214.9(10)
Dy1–O1	249	Dy2–O3	243	Dy3–O5	252
Dy1–O2	252	Dy2–O4	249	Dy3–O6	256
O1A–Dy1–N2B	154.2(4)	O2A–Dy2–N4B	155.4(4)	O3A–Dy3–N6B	157.3(4)
O3A–Dy1–N6	153.0(4)	O2B–Dy2–N2A	154.4(5)	O3B–Dy3–N6A	158.8(5)
O1B–Dy1–O1A	115.6(4)	O2A–Dy2–O2B	114.3(4)	O3A–Dy3–O3B	114.1(4)
O1–Dy1–O2	124	O3–Dy2–O4	128	O5–Dy3–O6	133

Before going further into detail, it has to be clarified, that the X-ray diffraction data only poorly determines the periphery of the complex, including the THF coligands, so the discussion is limited to the complex molecule. Nevertheless, the chemical constitution of the coligands being THF can be considered reliable. These weaker coligands lead to notable shifts in the bonding distances between the Dy centres and the phenolate O-donors, which are all significantly below 220 pm and the overall shortest found among all saltag-based lanthanoid complexes reported
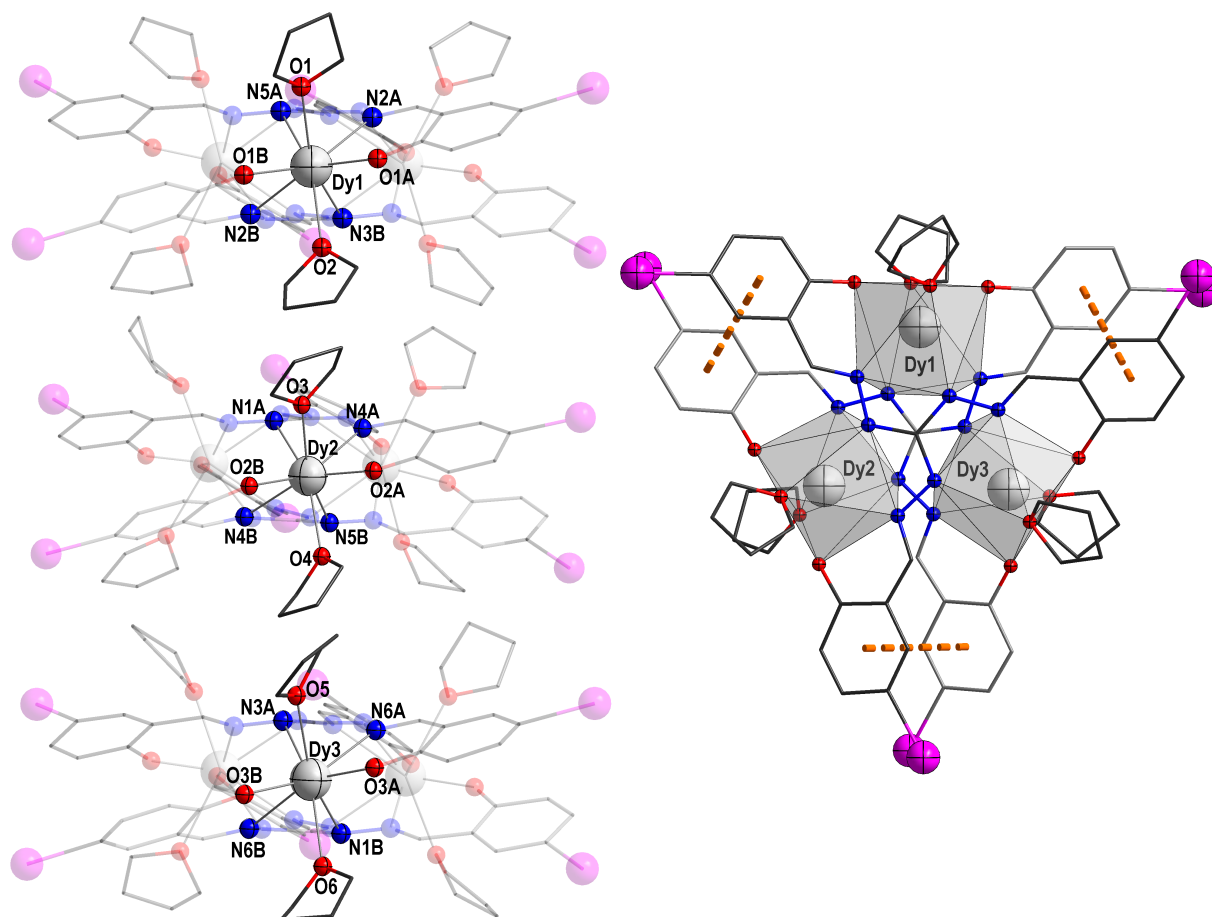
Figure 4.19: Left: Molecular structure of neutral complex $[Dy_3(H_{0.5}saltag^I)_2(thf)_6]$ (**22**) with atom labels shown in three directions for the three crystallographically independent centres Dy1, Dy2 and Dy3. C atoms are wire nodes, Dy: light grey, N: blue, O: red, I: magenta. H atoms are omitted for clarity. Parts of the molecule not involved in the coordination of the labelled metal centres have been rendered transparent for clarity. **Right:** Illustration of the distorted coordination polyhedra of **22**. View along the crystallographic a-axis. The orange dashed lines illustrate the intramolecular $\pi\cdots\pi$-interactions. Colour code is identical.

in this work. At the same time, the corresponding bonding angles around 115° are comparable to the other compounds, thus, a significantly larger single-ion magnetic anisotropy can be expected for **22**.

Continuous shape measures[251–253] on all three Dy sites revealed the triangular dodecahedron as closest reference polyhedron with deviation parameters of 1.379 (Dy1), 1.252 (Dy2) and 1.541 (Dy3). This indicates the overall local symmetry to be lower than in compounds **19** and **21**.

Also in compound **22** the two tag planes and the $\square Dy_3$ plane show almost ideal parallelism with intersecting angles below 2°. The average protrusion of the phenolate O-donors from the $\square Dy_3$ plane amounts 29.8 pm, which is the largest value among the trinuclear congeners presented in this work.

Comparative Remarks

Since the trinuclear lanthanoid complexes' structures show a nearly ideal equilateral triangle arrangement of the Dy centres, some structural parameters that allow for a preliminary relative estimation of the local magnetic anisotropy, the alignment of the corresponding easy axes of magnetisation in the magnetic ground state and possible magnetic interaction are comparatively arrayed in table 4.16. Based on that, an assignment of the compounds into one of the three ideal scenarios schemed in fig. 1.14 of the introduction is aspired.

First, the local symmetry represented by the shape deviation parameter[251–253] for the triangular dodecahedron reference polyhedron (Sh-TDD) indicates **21** to feature the highest local symmetry at the individual Dy centres. This is beneficial for the single-ion magnetic relaxation, but does not necessarily affect the magnetic anisotropy.

In contrast, the averaged bonding distances of the phenolate O-donors $d_{av}[O_{Ph}–Dy]$ are a hard measure for a preliminary estimation of local magnetic anisotropy.[127,129,272] Here, compound **22** shows the overall shortest bonds, hence the largest magnetic anisotropy can be expected. The averaged distance of Dy2 in **20** is also remarkably low, but due to its fundamentally different seven-coordinate environment and the low binding angle $\angle O_{Ph}–Dy–O_{Ph}$ lower magnetic anisotropy has to be expected. The latter angle is a second essential factor for the maximisation of local magnetic anisotropy in these systems and ideally approaches 180°.[129] In this respect **22** exhibits again the most beneficial overall values. However, the differences might be less significant, especially when compared to the values of **21**.

A crucial feature to functionally classify the compounds is the orientation of the easy axes of magnetisation in the magnetic ground state of the single ions with respect to each other. For a prediction of these axes based on structural features, a line through the anisotropy determining phenolate O-donors was utilised as an approximation, whose preciseness will be resumed in the forthcoming magnetic properties part. Analysing the intersecting angles of these lines with the plane spanned by the three Dy centres $\angle O–O_{Dy}$ - $\square Dy_3$ reveals a nearly in-plane alignment of the presumed easy axes, which is in average closest for compounds **20** and **21**. This, in principle, would allow for an in-plane frustration or a canted toroidal ground state as ideal arrangements (compare section 1.3 in the introduction), so the intersecting angle of the axes

Table 4.16: Comparison of structural parameters obtained from crystal structures of the trinuclear Dy(III) complexes reported in this work. The deviation parameters from ideal triangular dodecahedron (Sh-TDD) coordination polyhedra determined via continuous shape measures 251-253 are given in the upper part of the table. The lower half lists averaged bond lengths d(O$_{Ph}$–Dy), the bonding angle of the phenolate-O donors ∠O$_{Ph}$–Dy–O$_{Ph}$, which form the shortest coordinative bonds with the metal centres, the intersecting angle of the lines through the phenolate-O donors of each Dy centre with the plane formed by the three Dy centres ∠O–O$_{Dy}$ - □Dy$_3$, the intersecting angle between the lines through the phenolate-O donors of each Dy centre ∠O–O$_{Dy}$ - O–O$_{Dy'}$ as well as the intramolecular metal distances Dy···Dy$_{intra}$. *This centre is hepta-coordinate, the shape deviation parameter refers to a capped octahedron as reference.

Centre	19			20			21		22		
	Dy1	Dy2	Dy3	Dy1	Dy2	Dy3	Dy1	Dy2	Dy1	Dy2	Dy3
Sh-TDD	1.330	0.970	1.094	1.655	1.737*	1.180	0.789	0.999	1.379	1.252	1.541
d_{av}[O$_{Ph}$–Dy]/ pm	220.8	221.8	222.0	223.5	218.7	223.6	219.3	220.7	218.6	217.0	215.0
∠O$_{Ph}$–Dy–O$_{Ph}$/°	110.4	109.2	112.3	116.4	99.3	115.3	113.3	113.8	115.6	114.3	114.1
∠O–O$_{Dy}$ - □Dy$_3$/°	8.2	10.5	1.2	1.3	8.0	1.4	4.9	3.9	7.4	7.8	13.2
∠O–O$_{Dy}$ - O–O$_{Dy'}$/°	60.4	59.3	63.5	57.3	64.4	58.9	59.7	62.2	60.2	64.8	62.9
d[Dy···Dy$_{intra}$]/ pm	511	500	507	487	499	496	508	511	510	507	508

$\angle$O–O$_{Dy}$ - O–O$_{Dy'}$ needs to be investigated as well. For all treated compounds these angles are very close to 60°, which would be the ideal vortex arrangement giving rise to a toroidal ground state, hence, single-molecule toroic (SMT) properties can be expected especially in **21**.

The occurrence of such a phenomenon also relies on magnetic exchange interaction. A structural parameter, which directly correlates with the dipolar contribution of the magnetic interaction is the intramolecular distance between the metal centres $d[\text{Dy}\cdots\text{Dy}_{\text{intra}}]$ (see eq. 1.13). While these values are somewhat below 500 pm for **20**, the other compounds feature comparable distances slightly above 500 pm.

4.3.3 Magnetic Properties

For all trinuclear Dy compounds presented in this section DC and AC magnetic susceptibility measurements were carried out. The detailed temperature dependencies obtained by these investigations are collated in appendix B.3. A full-matrix-diagonalisation fitting of the DC susceptibility was not attempted due to the complex energy structure of the molecules. However, for **19** a fit aided by calculational results and for **21** fitting of data from an isostructural Gd(III) provide estimates of the dimension of magnetic interactions and are discussed in the subsequent paragraphs, respectively.

From the AC magnetic susceptibility, temperature-dependent relaxation times τ_T were derived via a fit to a generalised Debye model (eq. (1.20)), which yielded Cole-Cole plots also depicted in appendix B.3. In contrast to the dinuclear compounds, the relaxation behaviour was then fitted to the relaxation law given in eq. (4.4), which replaces the Raman process with another vibration-related Orbach process (thermal barrier Δ_{vib2} and rate contant A_{vib2}), because a fit with a Raman process was scarcely applicable.

$$\tau_T^{-1} = A_{\mathrm{CF}} \cdot \exp\left(\frac{-\Delta_{\mathrm{CF}}}{k_{\mathrm{B}T}}\right) + A_{\mathrm{vib1}} \cdot \exp\left(\frac{-\Delta_{\mathrm{vib1}}}{k_{\mathrm{B}T}}\right) + A_{\mathrm{vib2}} \cdot \exp\left(\frac{-\Delta_{\mathrm{vib2}}}{k_{\mathrm{B}T}}\right) + C_{\mathrm{QTM}} \tag{4.4}$$

This very treatment of presumed Raman processes in molecular magnets is encouraged in a recent discussion by Gu and Wu,[295] to better account for the rich phonon spectrum and possible spin-phonon coupling occurring. Furthermore, it bears the advantage, that all rate constants are directly comparable since they feature the same unit and mathematical meaning. In the following paragraphs the relaxation behaviour of the individual trinuclear compounds is outlined and compared.

Checks for magnetic hysteresis at 2 K, sigmoidal shape of magnetisation curves due to a toroidal ground state[221,222] and divergence in field-cooled and zero field-cooled magnetisation curves were done in all cases, but are not further mentioned if no such behaviour was apparent.

[Dy₃(H₀.₅saltag^Br)₂(MeOH)₆] · 3.5 MeOH (19)

The interpretation of the magnetic survey of compound **19** is supported by CAS-SCF calculations by Böhme,[272] which uncovered relative energies of the crystal-field split states (table B.8) and the orientation of g_z in the ground state KD1 (easy axis of magnetisation, table B.8 and fig. B.12). The latter exhibit significant deviations of some 20° from the line through the phenolate O-donors mentioned afore (compare table B.8), so for this very molecule these lines are no good approximation of the easy axes of magnetisation. Unfortunately, the aberration from the ideal toroidal arrangement of the easy axes, meaning intersecting angles of 60° and a cutting angle with the □Dy₃ plane of 0°, is significantly larger than for the lines through the phenolate O-donors (compare tables 4.16 and B.8). Hence, the expectation of observing a pure toroidal and thus non-magnetic ground state is lowered.

POLY-ANISO[222,291] simulations of the DC magnetic susceptibility's temperature dependence

(fig. B.13) yield a dipolar component of magnetic interaction of $-1.29\,\mathrm{cm}^{-1}$ and a superexchange contribution of $-0.15\,\mathrm{cm}^{-1}$ assuming an equilateral triangle topology. Especially the latter amounts only about one quarter of what was obtained for dinuclear compound **15** with the same method, despite comparable metal$\cdots$metal distances and equal bridging mode. Therefore, the overall magnetic interaction in the trinuclear complexes can be considered somewhat weaker than in the structurally related dinuclear compounds.
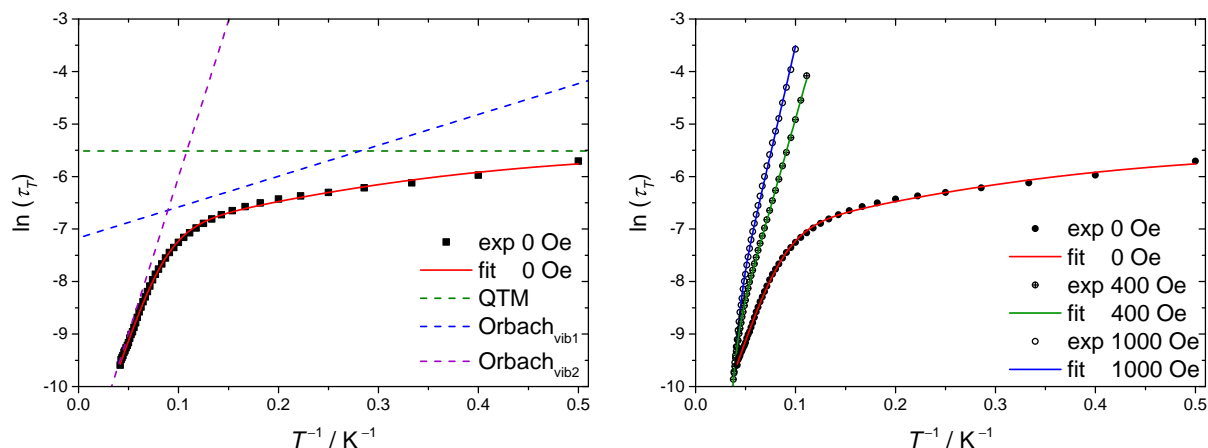
Figure 4.20: Logarithmic plot of the relaxation time τ_T of **19** at different static magnetic fields H_{DC} against T^{-1}. The corresponding fits of the relaxation behaviour to the multiprocess relaxation law given in eq. 4.4 yielded the parameters given in table 4.18 and are drawn as solid lines. The dashed lines in the left graph illustrate the discrete relaxation processes also revealing the temperature range, in which they are dominant, respectively.

Table 4.17: Collection of Debye model fittable temperature ranges and alpha parameters from the AC magnetic susceptibility measurements on **19** at different static magnetic fields H_{DC} applied as well as parameters extracted from fits of the temperature dependence of the corresponding magnetic relaxation times τ_T to the multiprocess relaxation law given in eq. 4.4. Fixed parameters are marked with an asterisk.

H_{DC}	0 Oe	400 Oe	1000 Oe
fittable T-range (AC sus.)	$2\cdots24\,\mathrm{K}$	$9\cdots27\,\mathrm{K}$	$10\cdots25\,\mathrm{K}$
α-range (AC sus.)	$0.378(7)\cdots0.183(6)$	$0.552(8)\cdots0.192(10)$	$0.486(6)\cdots0.239(16)$
$\Delta_{\mathrm{CF}}/\,\mathrm{cm}^{-1}$	-	214*	214*
$A_{\mathrm{CF}}/\,\mathrm{s}^{-1}$	-	$1.21(3)\cdot10^9$	$1.81(7)\cdot10^9$
$\Delta_{\mathrm{vib1}}/\,\mathrm{cm}^{-1}$	4.0(4)	-	-
$A_{\mathrm{vib1}}/\,\mathrm{s}^{-1}$	$1.30(8)\cdot10^3$	-	-
$\Delta_{\mathrm{vib2}}/\,\mathrm{cm}^{-1}$	41.4(6)	47.0(2)	57.2(5)
$A_{\mathrm{vib2}}/\,\mathrm{s}^{-1}$	$1.57(7)\cdot10^5$	$1.16(2)\cdot10^5$	$1.25(7)\cdot10^5$
$C_{\mathrm{QTM}}/\,\mathrm{s}^{-1}$	$2.5(2)\cdot10^2$	-	-

Dedicating to the AC magnetic susceptibility of **19** (fig. B.14), at zero static magnetic field H_{DC} the in-phase component χ' as well as the out-of-phase component χ'' attain global maxima at very low temperatures (below 2 K), which is indicative for prominent QTM being operative. This tendency and thus the QTM is reduced upon application of non-zero static magnetic fields leading to local maxima at higher temperatures, which is the common trend also observed

in mononuclear SMMs. So apparently, the counter-intuitive field dependence of magnetic relaxation in the exchange-biased dinuclear systems is not present in this trinuclear compound. This is in accordance with the expectation, that the geometric frustration of the trinuclear compounds quenches the beneficial magnetic exchange-based suppression of QTM found in the dinuclear systems.[209]

In agreement with the pronounced field dependence of the AC susceptibility, also the temperature range in which τ_T is accessible differs (table 4.17), so the very low temperatures are only covered in the absence of H_{DC}. The dispersion parameter α is in comparable dimensions to the structurally related dinuclear and mononuclear[239] compounds bearing MeOH coligands, so the minor structural differences of the three Dy centres do not further increase the broadness of the magnetic relaxation.

The logarithmic representation of the temperature dependence of τ_T at zero field H_{DC} shown in fig. 4.20 exhibits two linear areas. A fit of this curve to eq. 4.4 reveals, that none of the two corresponding relaxation processes relates to the crystal field states, because the lowest possible thermal barrier (KD1→KD2) is above $200\,\text{cm}^{-1}$ according to the *ab-initio* calculations and the obtained thermal barriers (see table 4.4) are way below that. Hence, both processes are interpreted as VMCRM and the crystal field related Orbach process is not covered by data points. A tunneling rate, which is about five orders of magnitude larger than what is found in the best-performing dinuclear compound **15** is obtained emphasising the mentioned cancellation of the exchange-bias suppression of QTM.

With static magnetic fields H_{DC} applied, the low barrier VMCRM$_1$ (Δ_{vib1}) as well as QTM are no longer covered by the data and thus omitted from the fit. However, the crystal field related Orbach process is well described and the curves were perfectly fittable when fixing the thermal barrier to the value $\Delta_{CF} = 214\,\text{cm}^{-1}$ obtained as an averaged energy gap KD1→KD2 from the *ab-initio* calculations (table B.8). Although the rate constants of A_{vib2} and A_{CF} are very similar, the thermal barrier Δ_{vib2} apparently shows a slight field dependence. This observation has to be evaluated cautiously, because different processes are included in the respective fits with and without H_{DC} applied, so that the effect might be marginal if the whole temperature range was accessible. In either case, weak fields H_{DC} suppress QTM, but since τ_T is pushed off the accessible window in the low-temperature QTM regime already at $H_{DC} = 400\,\text{Oe}$ and due to the overlap with VMCRM$_1$ even when approaching $2\,\text{K}$, no quantification of this effect is possible so far.

PPN[Dy$_3$(saltag$^{\text{I}}$)$_2$(MeOH)$_5$] · 5 MeOH   (20 and 20@Y/Lu)

The discussion of the magnetic properties of the most unsymmetric among the trinuclear Dy complexes in this work, compound **20**, is done in steady comparison with the corresponding data of an isostructural material **20@Y/Lu**, which is diamagnetically diluted into an Y/Lu-matrix. The mixture of Y and Lu was chosen to selectively populate the seven-coordinate, smaller coordination pocket of **20** with the smaller Lu(III) ion, because this pocket is expected to mediate the lowest magnetic anisotropy to a Dy(III) ion as compared to the two other, more

similar pockets. With the Y(III) ion which is closer to Dy(III) in terms of ionic radius a statistic distribution among the two remaining pockets is expected. The Dy content of the material was estimated to be 25 % via magnetisation measurements in comparison to **20**. Although higher dilutions would be beneficial to guarantee magnetically isolated Dy centres from a statistical point of view, the AC susceptibility signal quality of more diluted materials was poor, so the material with the ratio Dy:Y/Lu = 1:3 is chosen for the discussion here.

At zero field H_{DC} (table B.9), the AC susceptibility of **20** looks similar to **19**. However, with increasing field H_{DC} (tables B.10 and B.11) the evolving local maxima at higher temperatures are broader than for the previous compound and especially at 1000 Oe a bimodality of the curves can be recognised. This is in accordance with one very distinct seven-coordinate Dy centre, which should significantly differ in its magnetic relaxation behaviour. Although the corresponding curves for **20@Y/Lu** are a bit noisy, this bimodal distribution of frequency shifted maxima χ' and χ'' is sharper and better resolved than for the undiluted congener. This observation showcases, that the idea of a selective Dy depopulation of the distinct seven-coordinate pocket by adding Lu as matrix did not succeed, because the second relaxation is still present. Nevertheless, the dilution improved the separation of the relaxations.

Relaxation times τ_T could be extracted in rather narrow temperature ranges for **20** (table 4.18) as compared to **19**. Due to the tremendous broadness, at $H_{DC} = 1000$ Oe no reasonable determination of τ_T was possible at all. The dispersion parameters α are the highest among all Dy compounds presented in this work. In contrast, for **20@Y/Lu**, independent of the applied field, τ_T is available from 11 to 21 K based on AC susceptibility and direct relaxation measurements cover temperatures around 2 K. Lower and more homogeneous α-values indicate the successful uncoupling of the relaxation processes. However, τ_T of the distinct relaxation shifting its maximum in χ'' from 6 to 10 K, which presumably belongs to Dy centres in the seven-coordinate pocket could not be extracted from the AC susceptibility.
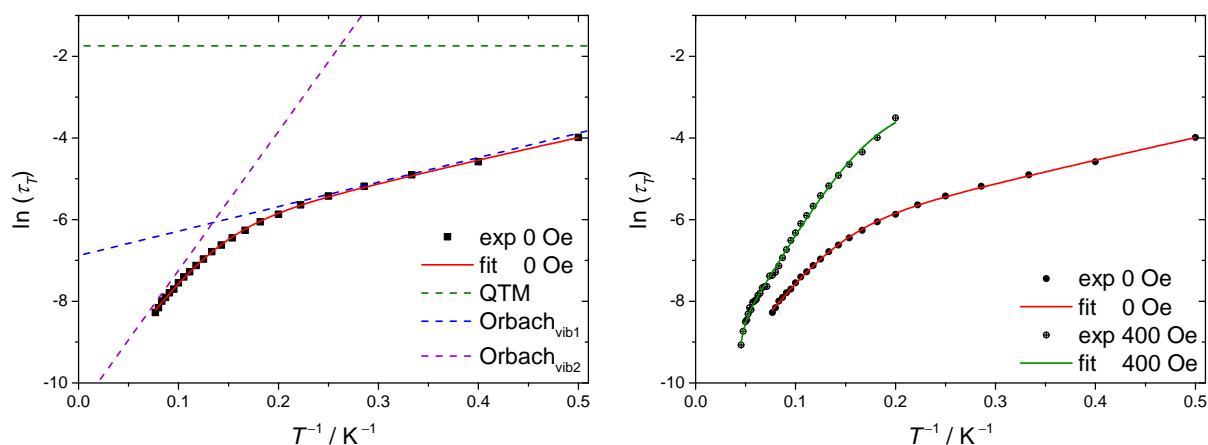
Figure 4.21: Logarithmic plot of the relaxation time τ_T of **20** at different static magnetic fields H_{DC} against T^{-1}. The corresponding fits of the relaxation behaviour to the multiprocess relaxation law given in eq. 4.4 yielded the parameters given in table 4.18 and are drawn as solid lines. The dashed lines in the left graph illustrate the discrete relaxation processes also revealing the temperature range, in which they are dominant, respectively.

Table 4.18: Collection of Debye model fittable temperature ranges and alpha parameters from the AC magnetic susceptibility measurements on **20** and **20@Y/Lu** at different static magnetic fields H_{DC} applied as well as parameters extracted from fits of the temperature dependence of the corresponding magnetic relaxation times τ_T to the multiprocess relaxation law given in eq. 4.4. Fixed parameters are marked with an asterisk.

H_{DC}	value	[Dy$_3$] (**20**)	[Dy@Y/Lu$_3$] (**20@Y/Lu**)
0 Oe	fittable T-range (AC sus.)	$2 \cdots 13$ K	$11 \cdots 21.5$ K
	fittable T-range (direct rel.)	-	$2 \cdots 2.4$ K
	α-range (AC sus.)	$0.565(8) \cdots 0.314(13)$	$0.39(3) \cdots 0.16(4)$
	α-range (direct rel.)	-	$0.217(13) \cdots 0.18(15)$
	$\Delta_{CF}/$ cm^{-1}	-	200*
	$A_{CF}/$ s^{-1}	-	$2.7(6) \cdot 10^9$
	$\Delta_{vib1}/$ cm^{-1}	4.2*	4.2*
	$A_{vib1}/$ s^{-1}	$9.7(2) \cdot 10^2$	0.16(2)
	$\Delta_{vib2}/$ cm^{-1}	23.7(5)	56.4(14)
	$A_{vib2}/$ s^{-1}	$4.2(3) \cdot 10^4$	$1.9(3) \cdot 10^5$
	$C_{QTM}/$ s^{-1}	6(2)	0.0083(12)
400 Oe	fittable T-range (AC sus.)	$5 \cdots 22$ K	$11.5 \cdots 20.5$ K
	fittable T-range (direct rel.)	-	$2 \cdots 3$ K
	α-range (AC sus.)	$0.423(5) \cdots 0.18(2)$	$0.196(18) \cdots 0.16(2)$
	α-range (direct rel.)	-	$0.202(7) \cdots 0.167(9)$
	$\Delta_{CF}/$ cm^{-1}	200*	200*
	$A_{CF}/$ s^{-1}	$1.6(3) \cdot 10^9$	$3.9(7) \cdot 10^9$
	$\Delta_{vib1}/$ cm^{-1}	4.2*	4.2(2)
	$A_{vib1}/$ s^{-1}	$9.4(8) \cdot 10^1$	0.122(9)
	$\Delta_{vib2}/$ cm^{-1}	28.5(6)	58(3)
	$A_{vib2}/$ s^{-1}	$3.3(2) \cdot 10^4$	$1.2(3) \cdot 10^5$
1000 Oe	fittable T-range (AC sus.)	-	$11 \cdots 21.5$ K
	fittable T-range (direct rel.)	-	$2 \cdots 3$ K
	α-range (AC sus.)	-	$0.24(2) \cdots 0.16(3)$
	α-range (direct rel.)	-	$0.224(5) \cdots 0.160(7)$
	$\Delta_{CF}/$ cm^{-1}	-	200*
	$A_{CF}/$ s^{-1}	-	$2.5(4) \cdot 10^9$
	$\Delta_{vib1}/$ cm^{-1}	-	4.2*
	$A_{vib1}/$ s^{-1}	-	0.089(3)
	$\Delta_{vib2}/$ cm^{-1}	-	60(2)
	$A_{vib2}/$ s^{-1}	-	$1.6(3) \cdot 10^5$
	$C_{QTM}/$ s^{-1}	-	0.00142(17)
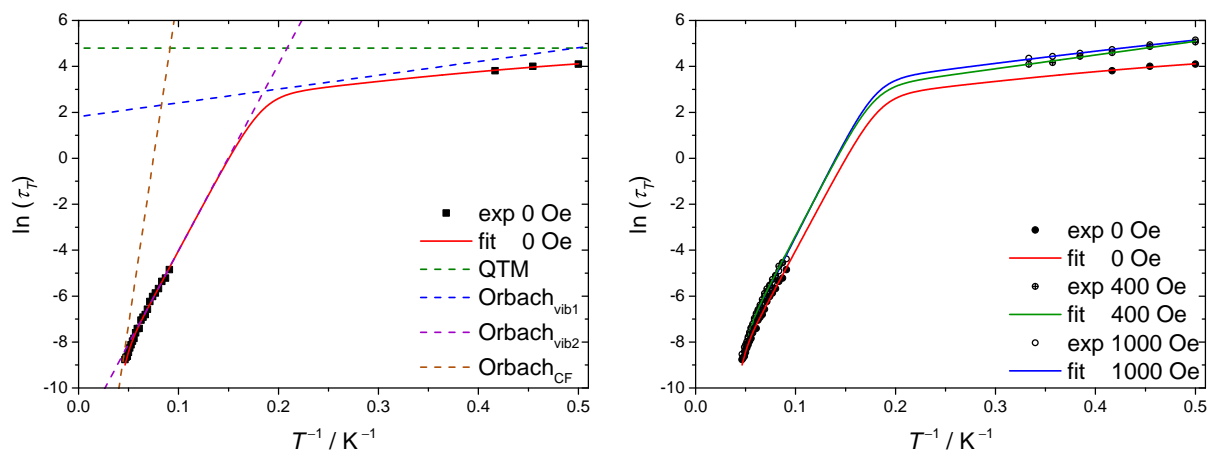
Figure 4.22: Logarithmic plot of the relaxation time τ_T of **20@Y/Lu** at different static magnetic fields H_{DC} against T^{-1}. The corresponding fits of the relaxation behaviour to the multiprocess relaxation law given in eq. 4.4 yielded the parameters given in table 4.18 and are drawn as solid lines. The dashed lines in the left graph illustrate the discrete relaxation processes also revealing the temperature range, in which they are dominant, respectively.

The available τ_T points are logarithmically plotted in figures 4.21 (**20**) and 4.22 (**20@Y/Lu**). Fitting the curves to eq. 4.4 yielded the parameters collated in table 4.18. For these fits, the thermal barrier Δ_{CF} was fixed to $200\,\mathrm{cm}^{-1}$, which in lack of *ab-initio* calculations on this compound is an assumption derived from the previous compound. Since the temperature regime of the crystal field related Orbach process is only marginally touched by the data points (above $20\,\mathrm{K}$, compare figs. 4.21 and 4.22), the impact of this value on the fit results is minor.

In all curves with data around $2\,\mathrm{K}$ it stands out, that temperature independence (straight horizontal course) of the magnetic relaxation is not reached at $2\,\mathrm{K}$. Therefore, in the curve with the highest τ_T at $2\,\mathrm{K}$ (**20@Y/Lu** at $H_{DC} = 400\,\mathrm{Oe}$), the QTM rate constant C_{QTM} was set to zero and the competing VMCRM$_1$ (Δ_{vib1}) is then very well defined. The obtained thermal barrier Δ_{vib1} of $4.2\,\mathrm{cm}^{-1}$ was fixed to this value for all other fits. Accordingly, the tunneling rates C_{QTM} of all other fits can be interpreted as an increase related to the tunneling rate of **20@Y/Lu** at $H_{DC} = 400\,\mathrm{Oe}$, which cannot be determined based on the present data. Given this constraint, the magnetic dilution reduces C_{QTM} by three orders of magnitude. This difference can thus be considered the QTM contribution arising from interactions with neighbouring Dy centres.

The thermal barrier Δ_{vib1} of VMCRM$_1$ as well as the rate constant A_{vib1} in case of **20** at $H_{DC} = 0\,\mathrm{Oe}$ is almost identical to the one found for **19**. Application of a magnetic field as well as magnetic dilution significantly decreases its rate constant but does not change the thermal barrier. This behaviour is hard to classify within the common arsenal of relaxation processes described in section 1.3. Since the process appears to be related to the trinuclear nature of the molecule (for it does not appear in the dinuclear and mononuclear relatives), its molecular origin remains an exciting, yet open question.

Contrarily, VMCRM$_2$ shows no field dependence at all in the diluted compound **20@Y/Lu**, merely when going to undiluted **20** its barrier Δ_{vib2} is roughly halved and the rate constant A_{vib2} is decreased by one order of magnitude. This can reasonably be related to molecular vibrational

modes,[143,173] which indeed should change in energy with respect to metal centres of different size and Lewis acidity.

(H$_{0.5}$DMAP)$_2$[Dy$_3$(saltag^I)$_2$(MeOH)$_6$] · 2 MeOH   (21 and 21@Y)

To get another rough estimate on the superexchange contribution to magnetic interaction in the trinuclear lanthanoid complexes based on experimental data, the temperature-dependent DC susceptibility of a Gd complex isostructural to **21** was investigated (fig. 4.23). Treating each Gd centre as an isotropic spin $S = \frac{7}{2}$, the curve was fitted in a full matrix diagonalisation approach to the Hamiltonian given in eq. (4.5), which represents an equilateral triangle spin topology.

$$\widehat{H} = -J_{ex}\left(\widehat{S}_1\widehat{S}_2\widehat{S}_3\right) \; + \; g_{iso}\mu_B B \sum_{i=1}^{3} \widehat{S}_i \qquad (4.5)$$
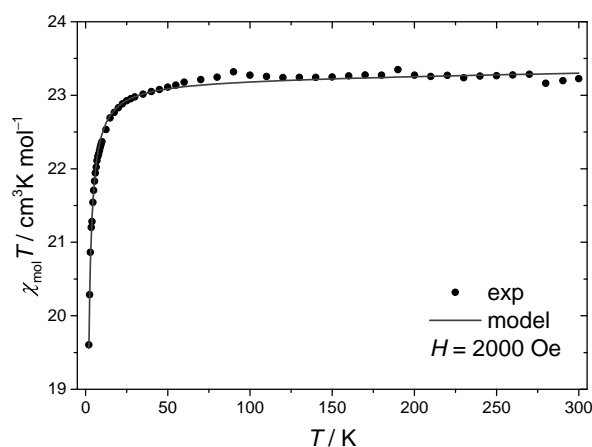
Figure 4.23: Temperature dependence of molar magnetic susceptibility $\chi_{mol}T$ for (H$_{0.5}$DMAP)$_2$[Gd$_3$(saltag^I)$_2$(MeOH)$_6$] · 2 MeOH (black) and the corresponding fit (grey) to the Hamiltonian given in eq. 4.5 at an applied magnetic field of $H = 2000$ Oe.

This fit yielded the parameters $g_{iso} = 1.98$ and $J_{ex} = -0.02\,\text{cm}^{-1}$. While the g_{iso} is in good agreement with the expected value of 2 for isotropic and purely electronic spins without orbit contribution, the exchange coupling constant J_{ex} is one order of magnitude smaller than what was determined based on *ab-initio* calculational data for compound **19**. This discrepancy might of course originate from differences in the distribution of spin density between the Gd and the Dy centres. However, the agreement of both approaches was much better for the dinuclear lanthanoid complexes (structure of compound **15**).

Of course, the slightly distinct structures of **21** and **19** may also have their part in different exchange coupling contributions, but CAS-SCF calculations on **21** carried out by Böhme[272] reveal, that at least the low energy spectrum of states (table B.12) is rather similar. The g_z components of the ground state KDs (easy axes of magnetisation, depicted in fig. B.16) obtained from these calculations exhibit significantly lower deviations from the lines through the phenolate

O-donors (see table B.12) of about 13° as compared to **19**. Hence, these lines discussed within the crystal structure description are a moderate approximation of the easy axis of magnetisation in case of **21**.

Analysing the agreement of the alignment of the easy axes of magnetisation with the ideal toroidal case (equilateral triangle in the □Dy$_3$ plane), the two symmetry equivalent Dy centres Dy2 are close to this ideal alignment featuring a cutting angle of 58° and an intersecting angle with the □Dy$_3$ plane of 15.3° each. However, the distinct metal centre Dy1 exhibits somewhat larger deviations, namely respective angles of 72.4° and 18.4°. Nevertheless, compound **21** does not only show the highest molecular symmetry but also the closest proximity to ideal toroidal arrangement of the easy axes of magnetisation among all trinuclear lanthanoid complexes presented in this work. Therefore, the observation of a non-magnetic toroidal ground state, if at all, is most probable for this compound.

After the description of the trinuclear ensemble in **21** from the static magnetism point of view its relaxation behaviour as probed by AC magnetic susceptibility is of interest. For deeper insight this is once more surveyed in direct comparison with an isostructural material **21@Y**, where Dy is doped into the diamagnetic Y matrix in the molar ratio 1:6.6. This grade of dilution is once again a compromise between magnetic isolation of single Dy centres and quality of the obtained AC susceptibility data.

Looking at the temperature dependence of in-phase and out-of-phase components of the magnetic susceptibility (tables B.13, B.14 and B.15), the general trends and magnetic field dependencies are akin to the two previous trinuclear complexes. However, the peaks around the frequency shifted maxima are overall sharper and better resolved, especially, no sign of bimodality becomes apparent, neither for **21**, nor for **21@Y**. This observation is in accordance with the higher local as well as molecular symmetry of **21** as compared to the other trinuclear congeners.
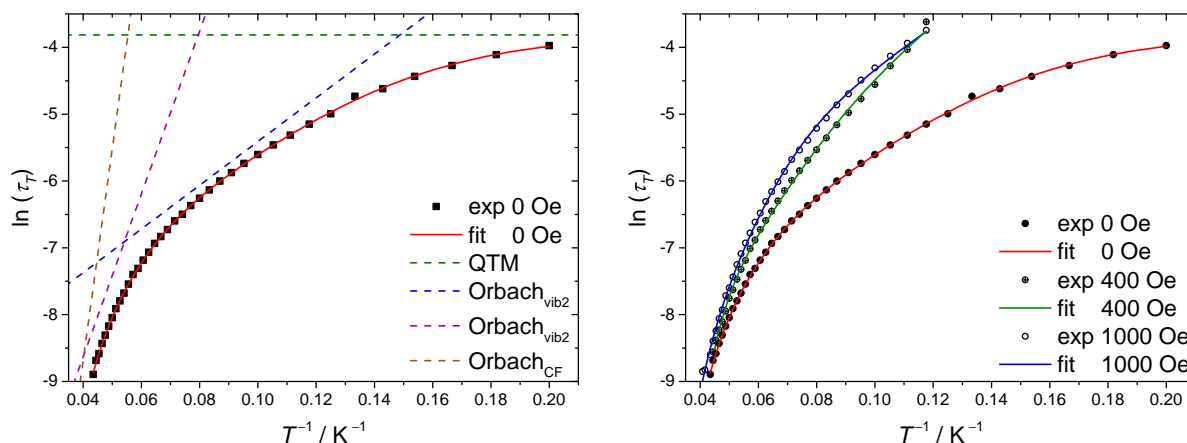
Figure 4.24: Logarithmic plot of the relaxation time τ_T of **21** at different static magnetic fields H_{DC} against T^{-1}. The corresponding fits of the relaxation behaviour to the multiprocess relaxation law given in eq. 4.4 yielded the parameters given in table 4.19 and are drawn as solid lines. The dashed lines in the left graph illustrate the discrete relaxation processes also revealing the temperature range, in which they are dominant, respectively.

Table 4.19: Collection of Debye model fittable temperature ranges and alpha parameters from the AC magnetic susceptibility measurements on **21** and **21@Y** at different static magnetic fields H_{DC} applied as well as parameters extracted from fits of the temperature dependence of the corresponding magnetic relaxation times τ_T to the multiprocess relaxation law given in eq. 4.4. Fixed parameters are marked with an asterisk.

H_{DC}	value	[Dy$_3$] (**21**)	[Dy@Y$_3$] (**21@Y**)
0 Oe	fittable T-range (AC sus.)	$5\cdots23\,$K	$9.5\cdots24\,$K
	fittable T-range (direct rel.)	-	$2\cdots2.4\,$K
	α-range (AC sus.)	$0.396(7)\cdots0.133(9)$	$0.217(5)\cdots0.109(9)$
	α-range (direct rel.)	-	$0.225(9)\cdots0.140(8)$
	$\Delta_{CF}/\,$cm^{-1}	220*	220*
	$A_{CF}/\,$s^{-1}	$1.9(2)\cdot10^9$	$5(2)\cdot10^8$
	$\Delta_{vib1}/\,$cm^{-1}	22.7(5)	20.47(14)
	$A_{vib1}/\,$s^{-1}	$5.9(4)\cdot10^3$	$1.86(6)\cdot10^3$
	$\Delta_{vib2}/\,$cm^{-1}	85(4)	78(3)
	$A_{vib2}/\,$s^{-1}	$7(2)\cdot10^5$	$2.9(7)\cdot10^5$
	$C_{QTM}/\,$s^{-1}	45.3(11)	0.0135(3)
400 Oe	fittable T-range (AC sus.)	$8.5\cdots22.5\,$K	$10\cdots27\,$K
	α-range (AC sus.)	$0.330(6)\cdots0.204(17)$	$0.180(8)\cdots0.14(2)$
	$\Delta_{CF}/\,$cm^{-1}	220*	220*
	$A_{CF}/\,$s^{-1}	$3.7(3)\cdot10^9$	$6.2(9)\cdot10^8$
	$\Delta_{vib1}/\,$cm^{-1}	21*	21*
	$A_{vib1}/\,$s^{-1}	$1.23(8)\cdot10^3$	$9.8(5)\cdot10^2$
	$\Delta_{vib2}/\,$cm^{-1}	55(2)	79(3)
	$A_{vib2}/\,$s^{-1}	$8.2(15)\cdot10^4$	$2.6(6)\cdot10^5$
1000 Oe	fittable T-range (AC sus.)	$8.5\cdots24.5\,$K	$10\cdots24\,$K
	α-range (AC sus.)	$0.162(6)\cdots0.254(16)$	$0.172(9)\cdots0.20(2)$
	$\Delta_{CF}/\,$cm^{-1}	220*	220*
	$A_{CF}/\,$s^{-1}	$1.41(18)\cdot10^9$	$1.21(14)\cdot10^9$
	$\Delta_{vib1}/\,$cm^{-1}	21*	21*
	$A_{vib1}/\,$s^{-1}	$1.45(3)\cdot10^3$	$9.3(4)\cdot10^2$
	$\Delta_{vib2}/\,$cm^{-1}	80(2)	74(3)
	$A_{vib2}/\,$s^{-1}	$4.7(9)\cdot10^5$	$1.7(4)\cdot10^5$
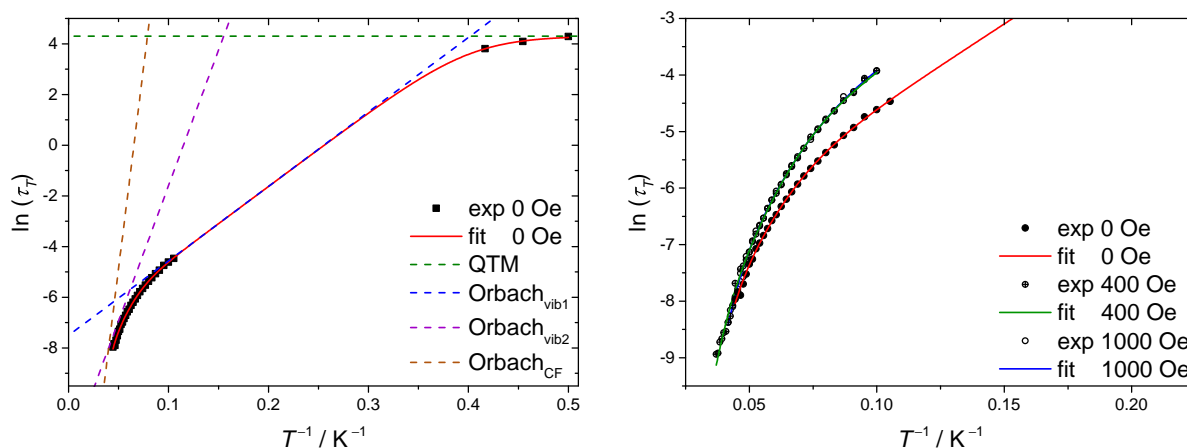
Figure 4.25: Logarithmic plot of the relaxation time τ_T of **21@Y** at different static magnetic fields H_{DC} against T^{-1}. The corresponding fits of the relaxation behaviour to the multiprocess relaxation law given in eq. 4.4 yielded the parameters given in table 4.19 and are drawn as solid lines. The dashed lines in the left graph illustrate the discrete relaxation processes also revealing the temperature range, in which they are dominant, respectively.

Following this trend, considerably lower dispersion parameters α obtained from the fits of τ_T are observed, especially for **21@Y**, and the fittable temperature ranges are similar also for the different static magnetic fields H_{DC} (table 4.19). In case of **21@Y** direct relaxation measurements were successful at very low temperatures around 2 K. An interesting aspect of the data at $H_{DC} = 1000$ Oe is the increase of the α-parameter upon raising temperature, which is a contrary trend to what is usually observed.

Logarithmic plots of the extracted temperature-dependent relaxation times τ_T are drawn in figs. 4.24 and 4.25 for compounds **21** and **21@Y**, respectively. The parameters obtained from the corresponding fits to the relaxation law given in eq. (4.4) are listed in table 4.19. The energy barrier of the crystal field-related Orbach process Δ_{CF} was fixed to 220 cm^{-1} for all fits, which is the average of the energetic gaps between KD1 and KD2 of all three Dy centres as revealed by the CAS-SCF calculations (table B.12). Although only marginally covered by data points in the absence of a static magnetic field, the process is determined at non-zero H_{DC} applied and shows good compatibility with the thermal barrier based on the calculations.

The first VMCRM process is well determined in the zero field curves of **21** and **21@Y**, therefore the average of the obtained thermal barriers Δ_{vib1} of 21 cm^{-1} was fixed for further fits with applied magnetic fields. This thermal barrier is significantly larger than in the previous trinuclear Dy complexes and its rate constant A_{vib1} is no longer depending on magnetic field or diamagnetic dilution, but similar in all fits.

Analogous observations can be made for the second VMCRM process, whose thermal barrier Δ_{vib2} and rate constant A_{vib2} remain preponderantly constant upon dilution and changes of H_{DC}, merely **21** at $H_{DC} = 400$ Oe is an outlier in that respect. The latter cannot be rationalised at the present state of insight into the system.

Eventually, the QTM rate C_{QTM} could only be determined in the absence of a static magnetic field H_{DC}. Diamagnetic dilution of **21** into **21@Y** reduces C_{QTM} by three orders of magnitude, so

the effect is similar to what is found for **20**. This indicates comparable contributions of magnetic interactions between the Dy centres to the QTM process in both compounds.
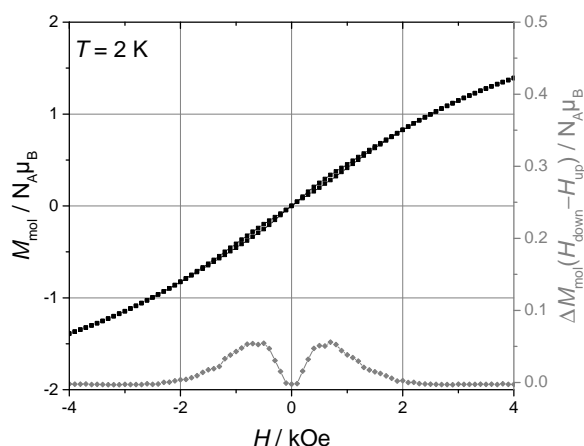
Figure 4.26: Hysteresis curve of **21@Y** at 2 K, the grey curve illustrates the difference between the curve with decreasing magnetic field and the curve with increasing magnetic field.

The diamagnetically diluted material **21@Y** exhibits weak hysteresis at 2 K, which is depicted in fig. 4.26. A collapse of the hysteresis at zero field due to QTM can be recognised, which is often observed for mononuclear lanthanoid-based SMMs.

[Dy$_3$(H$_{0.5}$saltag^l)$_2$(thf)$_6$]   (22)

Compound **22** is comparable to **19** in terms of local and molecular symmetry, but features the crucial difference of weaker, aprotic THF coligands instead of MeOH as in the other trinuclear Dy complexes in this work. Unfortunately, neither *ab-initio* calculations nor diamagnetic dilution studies are available for this compound, yet. Nevertheless, some essential insight can be gained from AC magnetic susceptibility measurements.

In the temperature dependence of χ' and χ'' (fig. B.19), the frequency shifted local maxima are well resolved already in the absence of a static magnetic field H_{DC}. This suggests reduced QTM and relaxation at very low temperatures as compared to the other trinuclear Dy complexes in this work. The fittable temperature range is very equal for all static magnetic fields H_{DC} (see table 4.20) and at zero field direct relaxation data was accessible around 2 K. The corresponding α-parameters are comparable to **19**, but in contrast to that compound they do not increase with raised H_{DC}.

Extracted relaxation times τ_T are shown as a function of temperature with a logarithmic scale in figure 4.27. Parameters yielded from fits of these curves to eq. (4.4) are gathered in table 4.20. In lack of *ab-initio* calculations, the value of 220 cm^{-1} taken as an approximation from the results on **21** was fixed as thermal barrier Δ_{CF} of the crystal field state-related Orbach process. Actually, a somewhat higher barrier due to enhanced magnetic anisotropy would be expected because of the weaker THF coligands. However, the crystal field state-related Orbach process is only marginally covered by data points, so that the impact of the thermal barrier Δ_{CF}

Table 4.20: Collection of Debye model fittable temperature ranges and alpha parameters from the AC magnetic susceptibility measurements on **22** at different static magnetic fields H_{DC} applied as well as parameters extracted from fits of the temperature dependence of the corresponding magnetic relaxation times τ_T to the multiprocess relaxation law given in eq. 4.4. Fixed parameters are marked with an asterisk.

H_{DC}	0 Oe	400 Oe	1000 Oe
fittable T-range (AC sus.)	$12 \cdots 28.5\,\mathrm{K}$	$12 \cdots 29\,\mathrm{K}$	$12 \cdots 27\,\mathrm{K}$
fittable T-range (dir. rel.)	$2 \cdots 3.5\,\mathrm{K}$	-	-
α-range (AC sus.)	$0.336(8) \cdots 0.206(16)$	$0.264(11) \cdots 0.18(3)$	$0.309(10) \cdots 0.16(2)$
α-range (dir. rel.)	$0.291(6) \cdots 0.146(5)$	-	-
$\Delta_{CF}/\mathrm{cm}^{-1}$	220*	220*	220*
A_{CF}/s^{-1}	$5.2(5){\cdot}10^8$	$4.3(3){\cdot}10^8$	$5.9(6){\cdot}10^8$
$\Delta_{vib1}/\mathrm{cm}^{-1}$	12.7(10)	-	-
A_{vib1}/s^{-1}	1.4(6)	-	-
$\Delta_{vib2}/\mathrm{cm}^{-1}$	58(2)	61.9(16)	61.6(15)
A_{vib2}/s^{-1}	$4.1(6){\cdot}10^4$	$4.3(6){\cdot}10^4$	$5.8(7){\cdot}10^4$
C_{QTM}/s^{-1}	0.00524(17)	-	-

on the overall fit is limited.

The first VMCRM-related Orbach process is only determined at zero field and therefore left out in the fits with H_{DC} applied. Δ_{vib1} of $12.7\,\mathrm{cm}^{-1}$ in **22** is larger than in the low-symmetry congeners with MeOH coligands **19** and **20**, but lower than in **21**, which features higher local and molecular symmetry.

In contrast, the temperature regime of the second VMCRM-related Orbach process is covered in all three fits. No field dependence of its thermal barrier Δ_{vib2} is apparent from the fit results, the corresponding rate constants A_{vib2} somewhat grow with increasing field, which might be related to suppression of other processes not included in the fits with H_{DC} applied.

Eventually, the QTM process at zero field exhibits a rate constant C_{QTM} of 0.005, which is by far the lowest found among all trinuclear Dy complexes in this work and rather comparable to the one of dinuclear complex **15**. It is also one order of magnitude smaller as compared to the diamagnetically diluted materials **20@Y/Lu** and **21@Y**. Since this is the only crucial difference, the tremendous reduction of QTM in **22** has to be related to its aprotic, weak THF coligands, which (in contrast to MeOH) do not bear rotatable atom groups.

In agreement with the low QTM, compound **22** shows a narrow hysteresis at 2 K (fig. 4.28), which has a butterfly shape meaning that magnetisation moves towards zero at zero field applied. This difference to the hysteretic behaviour of the dinuclear compounds might be related to the geometrically spin frustrated situation.[209] It remains an exciting, yet open question, whether the QTM can be further reduced by diamagnetic dilution and hence exclusion of magnetic interactions between the Dy centres. With that information, contributions to QTM by magnetic interactions on one side and degrees of freedom and nuclear spins of the coligands on the other side could be deconvoluted.

Anyway, the removal of protons and rotatable groups from the surrounding of the Dy centres has tremendous beneficial effects on their magnetic relaxation and must be considered a design
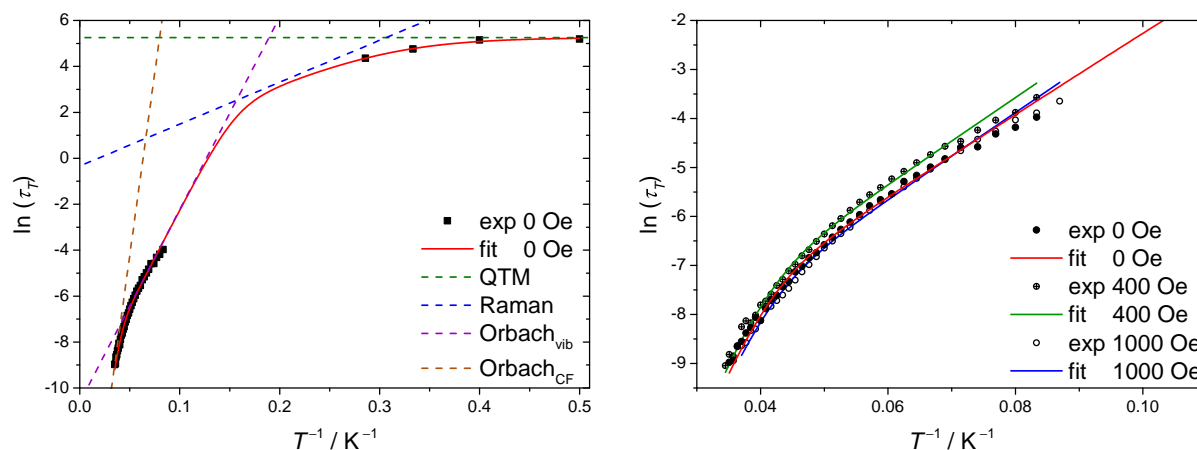
Figure 4.27: Logarithmic plot of the relaxation time τ_T of **22** at different static magnetic fields H_{DC} against T^{-1}. The corresponding fits of the relaxation behaviour to the multiprocess relaxation law given in eq. 4.4 yielded the parameters given in table 4.20 and are drawn as solid lines. The dashed lines in the left graph illustrate the discrete relaxation processes also revealing the temperature range, in which they are dominant, respectively.
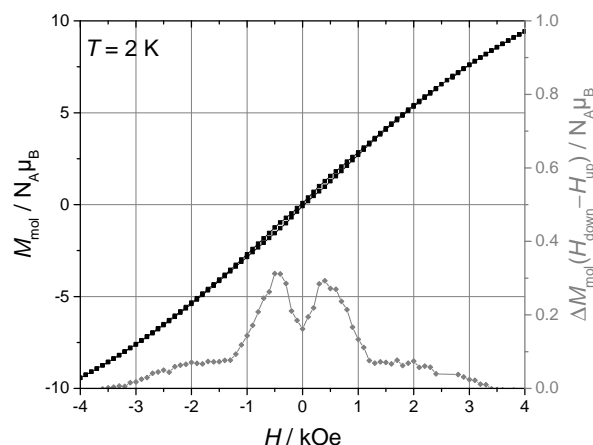
Figure 4.28: Hysteresis curve of **22** at 2 K, the grey curve illustrates the difference between the curve with decreasing magnetic field and the curve with increasing magnetic field.

criterion for the improvement of lanthanoid-based molecular magnets with tag ligands.

4.3.4 Concluding Remarks

Synthetic access to several trinuclear lanthanoid sandwich complexes based on halogenated saltag ligands with both, polar protic and polar aprotic solvent coligands was successfully developed. It stands out, that firstly high local and molecular symmetry and secondly the removal of proton and rotatable groups significantly slows down magnetic relaxation. Magnetic isolation of Dy centres in isostructural Y matrices in case of **20** and **21** reduces the QTM by about three orders of magnitude, which is thus related to a contribution from magnetic interactions between the Dy centres.

The arrangement of the ground state easy axes of magnetisation approximated based on structural parameters for all compounds and probed by *ab-initio* calculations for **19** and **21**

suggests the presence of mixed moment toroidal ground states and hence SMT properties. The best agreement of the calculated easy axes with an ideal toroic alignment is found in **21** with averaged intersecting angles with the $\square Dy_3$ plane of 16°. This is still a rather high deviation compared with the corresponding angle in the archetypal Dy triangle SMT by Powell *et al.*[221] amounting 5°.[222] In a second compound by Rajaraman *et al.*[224] in which the toroidal ground state could be experimentally proven, these very angles are unfortunately not given. Both compounds exhibit a sigmoidal shape of the magnetisation curve at 2 K, which could not be detected for the compounds in this work. However, the single-ion anisotropy of compounds **19** and **21** (tables B.8 and B.12) is comparable to what is found in Powell's complex[222] and higher than in Rajaraman's complex.[224]

For all compounds presented in this section high-frequency PPMS AC magnetic susceptibility is desirable to achieve a better description of the crystal field state-related Orbach processes and compare them with the energy structure from the *ab-initio* calculations. The latter should also be carried out on the remaining compounds **20** and **22** to complete the picture. Especially for **21** a possible mixed moment toroidal ground state might be uncovered via micro-SQUID measurements below 2 K.[224,225]

An optimisation of the saltag-based trinuclear Dy complexes should first of all aim for higher molecular symmetry. The $[Dy_3saltag_2]^-$ moiety allows for crystallographic C_3 symmetry which can be induced by suitable countercations. Weakly interacting aprotic countercations should be chosen to exclude the presence of remainder tautogenic protons, which can facilitate magnetic relaxation. At the same time, such countercations might improve the quality of crystal structures and hence thin out the low energy phonon spectrum.[174,175] A good candidate might be the triphenyl(triphenylmethyl)-phosphonium cation, which is structurally related to the PPN$^+$ cation successfully used for **20**, but features C_3 point symmetry.

Further potential for optimisation of the trinuclear systems towards high magnetic anisotropy and slow relaxation of magnetisation lies in the coligands. As the distinct behaviour of **22** in comparison with the other compounds shows, aprotic O-donors embedded in cyclic molecules are very advantageous coligands. Of course, THF is one molecule fulfilling these requirements, but replacing it with phthalane might further enhance slow relaxation of magnetisation due to its higher rigidity.

4.4 Tetranuclear Dysprosium Complex

The tetranuclear Dy complex presented in this section was not a deliberately aimed target within the scope of this work, but more a serendipitous product of unexpected reactivity. Nevertheless, the journalisation of this very particular reactivity and the description of the complex's rather unusual structure motivates its inclusion here.

4.4.1 Synthesis and Characterisation

The reaction of three equivalents $DyCl_3 \cdot 6\,H_2O$ with two equivalents of the $H_2pytag \cdot HCl$ ligand in MeOH with an excess pyridine leads to the formation of a tetranuclear Dy complex $[Dy_4(pytag^{cyc})_2(O_2)_2Cl_4(MeOH)_6]Cl_2 \cdot 3\,MeOH \cdot H_2O$ (**23**) In this compound, four Dy(III) ions are bound by two modified chelate ligands $pytag^{cyc-}$, which formally results from an oxidative cyclisation reaction of the original H_2pytag under generation of a central 1,2,4-triazole heterocyclic moiety. Comparable reactivity was already observed by Schuch for the $H_5saltag$ ligand in the presence of Ni(II) ions and aliphatic amines.[239]
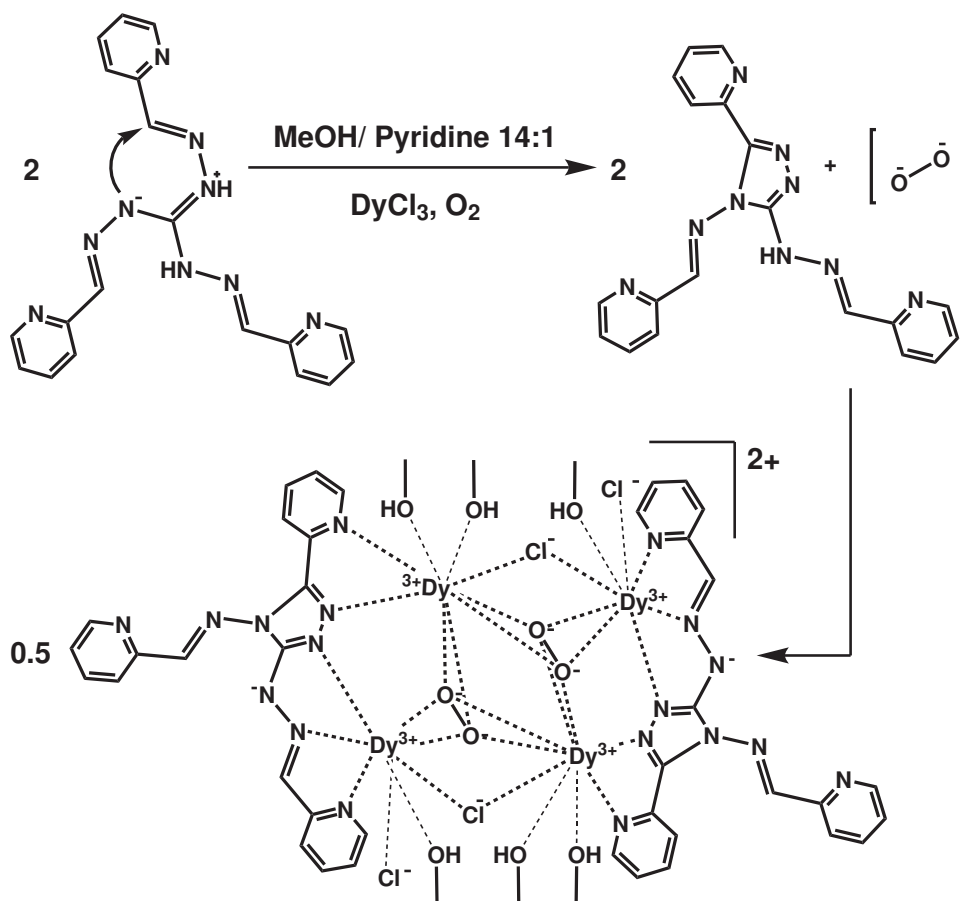
Figure 4.29: Principal reaction scheme of the synthetic route to complex dication $[Dy_4(pytag^{cyc})_2(O_2)_2Cl_4(MeOH)_6]^{2+}$ in **23**. Illustrations do not propose a mechanism but only demonstrate connectivity, charge and species evolving during the reaction.

A general scheme of the reaction, which must not be considered a mechanistic proposal, is

drawn in fig. 4.29. The presumed oxidising agent is molecular oxygen from the surrounding air. Since the cyclisation is a one-electron-oxidation, it has to occur at two H_2pytag molecules to enable the evolution of a formal peroxo-dianion O_2^{2-}. This uncommon species appears to be trapped by the harshly Lewis-acidic but redox-inert Dy(III) ions and is found twice in the composition of the complex. At the same time this necessitates the oxidation of four H_2pytag molecules to generate one complex dication of **23**. This ratio is not provided by the stoichiometry put into the reaction, which explains the very low yields below 10 %.

Besides the single-crystal X-ray diffraction, which initially suggested the unexpected composition of compound **23** it could also be confirmed by elemental analysis and thermogravimetry. However, both methods indicate the partial loss or exchange by water molecules of the cocrystallised and coordinating MeOH. Despite synthetic attempts, till now no analogous complexes of other late lanthanoids could be isolated.

Stable binding of peroxo-dianions in multinuclear lanthanoid arrangements is reported few times in literature,[296–299] also the tetranuclear case with two O_2^{2-} ligands incorporated is already described with additional pyridine and chlorido ligands.[300]

4.4.2 Crystal Structure

Compound **23** crystallises in triclinic space group $P\bar{1}$ (#2). The inversion centre lies within the complex dication $[Dy_4(pytag^{cyc})_2(O_2)_2Cl_4(MeOH)_6]^{2+}$, so that two of the four Dy centres are equivalent by symmetry. Bond lengths and selected angles of the coordination environment of both crystallographically independent metal centres Dy1 and Dy2 are listed in table 4.21 and corresponding depictions can be found in fig. 4.30.

A terminal coordination of the $pytag^{cyc-}$ chelate ligand with one $[N_3]$ and one $[N_2]$ pocket to the distinct metal centres Dy1 and Dy2, respectively, is found. Both centres are bridged by the N–N moiety of the central 1,2,4-triazole in the $pytag^{cyc-}$ as well as by both O-donor atoms O1 and O2 of the O_2^{2-} group. Dy1 is further coordinated by Cl1 and MeOH-based donor O5, which feature a *trans*-angle of 159° and bonding angles around 90° with all other neighbouring donors of Dy1. For Dy2 a comparable position is taken by the MeOH-based donors O3 and O4 (*trans*-angle = 151°). For the completion of the coordination spheres, the inversion symmetry generated second half of the tetranuclear complex is involved. Dy1 is bridged to Dy2' via Cl2 as well as the already mentioned O_2^{2-} group consisting of O1 and O2. Correspondingly, Dy2 is also coordinated by bridging donors Cl2', O1' and O2'. This leads to an overall eightfold $[Cl_2N_3O_3]$ coordination of Dy1 and a formal coordination number nine with a $[ClN_2O_6]$ donor set at Dy2. The coordinative bond lengths range from 232 to 276 pm with the O-donors exhibiting the shortest an the Cl-donors featuring the longest distances. Despite the high charge at the O_2^{2-} group, due to the $\mu_3 - \eta^2 : \eta^2 : \eta^2$ coordination mode the bonding distance is comparable to the neutral MeOH ligands. No particular axis or plane of short contacts can be determined.

Analysing these very coordination environments by means of continuous shape measures,[251–253] a triangular dodecahedron and a spherical capped square antiprism are revealed as closest reference polyhedra for Dy1 and Dy2, respectively. However, the corresponding deviation parameters of 4.382 and 4.111 are very large, so that these reference geometries
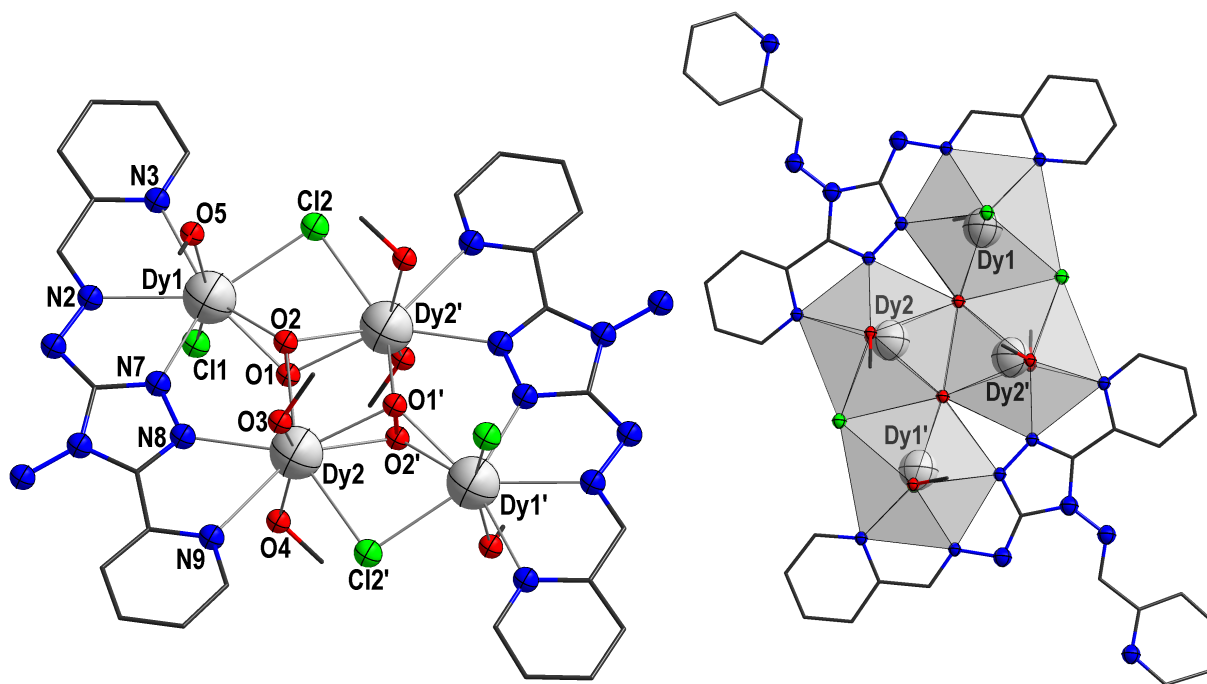
Figure 4.30: Left: Molecular structure of complex dication [Dy$_4$(pytag^{cyc})$_2$(O$_2$)$_2$Cl$_4$(MeOH)$_6$]$^{2+}$ in **23** with atom labels, C atoms are wire nodes, Dy: light grey, N: blue, O: red, Cl: light green. H atoms and counteranions are omitted for clarity. **Right:** Illustration of the distorted pentagonal bipyramidal coordination polyhedra of **23**. View along crystallographic *c*-axis, colour code is identical.

Table 4.21: Selected bond lengths (pm) and angles (°) from the coordination environment of Dy1 and Dy2 in **23**. The corresponding numbering scheme is depicted in fig. 4.30. The different Dy$\cdots$Dy distances are given in the bottom rows. Symmetry generated equivalent atoms are marked with '$(1 - x, 3 - y, 3 - z)$. c(A/B) is the centroid between atoms A and B.

Dy1–N2	252.4(5)	Dy2–N8	243.8(5)
Dy1–N3	257.5(5)	Dy2–N9	279.5(5)
Dy1–N7	234.4(4)	Dy2–O1	241.0(4)
Dy1–O1	233.6(4)	Dy2–O2	238.2(4)
Dy1–O2	237.5(4)	Dy2–O1′	233.8(4)
Dy1–O5	232.2(5)	Dy2–O2′	235.6(4)
Dy1–Cl1	265.81(16)	Dy2–O3	231.9(5)
Dy1–Cl2	270.22(14)	Dy2–O4	235.3(5)
		Dy2–Cl2′	275.59(15)
O5–Dy1–Cl1	159.17(11)	O3–Dy2–O4	151.48(16)
Dy1–c(O1/O2)–Dy2	137.9(2)	Dy2–c(O1′/O2′)–Dy1′	118.5(2)
Dy1–Cl2–Dy2′	88.9(2)	Dy2–c(O1/O2)–Dy2′	103.6(2)
Dy1–N7–N8–Dy2	1.7(2)		
Dy1–Dy2	420.0(5)	Dy2–Dy1′	382.3(5)
Dy1–Dy1′	721.5(5)	Dy2–Dy2′	353.1(5)

are hardly suited to describe the coordination geometry. Instead, an approximation of the O_2^{2-} group as one donor (d_{O1-O2} = 153 pm, bite angles $\approx38°$) represented by its centroid c(O1/O2) delivers a pentagonal bipyramid as closest reference polyhedron for both centres with deviation parameters of 1.496 (Dy1) and 1.312 (Dy2).

A distorted pentagonal bipyramid coordination can also be recognised in the right picture of fig. 4.30. Indeed, the averaged protrusion of all "equatorial" donors in the pentagonal planes from the $\square$Dy$_4$ is only 11 pm (largest value 30 pm of Cl2) and the dihedral angle at the bridging N–N group is almost zero (see table 4.21). Interestingly, this strict arrangement within the metal plane of all but two donors per metal ion is analogously found in the literature-known related $[Dy_4(O_2)_2]^{8+}$ compound,[300] so the central $[Dy_4(O_2)_2]^{8+}$ building block appears to promote this very arrangement.

The rather small intramolecular Dy$\cdots$Dy distances (see table 4.21) especially between Dy2 and Dy2′ are another feature worth emphasising. Intermolecular interactions are not apparent in the crystal structure of **23**, the shortest intermolecular Dy$\cdots$Dy distance is 834 pm.

4.4.3 Concluding Remarks

The tetranuclear compound $[Dy_4(\text{pytag}^{cyc})_2(O_2)_2Cl_4(\text{MeOH})_6]Cl_2 \cdot 3\,\text{MeOH} \cdot H_2O$ (**23**) was serendipitously obtained after accidental air oxidation of the H$_2$pytag ligand. O_2^{2-} species formed during the reaction are trapped in the resulting complex dication. Due to very low yields, long isolation times and high sensitivity of the crystalline material to decomposition no valid set of magnetic data of **23** could be acquired yet.

Nevertheless, **23** exhibits some structural features, which are rather beneficial from a magnetic point of view. First of all, the distorted pentagonal bipyramidal coordination of all four metal centres provides a local C_5 pseudosymmetry, which is very desirable for suppression of QTM.[165] This pseudosymmetry is also found in a related compound lacking structure determining rigid chelate ligands,[300] so the central $[Ln_4(O_2)_2]^{8+}$ moiety appears to promote this symmetry, which makes it an interesting building block for lanthanoid based molecular magnets in general.

At the same time, the short metal$\cdots$metal distances in the core fragment should mediate noteworthy dipolar interactions between the lanthanoid centres in case of pronounced magnetic anisotropy. Therefore, the targeted synthesis of the $[Ln_4(O_2)_2]^{8+}$ fragment with different ligand systems supporting prolate and oblate lanthanoid ions remains of great interest.

Eventually, another conclusion from this section is the necessity to exclude air for the synthesis of lanthanoid complexes, if complexation with the intact H$_2$pytag ligand is aspired.

Summary

The designated aim of this work, to provide molecular magnets to bring forward particular aspects of quantum technologies exploiting tritopic C_3-symmetric ligands based on triaminoguanidine and aromatic aldehydes, was pursued via various pathways. Before treading them, the generation of the appropriate chelate ligands is a prerequisite treated in chapter 2. Besides several well-known triaminoguanidine-based ligands, H_5saltag^I and H_5quintag had not been utilised for the synthesis of molecular magnets prior to this work. The latter ligand is featuring four donor sites per pocket in contrast to other triaminoguanidine-based ligands reported so far.

As a first cornerstone, establishing electric field control over electronic spins in molecular magnets, which are potential Qubit candidates for quantum-based computing would be a great achievement. Along this line, the trinuclear Cu(II) complexes presented in section 3.1 deliver an ideal geometrically frustrated arrangement of isotropic antiferromagnetically coupled spins, which is predicted to couple spins and electric fields via spin-chirality. The frustrated ground state of these molecules is proven by their crystallographic symmetry, magnetic susceptibility measurements and CW X-band ESR studies. Large antiferromagnetic coupling constants around $-300\,\text{cm}^{-1}$ were determined for compounds **1**, **3**, **4** and **5**, which ensures an energetically well isolated $S = \frac{1}{2}$ molecular spin ground state. Hints about the Dzyaloshinsky-Moriya interaction operative in these complexes being negligible could be extracted from the ESR spectra.

By means of chemical modification intermolecular magnetic interactions, which are perturbations to the low energy state structure of the spin system, could be reduced significantly, so that experiments on bulk materials become viable. For the presumably most suitable compound of this family, [Cu$_3$(saltag^H)(py)$_6$]ClO$_4$ (**1**), pulsed ESR experiments in frozen solution with electric fields applied as well as electric field modulated CW X-band ESR measurements show first traces of the proposed spin-electric coupling. For the latter technique, non-centrosymmetric single-crystals are beneficial. While **1** features a polar space group, the entire absence of crystallographic reflection symmetry could be realised in [Cu$_3$(quintag)(py)$_3$]ClO$_4$ (**6**). This is also the first 3d transition metal complex of the novel H_5quintag ligand. This very compound exhibits a weak ferromagnetic interaction between two molecular spin triangles forming hemispherical

dimers in the crystal structure. Therefore it is a realisation of two entangled geometrically frustrated spin qubits. A serendipitous partial ligand oxidation of H_5quintag to H_6quinox, where one hydrazone moiety per chelate ligand is formally converted into a carboxylic acid hydrazide, occurs during the synthesis of **7**. This results in a hexanuclear complex with an armchair topology of Cu(II) centres and a metallacyclophane structure, which despite exclusively antiferromagnetic exchange interactions, features an $S = 1$ molecular spin ground state.

A geometrically frustrated, antiferromagnetically coupled spin triangle situation, was also found in trinuclear Fe(III) high-spin complex fragments, which were successfully bridged into heptanuclear iron complexes via hexacyanometalates as described in section 3.2. The main difference between the two complexes reported there, is the nature of the bridging unit, which is a paramagnetic ferricyanide in one case (**9**) and a diamagnetic ferrocyanide in the other case (**10**), as could be determined by the combined analysis of crystallographic, magnetic susceptibility and Mößbauer data. The difference is perfectly reflected by a significant ferromagnetic intertriangle exchange in **9**, which is very small in **10**. From a functional point of view these systems can be considered as two entangled spin qubits, which could be manipulable by electric fields, whereat the degree of entanglement can be tuned by chemical modification of the hexacyanometalate bridge.

Somewhat different functionality can be expected from Cr(III) complexes discussed in section 3.3. Both, the dinuclear complex **11** and the trinuclear complex **12** show exceptionally high ferromagnetic coupling for homometallic Cr(III) compounds. So the complexes being rather inert to ligand exchange are valuable building blocks for engendering possible extended homo- or heteronuclear high-spin aggregates, which are desired for their magnetic refrigeration capabilities. In the trinuclear complex **12**, also significant Dzyaloshinsky-Moriya interaction is apparent from X-band ESR spectra. Since this phenomenon is hardly described for ferromagnetically coupled Cr(III) topologies, it is exciting at least from an academic point of view.

Besides 3d transition metal complexes, lanthanoid complexes of triaminoguanidine-based ligands form the second main component of this work. Although lanthanoid complexes in general offer versatile exciting properties, this work exclusively focuses on their magnetic functionality. Therefore, despite the synthetic availability of isostructural complexes of all late lanthanoids, essentially Dy(III) complexes are investigated. The central targeted feature is single-molecule magnet (SMM) behaviour, which in perspective might enable applications in data storage and quantum-based computing. Hence, the crucial issue is magnetic relaxation.

In section 4.1 two monodysprosium dialkali metal complexes **13** and **14** are characterised, which are putatively isostructural. Both show the phenomenon of slow relaxation of magnetisation leading to hysteretic behaviour at 2 K, which collapses in the absence of a magnetic field due to prominent quantum tunneling of magnetisation (QTM) and as such is commonly observed especially for mononuclear lanthanoid-based SMMs. Nevertheless, significant differences in the magnetic relaxation behaviour of both compounds are apparent from AC magnetic susceptibility measurements, which cannot be rationalised hitherto, especially due to low structural resolution available for both compounds so far.

Several dinuclear Dy(III) complexes with the unitary core fragment $[Dy_2(H_2saltag^{Br})_2]$ were

successfully synthesised and are described in section 4.2. In general, intramolecular magnetic interactions operative in these compounds lead to a suppression of QTM. This effect is most pronounced in **15**, which thus exhibits open hysteresis at 2 K and the highest blocking temperature T_B among them of over 3 K. The beneficial nature of magnetic interaction could be clearly proven by comparative magnetic surveys with isostructural diamagnetically diluted materials. An analysis of the magnetic relaxation behaviour at higher temperatures as revealed by AC magnetic susceptibility shows, that for the vibrational mode correlated relaxation of magnetisation (VMCRM) and Raman processes dominating these temperature regimes local and molecular symmetry as well as the rigidity of the solvent-based coligands is highly influential. Correspondingly, these processes are most efficiently suppressed in compounds **16** featuring a molecular C_2 symmetry and **17** bearing pyridine coligands.

With different saltag ligands, also trinuclear Dy(III) complexes of the general composition $[Dy_3(saltag)_2]^-$ dealt with in section 4.3 are feasible. Here, in addition to the SMM properties, the orientation of the single-ion easy axes of magnetisation as revealed by *ab-initio* calculations suggests the presence of single-molecule toroic (SMT) behaviour, which is predicted to enable molecular magnetoelectric effects, especially for compound **21**. Unfortunately, no experimental proof of a toroic state could be found within the experiments carried out in the frame of this work. In terms of SMM properties, the formally frustrated triangular arrangement is not advantageous for suppression of magnetic relaxation at very low temperatures. However, the relaxation was again shown to be highly dependent on the solvent based coligands. While MeOH is vastly inappropriate due to its protic nature and rotatable methyl group, a tremendous diminution of QTM and VMCRM was achieved by replacement of the MeOH coligands with THF in **22**. The latter compound accordingly exhibits weak magnetic hysteresis at 2 K.

Among all magnetic relaxation studies, the rigidity of the triaminoguanidine-based ligands must be highlighted as very advantageous, since comparably low VMCRM rates were detected and the relaxation under the thermal barrier provided by magnetic anisotropy is mainly related to the solvent-based coligands. So the use of such chelate ligands for systems, where slow magnetic relaxation is of relevance, is thoroughly advisable.

Finally, a tetranuclear Dy complex binding two peroxo dianions to a $[Dy_4(O_2)_2]^{8+}$ core fragment was isolated after serendipitous oxidation of the H_2pytag ligand to a chelate ligand $Hpytag^{cyc}$ featuring a central 1,2,4-triazole moiety during the synthesis. The resulting complex **23** is coordinatively saturated by two $pytag^{cyc-}$ and further chlorido and MeOH ligands. A magnetic characterisation is lacking at this point, however, the Dy centres feature a local pseudo C_5 symmetry, which should effectively suppress QTM processes.

From a chemical point of view, tritopic C_3-symmetric ligands based on triaminoguanidine and aromatic aldehydes form the fundament of this work. On that, two pillars, namely polynuclear 3d transition metal complexes and polynuclear lanthanoid complexes carry a roof of molecular magnetic functionality. The magnetic studies within both pillars could clearly show benefits of the polynuclearity and interactive nature of the magnetic centres as well as molecular symmetry with respect to suitability for potential quantum technology applications. Hence, the consistently used central ligand scaffold can be considered the mediator of cooperativity in
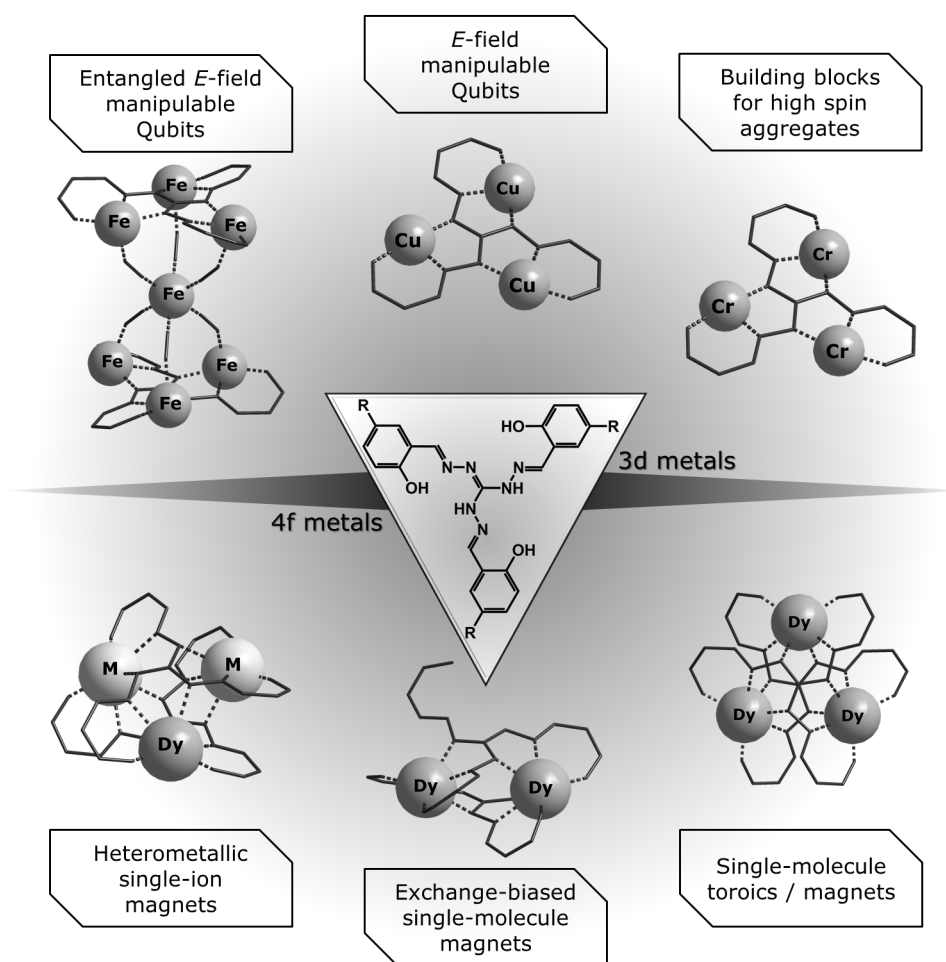
Figure 5.1: Graphical summary of the structural motifs synthesised utilising triaminoguanidine based C_3-symmetric ligands and magnetically characterised in the frame of this work. In the boxes, an assignment in which respect the corresponding molecular magnets might contribute to advancing quantum technologies is given.

that sense. For some compounds consequent steps towards quantum technologies have already been undertaken, for others further optimisation especially with chemical tools is indispensable. Directions of impact for improvement of the particular compound classes and continuative experiments are encouraged in the respective sections.

Zusammenfassung

Das ausgemachte Ziel dieser Arbeit, molekulare Magneten unter Ausnutzung tritoper C_3-symmetrischer Liganden basierend auf Triaminoguanidin und aromatischen Aldehyden zu entwickeln, um den Fortschritt in bestimmten Aspekten von Quantentechnologie zu unterstützen, wurde auf verschiedenen Wegen verfolgt. Bevor diese beschritten werden können, ist die Bereitstellung passender Chelatliganden Voraussetzung, die in Kapitel 2 behandelt wird. Neben einigen wohlbekannten Triaminoguanidin-basierten Liganden wurden H_5saltag^I und H_5quintag nie zuvor für die Synthese molekularer Magneten verwendet. Letzterer weist vier Donorstellen pro Tasche auf, was im Gegensatz zu anderen bisher beschriebenen Triaminoguanidin-basierten Liganden steht.

Ein erster wichtiger Meilenstein wäre die Etablierung einer Kontrolle elektronischer Spins in molekularen Magneten, welche potentielle Qubit-Kandidaten für quantenbasierte Rechnungen darstellen, mittels elektrischer Felder. Mit dieser Zielstellung liefern die trinuklearen Cu(II)-Komplexe, welche in Abschnitt 3.1 vorgestellt werden, eine ideal geometrisch frustrierte Anordnung isotroper, antiferromagnetisch gekoppelter Spins, für die eine Kopplung von Spins und elektrischen Feldern über Spinchiralität vorhergesagt ist. Der frustrierte Grundzustand dieser Moleküle wird durch ihre kristallographische Symmetrie, magnetische Suszeptibilitätsmessungen und CW X-band ESR Studien bewiesen. Stark antiferromagnetische Kopplungskonstanten um $-300\,\mathrm{cm}^{-1}$ wurden für die Verbindungen **1**, **3**, **4** und **5** bestimmt, was einen energetisch wohl-isolierten molekularen $S = \frac{1}{2}$ Spingrundzustand sicherstellt. Hinweise darauf, dass Dzyaloshinsky-Moriya Wechselwirkungen in diesen Komplexen nur in vernachlässigbaren Größenordnungen auftreten, konnten den ESR-Spektren entnommen werden.

Mithilfe chemischer Modifikationen konnte eine signifikante Verringerung intermolekularer magnetischer Wechselwirkungen erzielt werden, die Störungen der Zustandsstruktur des Spinsystems bei niedriger Energie darstellen, sodass Versuche in Reinsubstanz zugänglich werden. Für die mutmaßlich am besten geeignete Verbindung dieser Serie, $[\mathrm{Cu_3(saltag^H)(py)_6}]\mathrm{ClO_4}$ (**1**), zeigen gepulste ESR-Experimente in gefrorener Lösung mit angelegten elektrischen Feldern sowie elektrisches Feld modulierte CW X-band ESR Messungen erste Spuren der vorgeschlagenen Spin-elektrischen Kopplung. Für die letztgenannte Technik sind nicht-zentrosymmetrische

Einkristalle von Vorteil. Obgleich **1** eine polare Raumgruppe aufweist, zeigt sich in Verbindung [Cu$_3$(quintag)(py)$_3$]ClO$_4$ (**6**) die vollständige Abwesenheit kristallographischer Spiegelsymmetrie. Es handelt sich außerdem um den ersten 3d-Übergangsmetallkomplex des neuartigen H$_5$quintag Liganden. Eben dieser Verbindung wohnt eine schwache ferromagnetische Wechselwirkung zwischen jeweils zwei molekularen Spindreiecken inne, die hemisphärische Dimere in der Kristallstruktur ausbilden. Die Verbindung kann daher als Realisierung zweier verschränkter geometrisch frustrierter Spin-Qubits betrachtet werden. Eine ungewollt auftretende teilweise Oxidation des Liganden H$_5$quintag zu H$_6$quinox, wobei eine Hydrazon-Gruppe pro Chelatligand formal in ein Carbonsäurehydrazid umgewandelt wird, findet während der Synthese von **7** statt. Dies führt zu einem hexanuklearen Komplex mit einer Sessel-Topologie der Cu(II)-Zentren und einer Metallacyclophan-Struktur, welcher trotz ausschließlich antiferromagnetischer Wechselwirkungen einen molekularen $S = 1$ Spingrundzustand zeigt.

Eine geometrisch frustrierte, antiferromagnetisch gekoppelte Spindreieckssituation wurde gleichermaßen in trinuklearen Fe(III) *high spin* Komplexfragmenten vorgefunden, die mittels Hexacyanometallaten erfolgreich zu heptanuklearen Eisenkomplexen verbrückt wurden, wie in Abschnitt 3.2 beschrieben ist. Der Hauptunterschied zwischen den beiden hier vorgestellten Komplexen ist die Natur der verbrückenden Einheit, die in einem Fall (**9**) ein paramagnetisches Ferricyanid und im anderen Fall (**10**) ein diamagnetisches Ferrocyanid ist, wie durch gemeinsame Analyse kristallographischer, magnetischer Suszeptibilitäts- und mößbauerspektroskopischer Daten ermittelt werden konnte. Dieser Unterschied wird durch eine signifikante ferromagnetische interdreiecks-Austauschwechselwirkung in **9** widergespiegelt, welche in **10** sehr gering ist. Aus funktioneller Sicht können diese Systeme als zwei verschränkte Spin-Qubits betrachtet werden, manipulierbar durch elektrische Felder, wobei der Grad der Verschränkung durch chemische Modifikation der Hexacyanometallat-Brücke beeinflussbar ist.

Eine etwas andere Funktionalität ist für die Cr(III)-Komplexe zu erwarten, die in Abschnitt 3.3 diskutiert werden. Sowohl der dinukleare Komplex **11** als auch der trinukleare Komplex **12** zeigen für homometallische Cr(III)-Verbindungen außergewöhnlich hohe ferromagnetische Kopplungen. Da die Komplexe eher inert gegenüber Ligandenaustausch sind, bilden sie wertvolle Bausteine um mögliche erweiterte homo- oder heteronukleare Hochspinaggregate zu erzeugen, die unter anderem aufgrund ihrer Eignung für magnetische Kühlung gefragt sind. Im trinuklearen Komplex **12** zeigt sich außerdem merkliche Dzyaloshinsky-Moriya Wechselwirkung anhand von X-band ESR-Spektren. Da dieses Phänomen für ferromagnetisch gekoppelte Cr(III)-Topologien bisher kaum beschrieben ist, ist es mindestens von akademischem Interesse.

Neben 3d-Übergangsmetallkomplexen bilden Lanthanoidkomplexe triaminoguanidinbasierter Liganden die zweite Hauptkomponente dieser Arbeit. Obzwar Lanthanoidkomplexe generell vielfältige spannende Eigenschaften zeigen, beschäftigt sich diese Arbeit ausschließlich mit ihren magnetischen Eigenschaften. Daher werden trotz der synthetischen Verfügbarkeit isostruktureller Komplexe aller späten Lanthanoide hauptsächlich Dy(III)-Komplexe untersucht. Die zentral anvisierte Eigenschaft ist Einzelmolekülmagnet(SMM)-verhalten, die perspektivisch Anwendungen als Datenspeicher und für quantenbasiertes Rechnen ermöglichen könnte. Demgemäß ist magnetische Relaxation das zentrale Problem.

Im Abschnitt 4.1 werden zwei Monodysprosium-Dialkalimetallkomplexe **13** und **14** charakterisiert, die mutmaßlich isostrukturell sind. Beide zeigen das Phänomen langsamer Relaxation der Magnetisierung, was zu hysteretischem Verhalten bei 2 K führt. Aufgrund von ausgeprägtem Quantentunneln der Magnetisierung (QTM) bricht die Hysterese jedoch in Abwesenheit eines Magnetfelds zusammen. Dieses Phänomen wird insbesondere für mononukleare lanthanoidbasierte SMMs häufig beobachtet. Dessen ungeachtet sind signifikante Unterschiede im magnetischen Relaxationsverhalten beider Verbindungen aus den magnetischen AC-Suszeptibilitätsmessungen ersichtlich, die bislang insbesondere wegen der geringen verfügbaren strukturellen Auflösung der Verbindungen nicht erklärt werden können.

Mehrere dinukleare Dy(III)-Komplexe mit dem einheitlichen Kernfragment $[Dy_2(H_2saltag^{Br})_2]$ wurden erfolgreich synthetisiert und sind in Abschnitt 4.2 beschrieben. Generell bewirken intramolekulare magnetische Wechselwirkungen eine Unterdrückung des QTM in diesen Verbindungen. Jener Effekt ist in Verbindung **15** am stärksten ausgeprägt, die demgemäß offene Hysterese bei 2 K und die höchste Blocktemperatur T_B von über 3 K unter diesen Komplexen zeigt. Die vorteilhaften Auswirkungen der magnetischen Wechselwirkungen konnten eindeutig durch vergleichende magnetische Untersuchungen mit isostrukturellen diamagnetisch verdünnten Materialien belegt werden. Eine Analyse des magnetischen Relaxationsverhaltens bei höheren Temperaturen, aufgezeigt durch magnetische AC-Suszeptibilitätsmessungen, ergibt, dass die lokale und molekulare Symmetrie sowie die Rigidität der lösungsmittelbasierten Koliganden einen starken Einfluss auf die schwingungsmodenkorrelierte Relaxation der Magnetisierung (VMCRM) und die Raman-Prozesse haben, welche dieses Temperaturregime dominieren. Dementsprechend werden diese Prozesse am effektivsten in den Verbindungen **16**, die eine C_2-Symmetrie aufweist, und **17**, die Pyridin-Koliganden trägt, unterdrückt.

Mit verschiedenen saltag-Liganden sind auch trinukleare Dy(III)-Komplexe der grundlegenden Zusammensetzung $[Dy_3(saltag)_2]^-$ zugänglich, die in Abschnitt 4.3 behandelt werden. Zusätzlich zu SMM-Eigenschaften weist die durch *ab-initio* Rechnungen ermittelte Orientierung der Einzelionen-Hauptmagnetisierungsachsen zueinander auf das Vorliegen von toroidalem Einzelmolekül(SMT)-Verhalten hin. Solches Verhalten ist vor allem in Verbindung **21** wahrscheinlich und soll laut theoretischen Vorhersagen magnetoelektrische Effekte ermöglichen. Leider konnte kein experimenteller Beweis eines toroidalen Zustands innerhalb der Untersuchungen im Rahmen dieser Arbeit erbracht werden. Hinsichtlich SMM-Eigenschaften ist die formal frustrierte dreieckige Anordnung nicht vorteilhaft für die Unterdrückung magnetischer Relaxation bei sehr niedrigen Temperaturen. Allerdings konnte einmal mehr gezeigt werden, dass die magnetische Relaxation in höchstem Maße von den lösungsmittelbasierten Koliganden abhängt. Während MeOH aufgrund seiner protischen Natur und der rotierbaren Methylgruppe ausgesprochen ungeeignet ist, wurde eine erhebliche Verringerung des QTM und VMCRM durch das Ersetzen der MeOH Koliganden mit THF in **22** erreicht. Letzterer Komplex zeigt passend dazu eine schwache magnetische Hysterese bei 2 K.

Über alle magnetischen Relaxationsstudien hinweg muss die Steifigkeit der triaminoguanidinbasierten Liganden als sehr vorteilhaft hervorgehoben werden. Es wurden vergleichsweise
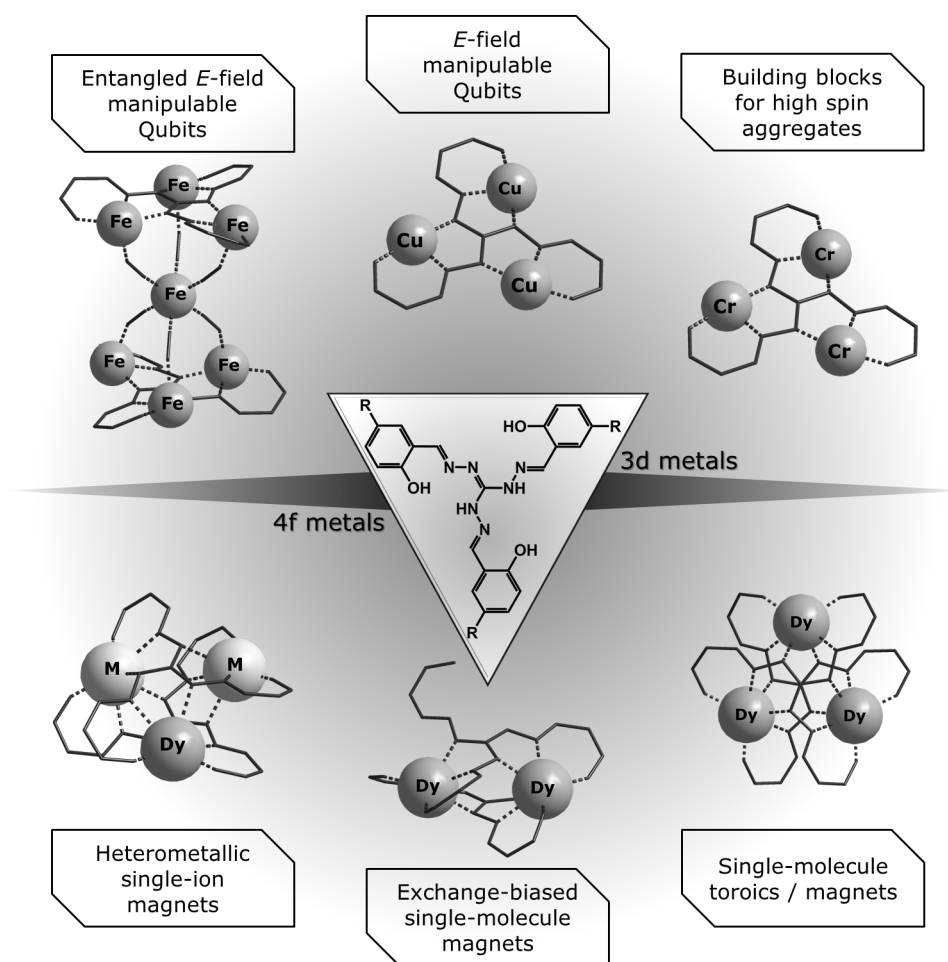
Abbildung 6.1: Graphische Zusammenfassung der Strukturmotive, die unter Verwendung von Triaminoguanidin-basierten C_3 symmetrischen Liganden im Rahmen dieser Arbeit synthetisiert und magnetisch charakterisiert wurden. In den Kästen erfolgt eine Zuordnung, inwiefern die jeweiligen molekularen Magneten zum Fortschritt von Quantentechnologien beitragen könnten.

niedrige VMCRM-Raten detektiert und die Relaxation unter der durch magnetische Anisotropie hervorgerufenen thermischen Barriere hängt hauptsächlich mit den lösungsmittelbasierten Koliganden zusammen. Somit ist der Einsatz solcher Chelatliganden für Systeme, bei denen langsame magnetische Relaxation relevant ist, zutiefst empfehlenswert.

Schließlich wurde ein tetranuklearer Dy-Komplex isoliert, der zwei Peroxo-Dianionen in einem $[Dy_4(O_2)_2]^{8+}$ Kernfragment bindet. Nach ungewollter Oxidation des H$_2$pytag Liganden während der Synthese entstand der Chelatligand Hpytag^{cyc}, der eine zentrale 1,2,4-Triazol-Einheit aufweist. Der resultierende Komplex **23** wird von zwei pytag$^{cyc\,-}$ und weiteren Chlorido und MeOH Liganden koordinativ abgesättigt. Eine magnetische Charakterisierung steht zum jetzigen Zeitpunkt noch aus, allerdings weisen die Dy-Zentren eine lokale C_5 Pseudosymmetrie auf, die effektiv QTM-Prozesse unterdrücken sollte.

Aus chemischer Sicht bilden tritope C_3-symmetrische Liganden basierend auf Triaminoguanidin und aromatischen Aldehyden das Fundament dieser Arbeit. Darauf tragen zwei Säulen, nämlich polynukleare 3d-Übergangsmetallkomplexe und polynukleare Lanthanoidkom-

plexe ein Dach von molekularmagnetischer Funktionalität. Die magnetischen Studien innerhalb beider Säulen ergaben klare Vorteile der Polynuklearität und wechselwirkenden Natur der magnetischen Zentren sowie der molekularen Symmetrie in Bezug auf Eignung für potentielle Anwendungen in der Quantentechnologie. Dementsprechend, kann das einheitlich verwendete zentrale Ligandgerüst in diesem Sinne als Vermittler von Kooperativität verstanden werden. Für einige Verbindungen wurden bereits folgerichtige Schritte hin zu Quanten-Technologien unternommen, bei anderen ist eine Optimierung insbesondere mit chemischen Werkzeugen unerlässlich. Stoßrichtungen für Verbesserungen der einzelnen Verbindungsklassen und weiterführende Experimente werden in den jeweiligen Abschnitten angeregt.

EXPERIMENTAL PROCEDURES

7.1 Instrumentation & Materials

If not stated differently, all chemicals used were purchased from commercial sources in synthesis grade and used without further purification. Common solvents were distilled prior to use, alcohols, acetonitrile, ethers and pyridine were distilled over CaH_2 prior to use. For all analyses exclusively crystalline material of the synthesised compounds was used.

Infrared spectroscopy:

IR-spectra were recorded on an FT-IR spectrometer of the Type Vertex 70 by Bruker. The solid Samples were placed on a Golden-Gate-ATR unit by Specac for measurement.

Mass spectrometry:

Electrospray-Ionisation (ESI) mass spectra were recorded on a MAT SSQ710 spectrometer by Bruker.

Elemental analyses:

The elemental analyses were measured on a EURO EA CHNSO Analyser by HEKAtech and a VARIO EL III Analyser by Elementar Analysensysteme.

Thermogravimetry:

Thermogravimetric analyses were carried out on a simultaneous thermogravimetry - dynamic differential calorimetry apparatus STA 409 PC by Netzsch.

NMR-spectroscopy:

NMR-spectra were measured on an AVANCE 400 spectrometer by Bruker at ambient temperature.

X-ray diffractometry:

If not stated differently, on single-crystals, X-ray diffractometry data was collected on a Nonius Kappa CCD-diffractometer with Mo-K$_\alpha$ radiation (λ = 71,073 pm, graphite-monochromator) in a nitrogen stream. Structures were solved by direct methods (SHELXS)[301,302] and structural refinement performed via full-matrix least squares techniques against F^2 with (SHELXL).[301,302] Synchrotron X-ray diffraction data was collected at P11 beamline at PETRA III, DESY Hamburg.[303,304]

X-ray diffraction measurements on powdered samples were performed on a Stoe Powder Diffractometer with a Mythen 1K detector at room temperature. Measurements were done using capillary tubes while the Debye Scherrer Scan Mode was applied with a 2Θ scan type.

SQUID magnetometry:

If not stated differently, magnetic measurements were performed on powdered samples in gelatine capsules on a Quantum-Design MPMS-5 SQUID magnetometer. For crystals sensitive to decomposition, the sample was immediately put into a PTFE capsule designed for inert sample preparation, which was charged with paraffin oil (melting point $-25°$ C) beforhand and ground in that very capsule under paraffin.

The temperature-dependent magnetic susceptibility data (DC) were collected in a temperature range from 2 to 300 K applying a magnetic field of 1000 and 2000 Oe. The temperature and frequency dependent magnetic susceptibility (AC) measurements were performed in the temperature range stated, respectively, applying magnetic fields of 0, 400 and 1000 Oe with an alternating field amplitude of 1 Oe using various frequencies from 10 – 1500 Hz. All data were corrected for the susceptibility of the capsule and the diamagnetic contribution of the sample. For direct relaxation measurements, an initial magnetic field of 10 kOe is set, which is subsequently switched to 0, 400 or 1000 Oe, respectively, and the magnetisation is continuously measured in time intervals of about 12 s.

Processing and fitting of magnetic data was carried out by means of the programs DAVE,[305] PHI[255] and Origin.[306] Fitting criteria for the extraction of relaxation times τ_T from AC-susceptibility as well as direct relaxation measurements were a numeric fit error of τ_T below 10% and a maximum appearing in the χ'' vs. ω plot (for AC-susceptibility).

ESR spectroscopy:

X-band ESR spectra were measured on a Bruker Elexsys 580 spectrometer equipped with a He-flow cryostat for temperature control. The samples are contained in standard 3 mm diameter quartz ESR tubes. Simulations of the spectra were carried out by means of EasySpin program.[307]

7.2 Ligand Syntheses

Triaminoguanidine hydrochloride was synthesised according to a literature known method. The triaminoguanidine based ligands $H_5saltag^H \cdot HCl$,[227] $H_5saltag^{Br} \cdot HCl$[234] and $H_2pytag \cdot HCl$[249] were prepared via slightly modified respective literature procedures, which are analogue to the one given for $H_5saltag^I \cdot HCl$.

$H_5saltag^I \cdot HCl$

A MeOH (15 mL) solution of 4-iodosalicylaldehyde (1.84 g, 7.42 mmol) is stirred at 50 °C and triaminoguanidine hydrochloride (0.34 g, 2.43 mmol) is dissolved in water (5 mL) and added dropwise. The mixture is stirred at 50 °C for two more hours and subsequently stirred overnight at room temperature, which is accompanied by the formation of a light yellow and very fine precipitate. The precipitate ideally is allowed to ripen in the sealed vessel for one day. Then, the suspension is filtered through a glass frit (G2 or G3) repeatedly to exploit the formed cake

for filtration. The solid on the frit is washed with cold MeOH and twice with Et_2O. Still, a significant product fraction is dispersed in the combined filtrates, which is separated via centrifugation, followed by the same washing steps in the centrifuge. The collected solid is dried under vacuum (hose frit and tissue in ground joint!) at 50 °C for at least half a day and stored in an evacuated desiccator loaded with P_2O_5. Typical yields are above 90 %. Possible residual water content can be determined by means of thermogravimetric analysis. The product needs to be stored in brown glass containers.

^{1}H-NMR: 400 MHz, in DMSO-d_6, δ [ppm] = 6.87 (d, 3H), 7.61 (d, 3H), 8.48 (s, 3H), 8.97 (s, 3H), 10.79 (s, 3H), 12.11 (s, 3H).

IR $\widetilde{\nu}$ [cm^{-1}] = 3639 (w), 3083 (m, br), 1630/1604 (vs, br), 1479 (s), 1411 (s), 1352 (m), 1282 (s), 1239 (s), 1177 (m), 1124 (m), 1090 (s), 955 (m), 818 (s).

H₅quintag · HCl

8-Hydroxyquinoline-2-carboxaldehyde (5.01 g, 28.9 mmol) is suspended in MeOH (250 mL, high dilution needed to maintain a stirrable suspension later in the synthesis) and heated under reflux to achieve dissolution. To the warm solution, an aqueous (15 mL) solution of triaminoguanidine hydrochloride (1.33 g, 9.45 mmol) is added and the resulting orange slurry is stirred overnight. The formed solid is separated by centrifugation and washed with MeOH and Et_2O by resuspension and subsequent centrifugation. The obtained solid is consecutively dried under air, under vacuum at 50° C and finally in an evacuated desiccator loaded with P_2O_5. Grinding of the material between the drying steps is beneficial. Typical yields are above 80 %, a possible residual water content can be determined by thermogravimetric analysis. The product needs to be stored in brown glass containers.

^{1}H-NMR: 400 MHz, in DMSO-d_6, δ [ppm] = 7.20 (d, 3H), 7.51 (m, 6H), 8.50 (d, 3H), 8.64 (d, 3H), 9.05 (s, 3H), 10.02 (s, 3H).

IR $\widetilde{\nu}$ [cm^{-1}] = 3323 (w), 3048 (m, br), 1624 (vs, br), 1591 (s), 1564 (m), 1505 (s), 1464 (s), 1384 (m), 1330 (s), 1236 (s), 1192 (m), 1105 (vs, br), 832 (s), 755 (s).

7.3 3d Metal Complexes

[Cu₃(saltag^H)(py)₆]ClO₄ · 0.5 HpyClO₄ · 2 H₂O (1)[250]

$Cu(ClO_4)_2 \cdot 6\,H_2O$ (619 mg, 1.67 mmol) and H_5saltag · HCl (252 mg, 0.56 mmol) are dissolved in DMF (50 mL) under mild heating. A solution of triethylamine (340 mg, 3.36 mmol) in DMF (5 mL) is added and the whole mixture transferred dropwise over 30 min into refluxing MeOH (30 mL) followed by the subsequent addition of DMF (5 mL) and MeOH (20 mL) to the still boiling reaction mixture. After further refluxing for 5 min the suspension is slowly cooled down to 3 °C and maintained at this temperature for several hours. The precipitated green solid is filtered off, washed with MeOH and dried in air overnight to give an amorphous precursor material.

This material is suspended in EtOH (20 mL) and under reflux conditions the same volume of pyridine (20 mL) is added stepwise over a period of 5 min followed by further 30 min of heating. The hot suspension is filtered and the filtrate subsequently cooled to $-25\,°C$ (with intermediate steps at $3\,°C$ and $-10\,°C$ each maintained for about 24 h) to give a first crop of very small dark green crystals with a blueish shimmer (yield ≈ 50 mg). Heating the solid remaining in the filter in pyridine (5 mL) gives a saturated solution of the complex, which is filtered into a test tube at room temperature, followed by subsequent layering with a pyridine/EtOH mixture (3 mL) and an EtOH solution of $NaClO_4$ (≈ 100 mg). After sealing, leaving the tube unmoved at room temperature for several weeks affords large crystals of **1**.

ESI-MS (positive in MeOH): m/z = 634 (40%, $[Cu_3(saltag) \cdot MeOH]^+$), 666 (100%, $[Cu_3(saltag) \cdot 2\,MeOH]^+$), 698 (25%, $[Cu_3(saltag) \cdot 3\,MeOH]^+$).

Elemental Analysis: Calculated for $C_{54.5}H_{48}N_{12.5}Cu_3Cl_{1.5}O_9$ (M-2H$_2$O): C 51.71; H 3.82; N 13.83%. Found: C 52.03; H 3.82; N 14.03%.

IR $\widetilde{\nu}\,[cm^{-1}]$ = 3058 (w), 3017 (w), 1596 (s), 1478/1463/1443 (vs), 1361 (s), 1198 (s), 1095/1065 (vs), 751 (s), 697 (vs).

$[Zn_3(saltag^H)(py)_6]ClO_4 \cdot 0.5\,H_2O$ (2)

$Zn(ClO_4)_2 \cdot 6\,H_2O$ (256 mg, 0.69 mmol) is dissolved in pyridine (2 mL) in a test tube and carefully layered with pyridine (3 mL). Subsequently a solution of $H_5saltag^H \cdot HCl$ (92 mg, 0.2 mmol) in a mixture of pyridine (1.5 mL) and MeOH (5 mL) is layered above in the test tube, which is then sealed and left unmoved at room temperature for two weeks. Collection of the rod shaped crystals followed by dabbing on filter paper yields about 150 mg of **2**.

Elemental analysis: Calculated for $C_{52}H_{46}N_{12}O_{7.5}ClZn_3$ (M): C 52.45; H 3.89; N 14.12. Found: C 52.24; H 3.80; N 14.25.

IR: $\widetilde{\nu}\,[cm^{-1}]$ = 3076 (w), 3016 (w), 1598 (s), 1447/1430 (vs, br), 1361 (s), 1193 (s), 1093/1066 (vs, br), 914 (m), 753 (s), 625 (s).

$[Cu_3(saltag^H)(py)_6]NO_3$ (3)

A mixture prepared by subsequent addition of DMF solutions of $Cu(NO_3)_2 \cdot 3\,H_2O$ (210 mg, 0.87 mmol in 5 mL), $H_5saltag^H \cdot HCl$ (126 mg, 0.28 mmol in 10 mL) and NEt_3 (169 mg, 1.67 mmol in 5 mL) is heated and slowly added to boiling MeOH (25 mL). The resulting suspension is left until cooled to room temperature and stored at $3\,°C$ for 24 h followed by filtration. The obtained solid precursor material is washed with MeOH and dried under air overnight. This solid is refluxed in pyridine (10 mL) with some MeOH to lower the heat in the vessel for one hour. The mixture needs to cool down to room temperature before it is filtered into a test tube. The dark green solution is now layered, first with MeOH (3 mL including some drops of pyridine), then with a solution of $NaNO_3$ (≈ 100 mg) in MeOH (10 mL). Sealing the tube and leaving it unmoved at room temperature for at least one month leads to formation of first dark green rod shaped crystals. Opening the test tube to slowly evaporate the solvent affords further crystal

growth. Crystals are picked from the liquor and dabbed to dryness on filter paper, like this yields of about 60 mg are achieved.

ESI-MS (positive in MeOH/DMF): $m/z = 602$ (100 %): $[Cu_3(saltag^H)]^+$ ($C_{22}H_{15}Cu_3N_6O_3^+$); (negative in MeOH/DMF): $m/z = 821$ (100 %): $[Cu_3(saltag^H-H^+)(py)_2NO_3]^-$ ($C_{32}H_{24}Cu_3N_9O_6^-$).

Elemental analysis: Calculated for $C_{47}H_{44}Cu_3N_{12}O_8$ (M−Py+2H$_2$O): C 51.53; H 4.05; N 15.34. Found: C 51.91; H 3.87; N 15.32.

IR: $\widetilde{\nu}$ [cm^{-1}] = 3362 (w, br), 3072 (w, mult), 2930 (w), 1597 (s), 1478 (vs), 1446 (s), 1360 (s), 1336 (s, br), 1198 (s), 1114 (s), 753 (vs), 696 (vs).

[Cu₃(saltag^H)(py)₃]OTf   (4)

The synthesis is similar to the one of **3**, but uses Cu(OTf)$_2$ (305 mg, 0.84 mmol) instead of Cu(NO$_3$)$_2 \cdot 3$ H$_2$O and replaces NaNO$_3$ with NaOTf ($\approx$ 100 mg). Dark green crystals are obtained some weeks after layering, their shape is rather trigonal or hexagonal conoid.

ESI-MS (positive in MeOH): $m/z = 666$ (100 %): $[Cu_3(saltag^H)(MeOH)_2]^+$ ($C_{24}H_{23}Cu_3N_6O_5^+$).

Elemental analysis: Calculated for $C_{38}H_{30}Cu_3F_3N_9O_6S$ (M): C 46.18; H 3.06; N 12.75; S 3.24. Found: C 45.96; H 3.00; N 12.39; S 2.99.

IR: $\widetilde{\nu}$ [cm^{-1}] = 3087 (w), 3055 (w), 3010 (w), 1597 (s), 1480/1450 (vs, br), 1360 (s), 1337 (s), 1261 (vs), 1198 (s), 1139 (s), 1026 (vs), 751 (vs), 690 (vs).

[Cu₃(saltag^H)(bpy)₃]OTf   (5)

The synthesis procedure is borrowed from literature.[246] Cu(OTf)$_2$ (362 mg, 1 mmol) and H$_5$saltag$^H \cdot$ HCl (151 mg, 0,33 mmol) are dissolved separately in DMF (4 mL each) and combined together with a solution of NEt$_3$ (202 mg, 2 mmol) in DMF (2 mL) and left to stand overnight. The resulting mixture is filtered into a test tube and consecutively layered with a DMF/MeOH mixture (4 mL, 3:1) and a solution of 2,2'-bipyridine (151 mg, 1 mmol) in MeOH (12 mL). The tube is sealed and left unmoved at room temperature. Dark green crystals form after some weeks, which are collected from the test tube and dabbed to dryness on filter paper (yield $\approx$ 80 mg).

ESI-MS (positive in MeOH): $m/z = 634$ (15 %): $[Cu_3(saltag^H)(MeOH)]^+$ ($C_{23}H_{19}Cu_3N_6O_4^+$).

Elemental analysis: Calculated for $C_{59}H_{53}Cu_3F_3N_{14}O_8S$ (M+2dmf): C 51.88; H 3.91; N 14.36; S 2.35. Found: C 51.61; H 4.13; N 14.14; S 2.11.

IR: $\widetilde{\nu}$ [cm^{-1}] = 3077 (w), 2933 (w), 1670 (m), 1592 (s), 1471/1461 (vs, br), 1385 (s), 1336 (m), 1258 (s, br), 1197 (s), 1151 (s), 1100 (s), 1027 (vs), 760 (vs), 690 (vs).

[Cu₃(quintag)(py)₃]ClO₄   (6)

To a solution of Cu(ClO$_4$)$_2 \cdot 6$ H$_2$O (117 mg, 0.32 mmol) in MeOH (5 mL) H$_5$quintag $\cdot$ HCl (66 mg, 0,1 mmol) is added as DMF (2.5 mL) solution. Upon subjoining of NEt$_3$ (65 mg, 0.64 mmol) in MeOH (5 mL) a precipitate starts to form. This suspension is stored at 3 °C overnight. Subse-

quent filtration followed by washing with MeOH and drying under air yields the dark reddish brown precursor material, which is redissolved in pyridine (≈ 2 mL, without heating!). The resulting obscure brown solution is filtered into a test tube and sequentially layered with a pyridine MeOH mixture (2 mL, 1:1) and a MeOH (5 mL) solution of $NaClO_4$ (≈ 80 mg). The tube is sealed and left unmoved at room temperature. Dark brown crystals grow within several months without visible change in the extinction of the mother liquor, which are cropped, dabbed to dryness on filter paper (yield ≈ 20 mg).

Elemental analysis: Calculated for $C_{59}H_{53}Cu_3F_3N_{14}O_8S$ (M+0.5MeOH+0.5H_2O): C 50.00; H 3.25; N 15.05. Found: C 49.93; H 3.58; N 14.96.

IR: $\widetilde{\nu}$ [cm^{-1}] = 3156 (br), 3059 (w), 2921 (m), 2851 (m), 2812 (w), 1591 (w), 1554 (m), 1498 (s), 1436 (s), 1369 (s), 1330 (s), 1120 (s, br), 1032 (s), 826 (s, sh), 744 (vs), 702 (s), 674 (s).

$[Cu_6(quintag^{ox})_2(py)_4] \cdot py \cdot 2\,MeOH$ (7)

Heat is applied to a solution of $CuCl_2 \cdot 2\,H_2O$ (52 mg, 0.3 mmol) in MeOH (5 mL) keeping it somewhat below the boiling point, when the addition of H_5quintag $\cdot$ HCl (66 mg, 0,1 mmol) in DMF (2 mL) initiates the formation of a rust-red precipitate. Under continuous heating NEt_3 (65 mg, 0.64 mmol) in MeOH (5 mL) solution is subjoined leading to interim dissolution of the precipitation immediately followed by the formation of a dark solid. The suspension is cooled to room temperature and stored at 3 °C overnight. After filtration and washing with MeOH the obtained solid is dried under air. This precursor material is redissolved in pyridine (2 mL), filtered into a test tube and carefully layered with first a pyridine/MeOH mixture (2 mL, 1:1) and second MeOH (8 mL) and finally sealed and left unmoved at room temperature. Small dark brown crystals form after several weeks without visible change in the extinction of the mother liquor. After picking the crystals from the tube, they are dabbed to dryness on filter paper (yield ≈ 15 mg). After mechanical intrusion into the solution further amounts of microcrystalline solid forms at the tube walls suggesting that significantly longer crystallisation times and/or opening the vessel for solvent evaporation and ambient moisture diffusion could increase the yield.

Elemental analysis: Calculated for $C_{62}H_{42}Cu_6N_{18}O_{12}$ (M-2py+2H_2O): C 46.18; H 2.63; N 15.64. Found: C 46.22; H 2.49; N 15.27.

IR: $\widetilde{\nu}$ [cm^{-1}] = 3300 (m, br), 3029 (w), 1567/1553 (m), 1484 (s), 1443 (s), 1369 (s), 1331 (s), 1105 (s), 828 (s), 741 (vs), 669 (m), 611 (s, sh).

$[K(18\text{-crown-}6)][(Fe_3saltag^HCl_3(py)_6)_2\mu(Fe(CN)_6)]$ (9)

$FeCl_3 \cdot 6H_2O$ (106 mg, 0.39 mmol) and $H_5L^H \cdot$HCl (59 mg, 0.13 mmol) are jointly dissolved in pyridine (8 mL) resulting in an intense dark green solution. A mixture of $K_3[Fe(CN)_6]$ (21 mg, 0.065 mmol) and 18-crown-6 (75 mg, 0.28 mmol) in MeOH (3 mL) is added as a clear solution and the whole solution is stirred for another 5 min. Then the solution is transferred into a 25 mL tube through a paper filter followed by careful layering with toluene/pyridine (1:1, 2 mL) and toluene (12 mL). Storage of the sealed tube at 3 °C without any movement for about four weeks

leads to slow diffusion of the layers yielding dark green crystals. The crystalline material is isolated, adherent solvent is dabbed off by means of filter paper and is dried under air overnight (yield $\approx$ 90 mg, 0.03 mmol, 50 %).

Elemental analysis: Calculated for $C_{114}H_{110}Cl_9Fe_7KN_{27}O_{12}$ (M+toluene): C, 48.91; H, 3.96; N, 13.51. Found: C, 48.88; H, 4.17; N, 13.27.

IR: $\tilde{\nu}$ [cm^{-1}] = 3386 (w, br), 3060 (w), 2579 (w, br), 2062 (vs), 1595 (s), 1542 (m), 1447 (vs), 1425 (s), 1366 (s), 1097 (vs).

[(KFe$_3$saltag^{Br}Cl$_3$(py)$_3$)$_2\mu$(Fe(CN)$_6$)] (10)

Dissolution of FeCl$_3$·6H$_2$O (106 mg, 0.39 mmol) and H$_5$L^{Br}·HCl (90 mg, 0.13 mmol) in pyridine (8 mL) gives a dark green clear solution to which a mixture of K$_3$[Fe(CN)$_6$] (21 mg, 0.065 mmol) and 18-crown-6 (70 mg, 0,26 mmol) dissolved in MeOH (2 mL) is added. After 5 min of further stirring the solution is filtered into a 25 mL tube and carefully layered first with toluene/pyridine (1:1, 2 mL) then with a solution of NBz$_3$ (75 mg/0,26 mmol) in toluene (12 mL). The sealed tube is stored at +3° C without any movement. After approximately 5 weeks dark green crystalline **2** suitable for single-crystal x-ray diffraction has formed. Adherent solvent residues are removed from the crystals by dabbing with filter paper and they are subsequently dried under air overnight (yield $\approx$ 110 mg, 0.04 mmol, 60 %)).

Elemental analysis: Calculated for $C_{87.5}H_{65.5}Br_6Cl_6Fe_7K_2N_{25.5}O_8$ (M·1.5 pyridine): C, 38.03; H, 2.39; N, 12.93. Found: C, 37.98; H, 2.51; N, 12.42.

IR: $\tilde{\nu}$ [cm^{-1}] = 3072 (w), 2066 (vs), 1590 (s), 1527 (s), 1459 (s), 1429 (vs), 1393 (s), 1355 (vs), 1297 (s), 1183 (s), 1066 (s).

[Cr$_2$(Hsaltag^{Br})Cl$_2$(py)$_4$] · 2 .5 py · 2 H$_2$O (11)

CrCl$_3$ · 6 H$_2$O (207 mg, 0.78 mmol) is dissolved in pyridine (10 mL) and heated to $\approx$ 100 °C. Under continuous heating a solution of H$_5$saltag^{Br} · HCl (179 mg, 0.26 mmol) in pyridine (10 mL) is added dropwise followed by 30 min of heating. Then an equimolar solution of NaBPh$_4$ and 18-crown-6 (0.26 mmol each) in MeOH (1.5 mL) is added and the mixture is slowly cooled to room temperature. After filtration, a partition of one quarter of the filtrate is left to stand allowing for very slow evaporation of the solvent. After 3 months dark brown rod shaped crystals of **11** could be isolated (yield: 23 mg, 25 % related to $\frac{1}{4}$ of H$_5$saltag^{Br} · HCl). For magnetic measurements and single-crystal X-ray diffraction (synchrotron) fresh crystals from the mother liquor were used after removal of adherent solvent by dabbing on filter paper. For other analyses the sample was dried under air.

Thermogravimetry: residual mass Cr$_2$O$_3$: 12.79 %; Cr content, extracted: 8.75 %, calculated for [Cr$_2$(Hsaltag^{Br})Cl$_2$(py)$_4$] · 2 H$_2$O ($C_{42}H_{37}Br_3Cl_2Cr_2N_{10}O_5$): 8.84 %.

IR: $\tilde{\nu}$ [cm^{-1}] = 3063 (w), 1606 (m), 1589 (m), 1460 (vs), 1420 (s), 1340 (s), 1185 (s), 1096 (s), 1068 (s), 934 (m), 824 (s), 758 (s), 690/674 (vs).

[Cr₃(saltag^Br)Cl₃(py)₆]ClO₄ · py · H₂O   (12)

CrCl₃ · 6 H₂O (83 mg, 0.31 mmol) and H₅saltag^Br · HCl (69 mg, 0.1 mmol) are jointly dissolved in pyridine (5 mL) and heated to $\approx 100\,°C$ for 40 min, before the mixture is left to slowly cool to room temperature. Subsequently it is filtered into a test tube and carefully layered with first a mixture of pyridine and MeOH (3 mL, 1:1) and second a solution of NaClO₄ · H₂O (250 mg) in MeOH (10 mL). After 2 months dark, rod shaped crystals of **12** had grown (yield: 16 mg, 10 % related to H₅saltag^Br · HCl), which were taken from the mother liquor and directly used for all further experiments after removal of adherent solvent by dabbing on filter paper.

ESI-MS (positive in MeOH/pyridine): m/z = 1305 (100 %): [Cr₃(saltag^Br)Cl₃(py)₅]⁺ (C₄₇H₃₇Br₃Cl₃Cr₃N₁₁O₃⁺); 1385 (30 %) [Cr₃(saltag^Br)Cl₃(py)₆]⁺ (C₅₂H₄₂Br₃Cl₃Cr₃N₁₂O₃⁺).

Elemental analysis: Calculated for C₅₇H₄₉Br₃Cl₄Cr₃N₁₃O₈ (M): C 43.29; H 3.12; N 11.51. Found: C 43.65; H 3.22; N 11.32.

IR: $\widetilde{\nu}$ [cm⁻¹] = 3085 (w), 1605/1593 (s), 1526 (m), 1466 (vs), 1399 (m), 1364 (s), 1294 (m), 1186 (s), 1091/1068 (vs, br), 1016 (m), 940 (w), 831 (s), 783 (s), 689/673 (vs), 588 (vs).

7.4 4f Metal Complexes

[DyK₂(H₃saltag^Nph)₂(dmf)₃(MeOH)₃]BPh₄   (13)

Dy(NO₃)₃ · 6 H₂O (95 mg, 0.217 mmol, 1.1 eq) and H₅saltag^Nph · HNO₃ (252 mg, 0.4 mmol, 2 eq) is suspended (ultrasonication!) in MeOH (35 mL) and a solution of NEt₃ (80 mg, 0.8 mmol, 4 eq) in MeOH (10 mL) is added dropwise under stirring. Subsequently, a solution of KBPh₄ (144 mg, 0.4 mmol, 2 eq) in a DMF/MeOH mixture (1:2, 9 mL) is added and the resulting, lightly turbid orange mixture is filtered. The clear solution is sealed and left to stand unmoved at ambient conditions. Within some days, hexagonally shaped orange crystals are formed, accompanied by an amorphous precipitation at the ground of the vessel. The crystals are picked from the liquid, carefully washed with ice-cold MeOH to remove adherent amorphous material and finally dabbed on filter paper to remove adherent solvent.

This procedure yields intact crystalline material (60 mg), which was used for all further experiments except for single-crystal X-ray diffraction, where crystals were picked directly from the mother liquor.

ESI-MS (positive in MeOH): m/z = 1294 (100 %): [Dy(H₄saltag^Nph)₂]⁺ (C₆₈H₅₀DyN₁₂O₆⁺).

Elemental analysis: Calculated for C₁₀₃H₉₇BDyK₂N₁₅O₁₁ (M−MeOH): C 62.72; H 4.96; N 10.65. Found: C 63.23; H 5.08; N 10.73.

IR: $\widetilde{\nu}$ [cm⁻¹] = 3518 (w), 3055 (m), 2928 (w), 1653 (s), 1597/1578 (vs), 1465 (s), 1185 (s), 1104 (s, br), 1018 (s), 815 (s), 737 (vs).

[DyNa₂(H₃saltag^Nph)₂(dmf)₃(MeOH)₃]BPh₄   (14)

The compound is prepared utilising the exact same procedure as for **10**, except for the addition of the equimolar amount of NaBPh₄ (138 mg, 0.4 mmol, 2 eq) instead of KBPh₄. Again, for all

further experiments exclusively the obtained intact crystalline material (50 mg) was used.

ESI-MS (positive in MeOH): m/z = 1294 (100 %): $[Dy(H_4saltag^{Nph})_2]^+$ ($C_{68}H_{50}DyN_{12}O_6^+$).

Elemental analysis: Calculated for $C_{104}H_{101}BDyNa_2N_{15}O_{12}$ (M): C 63.33; 5.16; 10.65. Found: C 63.78; H 5.24; N 10.78.

IR: $\widetilde{\nu}$ [cm^{-1}] = 3521 (w), 3055 (m), 2929 (w), 1653 (s), 1598/1578 (vs), 1465 (s), 1186 (s), 1104 (s, br), 1018 (s), 815 (s), 738 (vs).

$[Dy_2(H_2saltag^{Br})_2(dmf)_4]\cdot 1.75H_2O$ (15)

$H_5saltag^{Br}\cdot HCl$ (138 mg, 0.2 mmol) and $DyCl_3\cdot 6H_2O$ (120 mg, 0.32 mmol) were dissolved in *N,N*-dimethylformamide (2 mL) followed by addition of MeCN (10 mL). To the resulting cloudy mixture a solution of NEt$_3$ (134 mg, 1.32 mmol) in MeCN (5 mL) is given under mild heating, so that a clear yellow solution is formed. After filtration of the warm solution, it is left unmoved at room temperature in a sealed glass vessel to afford rhombic orange crystals after one week. The crystals are picked singly via spatula, briefly washed with MeOH and dried under air (yield $\approx$ 80 mg, 0.04 mmol, 40 %).

ESI-MS (positive in MeOH): m/z = 1626 ($[Dy_2(H_3saltag^{Br})_2]^+$, 100 %), 1647 ($[Dy_2Na(H_2saltag^{Br})_2]^+$, 30 %); (negative in MeOH+MeCN) m/z = 1625 ($[Dy_2(H_1saltag^{Br})_2]^-$, 100 %).

Elemental analysis: Calculated for $C_{56}H_{59.5}Br_6Dy_2N_{16}O_{11.75}$ (M) C 34.51; H 3.08; N 11.50; found C 34.82; H 3.05; N 11.46.

Thermogravimetric Analysis: Residual mass Dy$_2$O$_3$ at 1000 °C: 19.63 %; Dy content, extracted: 17.10 %, calculated for $[Dy_2(H_2saltag^{Br})_2(dmf)_4]\cdot H_2O$ ($C_{56}H_{58}Br_6Dy_2N_{16}O_{11}$): 16.79 %.

IR: $\widetilde{\nu}$ [cm^{-1}] = 2929 (w), 1649 (s), 1601 (m), 1519 (s), 1462 (vs), 1177 (s), 1103 (s), 821 (s).

$[DyY(H_2saltag^{Br})_2(dmf)_4]\cdot 1.75H_2O$ (15@Y)

For the preparation of the diamagnetically diluted sample $[DyY(H_2saltag^{Br})_2dmf_4H_2O]$ the same experimental procedure as for **15** was utilised. The used amount of $DyCl_3\cdot 6H_2O$ is replaced by a mixture of $DyCl_3\cdot 6H_2O$ and $YCl_3\cdot 6H_2O$ in the molar ratio 1:5. The isostructurality with **15** was checked by powder X-ray diffraction.

$[Gd(H_2saltag^{Br})_2(dmf)_4]\cdot 1.75H_2O$

For the preparation of $[Gd(H_2saltag^{Br})_2dmf_4H_2O]$ the same experimental procedure as for **15** was utilised. The used amount of $DyCl_3\cdot 6H_2O$ is replaced by $GdCl_3\cdot 6H_2O$. The isostructurality with **15** was checked by powder X-ray diffraction.

$[Dy_2(H_2saltag^{Br})_2(dmf)_4]\cdot 2DMF$ (16)

$DyCl_3\cdot 6H_2O$ (113 mg, 0.30 mmol and $H_5saltag^{Br}\cdot HCl$ (138 mg, 0.2 mmol) are jointly dissolved in DMF (2 mL) under mild heating and a solution of NEt$_3$ in DMF (1 mL) is added. The mix-

ture is cooled to room temperature and subsequently filtered. Slow diffusion of water into the unmoved filtrate affords orange crystals of **16** after several weeks.

An alternative method to access crystalline material more quickly is the addition of a DMF/water (1 mL, 4:3) mixture to the filtrate at 80 °C solution temperature. Crystals obtained by this method look a lot more yellowish, however their identity was checked by powder X-ray diffraction. If this procedure is adopted for other lanthanoid ions, the DMF:water ratio has to be adjusted. For earlier lanthanoids the water content needs to be lowered, while for later lanthanoids it needs to be increased. Typical yields are around 50 mg.

Elemental analysis: Calculated for $C_{62}H_{70}Br_6Dy_2N_{18}O_{12}$ (M) C 36.08; H 3.42; N 12.22; found C 36.12; H 3.58; N 12.02.

IR: $\widetilde{\nu}$ [cm^{-1}] = 3368 (w), 2930 (w), 1648 (vs), 1518 (s), 1462 (vs), 1413 (m), 1375 (s), 1350 (s), 1314 (s), 1178 (m), 1102 (s), 822 (s), 676 (s), 652 (s), 634/624 (s).

[Dy$_2$(H$_2$saltag^{Br})$_2$(py)$_4$] · H$_2$O · py   (17)

Dy(OTf)$_3$ (189 mg, 0.31 mmol) and H$_5$saltag^{Br} · HCl (138 mg, 0.2 mmol) are suspended in MeCN (5 mL). Under reflux conditions, pyridine is added until the mixture turns into a clear solution apart from a slight residual turbidity (approximately 1.5 mL). At this point, the solution is filtered hot into a preheated vessel, which is subsequently sealed (ideally while the solution is still warm) and left unmoved at room temperature. Yellowish orange crystals of **17** form within some days (yield ≈ 90 mg).

ESI-MS (positive in MeOH+THF): m/z = 1961 ([Dy$_2$(H$_3$saltag^{Br})$_2$(py)$_4$ · H$_2$O]$^+$, <5 %); (negative in MeOH+THF) m/z = 1959 ([Dy$_2$(H$_1$saltag^{Br})$_2$(py)$_4$ · H$_2$O]$^-$, 100 %).

Elemental analysis: Calculated for $C_{66.5}H_{52.5}Br_6Dy_2N_{16.5}O_7$ (M−0.5py) C 39.95; H 2.65; N 11.56; found C 39.76; H 2.59; N 11.87.

[Dy$_2$(H$_2$saltag^{Br})$_2$(MeOH)$_4$]   (18)

DyCl$_3$ · 6 H$_2$O (208 mg, 0.55 mmol) and H$_5$saltag^{Br} · HCl (306 mg, 0.44 mmol) are jointly dissolved in MeOH (20 mL) under mild heating. A MeOH (10 mL) solution of NEt$_3$ (268 mg, 2.65 mmol) is added followed by filtration of the solution, which is then sealed and left unmoved at room temperature. Crystals of the product emerge within some days, however they are subject to weathering as soon as they form even in their mother liquor. Storage at +3 °C or lower temperatures can somewhat extend the storability as intact crystals. Yields above 100 mg can be expected. However, this reaction is prone to formation of product mixtures and the isolated material must be checked for homogeneity.

Elemental analysis: Calculated for $C_{44}H_{36}Br_6Dy_2N_{12}O_{10}$ (M−4MeOH+4H$_2$O) C 31.14; H 2.14; N 9.90; found C 31.01; H 2.53; N 9.93.

[Dy₃(H₀.₅saltag^Br)₂(MeOH)₆] · 3.5 MeOH   (19)

To a suspension of $DyCl_3 \cdot 6 H_2O$ (130 mg, 0,34 mmol) and $H_5saltag^{Br} \cdot HCl$ (138 mg, 0.2 mmol) in MeOH (10 mL), a solution of NEt_3 (135 mg, 1.3 mmol) in MeOH (5 mL) is added under mild heating and the solution is stirred until cooled to room temperature. After filtration the solution is sealed and left unmoved at room temperature. Crystals of **19** grow within several days. Typical yields are about 60 mg.

ESI-MS (negative in MeOH/DMF): m/z = 1783.5 ($[Dy_3(saltag^{Br}_2)]^-$, 100 %).

Elemental analysis: Calculated for $C_{47}H_{43}Br_6Dy_3N_{12}O_{12}$ (M−7.5MeOH+3H₂O): C 29.18; H 2.24; N 8.69. Found: C 29.14; H 2.16; N 9.03.

IR: $\widetilde{\nu}$ [cm⁻¹] = 3568 (m), 3162 (m, br), 1589 (m), 1524 (s), 1461 (vs), 1413 (s), 1352 (s), 1291 (s), 1178 (s), 817 (s), 636 (vs).

PPN[Dy₃(saltag^I)₂(MeOH)₅] · 5 MeOH   (20)

$DyCl_3 \cdot 6 H_2O$ (130 mg, 0.34 mmol) and $H_5saltag^{Br} \cdot HCl$ (166 mg, 0.2 mmol) are suspended in MeOH (15 mL) and subsequently a solution of NEt_3 (253 mg, 2.5 mmol) in MeOH (10 mL) is added dropwise. The clear mixture is mildly heated for two minutes and filtered twice, before a MeOH solution (3 mL) containing bis-(triphenylphosphoranylidene)-ammonium chloride (PP-NCl, 115 mg, 0.2 mmol) is added. The vessel is sealed and left unmoved at room temperature, large crystals of **20** (usually around 80 mg) grow within few days. Under air, the crystals turn superficially turbid almost immediately, but storage of intact crystals succeeds under nujol oil for several days.

Elemental analysis: Calculated for $C_{80}H_{70}I_6Dy_3N_{13}O_{14}P_2$ (M−10MeOH+8H₂O): C 34.96; H 2.57; N 6.63. Found: C 34.98; H 2.43; N 6.32.

IR: $\widetilde{\nu}$ [cm⁻¹] = 3300 (br), 3056 (w), 2940 (w), 2832 (w), 2639 (vw), 1586 (m), 1522 (m), 1460 (vs), 1409 (vs, br), 1344 (vs), 1304 (vs, br), 1176 (s), 1114 (s), 1019 (s), 948 (m), 819 (s), 722 (s), 691 (s), 629 (vs).

PPN[DyYLu(saltag^I)₂(MeOH)₅] · 5 MeOH   (20@Y/Lu)

For the preparation of the diamagnetically diluted sample $PPN[DyYLu(saltag^I)_2(MeOH)_5]$ the same experimental procedure as for **20** was utilised. The used amount of $DyCl_3 \cdot 6 H_2O$ is replaced by a mixture of $DyCl_3 \cdot 6 H_2O$, $YCl_3 \cdot 6 H_2O$ and $LuCl_3 \cdot 6 H_2O$ in the molar ratio 1:1:1. The isostructurality with **20** was checked by powder X-ray diffraction. The Dy content was estimated to be 25% via magnetisation measurements normalised to the sample mass in comparison to **20**.

(H₀.₅DMAP)₂[Dy₃(saltag^I)₂(MeOH)₆] · 2 MeOH   (21)

Conjoint dissolution of $DyOTf_3$ (189 mg, 0.31 mmol) and $H_5saltag^I \cdot HCl$ (166 mg, 0.2 mmol) in MeOH (15 mL) at room temperature (no heating!) is followed by addition of a MeOH (10 mL)

solution of 4-dimethylaminopyridine (DMAP, 171 mg, 1.4 mmol) and the mixture is immediately filtered. The filtrate is sealed and left unmoved at room temperature. Orange crystals of **21** grow overnight (yield around 90 mg).

Large crystals are feasible in longer crystallisation times by reducing the amount of 4-dimethylaminopyridine added (minimum 11 equivalents related to 2 equivalents of chelate ligand) and the use of more solvent. Stability of the crystals under air is given for some hours, for longer storage nujol oil must be used.

Elemental analysis: Calculated for $C_{64}H_{73}I_6Dy_3N_{16}O_{14}$ (M+2H$_2$O): C 30.27; H 2.90; N 8.83. Found: C 30.34; H 2.95; N 8.36.

IR: $\widetilde{\nu}$ [cm^{-1}] = 3200 (m, br), 2936 (m), 2832 (w) 1589 (m), 1522 (s), 1460 (vs), 1415 (s, br), 1349 (s), 1306 (s, br), 1177 (s), 1027 (s), 998 (s), 815/802 (vs), 629 (vs).

(H$_{0.5}$DMAP)$_2$[Gd$_3$(saltag^I)$_2$(MeOH)$_6$] · 2 MeOH

For the preparation of the Gd compound (H$_{0.5}$DMAP)$_2$[Gd$_3$(saltag^I)$_2$(MeOH)$_6$] the same experimental procedure as for **21** was utilised. The used amount of DyOTf$_3$ is replaced by an equimolar amount of GdOTf$_3$. The isostructurality with **21** was checked by powder X-ray diffraction.

(H$_{0.5}$DMAP)$_2$[Dy$_{0.4}$Y$_{2.6}$(saltag^I)$_2$(MeOH)$_6$] · 2 MeOH (21@Y)

The diamagnetically diluted material was prepared utilising the same experimental procedure as for **21**. The used amount of DyOTf$_3$ is replaced by a mixture of DyOTf$_3$ and YOTf$_3$ in the molar ratio 1:5. The isostructurality with **21** was checked by powder X-ray diffraction. The Dy content was estimated to be 13% via magnetisation measurements normalised to the sample mass in comparison to **21**.

[Dy$_3$(H$_{0.5}$saltag^I)$_2$(thf)$_6$] (22)

For the successful synthesis, 1,3-propanediol has to be predried over molar sieve (3 Å) to reduce the water content as far as possible. Still, the synthesis itself can be carried out under ambient conditions if run straight. H$_5$saltag^I · HCl (166 mg, 0.2 mmol) and DyOTf$_3$ (200 mg, 0.32 mmol) are dissolved in a mixture of 1,3-propanediol and THF (10 mL, 1:1) and subsequently a solution of 4-DMAP (190 mg, 1.55 mmol) in 1,3-propanediol/THF (6 mL, 1:1) is added. The clear solution is filtered into a glass vessel, which is sealed tightly and stored unmoved at 3° C. After about one month, crystals had grown, which were picked out from the mother liquor and carefully washed with ice-cold *i*-PrOH to remove adhesive 1,3-propanediol (yield ≈ 40 mg). Intactness of the crystals under air is limited to some minutes, however, can be extended by storage under nujol oil.

Elemental analysis: Calculated for $C_{72.66}H_{79.66}I_6Dy_3N_{13.33}O_{12}$ (M−0.66H$^+$+0.66HDMAP$^+$): C 33.82; H 3.11; N 7.24. Found: C 33.70; H 3.17; N 7.32.

IR: $\widetilde{\nu}$ [cm^{-1}] = 3300 (m), 2925 (m), 2872 (m) 1596 (m), 1522 (s), 1462 (vs), 1417 (s), 1352 (s), 1318 (s), 1180 (s), 1051 (s, br), 885 (m), 819 (vs), 629 (vs).

[Dy$_4$(pytag^{cyc})$_2$(O$_2$)$_2$Cl$_4$(MeOH)$_6$]Cl$_2 \cdot$ 3 MeOH $\cdot$ H$_2$O (23)

DyCl$_3 \cdot$ 6 H$_2$O (120 mg, 0.31 mmol, 0.31 eq) and H$_2$pytag $\cdot$ HCl (91 mg, 0.2 mmol, 2 eq) are dissolved in MeOH (10 mL). A mixture of MeOH and pyridine (4:1, 5 mL) is added. Subsequently, the solution is filtered into a closed vessel and left to stand at ambient conditions. After approximately 4 months tiny but well shaped orange crystals suitable for single-crystal X-ray diffractometry start to form, which do not visibly grow in size but in number upon further standing.

After roughly 5 months a crop of crystals (15 mg) was isolated from the mother liquor, dabbed on filter paper to remove adherent liquid and immediately used for analyses and further experiments. Once off the mother liquor the crystals are very sensitive to decomposition (probably due to loss of cocrystallised solvent and H$_2$O exchange).

Elemental analysis: Calculated for C$_{38}$H$_{46}$Cl$_6$Dy$_4$N$_{18}$O$_{13}$ (M−9MeOH+8H$_2$O): C 25.00; H 2.54; N 13.81. Found: C 24.98; H 2.46; N 13.24.

Thermogravimetry: Residual mass Dy calculated for C$_{42}$H$_{48}$Cl$_6$Dy$_4$N$_{18}$O$_{10}$ (M−5MeOH+H$_2$O): 35.56 %, found 35.65 %.

IR: $\widetilde{\nu}$ [cm^{-1}] = 3352 (m, br), 3059 (m, br), 1530 (s), 1465 (s), 1409 (s), 1339 (m), 1050 (s), 1014 (m), 777 (s), 607 (s).

Bibliography

[1] A. Kloss, *Geschichte des Magnetismus*, Vde Verlag GmbH, 1994.

[2] F. C. Lane, *The American Historical Review*, 1963.

[3] K. Richter, *Das Leben des Physikers Johann Wilhelm Ritter : ein Schicksal in der Zeit der Romantik*, Verlag Hermann Böhlau Weimar, 2003.

[4] M. Jacobi, *Physik in unserer Zeit*, 2006, **37**, 116–121.

[5] H. Rechenberg, *European Journal of Physics*, 1997, **18**, 145–149.

[6] *Molecular Magnetic Materials*, ed. B. Sieklucka and D. Pinkowicz, Wiley VCH Verlag GmbH, 2016.

[7] A. Smith, C. R. Bahl, R. Bjørk, K. Engelbrecht, K. K. Nielsen and N. Pryds, *Advanced Energy Materials*, 2012, **2**, 1288–1318.

[8] A. Smith, *The European Physical Journal H*, 2013, **38**, 507–517.

[9] R. Frisch and O. Stern, *Zeitschrift für Physik*, 1933, **85**, 4–16.

[10] I. Estermann and O. Stern, *Zeitschrift für Physik*, 1933, **85**, 17–24.

[11] J. H. van Vleck, *The Theory Of Electric And Magnetic Susceptibilities*, Oxford Clarendon Press, 1932.

[12] M. I. Darby, *British Journal of Applied Physics*, 1967, **18**, 1415–1417.

[13] C. Benelli and D. Gatteschi, *Introduction to Molecular Magnetism: From Transition Metals to Lanthanides*, Weinheim: Wiley-VCH, 2015.

[14] W. Klemm, *Magnetochemie*, Akademische Verlags-Gesellschaft Leipzig, 1936.

[15] R. Hoppe, *Zeitschrift für anorganische und allgemeine Chemie*, 1996, **622**, 1–8.

[16] B. C. Guha, *Proceedings of the Royal Society of London. Series A. Mathematical and Physical Sciences*, 1951, **206**, 353–373.

[17] J. N. van Niekerk and F. R. L. Schoening, *Acta Crystallographica*, 1953, **6**, 227–232.

[18] B. Bleaney and K. D. Bowers, *Proceedings of the Royal Society of London. Series A. Mathematical and Physical Sciences*, 1952, **214**, 451–465.

[19] P. W. Anderson, *Physical Review*, 1950, **79**, 350–356.

[20] D. Bloch, *Journal of Physics and Chemistry of Solids*, 1966, **27**, 881–885.

[21] J. B. Goodenough, *Physical Review*, 1955, **100**, 564–573.

[22] J. B. Goodenough, *Journal of Physics and Chemistry of Solids*, 1958, **6**, 287–297.

[23] J. Kanamori, *Journal of Physics and Chemistry of Solids*, 1959, **10**, 87–98.

[24] A. Palii, B. Tsukerblat, J. M. Clemente-Juan and E. Coronado, *International Reviews in Physical Chemistry*, 2010, **29**, 135–230.

[25] C. Zener, *Physical Review*, 1951, **82**, 403–405.

[26] J. A. R. Hartman, R. L. Rardin, P. Chaudhuri, K. Pohl, K. Wieghardt, B. Nuber, J. Weiss, G. C. Papaefthymiou, R. B. Frankel and S. J. Lippard, *Journal of the American Chemical Society*, 1987, **109**, 7387–7396.

[27] S. Drüeke, P. Chaudhuri, K. Pohl, K. Wieghardt, X.-Q. Ding, E. Bill, A. Sawaryn, A. X. Trautwein, H. Winkler and S. J. Gurman, *Journal of the Chemical Society, Chemical Communications*, 1989, 59–62.

[28] J. Ferrando-Soria, J. Vallejo, M. Castellano, J. Martínez-Lillo, E. Pardo, J. Cano, I. Castro, F. Lloret, R. Ruiz-García and M. Julve, *Coordination Chemistry Reviews*, 2017, **339**, 17–103.

[29] I. Dzyaloshinsky, *Journal of Physics and Chemistry of Solids*, 1958, **4**, 241–255.

[30] T. Moriya, *Physical Review*, 1960, **120**, 91–98.

[31] A. Rajca, *Chemical Reviews*, 1994, **94**, 871–893.

[32] S. Mitsubori, T. Ishida, T. Nogami and H. Iwamura, *Chemistry Letters*, 1994, **23**, 285–288.

[33] T. Glaser, *Coordination Chemistry Reviews*, 2013, **257**, 140–152.

[34] V. H. Crawford, H. W. Richardson, J. R. Wasson, D. J. Hodgson and W. E. Hatfield, *Inorganic Chemistry*, 1976, **15**, 2107–2110.

[35] O. Kahn, *Angewandte Chemie International Edition in English*, 1985, **24**, 834–850.

[36] O. Kahn, J. Galy, Y. Journaux, J. Jaud and I. Morgenstern-Badarau, *Journal of the American Chemical Society*, 1982, **104**, 2165–2176.

[37] O. Kahn, *Molecular Magnetism*, Wiley VCH, 1993.

[38] F. Torres, J. M. Hernández, X. Bohigas and J. Tejada, *Applied Physics Letters*, 2000, **77**, 3248–3250.

[39] J.-L. Liu, Y.-C. Chen, F.-S. Guo and M.-L. Tong, *Coordination Chemistry Reviews*, 2014, **281**, 26–49.

[40] M. S. Reis, *Coordination Chemistry Reviews*, 2020, **417**, 213357.

[41] R. Bagai and G. Christou, *Chemical Society Reviews*, 2009, **38**, 1011.

[42] G. E. Kostakis, A. M. Ako and A. K. Powell, *Chemical Society Reviews*, 2010, **39**, 2238.

[43] K. S. Pedersen, M. A. Sørensen and J. Bendix, *Coordination Chemistry Reviews*, 2015, **299**, 1–21.

[44] A. Escuer, J. Esteban, S. P. Perlepes and T. C. Stamatatos, *Coordination Chemistry Reviews*, 2014, **275**, 87–129.

[45] M. Atanasov, P. Comba, S. Hausberg and B. Martin, *Coordination Chemistry Reviews*, 2009, **253**, 2306–2314.

[46] A. Caneschi, D. Gatteschi, R. Sessoli, A. L. Barra, L. C. Brunel and M. Guillot, *Journal of the American Chemical Society*, 1991, **113**, 5873–5874.

[47] R. Sessoli, D. Gatteschi, A. Caneschi and M. A. Novak, *Nature*, 1993, **365**, 141–143.

[48] T. Glaser, M. Gerenkamp and R. Fröhlich, *Angewandte Chemie International Edition*, 2002, **41**, 3823–3825.

[49] T. Glaser, M. Heidemeier, S. Grimme and E. Bill, *Inorganic Chemistry*, 2004, **43**, 5192–5194.

[50] D. Plaul, *PhD thesis*, Friedrich-Schiller-Universität Jena, 2009.

[51] X. Ottenwaelder, J. Cano, Y. Journaux, E. Rivière, C. Brennan, M. Nierlich and R. Ruiz-García, *Angewandte Chemie International Edition*, 2004, **43**, 850–852.

[52] M.-C. Dul, X. Ottenwaelder, E. Pardo, R. Lescoue zec, Y. Journaux, L.-M. Chamoreau, R. Ruiz-Garciía, J. Cano, M. Julve and F. Lloret, *Inorganic Chemistry*, 2009, **48**, 5244–5249.

[53] D. P. DiVincenzo, *Fortschritte der Physik*, 2000, **48**, 771–783.

[54] C. Nay, *IBM Unveils World's First Integrated Quantum Computing System for Commercial Use*, newsroom.ibm.com, 2019.

[55] C. Nay, *IBM Opens Quantum Computation Center in New York; Brings World's Largest Fleet of Quantum Computing Systems Online, Unveils New 53-Qubit Quantum System for Broad Use*, www.prnewswire.com, 2019.

[56] I. Georgescu, S. Ashhab and F. Nori, *Reviews of Modern Physics*, 2014, **86**, 153–185.

[57] R. Hanson, L. P. Kouwenhoven, J. R. Petta, S. Tarucha and L. M. K. Vandersypen, *Reviews of Modern Physics*, 2007, **79**, 1217–1265.

[58] C. Kloeffel and D. Loss, *Annual Review of Condensed Matter Physics*, 2013, **4**, 51–81.

[59] V. Dobrovitski, G. Fuchs, A. Falk, C. Santori and D. Awschalom, *Annual Review of Condensed Matter Physics*, 2013, **4**, 23–50.

[60] E. Bourgeois, M. Gulka and M. Nesladek, *Advanced Optical Materials*, 2020, **8**, 1902132.

[61] F. Meier, J. Levy and D. Loss, *Physical Review Letters*, 2003, **90**, 047901.

[62] F. Troiani, M. Affronte, S. Carretta, P. Santini and G. Amoretti, *Physical Review Letters*, 2005, **94**, 190501.

[63] S. Carretta, P. Santini, G. Amoretti, F. Troiani and M. Affronte, *Physical Review B*, 2007, **76**, 024408.

[64] A. Gaita-Ariño, F. Luis, S. Hill and E. Coronado, *Nature Chemistry*, 2019, **11**, 301–309.

[65] J. M. Zadrozny, J. Niklas, O. G. Poluektov and D. E. Freedman, *ACS Central Science*, 2015, **1**, 488–492.

[66] F. K. Larsen, E. J. L. McInnes, H. E. Mkami, J. Overgaard, S. Piligkos, G. Rajaraman, E. Rentschler, A. A. Smith, G. M. Smith, V. Boote, M. Jennings, G. A. Timco and R. E. P. Winpenny, *Angewandte Chemie International Edition*, 2003, **42**, 101–105.

[67] A. Ardavan, O. Rival, J. J. L. Morton, S. J. Blundell, A. M. Tyryshkin, G. A. Timco and R. E. P. Winpenny, *Physical Review Letters*, 2007, **98**, 057201.

[68] F. Troiani, V. Bellini and M. Affronte, *Physical Review B*, 2008, **77**, 054428.

[69] F. Troiani, A. Ghirri, M. Affronte, S. Carretta, P. Santini, G. Amoretti, S. Piligkos, G. Timco and R. E. P. Winpenny, *Physical Review Letters*, 2005, **94**, 207208.

[70] S. Carretta, P. Santini, G. Amoretti, T. Guidi, J. R. D. Copley, Y. Qiu, R. Caciuffo, G. Timco and R. E. P. Winpenny, *Physical Review Letters*, 2007, **98**, 167401.

[71] J. Ferrando-Soria, E. M. Pineda, A. Chiesa, A. Fernandez, S. A. Magee, S. Carretta, P. Santini, I. J. Vitorica-Yrezabal, F. Tuna, G. A. Timco, E. J. McInnes and R. E. Winpenny, *Nature Communications*, 2016, **7**, 11377.

[72] T. Okubo, R. Maeda, M. Kondo, T. Mitani and S. Kitagawa, *Chemistry Letters*, 2006, **35**, 34–35.

[73] B. Georgeot and F. Mila, *Physical Review Letters*, 2010, **104**, 200502.

[74] F. Troiani, D. Stepanenko and D. Loss, *Physical Review B*, 2012, **86**, 161409.

[75] G. Toulouse, *Communications on Physics*, 1977, **2**, 115–119.

[76] O. Kahn, *Chemical Physics Letters*, 1997, **265**, 109–114.

[77] D. Dai and M.-H. Whangbo, *The Journal of Chemical Physics*, 2004, **121**, 672–680.

[78] J. Schnack, *Comptes Rendus Chimie*, 2007, **10**, 15–20.

[79] J. Schnack, *Dalton Transactions*, 2010, **39**, 4677.

[80] J. Yoon and E. I. Solomon, *Coordination Chemistry Reviews*, 2007, **251**, 379–400.

[81] B. R. Bułka, T. Kostyrko and J. Łuczak, *Physical Review B*, 2011, **83**, 035301.

[82] M. Trif, F. Troiani, D. Stepanenko and D. Loss, *Physical Review B*, 2010, **82**, 045429.

[83] M. Trif, F. Troiani, D. Stepanenko and D. Loss, *Physical Review Letters*, 2008, **101**, 217201.

[84] C. F. Hirjibehedin, *Science*, 2006, **312**, 1021–1024.

[85] F. E. Sowrey, C. Tilford, S. Wocadlo, C. E. Anson, A. K. Powell, S. M. Bennington, W. Montfrooij, U. A. Jayasooriya and R. D. Cannon, *Journal of the Chemical Society, Dalton Transactions*, 2001, 862–866.

[86] A. K. Boudalis, J. Robert and P. Turek, *Chemistry - A European Journal*, 2018, **24**, 14896–14900.

[87] M. F. Islam, J. F. Nossa, C. M. Canali and M. Pederson, *Physical Review B*, 2010, **82**, 155446.

[88] U. Kortz, N. K. Al-Kassem, M. G. Savelieff, N. A. A. Kadi and M. Sadakane, *Inorganic Chemistry*, 2001, **40**, 4742–4749.

[89] A. Vlachos, V. Psycharis, C. P. Raptopoulou, N. Lalioti, Y. Sanakis, G. Diamantopoulos, M. Fardis, M. Karayanni, G. Papavassiliou and A. Terzis, *Inorganica Chimica Acta*, 2004, **357**, 3162–3172.

[90] J. M. Clemente-Juan, E. Coronado, A. Gaita-Ariño, C. Giménez-Saiz, H.-U. Güdel, A. Sieber, R. Bircher and H. Mutka, *Inorganic Chemistry*, 2005, **44**, 3389–3395.

[91] A. Figuerola, V. Tangoulis, J. Ribas, H. Hartl, I. Brüdgam, M. Maestro and C. Diaz, *Inorganic Chemistry*, 2007, **46**, 11017–11024.

[92] S. Ferrer, F. Lloret, E. Pardo, J. M. Clemente-Juan, M. Liu-González and S. García-Granda, *Inorganic Chemistry*, 2011, **51**, 985–1001.

[93] W. M. C. Sameera, D. M. Piñero, R. Herchel, Y. Sanakis, J. E. McGrady, R. G. Raptis and E. M. Zueva, *European Journal of Inorganic Chemistry*, 2012, 3500–3506.

[94] A. N. Georgopoulou, I. Margiolaki, V. Psycharis and A. K. Boudalis, *Inorganic Chemistry*, 2017, **56**, 762–772.

[95] L. Mathivathanan, A. K. Boudalis, P. Turek, M. Pissas, Y. Sanakis and R. G. Raptis, *Physical Chemistry Chemical Physics*, 2018, **20**, 17234–17244.

[96] A. E. Filkale and M. K. Gangwar, *Journal of Molecular Structure*, 2020, **1218**, 128450.

[97] I. A. Sergienko and E. Dagotto, *Physical Review B*, 2006, **73**, 094434.

[98] D. Stepanenko, M. Trif, O. Tsyplyatyev and D. Loss, *Semiconductor Science and Technology*, 2016, **31**, 094003.

[99] T. Murao, *Physics Letters A*, 1974, **49**, 33–35.

[100] J. Robert, N. Parizel, P. Turek and A. K. Boudalis, *Physical Chemistry Chemical Physics*, 2019, **21**, 19575–19584.

[101] J. Robert, N. Parizel, P. Turek and A. K. Boudalis, *Journal of the American Chemical Society*, 2019, **141**, 19765–19775.

[102] M. Fittipaldi, A. Cini, G. Annino, A. Vindigni, A. Caneschi and R. Sessoli, *Nature Materials*, 2019, **18**, 329–334.

[103] T. Lis, *Acta Crystallographica Section B Structural Crystallography and Crystal Chemistry*, 1980, **36**, 2042–2046.

[104] R. F. Weinland and G. Fischer, *Zeitschrift für anorganische und allgemeine Chemie*, 1921, **120**, 161–180.

[105] G. E. Moore, *IEEE Solid-State Circuits Society Newsletter*, 2006, **11**, 33–35.

[106] R. W. Keyes, *IEEE Solid-State Circuits Society Newsletter*, 2006, **11**, 25–27.

[107] R. K. Cavin, P. Lugli and V. V. Zhirnov, *Proceedings of the IEEE*, 2012, **100**, 1720–1749.

[108] D. Weller and A. Moser, *IEEE Transactions on Magnetics*, 1999, **35**, 4423–4439.

[109] R. Wood, *IEEE Transactions on Magnetics*, 2000, **36**, 36–42.

[110] R. Boča, *Coordination Chemistry Reviews*, 2004, **248**, 757–815.

[111] S. Goswami, A. K. Mondal and S. Konar, *Inorganic Chemistry Frontiers*, 2015, **2**, 687–712.

[112] C. J. Milios, A. Vinslava, W. Wernsdorfer, S. Moggach, S. Parsons, S. P. Perlepes, G. Christou and E. K. Brechin, *Journal of the American Chemical Society*, 2007, **129**, 2754–2755.

[113] R. Inglis, C. J. Milios, L. F. Jones, S. Piligkos and E. K. Brechin, *Chemical Communications*, 2012, **48**, 181–190.

[114] T. Stamatatos, K. Abboud, W. Wernsdorfer and G. Christou, *Angewandte Chemie International Edition*, 2007, **46**, 884–888.

[115] T. N. Nguyen, W. Wernsdorfer, K. A. Abboud and G. Christou, *Journal of the American Chemical Society*, 2011, **133**, 20688–20691.

[116] A. J. Tasiopoulos, A. Vinslava, W. Wernsdorfer, K. A. Abboud and G. Christou, *Angewandte Chemie International Edition*, 2004, **43**, 2117–2121.

[117] S. Gao, *Molecular Nanomagnets and Related Phenomena*, Springer-Verlag GmbH, 2015.

[118] J. M. Frost, K. L. M. Harriman and M. Murugesu, *Chemical Science*, 2016, **7**, 2470–2491.

[119] S. M. Aldoshin, D. V. Korchagin, A. V. Palii and B. S. Tsukerblat, *Pure and Applied Chemistry*, 2017, **89**, 1119–1143.

[120] N. Ishikawa, M. Sugita, T. Ishikawa, S. ya Koshihara and Y. Kaizu, *Journal of the American Chemical Society*, 2003, **125**, 8694–8695.

[121] G. A. Craig and M. Murrie, *Chemical Society Reviews*, 2015, **44**, 2135–2147.

[122] F.-S. Guo, A. K. Bar and R. A. Layfield, *Chemical Reviews*, 2019, **119**, 8479–8505.

[123] C. Benelli and D. Gatteschi, *Chemical Reviews*, 2002, **102**, 2369–2388.

[124] L. Sorace and D. Gatteschi, *Lanthanides and Actinides in Molecular Magnetism*, Wiley-VCH Verlag GmbH & Co. KGaA, 2015, pp. 1–26.

[125] J. D. Rinehart and J. R. Long, *Chemical Science*, 2011, **2**, 2078.

[126] J. Sievers, *Zeitschrift für Physik B Condensed Matter*, 1982, **45**, 289–296.

[127] N. F. Chilton, D. Collison, E. J. L. McInnes, R. E. P. Winpenny and A. Soncini, *Nature Communications*, 2013, **4**, 2551.

[128] S. T. Liddle and J. van Slageren, *Chemical Society Reviews*, 2015, **44**, 6655–6669.

[129] N. F. Chilton, *Inorganic Chemistry*, 2015, **54**, 2097–2099.

[130] C. A. P. Goodwin, F. Ortu, D. Reta, N. F. Chilton and D. P. Mills, *Nature*, 2017, **548**, 439–442.

[131] F.-S. Guo, B. M. Day, Y.-C. Chen, M.-L. Tong, A. Mansikkamäki and R. A. Layfield, *Science*, 2018, **362**, 1400–1403.

[132] P. Zhang, L. Zhang, C. Wang, S. Xue, S.-Y. Lin and J. Tang, *Journal of the American Chemical Society*, 2014, **136**, 4484–4487.

[133] *Lanthanides and Actinides in Molecular Magnetism*, ed. R. A. Layfield and M. Murugesu, Wiley-VCH Verlag GmbH & Co. KGaA, 2015.

[134] R. Orbach and M. Blume, *Physical Review Letters*, 1962, **8**, 478–480.

[135] K. N. Shrivastava, *Physica Status Solidi (B)*, 1983, **117**, 437–458.

[136] D. N. Woodruff, R. E. P. Winpenny and R. A. Layfield, *Chemical Reviews*, 2013, **113**, 5110–5148.

[137] H. L. Feltham and S. Brooker, *Coordination Chemistry Reviews*, 2014, **276**, 1–33.

[138] D. Shao and X.-Y. Wang, *Chinese Journal of Chemistry*, 2020.

[139] K. S. Pedersen, J. Dreiser, H. Weihe, R. Sibille, H. V. Johannesen, M. A. Sørensen, B. E. Nielsen, M. Sigrist, H. Mutka, S. Rols, J. Bendix and S. Piligkos, *Inorganic Chemistry*, 2015, **54**, 7600–7606.

[140] V. V. Novikov, A. A. Pavlov, Y. V. Nelyubina, M.-E. Boulon, O. A. Varzatskii, Y. Z. Voloshin and R. E. Winpenny, *Journal of the American Chemical Society*, 2015, **137**, 9792–9795.

[141] Y. Rechkemmer, F. D. Breitgoff, M. van der Meer, M. Atanasov, M. Hakl, M. Orlita, P. Neugebauer, F. Neese, B. Sarkar and J. van Slageren, *Nature Communications*, 2016, **7**, 10467.

[142] E. Lucaccini, L. Sorace, M. Perfetti, J.-P. Costes and R. Sessoli, *Chemical Communications*, 2014, **50**, 1648–1651.

[143] A. Lunghi, F. Totti, R. Sessoli and S. Sanvito, *Nature Communications*, 2017, **8**, 14620.

[144] E. M. Chudnovsky and L. Gunther, *Physical Review Letters*, 1988, **60**, 661–664.

[145] L. Thomas, F. Lionti, R. Ballou, D. Gatteschi, R. Sessoli and B. Barbara, *Nature*, 1996, **383**, 145–147.

[146] J. R. Friedman, M. P. Sarachik, J. Tejada and R. Ziolo, *Physical Review Letters*, 1996, **76**, 3830–3833.

[147] D. Gatteschi and R. Sessoli, *Angewandte Chemie International Edition*, 2003, **42**, 268–297.

[148] W. Wernsdorfer, M. Murugesu and G. Christou, *Physical Review Letters*, 2006, **96**, 057208.

[149] L. Ungur and L. F. Chibotaru, *Physical Chemistry Chemical Physics*, 2011, **13**, 20086.

[150] L. Ungur, M. Thewissen, J.-P. Costes, W. Wernsdorfer and L. F. Chibotaru, *Inorganic Chemistry*, 2013, **52**, 6328–6337.

[151] L. Ungur, J. J. Le Roy, I. Korobkov, M. Murugesu and L. F. Chibotaru, *Angewandte Chemie International Edition*, 2014, **53**, 4413–4417.

[152] L. Ungur and L. F. Chibotaru, *Inorganic Chemistry*, 2016, **55**, 10043–10056.

[153] J. M. Zadrozny, M. Atanasov, A. M. Bryan, C.-Y. Lin, B. D. Rekken, P. P. Power, F. Neese and J. R. Long, *Chemical Science*, 2013, **4**, 125–138.

[154] M.-E. Boulon, G. Cucinotta, J. Luzon, C. Degl'Innocenti, M. Perfetti, K. Bernot, G. Calvez, A. Caneschi and R. Sessoli, *Angewandte Chemie International Edition*, 2012, **52**, 350–354.

[155] P. Zhang, M. Perfetti, M. Kern, P. P. Hallmen, L. Ungur, S. Lenz, M. R. Ringenberg, W. Frey, H. Stoll, G. Rauhut and J. van Slageren, *Chemical Science*, 2018, **9**, 1221–1230.

[156] F.-S. Guo, B. M. Day, Y.-C. Chen, M.-L. Tong, A. Mansikkamäki and R. A. Layfield, *Angewandte Chemie International Edition*, 2017, **56**, 11445–11449.

[157] A. J. Tasiopoulos, W. Wernsdorfer, K. A. Abboud and G. Christou, *Inorganic Chemistry*, 2005, **44**, 6324–6338.

[158] W. H. Harman, T. D. Harris, D. E. Freedman, H. Fong, A. Chang, J. D. Rinehart, A. Ozarowski, M. T. Sougrati, F. Grandjean, G. J. Long, J. R. Long and C. J. Chang, *Journal of the American Chemical Society*, 2010, **132**, 18115–18126.

[159] K. S. Cole and R. H. Cole, *The Journal of Chemical Physics*, 1941, **9**, 341–351.

[160] L. Scherthan, R. F. Pfleger, H. Auerbach, T. Hochdörffer, J. A. Wolny, W. Bi, J. Zhao, M. Y. Hu, E. E. Alp, C. E. Anson, R. Diller, A. K. Powell and V. Schünemann, *Angewandte Chemie International Edition*, 2020, **59**, 8818–8822.

[161] R. J. Blagg, L. Ungur, F. Tuna, J. Speak, P. Comar, D. Collison, W. Wernsdorfer, E. J. L. McInnes, L. F. Chibotaru and R. E. P. Winpenny, *Nature Chemistry*, 2013, **5**, 673–678.

[162] J.-L. Liu, J.-Y. Wu, Y.-C. Chen, V. Mereacre, A. K. Powell, L. Ungur, L. F. Chibotaru, X.-M. Chen and M.-L. Tong, *Angewandte Chemie International Edition*, 2014, **53**, 12966–12970.

[163] J. Liu, Y.-C. Chen, J.-L. Liu, V. Vieru, L. Ungur, J.-H. Jia, L. F. Chibotaru, Y. Lan, W. Wernsdorfer, S. Gao, X.-M. Chen and M.-L. Tong, *Journal of the American Chemical Society*, 2016, **138**, 5441–5450.

[164] Y.-C. Chen, J.-L. Liu, L. Ungur, J. Liu, Q.-W. Li, L.-F. Wang, Z.-P. Ni, L. F. Chibotaru, X.-M. Chen and M.-L. Tong, *Journal of the American Chemical Society*, 2016, **138**, 2829–2837.

[165] J.-L. Liu, Y.-C. Chen and M.-L. Tong, *Chemical Society Reviews*, 2018, **47**, 2431–2453.

[166] R. Sessoli and A. K. Powell, *Coordination Chemistry Reviews*, 2009, **253**, 2328–2341.

[167] Y.-G. Huang, F.-L. Jiang and M.-C. Hong, *Coordination Chemistry Reviews*, 2009, **253**, 2814–2834.

[168] A. Chakraborty, J. Goura, P. Kalita, A. Swain, G. Rajaraman and V. Chandrasekhar, *Dalton Transactions*, 2018, **47**, 8841–8864.

[169] A. Dey, J. Acharya and V. Chandrasekhar, *Chemistry – An Asian Journal*, 2019, **14**, 4433–4453.

[170] D. C. Izuogu, T. Yoshida, G. Cosquer, J. N. Asegbeloyin, H. Zhang, A. J. W. Thom and M. Yamashita, *Chemistry – A European Journal*, 2020, **26**, 6036–6049.

[171] S. K. Langley, D. P. Wielechowski, V. Vieru, N. F. Chilton, B. Moubaraki, B. F. Abrahams, L. F. Chibotaru and K. S. Murray, *Angewandte Chemie International Edition*, 2013, **52**, 12014–12019.

[172] M. A. Sørensen, U. B. Hansen, M. Perfetti, K. S. Pedersen, E. Bartolomé, G. G. Simeoni, H. Mutka, S. Rols, M. Jeong, I. Zivkovic, M. Retuerto, A. Arauzo, J. Bartolomé, S. Piligkos, H. Weihe, L. H. Doerrer, J. van Slageren, H. M. Rønnow, K. Lefmann and J. Bendix, *Nature Communications*, 2018, **9**, 1292.

[173] L. Escalera-Moreno, J. J. Baldoví, A. Gaita-Ariño and E. Coronado, *Chemical Science*, 2018, **9**, 3265–3275.

[174] M. J. Giansiracusa, A. K. Kostopoulos, D. Collison, R. E. P. Winpenny and N. F. Chilton, *Chemical Communications*, 2019, **55**, 7025–7028.

[175] A. Chiesa, F. Cugini, R. Hussain, E. Macaluso, G. Allodi, E. Garlatti, M. Giansiracusa, C. A. P. Goodwin, F. Ortu, D. Reta, J. M. Skelton, T. Guidi, P. Santini, M. Solzi, R. D. Renzi, D. P. Mills, N. F. Chilton and S. Carretta, *Physical Review B*, 2020, **101**, 174402.

[176] Y.-S. Ding, N. F. Chilton, R. E. P. Winpenny and Y.-Z. Zheng, *Angewandte Chemie International Edition*, 2016, **55**, 16071–16074.

[177] S. K. Gupta, T. Rajeshkumar, G. Rajaraman and R. Murugavel, *Chemical Science*, 2016, **7**, 5181–5191.

[178] A. B. Canaj, M. K. Singh, C. Wilson, G. Rajaraman and M. Murrie, *Chemical Communications*, 2018, **54**, 8273–8276.

[179] Y.-S. Ding, T. Han, Y.-Q. Zhai, D. Reta, N. F. Chilton, R. E. P. Winpenny and Y.-Z. Zheng, *Chemistry – A European Journal*, 2020, **26**, 5893–5902.

[180] A. B. Canaj, S. Dey, C. Wilson, O. Céspedes, G. Rajaraman and M. Murrie, *Chemical Communications*, 2020, **56**, 12037–12040.

[181] M. A. Sørensen, H. Weihe, M. G. Vinum, J. S. Mortensen, L. H. Doerrer and J. Bendix, *Chemical Science*, 2017, **8**, 3566–3575.

[182] W. Wernsdorfer, A. Caneschi, R. Sessoli, D. Gatteschi, A. Cornia, V. Villar and C. Paulsen, *Physical Review Letters*, 2000, **84**, 2965–2968.

[183] N. Ishikawa, M. Sugita and W. Wernsdorfer, *Journal of the American Chemical Society*, 2005, **127**, 3650–3651.

[184] F. Pointillart, K. Bernot, S. Golhen, B. Le Guennic, T. Guizouarn, L. Ouahab and O. Cador, *Angewandte Chemie International Edition*, 2014, **54**, 1504–1507.

[185] Y.-C. Chen, J.-L. Liu, W. Wernsdorfer, D. Liu, L. F. Chibotaru, X.-M. Chen and M.-L. Tong, *Angewandte Chemie International Edition*, 2017, **56**, 4996–5000.

[186] M. J. Giansiracusa, E. Moreno-Pineda, R. Hussain, R. Marx, M. M. Prada, P. Neugebauer, S. Al-Badran, D. Collison, F. Tuna, J. van Slageren, S. Carretta, T. Guidi, E. J. L. McInnes, R. E. P. Winpenny and N. F. Chilton, *Journal of the American Chemical Society*, 2018, **140**, 2504–2513.

[187] P. P. Hallmen, H.-J. Werner, D. Kats, S. Lenz, G. Rauhut, H. Stoll and J. van Slageren, *Physical Chemistry Chemical Physics*, 2019, **21**, 9769–9778.

[188] W. Wernsdorfer, N. Aliaga-Alcalde, D. N. Hendrickson and G. Christou, *Nature*, 2002, **416**, 406–409.

[189] Y.-N. Guo, G.-F. Xu, W. Wernsdorfer, L. Ungur, Y. Guo, J. Tang, H.-J. Zhang, L. F. Chibotaru and A. K. Powell, *Journal of the American Chemical Society*, 2011, **133**, 11948–11951.

[190] I. F. Díaz-Ortega, J. M. Herrera, D. Aravena, E. Ruiz, T. Gupta, G. Rajaraman, H. Nojiri and E. Colacio, *Inorganic Chemistry*, 2018, **57**, 6362–6375.

[191] T. Han, Y.-S. Ding, Z.-H. Li, K.-X. Yu, Y.-Q. Zhai, N. F. Chilton and Y.-Z. Zheng, *Chemical Communications*, 2019, **55**, 7930–7933.

[192] M. Perfetti, M. Gysler, Y. Rechkemmer-Patalen, P. Zhang, H. Taştan, F. Fischer, J. Netz, W. Frey, L. W. Zimmermann, T. Schleid, M. Hakl, M. Orlita, L. Ungur, L. Chibotaru, T. Brock-Nannestad, S. Piligkos and J. van Slageren, *Chemical Science*, 2019, **10**, 2101–2110.

[193] E. C. Mazarakioti, J. Regier, L. Cunha-Silva, W. Wernsdorfer, M. Pilkington, J. Tang and T. C. Stamatatos, *Inorganic Chemistry*, 2017, **56**, 3568–3578.

[194] J. Xiong, H.-Y. Ding, Y.-S. Meng, C. Gao, X.-J. Zhang, Z.-S. Meng, Y.-Q. Zhang, W. Shi, B.-W. Wang and S. Gao, *Chemical Science*, 2017, **8**, 1288–1294.

[195] T. P. Latendresse, N. S. Bhuvanesh and M. Nippe, *Journal of the American Chemical Society*, 2017, **139**, 14877–14880.

[196] H.-M. Dong, H.-Y. Li, Y.-Q. Zhang, E.-C. Yang and X.-J. Zhao, *Inorganic Chemistry*, 2017, **56**, 5611–5622.

[197] T. Pugh, N. F. Chilton and R. A. Layfield, *Angewandte Chemie International Edition*, 2016, **55**, 11082–11085.

[198] F.-S. Guo and R. A. Layfield, *Chemical Communications*, 2017, **53**, 3130–3133.

[199] D. Errulat, B. Gabidullin, A. Mansikkamäki and M. Murugesu, *Chemical Communications*, 2020, **56**, 5937–5940.

[200] P. Evans, D. Reta, C. A. P. Goodwin, F. Ortu, N. F. Chilton and D. P. Mills, *Chemical Communications*, 2020, **56**, 5677–5680.

[201] S. Demir, I.-R. Jeon, J. R. Long and T. D. Harris, *Coordination Chemistry Reviews*, 2015, **289-290**, 149–176.

[202] Z.-X. Xiao, H. Miao, D. Shao, H.-Y. Wei, Y.-Q. Zhang and X.-Y. Wang, *Chemical Communications*, 2018, **54**, 9726–9729.

[203] J. D. Rinehart, M. Fang, W. J. Evans and J. R. Long, *Nature Chemistry*, 2011, **3**, 538–542.

[204] J. D. Rinehart, M. Fang, W. J. Evans and J. R. Long, *Journal of the American Chemical Society*, 2011, **133**, 14236–14239.

[205] S. Demir, J. M. Zadrozny, M. Nippe and J. R. Long, *Journal of the American Chemical Society*, 2012, **134**, 18546–18549.

[206] S. Demir, M. I. Gonzalez, L. E. Darago, W. J. Evans and J. R. Long, *Nature Communications*, 2017, **8**, 2144.

[207] F. Liu, D. S. Krylov, L. Spree, S. M. Avdoshenko, N. A. Samoylova, M. Rosenkranz, A. Kostanyan, T. Greber, A. U. B. Wolter, B. Büchner and A. A. Popov, *Nature Communications*, 2017, **8**, 16098.

[208] F. Liu, L. Spree, D. S. Krylov, G. Velkos, S. M. Avdoshenko and A. A. Popov, *Accounts of Chemical Research*, 2019, **52**, 2981–2993.

[209] V. Vieru, L. Ungur and L. F. Chibotaru, *The Journal of Physical Chemistry Letters*, 2013, **4**, 3565–3569.

[210] G. Lu, Y. Liu, W. Deng, G.-Z. Huang, Y.-C. Chen, J.-L. Liu, Z.-P. Ni, M. Giansiracusa, N. F. Chilton and M.-L. Tong, *Inorganic Chemistry Frontiers*, 2020, **7**, 2941–2948.

[211] L. Ungur, S.-Y. Lin, J. Tang and L. F. Chibotaru, *Chemical Society Reviews*, 2014, **43**, 6894–6905.

[212] X.-L. Li and J. Tang, *Dalton Transactions*, 2019, **48**, 15358–15370.

[213] R. Westerström, J. Dreiser, C. Piamonteze, M. Muntwiler, S. Weyeneth, K. Krämer, S.-X. Liu, S. Decurtins, A. Popov, S. Yang, L. Dunsch and T. Greber, *Physical Review B*, 2014, **89**, 060406.

[214] T. Pugh, F. Tuna, L. Ungur, D. Collison, E. J. McInnes, L. F. Chibotaru and R. A. Layfield, *Nature Communications*, 2015, **6**, 7492.

[215] R. Grindell, V. Vieru, T. Pugh, L. F. Chibotaru and R. A. Layfield, *Dalton Transactions*, 2016, **45**, 16556–16560.

[216] I. F. Díaz-Ortega, J. M. Herrera, T. Gupta, G. Rajaraman, H. Nojiri and E. Colacio, *Inorganic Chemistry*, 2017, **56**, 5594–5610.

[217] C. A. Gould, L. E. Darago, M. I. Gonzalez, S. Demir and J. R. Long, *Angewandte Chemie International Edition*, 2017, **56**, 10103–10107.

[218] B. S. Dolinar, D. I. Alexandropoulos, K. R. Vignesh, T. James and K. R. Dunbar, *Journal of the American Chemical Society*, 2018, **140**, 908–911.

[219] A. Soncini and L. F. Chibotaru, *Physical Review B*, 2010, **81**, 132403.

[220] D. I. Plokhov, A. I. Popov and A. K. Zvezdin, *Physical Review B*, 2011, **84**, 224436.

[221] J. Tang, I. Hewitt, N. T. Madhu, G. Chastanet, W. Wernsdorfer, C. E. Anson, C. Benelli, R. Sessoli and A. K. Powell, *Angewandte Chemie International Edition*, 2006, **45**, 1729–1733.

[222] L. Chibotaru, L. Ungur and A. Soncini, *Angewandte Chemie International Edition*, 2008, **47**, 4126–4129.

[223] J. Goura, E. Colacio, J. M. Herrera, E. A. Suturina, I. Kuprov, Y. Lan, W. Wernsdorfer and V. Chandrasekhar, *Chemistry - A European Journal*, 2017, **23**, 16621–16636.

[224] K. R. Vignesh, A. Soncini, S. K. Langley, W. Wernsdorfer, K. S. Murray and G. Rajaraman, *Nature Communications*, 2017, **8**, 1023.

[225] K. R. Vignesh, S. K. Langley, A. Swain, B. Moubaraki, M. Damjanović, W. Wernsdorfer, G. Rajaraman and K. S. Murray, *Angewandte Chemie International Edition*, 2018, **57**, 779–784.

[226] H. Kaemmerer, A. Baniodeh, Y. Peng, E. Moreno-Pineda, M. Schulze, C. E. Anson, W. Wernsdorfer, J. Schnack and A. K. Powell, *Journal of the American Chemical Society*, 2020, **142**, 14838–14842.

[227] I. M. Müller and R. Robson, *Angewandte Chemie*, 2000, **39**, 4357–4359.

[228] I. M. Müller, R. Robson and F. Separovic, *Angewandte Chemie International Edition*, 2001, **40**, 4385.

[229] I. M. Müller, D. Möller and C. A. Schalley, *Angewandte Chemie International Edition*, 2004, **44**, 480–484.

[230] I. M. Müller, S. Spillmann, H. Franck and R. Pietschnig, *Chemistry - A European Journal*, 2004, **10**, 2207–2213.

[231] I. M. Müller and D. Möller, *Angewandte Chemie International Edition*, 2005, **44**, 2969–2973.

[232] I. M. Müller, D. Möller and K. Föcker, *Chemistry - A European Journal*, 2005, **11**, 3318–3324.

[233] I. M. Oppel and K. Föcker, *Angewandte Chemie International Edition*, 2008, **47**, 402–405.

[234] I. M. Müller and D. Möller, *European Journal of Inorganic Chemistry*, 2005, 257–263.

[235] X.-J. Jiang, M. Li, H.-L. Lu, L.-H. Xu, H. Xu, S.-Q. Zang, M.-S. Tang, H.-W. Hou and T. C. W. Mak, *Inorganic Chemistry*, 2014, **53**, 12665–12667.

[236] A. Zharkouskaya, A. Buchholz and W. Plass, *European Journal of Inorganic Chemistry*, 2005, 4875–4879.

[237] A. Zharkouskaya, H. Görls, G. Vaughan and W. Plass, *Inorganic Chemistry Communications*, 2005, **8**, 1145–1148.

[238] W. Plass, *Coordination Chemistry Reviews*, 2009, **253**, 2286–2295.

[239] D. Schuch, *PhD thesis*, Friedrich-Schiller-Universität Jena, 2014.

[240] A. E. Ion, *PhD thesis*, Friedrich-Schiller-Universität Jena, 2006.

[241] A. E. Ion, E. T. Spielberg, H. Görls and W. Plass, *Inorganica Chimica Acta*, 2007, **360**, 3925–3931.

[242] A. Zharkouskaya, *PhD thesis*, Friedrich-Schiller-Universität Jena, 2006.

[243] E. T. Spielberg, *PhD thesis*, Friedrich-Schiller-Universität Jena, 2009.

[244] M. Böhme, D. Schuch, A. Buchholz, H. Görls and W. Plass, *Zeitschrift für anorganische und allgemeine Chemie*, 2020, **646**, 166–174.

[245] M. Böhme, A. E. Ion, B. Kintzel, A. Buchholz, H. Görls and W. Plass, *Zeitschrift für anorganische und allgemeine Chemie*, 2020, **646**, 999–1009.

[246] E. T. Spielberg, A. Gilb, D. Plaul, D. Geibig, D. Hornig, D. Schuch, A. Buchholz, A. Ardavan and W. Plass, *Inorganic Chemistry*, 2015, **54**, 3432–3438.

[247] B. Kintzel, *Master Thesis*, Friedrich-Schiller-Universität Jena, 2015.

[248] D. Hornig, *PhD thesis*, Friedrich-Schiller-Universität Jena, 2014.

[249] D. Plaul, M. Böhme, S. Ostrovsky, Z. Tomkowicz, H. Görls, W. Haase and W. Plass, *Inorganic Chemistry*, 2017, **57**, 106–119.

[250] B. Kintzel, M. Böhme, J. Liu, A. Burkhardt, J. Mrozek, A. Buchholz, A. Ardavan and W. Plass, *Chemical Communications*, 2018, **54**, 12934–12937.

[251] H. Zabrodsky, S. Peleg and D. Avnir, *Journal of the American Chemical Society*, 1993, **115**, 8278–8289.

[252] H. Zabrodsky, S. Peleg and D. Avnir, *IEEE Transactions on Pattern Analysis and Machine Intelligence*, 1995, **17**, 1154–1166.

[253] M. Pinsky and D. Avnir, *Inorganic Chemistry*, 1998, **37**, 5575–5582.

[254] A. W. Addison, T. N. Rao, J. Reedijk, J. van Rijn and G. C. Verschoor, *Journal of the Chemical Society, Dalton Transactions*, 1984, 1349–1356.

[255] N. F. Chilton, R. P. Anderson, L. D. Turner, A. Soncini and K. S. Murray, *Journal of Computational Chemistry*, 2013, **34**, 1164–1175.

[256] L. K. Thompson, S. K. Mandal, S. S. Tandon, J. N. Bridson and M. K. Park, *Inorganic Chemistry*, 1996, **35**, 3117–3125.

[257] L. K. Thompson, Z. Xu, A. E. Goeta, J. A. K. Howard, H. J. Clase and D. O. Miller, *Inorganic Chemistry*, 1998, **37**, 3217–3229.

[258] H. Grove, T. L. Kelly, L. K. Thompson, L. Zhao, Z. Xu, T. S. M. Abedin, D. O. Miller, A. E. Goeta, C. Wilson and J. A. K. Howard, *Inorganic Chemistry*, 2004, **43**, 4278–4288.

[259] J. Liu, J. Mrozek, W. K. Myers, G. A. Timco, R. E. Winpenny, B. Kintzel, W. Plass and A. Ardavan, *Physical Review Letters*, 2019, **122**, year.

[260] B. Kintzel, M. Fittipaldi, M. Böhme, A. Cini, L. Tesi, A. Buchholz, R. Sessoli and W. Plass, *Angewandte Chemie International Edition*, 2021.

[261] M. Küllmer and B. Kintzel, Private Communication.

[262] R. Hermenau and B. Kintzel, Private Communication.

[263] E. Weschke and B. Kintzel, Private Communication.

[264] E. Weschke and E. Schierle, *Journal of Large-Scale Research Facilities*, 2018, **4**, A127.

[265] A. G. Orpen, L. Brammer, F. H. Allen, O. Kennard, D. G. Watson and R. Taylor, *Journal of the Chemical Society, Dalton Transactions*, 1989, S1 – S83.

[266] E. Bill, Private Communication.

[267] D. W. H. Rankin, N. Mitzel and C. Morrison, *Structural Methods in Molecular Inorganic Chemistry*, John Wiley and Sons Inc, 2013.

[268] E. Fluck, W. Kerler and W. Neuwirth, *Angewandte Chemie International Edition in English*, 1963, **2**, 277–287.

[269] A. Garg and P. Goel, *Journal of Inorganic and Nuclear Chemistry*, 1969, **31**, 697–702.

[270] A. Garg and P. Goel, *Journal of Inorganic and Nuclear Chemistry*, 1970, **32**, 1547–1557.

[271] C. Mukherjee, V. Hoeke, A. Stammler, H. Bögge, J. Schnack and T. Glaser, *Dalton Transactions*, 2014, **43**, 9690–9703.

[272] M. Böhme, Private Communication, Jena.

[273] T. Glaser, V. Hoeke, K. Gieb, J. Schnack, C. Schröder and P. Müller, *Coordination Chemistry Reviews*, 2015, **289-290**, 261–278.

[274] F. V. D. Cruser and E. H. Miller, *Journal of the American Chemical Society*, 1906, **28**, 1132–1151.

[275] J. J. Alexander and H. B. Gray, *Journal of the American Chemical Society*, 1968, **90**, 4260–4271.

[276] R. P. Scaringe, W. E. Hatfield and D. J. Hodgson, *Inorganic Chemistry*, 1977, **16**, 1600–1605.

[277] E. E. Eduok, J. W. Owens and C. J. O'Connor, *Polyhedron*, 1984, **3**, 17–20.

[278] C. Reber, H. U. Guedel, L. Spiccia and W. Marty, *Inorganic Chemistry*, 1987, **26**, 3186–3191.

[279] R. Sanzenbacher, A. Böttcher, H. Elias, M. Hüber, W. Haase, J. Glerup, T. B. Jensen, M. Neuburger, M. Zehnder, J. Springborg and C. E. Olsen, *Inorganic Chemistry*, 1996, **35**, 7493–7499.

[280] T. Nakamura, K. Sasamori, T. Kodama, K. Kikuchi and W. Fujita, *Chemistry - An Asian Journal*, 2012, **8**, 348–350.

[281] T. J. Morsing, H. Weihe and J. Bendix, *European Journal of Inorganic Chemistry*, 2014, **2014**, 5990–5996.

[282] J. Glerup, D. J. Hodgson, E. Pedersen, A. Haaland, B. E. R. Schilling, R. Seip and K. Taugbøl, *Acta Chemica Scandinavica*, 1983, **37a**, 161–164.

[283] A. K. Boudalis, G. Rogez and P. Turek, *Inorganic Chemistry*, 2018, **57**, 13259–13269.

[284] H. Katsura, N. Nagaosa and A. V. Balatsky, *Physical Review Letters*, 2005, **95**, 057205.

[285] L. Mathivathanan, G. Rogez, N. B. Amor, V. Robert, R. G. Raptis and A. K. Boudalis, *Chemistry – A European Journal*, 2020, **26**, 12769–12784.

[286] M. Abo-Bakr, J. Feikes, K. Holldack, P. Kuske, W. B. Peatman, U. Schade, G. Wüstefeld and H.-W. Hübers, *Physical Review Letters*, 2003, **90**, 094801.

[287] J. Nehrkorn, K. Holldack, R. Bittl and A. Schnegg, *Journal of Magnetic Resonance*, 2017, **280**, 10–19.

[288] M. Böhme, S. Ziegenbalg, A. Aliabadi, A. Schnegg, H. Görls and W. Plass, *Dalton Transactions*, 2018, **47**, 10861–10873.

[289] T. Lohmiller, Private Communication.

[290] T. Wünscher, *MSc thesis*, Friedrich-Schiller-Universität Jena, 2018.

[291] L. Ungur, W. V. den Heuvel and L. F. Chibotaru, *New Journal of Chemistry*, 2009, **33**, 1224.

[292] T. Han, M. J. Giansiracusa, Z.-H. Li, Y.-S. Ding, N. F. Chilton, R. E. P. Winpenny and Y.-Z. Zheng, *Chemistry – A European Journal*, 2020, **26**, 6773–6777.

[293] M. Damjanović and W. Wernsdorfer, Private Communication.

[294] D. Reta and N. F. Chilton, *Physical Chemistry Chemical Physics*, 2019, **21**, 23567–23575.

[295] L. Gu and R. Wu, *Physical Review B*, 2020, **103**, 014401.

[296] W. J. Gee, J. G. MacLellan, C. M. Forsyth, B. Moubaraki, K. S. Murray, P. C. Andrews and P. C. Junk, *Inorganic Chemistry*, 2012, **51**, 8661–8663.

[297] G. B. Deacon, C. M. Forsyth, D. Freckmann, P. C. Junk, K. Konstas, J. Luu, G. Meyer and D. Werner, *Australian Journal of Chemistry*, 2014, **67**, 1860.

[298] X.-T. Wang, H.-M. Dong, X.-G. Wang, E.-C. Yang and X.-J. Zhao, *Zeitschrift für anorganische und allgemeine Chemie*, 2016, **642**, 1166–1172.

[299] H. Ke, X. Lu, W. Wei, W. Wang, G. Xie and S. Chen, *Dalton Transactions*, 2017, **46**, 8138–8145.

[300] B. Neumüller, F. Weller, T. Gröb and K. Dehnicke, *Zeitschrift für anorganische und allgemeine Chemie*, 2002, **628**, 2365–2371.

[301] G. M. Sheldrick, *Acta Cryst.*, 2015, **C71**, 3–8.

[302] G. M. Sheldrick, SHELXS97 *and* SHELXL97; *University of Göttingen*, 1997.

[303] A. Burkhardt, M. Warmer, N. Stuebe, J. Roever, B. Reime, S. Panneerselvam, T. Pakendorf, J. Meyer, P. Fischer and A. Meents, *Acta Crystallographica Section A Foundations and Advances*, 2014, **70**, C1725–C1725.

[304] D. Göries, B. Dicke, P. Roedig, N. Stübe, J. Meyer, A. Galler, W. Gawelda, A. Britz, P. Geßler, H. S. Namin, A. Beckmann, M. Schlie, M. Warmer, M. Naumova, C. Bressler, M. Rübhausen, E. Weckert and A. Meents, *Review of Scientific Instruments*, 2016, **87**, 053116.

[305] N. C. F. N. RESEARCH, *Data Analysis and Visualization Environment (DAVE)*, http://www.ncnr.nist.gov/dave/index.html, 2010.

[306] OriginLab, *Origin Pro 2016*, www.OriginLab.com, 2016.

[307] S. Stoll and A. Schweiger, *Journal of Magnetic Resonance*, 2006, **178**, 42–55.

List of Abbreviations

Concepts:

AC	Alternating Current
DC	Direct Current
DM	Dzyaloshinsky-Moriya
hs	high spin
ls	low spin
SIM	Single-Ion Magnet
SMM	Single-Molecule Magnet
SMT	Single-Molecule Toroic
STM	Scanning Tunneling Microscopy
(TA-)QTM	(Thermally Assisted) Quantum Tunneling of Magnetisation
VMCRM	Vibrational Mode Correlated Relaxation of Magnetisation
ZFS	Zero Field Splitting

Chemical compounds:

bpy	2,2′-bipyridine
DMAP	4-dimethylaminopyridine
DMF	*N,N*-dimethylformamide
OTf	trifluoromethanesulphonate
PPN	bis(triphenylphosphine)iminium
py	pyridine
pytag	1,2,3-tris[(pyridin-2-ylmethylidene)amino]guanidine
quintag	1,2,3-tris[(8-hydroxyquinol-2-ylmethylidene)amino]guanidine
saltag	1,2,3-tris[(2-hydroxybenzylidene)amino]guanidine
tag	triaminoguanidine
THF	tetrahydrofuran

Analytic methods:

EFM	Electric Field Modulated
(D)ESI	(Desorption) ElectroSpray Ionisation
ESR	Electron Spin Resonance
IR	InfraRed spectroscopy
M	composition of the respective compound as found in the crystal structure
MS	Mass Spectrometry
NMR	Nuclear Magnetic Resonance
SQUID	Superconductiing QUantum Interference Device
ZFC	Zero Field-Cooled/ Field-Cooled
w	weak IR band intensity
m	medium IR band intensity
s	strong IR band intensity/ singlet NMR signal
vs	very strong IR band intensity
br	broad IR band
d	doublet NMR signal

List of Compounds

3d metal complexes:

1	$[Cu_3(saltag^H)(py)_6]ClO_4 \cdot 0.5\,HpyClO_4 \cdot 2\,H_2O$
2	$[Zn_3(saltag^H)(py)_6]ClO_4 \cdot 0.5\,H_2O$
3	$[Cu_3(saltag^H)(py)_6]NO_3$
4	$[Cu_3(saltag^H)(py)_3]OTf$
5	$[Cu_3(saltag^H)(bpy)_3]OTf$
6	$[Cu_3(quintag)(py)_3]ClO_4$
7	$[Cu_6(quintag^{ox})_2(py)_4] \cdot py \cdot 2\,MeOH$
9	$[K(18\text{-}crown\text{-}6)][(Fe_3saltag^HCl_3(py)_6)_2\mu(Fe(CN)_6)]$
10	$[(KFe_3saltag^{Br}Cl_3(py)_3)_2\mu(Fe(CN)_6)]$
11	$[Cr_2(Hsaltag^{Br})Cl_2(py)_4] \cdot 2.5py \cdot 2\,H_2O$
12	$[Cr_3(saltag^{Br})Cl_3(py)_6]ClO_4 \cdot py \cdot H_2O$

4f metal complexes:

13	$[DyK_2(H_3saltag^{NPh})_2(dmf)_3(MeOH)_3]BPh_4$
14	$[DyNa_2(H_3saltag^{NPh})_2(dmf)_3(MeOH)_3]BPh_4$
15	$[Dy_2(H_2saltag^{Br})_2(dmf)_4] \cdot 1.75H_2O$
15@Y	$[DyY(H_2saltag^{Br})_2(dmf)_4] \cdot 1.75H_2O$
16	$[Dy_2(H_2saltag^{Br})_2(dmf)_4] \cdot 2\,DMF$
17	$[Dy_2(H_2saltag^{Br})_2(py)_4] \cdot H_2O \cdot py$
18	$[Dy_2(H_2saltag^{Br})_2(MeOH)_4]$
19	$[Dy_3(H_{0.5}saltag^{Br})_2(MeOH)_6] \cdot 3.5\,MeOH$
20	$PPN[Dy_3(saltag^I)_2(MeOH)_5] \cdot 5\,MeOH$
20@Y/Lu	$PPN[DyYLu(saltag^I)_2(MeOH)_5] \cdot 5\,MeOH$
21	$(H_{0.5}DMAP)_2[Dy_3(saltag^I)_2(MeOH)_6] \cdot 2\,MeOH$
21@Y	$(H_{0.5}DMAP)_2[Dy_{0.4}Y_{2.6}(saltag^I)_2(MeOH)_6] \cdot 2\,MeOH$
22	$[Dy_3(H_{0.5}saltag^I)_2(thf)_6]$
23	$[Dy_4(pytag^{cyc})_2(O_2)_2Cl_4(MeOH)_6]Cl_2 \cdot 3\,MeOH \cdot H_2O$

DANKSAGUNG

An dieser Stelle seien dem Autor einige Worte des Dankes an die vielen Menschen, die maßgeblich zum Gelingen dieser Arbeit beitrugen, gestattet. Zuallererst soll dabei Prof. Dr. Winfried Plass Erwähnung finden, der es vermochte mich trotz anfänglich vehementer Skepsis nachhaltig für das Forschungsgebiet des molekularen Magnetismus zu begeistern, der mir stets jeglichen kreativen Freiraum für das alles andere als vorhersehbare „schöpferische Werk" im Bereich der Koordinationschemie mit Lanthanoiden und 3d Übergangsmetallen zugestand, der mir durch die Teilnahme an vielen *summer-schools*, nationalen und internationalen Konferenzen das tatsächliche Eintauchen in multilateralen, internationalen und interdisziplinären Wissenschaftsdiskurs und kooperativen Wissenschaftsbetrieb ermöglichte, der durch das hartnäckige Anleiern und Unterstützen von wissenschaftlichen Kooperationen bewirkt hat, dass einige meiner hart erarbeiteten Resultate nicht nur mit spannenden Methoden untersucht werden können, sondern hoffentlich dadurch auch in der Zukunft Beachtung finden und nicht in Schubladen des Vergessens ihre letzte Ruhe finden und der natürlich auch stets für fruchtbare fachliche Diskussionen bereitstand.

Prof. Dr. Robert Kretschmer danke ich herzlich für die Anfertigung des Zweitgutachtens.

Dr. Axel Buchholz möchte ich für die immerwährende Unterstützung bei geräte- und auswertetechnischen Fragen wirklich aller Art, sowie seine Hilfe bei tausend kleinen Dingen am Rande des Wissenschaftsbetriebs danken.

Zwei Analysemethoden, die das Rückgrat dieser Arbeit darstellen, erfordern eine besonders explizite Botschaft des Dankes an die dahinterstehenden Personen. Für die Strukturaufklärung mittels Einkristallröntgendiffraktometrie sei hier Herrn Dr. Helmar Görls, der ein ums andere Mal auch bei stark abweichenden "mitgelieferten Strukturvorschlägen", hoher Symmetrie und komplexen Molekülstrukturen Lösungen erarbeitete, die für die jeweiligen Verbindungen das Tor zum Verständnis ihrer Eigenschaften öffneten, und Frau Dr. Anja Burkhard, die mit bloßem Auge nicht erkennbaren Kristallsplittern mithilfe von brillianter Synchrotronstrahlung und Geduld dennoch sehr gute Strukturdatensätze entlockte, vielfach gedankt. Meine Anforderungen an die SQUID-Magnetometrie mit unzähligen Proben, verschiedenen Präparationsformen und abenteuerlichen, tagelangen Messsequenzen wurden stets mit Verständnis und Präzision von

Declaration of Authorship /
Selbstständigkeitserklärung

I hereby declare, that the work presented is, to the best of my knowledge and belief, the result of my own investigations, except as indicated, and has not been submitted, either in part or whole, for a degree at any other university.

Ich erkläre hiermit, dass die vorliegende Arbeit selbstständig und ausschließlich unter Verwendung der angegebenen Hilfsmittel, persönlichen Mitteilungen und Quellen von mir angefertigt wurde. Ich habe keine gleiche oder in wesentlichen Teilen ähnliche Abhandlung bei einer anderen Hochschule als Dissertation eingereicht.

Jena,

Benjamin Kintzel

CRYSTAL STRUCTURE INFORMATION

In here the crystallographic and structure refinement details for all crystal structures discussed in this work are given.

Table A.1: Crystallographic data and structure refinement parameters for **1**.

formula	$C_{54.5}H_{50}Cl_{1.5}Cu_3N_{12.5}O_{10}$
formula weight (g mol^{-1})	1283.86
crystal system	trigonal
space group	$P31c$ (#159)
a (pm)	1506.4(2)
b (pm)	1506.4(2)
c (pm)	2904.2(6)
α (°)	90
β (°)	90
γ (°)	120
V (10^6 pm^3)	5707(2)
T (K)	80(2)
δ_{calc} (g cm^{-3})	1.494
Z	4
μ (mm^{-1})	0.862
Flack parameter	0.056(3)
wavelength (pm)	61.99
radiation type	synchrotron
Θ range of data collection (°)	$1.492 \leq \Theta \leq 27.112$
measured reflections	113617
independent reflections	12610
reflections used	12271
R_{int}	0.0380
no. of parameters	527
no. of restraints	7
goodness-of-fit	1.070
R_1 (all data)	0.0392
R_1	0.0383
wR_2 (all data)	0.1152
wR_2	0.1141

Table A.2: Crystallographic data and structure refinement parameters for **2**.

formula	$C_{52}H_{45}ClN_{12}O_7Zn_3$
formula weight (g mol^{-1})	1181.56
crystal system	hexagonal
space group	$P6_3/m$ (#176)
a (pm)	1505.29(2)
b (pm)	1505.29(2)
c (pm)	1460.74(2)
α (°)	90
β (°)	90
γ (°)	120
V (10^6 pm^3)	2866.45(9)
T (K)	133(2)
radiation type/ λ(pm)	MoKα/ 71.073
δ_{calc} (g cm^{-3})	1.369
Z	6
μ (mm^{-1})	1.350
Θ range of data collection (°)	$1.394 \leq \Theta \leq 27.462$
measured reflections	29003
independent reflections	2280
reflections used	2280
R_{int}	0.0569
no. of parameters	127
no. of restraints	12
goodness-of-fit	1.092
R_1 (all data)	0.0669
R_1	0.0638
wR_2 (all data)	0.1730
wR_2	0.1705

Table A.3: Crystallographic data and structure refinement parameters for **3**.

formula	$C_{53.5}H_{51}Cl_1Cu_3N_{12}O_{4.5}$
formula weight ($g\,mol^{-1}$)	1160.16
crystal system	hexagonal
space group	$P6_3/m$ (#176)
a (pm)	1470.8
b (pm)	1470.8
c (pm)	1472.6
α (°)	90
β (°)	90
γ (°)	120
T (K)	133(2)
radiation type/ λ(pm)	MoKα/ 71.073
Z	2

Table A.4: Crystallographic data and structure refinement parameters for **4**.

formula	$C_{38}H_{30}Cu_3F_3N_9O_6S$
formula weight $(g\,mol^{-1})$	988.39
crystal system	trigonal
space group	$R\overline{3}$ (#148)
a (pm)	1595.89(2)
b (pm)	1595.89(2)
c (pm)	2730.80(5)
α (°)	90
β (°)	90
γ (°)	120
V $(10^6\,pm^3)$	6023.19(19)
T (K)	133(2)
radiation type/ λ(pm)	$MoK\alpha$/ 71.073
δ_{calc} $(g\,cm^{-3})$	1.635
Z	6
μ (mm^{-1})	1.699
Θ range of data collection (°)	$3.328 \leq \Theta \leq 27.484$
measured reflections	11001
independent reflections	3027
reflections used	3027
R_{int}	0.0274
no. of parameters	221
no. of restraints	0
goodness-of-fit	1.081
R_1 (all data)	0.0317
R_1	0.0296
wR_2 (all data)	0.0841
wR_2	0.0825

Table A.5: Crystallographic data and structure refinement parameters for **5**. Mind that the cocrystallised solvent was "squeezed" out.

formula	$C_{53}H_{39}Cu_3F_3N_{12}O_6S$
formula weight $(g\,mol^{-1})$	1219.64
crystal system	trigonal
space group	$R\bar{3}$ (#148)
a (pm)	1968.38(18)
b (pm)	1968.38(18)
c (pm)	2740.14(16)
α (°)	90
β (°)	90
γ (°)	120
V $(10^6\,pm^3)$	9194.4(18)
T (K)	133(2)
radiation type/ λ(pm)	MoKα/ 71.073
δ_{calc} $(g\,cm^{-3})$	1.322
Z	6
μ (mm^{-1})	1.128
Θ range of data collection (°)	$1.907 \leq \Theta \leq 27.484$
measured reflections	31937
independent reflections	4682
reflections used	4682
R_{int}	0.0451
no. of parameters	235
no. of restraints	0
goodness-of-fit	1.058
R_1 (all data)	0.0525
R_1	0.0416
wR_2 (all data)	0.1164
wR_2	0.1108

Table A.6: Crystallographic data and structure refinement parameters for **6**. Mind that the cocrystallised solvent was "squeezed" out.

formula	$C_{46}H_{33}ClCu_3N_{12}O_7$
formula weight ($g\,mol^{-1}$)	1091.9
crystal system	trigonal
space group	$R3$ (#146)
a (pm)	2010.15(12)
b (pm)	2010.15(12)
c (pm)	2005.50(11)
α (°)	90
β (°)	90
γ (°)	120
V ($10^6\,pm^3$)	7017.9(9)
T (K)	133(2)
radiation type/ λ(pm)	MoKα/ 71.073
δ_{calc} ($g\,cm^{-3}$)	1.477
Z	6
μ (mm^{-1})	1.432
Θ range of data collection (°)	$1.549 \leq \Theta \leq 27.482$
measured reflections	13732
independent reflections	6490
reflections used	6490
R_{int}	0.0508
no. of parameters	395
no. of restraints	1
goodness-of-fit	1.099
R_1 (all data)	0.0755
R_1	0.0590
wR_2 (all data)	0.1354
wR_2	0.1240

Table A.7: Crystallographic data and structure refinement parameters for **7**.

formula	$C_{96}H_{80}Cu_6N_{24}O_{12}$
formula weight ($g\,mol^{-1}$)	2143.08
crystal system	monoclinic
space group	$P2_1/c$ (#14)
a (pm)	1686.41(3)
b (pm)	2026.87(3)
c (pm)	1388.19(2)
α (°)	90
β (°)	111.746(1)
γ (°)	90
V ($10^6\,pm^3$)	4407.34
T (K)	133(2)
radiation type/ λ(pm)	MoKα / 71.073
δ_{calc} ($g\,cm^{-3}$)	1.615
Z	2
μ (mm^{-1})	1.502
Θ range of data collection (°)	$1.872 \leq \Theta \leq 27.482$
measured reflections	34547
independent reflections	10090
reflections used	6490
R_{int}	0.0360
no. of parameters	629
no. of restraints	0
goodness-of-fit	1.052
R_1 (all data)	0.0459
R_1	0.0376
wR_2 (all data)	0.0903
wR_2	0.0852

Table A.8: Crystallographic data and structure refinement parameters for **9**.

formula	$C_{214}H_{204}Cl_{18}Fe_{14}K_2N_{54}O_{24}$
formula weight $(g\,mol^{-1})$	5414.5
crystal system	trigonal
space group	$R\bar{3}$ (#148)
a (pm)	1825.79(2)
b (pm)	1825.79(2)
c (pm)	8208.00(12)
α (°)	90
β (°)	90
γ (°)	120
V $(10^6\,pm^3)$	23863.4(6)
T (K)	133(2)
radiation type/ λ(pm)	MoKα/ 71.073
δ_{calc} $(g\,cm^{-3})$	1.13
Z	3
μ (mm^{-1})	0.850
Θ range of data collection (°)	$1.311 \leq \Theta \leq 27.483$
measured reflections	64781
independent reflections	11709
reflections used	11709
R_{int}	0.0771
no. of parameters	493
no. of restraints	0
goodness-of-fit	1.058
R_1 (all data)	0.1325
R_1	0.1192
wR_2 (all data)	0.3455
wR_2	0.3324

Table A.9: Crystallographic data and structure refinement parameters for **10**.

formula	$C_{127.5}H_{101.5}Br_6Cl_6Fe_7K_2N_{33.5}$
formula weight ($g\,mol^{-1}$)	3392.23
crystal system	monoclinic
space group	$P2_1/c$ (#14)
a (pm)	1555.40(2)
b (pm)	1980.19(4)
c (pm)	2425.46(5)
α (°)	90
β (°)	106.903(1)
γ (°)	90
V ($10^6\,pm^3$)	7147.7(2)
T (K)	133(2)
radiation type/ λ(pm)	MoKα / 71.073
δ_{calc} ($g\,cm^{-3}$)	1.576
Z	2
μ (mm^{-1})	2.603
Θ range of data collection (°)	$1.83 \leq \Theta \leq 27.10$
measured reflections	48631
independent reflections	15697
reflections used	15697
R_{int}	0.0838
no. of parameters	821
no. of restraints	1
goodness-of-fit	1.087
R_1 (all data)	0.0848
R_1	0.0627
wR_2 (all data)	0.1545
wR_2	0.1424

Table A.10: Crystallographic data and structure refinement parameters for **11**.

formula	$C_{43}H_{37}Br_3Cl_2Cr_2N_{10.2}O_{4.1}$
formula weight ($g\,mol^{-1}$)	1176
crystal system	monoclinic
space group	$P2_1/c$ (#14)
a (pm)	1890.8(4)
b (pm)	1580.4(3)
c (pm)	2121.1(4)
α (°)	90
β (°)	93.60(3)
γ (°)	90
V ($10^6\,pm^3$)	6325.8(22)
T (K)	80
radiation type/ λ(pm)	synchrotron/ 61.99
δ_{calc} ($g\,cm^{-3}$)	2.061
Z	4
measured reflections	135370
independent reflections	18333
goodness-of-fit	1.037
R_1 (all data)	0.0543
R_1	0.0478

Table A.11: Crystallographic data and structure refinement parameters for **12**. Mind that the cocrystallised solvent was "squeezed" out.

formula	$C_{52}H_{42}Br_3Cl_4Cr_3N_{12}O_7$
formula weight ($g\,mol^{-1}$)	1484.50
crystal system	trigonal
space group	$P\bar{3}$ (#147)
a (pm)	1524.65(2)
b (pm)	1524.65(2)
c (pm)	1615.92(2)
α (°)	90
β (°)	90
γ (°)	120
V ($10^6\,pm^3$)	3253.05(9)
T (K)	133(2)
radiation type/ λ(pm)	MoKα/ 71.073
δ_{calc} ($g\,cm^{-3}$)	1.516
Z	2
μ (mm^{-1})	2.554
Θ range of data collection (°)	$1.992 \leq \Theta \leq 27.48$
measured reflections	25963
independent reflections	4980
reflections used	4980
R_{int}	0.0433
no. of parameters	244
no. of restraints	0
goodness-of-fit	1.063
R_1 (all data)	0.0556
R_1	0.0480
wR_2 (all data)	0.1163
wR_2	0.1117

Table A.12: Crystallographic data and structure refinement parameters for **13**.

formula	$C_{99.5}H_{84.5}BDy_{0.29}K_{2.71}N_{13.5}O_{10}$
formula weight ($g\,mol^{-1}$)	1801.20
crystal system	trigonal
space group	$P\bar{3}$ (#147)
a (pm)	1809.3(3)
b (pm)	1809.3(3)
c (pm)	1648.4(3)
α (°)	90
β (°)	90
γ (°)	120
V ($10^6\,pm^3$)	4673.0(13)
T (K)	133(2)
radiation type/ λ(pm)	MoKα / 71.073
δ_{calc} ($g\,cm^{-3}$)	1.280
Z	2
μ (mm^{-1})	0.428
Θ range of data collection (°)	$2.57 \leq \Theta \leq 27.42$
measured reflections	33778
independent reflections	7125
reflections used	7125
R_{int}	0.0925
no. of parameters	363
no. of restraints	0
goodness-of-fit	1.257
R_1 (all data)	0.1801
R_1	0.1749
wR_2 (all data)	0.3801
wR_2	0.3773

Table A.13: Crystallographic data and structure refinement parameters for **14**.

formula	$C_{97.5}H_{82.5}BDy_{0.64}Na_{2.37}N_{13.5}O_{10}$
formula weight (g mol^{-1})	1779.64
crystal system	trigonal
space group	$P\bar{3}$ (#147)
a (pm)	1810.9(3)
b (pm)	1810.9(3)
c (pm)	1649.9(3)
α (°)	90
β (°)	90
γ (°)	120
V (10^6 pm^3)	4685.6(13)
T (K)	293(2)
radiation type/ λ(pm)	MoKα/ 71.073
δ_{calc} (g cm^{-3})	1.261
Z	2
μ (mm^{-1})	0.587
Θ range of data collection (°)	$2.25 \leq \Theta \leq 27.43$
measured reflections	14200
independent reflections	7130
reflections used	7130
R_{int}	0.0199
no. of parameters	352
no. of restraints	0
goodness-of-fit	1.260
R_1 (all data)	0.1726
R_1	0.1703
wR_2 (all data)	0.4019
wR_2	0.3992

Table A.14: Crystallographic data and structure refinement parameters for **15**.

formula	$C_{56}H_{59.5}Br_6Dy_2N_{16}O_{11.75}$
formula weight (g mol^{-1})	1949.08
crystal system	orthorhombic
space group	$Fdd2$ (#43)
a (pm)	2876.4(6)
b (pm)	3739.0(8)
c (pm)	2605.3(5)
α (°)	90
β (°)	90
γ (°)	90
V (10^6 pm^3)	28019(10)
T (K)	80(2)
δ_{calc} (g cm^{-3})	1.821
Z	16
μ (mm^{-1})	3.919
Flack parameter	0.104(2)
wavelength (pm)	61.99
radiation type	synchrotron
Θ range of data collection (°)	$1.558 \leq \Theta \leq 27.108$
measured reflections	139983
independent reflections	23268
reflections used	22353
R_{int}	0.0312
no. of parameters	834
no. of restraints	1
goodness-of-fit	1.040
R_1 (all data)	0.0368
R_1	0.0351
wR_2 (all data)	0.0994
wR_2	0.0981

Table A.15: Crystallographic data and structure refinement parameters for **16**.

formula	$C_{62}H_{70}Br_6Dy_2N_{18}O_{12}$
formula weight (g mol^{-1})	2063.82
crystal system	monoclinic
space group	$C2/c$ (#15)
a (pm)	2391.15(5)
b (pm)	3081.44(7)
c (pm)	1100.02(3)
α (°)	90
β (°)	95.611(1)
γ (°)	90
V (10^6 pm^3)	8066.3(3)
T (K)	133(2)
radiation type/ λ(pm)	MoKα / 71.073
δ_{calc} (g cm^{-3})	1.699
Z	4
μ (mm^{-1})	4.875
Θ range of data collection (°)	$2.08 \leq \Theta \leq 25.68$
measured reflections	7652
independent reflections	7652
reflections used	7652
R_{int}	0.0879
no. of parameters	464
no. of restraints	4
goodness-of-fit	1.188
R_1 (all data)	0.1061
R_1	0.0823
wR_2 (all data)	0.1688
wR_2	0.1606

Table A.16: Crystallographic data and structure refinement parameters for **17**.

formula	$C_{69}H_{55}Br_6Dy_2N_{17}O_7$
formula weight (g mol^{-1})	2038.76
crystal system	triclinic
space group	$P\bar{1}$ (#2)
a (pm)	1372.30(2)
b (pm)	1779.40(2)
c (pm)	1818.59(2)
α (°)	81.276(1)
β (°)	68.285(1)
γ (°)	80.826(1)
V (10^6 pm^3)	4052.00(9)
T (K)	133(2)
radiation type/ λ(pm)	MoKα / 71.073
δ_{calc} (g cm^{-3})	1.671
Z	2
μ (mm^{-1})	4.846
Θ range of data collection (°)	$1.764 \leq \Theta \leq 27.454$
measured reflections	34044
independent reflections	18364
reflections used	18364
R_{int}	0.0339
no. of parameters	941
no. of restraints	0
goodness-of-fit	1.067
R_1 (all data)	0.0482
R_1	0.0373
wR_2 (all data)	0.0776
wR_2	0.0727

Table A.17: Crystallographic data and structure refinement parameters for **18**.

formula	$C_{48}H_{44}Br_6Dy_2N_{12}O_{10}$
formula weight (g mol^{-1})	1753.41
crystal system	triclinic
space group	$P\bar{1}$ (#2)
a (pm)	990.36(2)
b (pm)	1535.28(4)
c (pm)	2311.36(4)
α (°)	107.652(1)
β (°)	100.526(1)
γ (°)	90.596(1)
V (10^6 pm^3)	3284.42(12)
T (K)	133(2)
radiation type/ λ(pm)	MoKα / 71.073
δ_{calc} (g cm^{-3})	1.773
Z	2
μ (mm^{-1})	5.964
Θ range of data collection (°)	$1.967 \leq \Theta \leq 27.473$
measured reflections	21518
independent reflections	13763
reflections used	13763
R_{int}	0.0397
no. of parameters	733
no. of restraints	0
goodness-of-fit	1.063
R_1 (all data)	0.0522
R_1	0.0420
wR_2 (all data)	0.0940
wR_2	0.0877

Table A.18: Crystallographic data and structure refinement parameters for **19**.

formula	$C_{53.5}H_{62.5}Br_6Dy_3N_{12}O_{15.5}$
formula weight (g mol^{-1})	2088.6
crystal system	triclinic
space group	$P\bar{1}$ (#2)
a (pm)	1286.6(3)
b (pm)	1355.5(3)
c (pm)	2067.2(4)
α (°)	78.75(3)
β (°)	71.91(3)
γ (°)	89.59(3)
V (10^6 pm^3)	3355.5(14)
T (K)	80
radiation type/ λ(pm)	synchrotron/ 61.99
δ_{calc} (g cm^{-3})	2.061
Z	2
μ (mm^{-1})	4.859
Θ range of data collection (°)	$0.92 \leq \Theta \leq 27.10$
measured reflections	68917
independent reflections	20615
reflections used	20615
R_{int}	0.0235
no. of parameters	911
no. of restraints	18
goodness-of-fit	1.026
R_1 (all data)	0.0492
R_1	0.0479
wR_2 (all data)	0.1316
wR_2	0.1306

Table A.19: Crystallographic data and structure refinement parameters for **20**.

formula	$C_{91.5}H_{100}I_6Dy_3N_{13}O_{17.5}P_2$
formula weight (g mol^{-1})	2972.68
crystal system	triclinic
space group	$P\bar{1}$ (#2)
a (pm)	1797.73(2)
b (pm)	1831.12(3)
c (pm)	1929.13(2)
α (°)	67.954(1)
β (°)	75.086(1)
γ (°)	61.259(1)
V (10^6 pm^3)	5137.80(13)
T (K)	133(2)
radiation type/ λ(pm)	synchrotron/ 61.99
δ_{calc} (g cm^{-3})	1.922
Z	2
μ (mm^{-1})	4.062
Θ range of data collection (°)	$2.200 \leq \Theta \leq 27.483$
measured reflections	68080
independent reflections	23412
reflections used	23412
R_{int}	0.0335
no. of parameters	1255
no. of restraints	0
goodness-of-fit	1.055
R_1 (all data)	0.0388
R_1	0.0336
wR_2 (all data)	0.0805
wR_2	0.0775

Table A.20: Crystallographic data and structure refinement parameters for **21**.

formula	$C_{66}H_{77}Dy_3I_6N_{16}O_{14}$
formula weight ($g\,mol^{-1}$)	2567.33
crystal system	monoclinic
space group	$C2/c$ (#15)
a (pm)	1864.24(2)
b (pm)	3461.63(5)
c (pm)	1385.65(2)
α (°)	90
β (°)	104.417(1)
γ (°)	90
V ($10^6\,pm^3$)	8660.4(2)
T (K)	133(2)
radiation type / λ(pm)	$MoK\alpha$ / 71.073
δ_{calc} ($g\,cm^{-3}$)	1.969
Z	4
μ (mm^{-1})	4.764
Θ range of data collection (°)	$2.545 \leq \Theta \leq 27.463$
measured reflections	58750
independent reflections	9895
reflections used	9895
R_{int}	0.0302
no. of parameters	491
no. of restraints	0
goodness-of-fit	1.098
R_1 (all data)	0.0245
R_1	0.0224
wR_2 (all data)	0.0524
wR_2	0.0513

Table A.21: Crystallographic data and structure refinement parameters for **22**.

formula	$C_{68}H_{73}Dy_3I_6N_{12}O_{12}$
formula weight (g mol^{-1})	2499.28
crystal system	monoclinic
space group	$P2_1/c$ (#14)
a (pm)	1146.08(2)
b (pm)	3193.20(7)
c (pm)	2728.78(6)
α (°)	90
β (°)	92.673(1)
γ (°)	90
V (10^6 pm^3)	8660.4(2)
T (K)	133(2)
radiation type/ λ(pm)	MoKα/ 71.073
δ_{calc} (g cm^{-3})	1.664
Z	4
μ (mm^{-1})	4.131
Θ range of data collection (°)	$0.982 \leq \Theta \leq 25.681$
measured reflections	120904
independent reflections	18909
reflections used	18909
R_{int}	0.0613
no. of parameters	760
no. of restraints	265
goodness-of-fit	1.041
R_1 (all data)	0.1297
R_1	0.1002
wR_2 (all data)	0.3155
wR_2	0.2931

Table A.22: Crystallographic data and structure refinement parameters for **23**.

formula	$C_{47}H_{66}Cl_4Dy_4N_{18}O_{14}$
formula weight (g mol^{-1})	1969.86
crystal system	triclinic
space group	$P\bar{1}$ (#2)
a (pm)	1076.48(3)
b (pm)	1187.25(3)
c (pm)	1413.05(4)
α (°)	79.337(1)
β (°)	83.836(1)
γ (°)	81.491(2)
V (10^6 pm^3)	1749.27(8)
T (K)	133(2)
radiation type/ λ(pm)	MoKα / 71.073
δ_{calc} (g cm^{-3})	1.873
Z	1
μ (mm^{-1})	4.520
Θ range of data collection (°)	$1.471 \leq \Theta \leq 27.485$
measured reflections	20827
independent reflections	7938
reflections used	7938
R_{int}	0.0459
no. of parameters	436
no. of restraints	0
goodness-of-fit	1.069
R_1 (all data)	0.0569
R_1	0.0396
wR_2 (all data)	0.0958
wR_2	0.0881

ADDITIONAL MAGNETIC DATA

B.1 Alkali Metal Ion Containing Monodysprosium Complexes (Section 4.1)
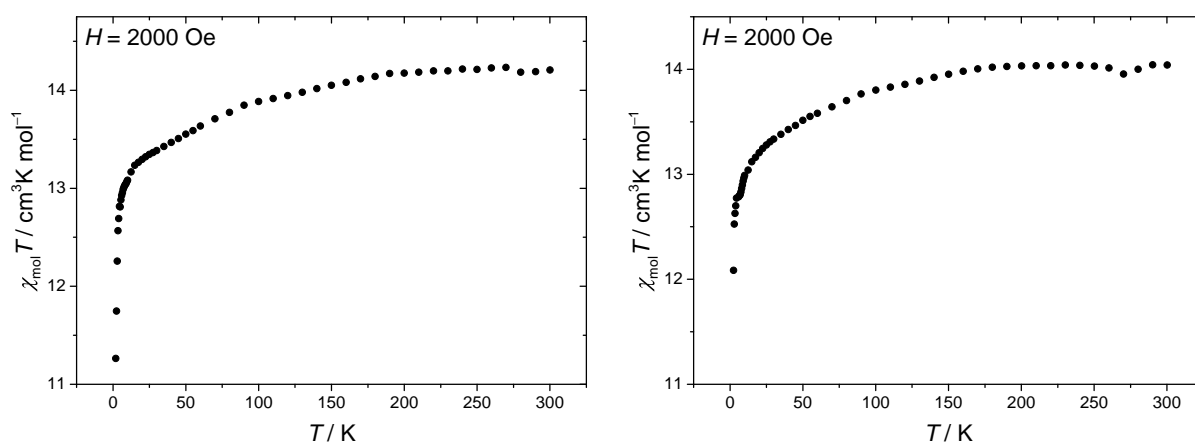
Figure B.1: Temperature dependence of molar magnetic susceptibility $\chi_{mol}T$ for **13** (**left**) and **14** (**right**) at an applied magnetic field of $H = 2000\,\text{Oe}$.

Table B.1: Temperature dependence of the in-phase (χ' **top**) and out-of-phase (χ'' **middle**) component of the magnetic susceptibility as revealed by AC magnetic susceptibility measurements on **13** (**left**) and **14** (**right**) with an AC field amplitude of 1 Oe at the frequencies given in the graph. Fitting of the data to a generalised Debye model (eq. (1.20)) to extract relaxation times τ_T yields the Cole-Cole plots (**bottom**) in the temperature range given in the graph.

[DyK$_2$(H$_3$saltag^{Nph})$_2$(dmf)$_3$(MeOH)$_3$]BPh$_4$ (**13**)	[DyNa$_2$(H$_3$saltag^{Nph})$_2$(dmf)$_3$(MeOH)$_3$]BPh$_4$ (**14**)

$$H_{DC} = 0\,\text{Oe}$$
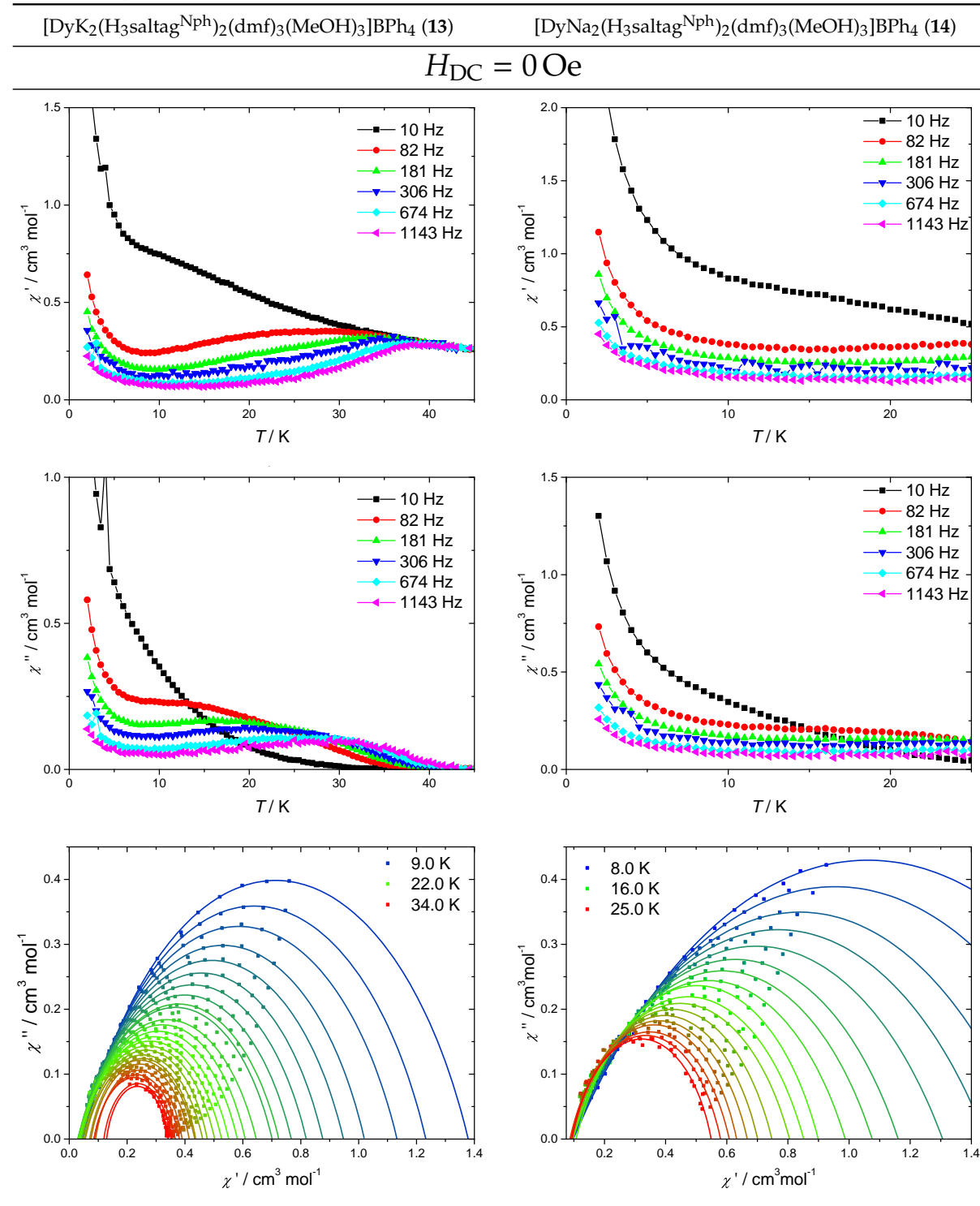
Table B.2: Temperature dependence of the in-phase (χ' **top**) and out-of-phase (χ'' **middle**) component of the magnetic susceptibility as revealed by AC magnetic susceptibility measurements on **13** (**left**) and **14** (**right**) with an AC field amplitude of 1 Oe applied at the frequencies given in the graph and a static magnetic field $H_{DC} = 400$ Oe applied. Fitting of the data to a generalised Debye model (eq. (1.20)) to extract relaxation times τ_T yields the Cole-Cole plots (**bottom**) in the temperature range given in the graph.

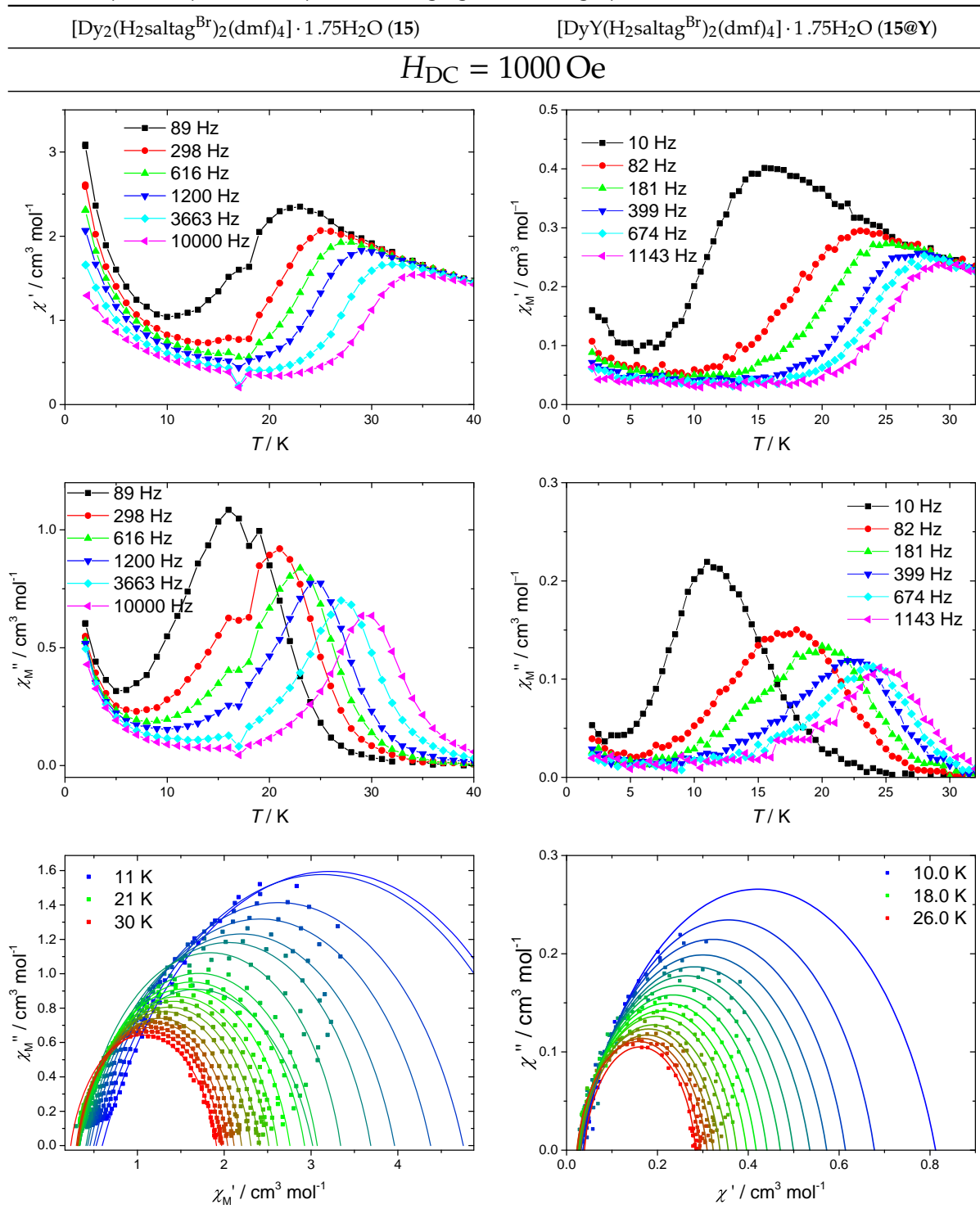| $[DyK_2(H_3saltag^{Nph})_2(dmf)_3(MeOH)_3]BPh_4$ (**13**)	$[DyNa_2(H_3saltag^{Nph})_2(dmf)_3(MeOH)_3]BPh_4$ (**14**)

$$H_{DC} = 400\,\text{Oe}$$

Table B.3: Temperature dependence of the in-phase (χ' **top**) and out-of-phase (χ'' **middle**) component of the magnetic susceptibility as revealed by AC magnetic susceptibility measurements on **13** (**left**) and **14** (**right**) with an AC field amplitude of 1 Oe applied at the frequencies given in the graph and a static magnetic field H_{DC} = 1000 Oe applied. Fitting of the data to a generalised Debye model (eq. (1.20)) to extract relaxation times τ_T yields the Cole-Cole plots (**bottom**) in the temperature range given in the graph.
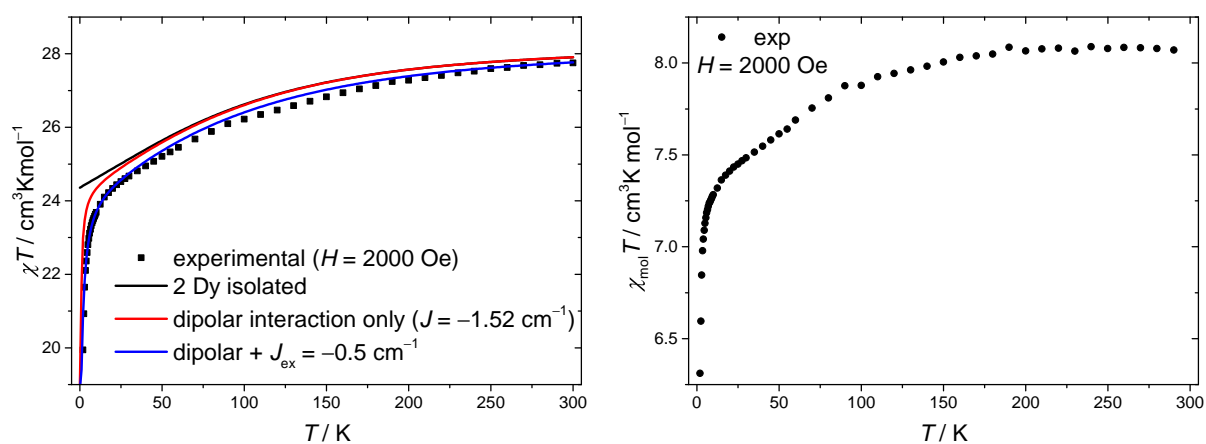
[DyK$_2$(H$_3$saltag^{Nph})$_2$(dmf)$_3$(MeOH)$_3$]BPh$_4$ (**13**)	[DyNa$_2$(H$_3$saltag^{Nph})$_2$(dmf)$_3$(MeOH)$_3$]BPh$_4$ (**14**)

$$H_{DC} = 1000\,\text{Oe}$$

B.2 Dinuclear Lanthanoid Complexes (Section 4.2)

[Dy$_2$(H$_2$saltag^{Br})$_2$(dmf)$_4$] · 1.75H$_2$O   (**15** and **15@Y**)

Table B.4: Relative energies E and g-components of the Kramers doublets (KD) of both Dy centres in **15** as revealed by CAS-SCF calculations by Böhme.[272] The main m_J-component of the respective KD is given as m_J* for the first three KDs (for the higher KDs it is no longer clearly determined due to strong admixture of m_J-states.

| | **Dy1** ($\angle$ O1-Dy1-O1A = 118.8°) | | | | | **Dy2** ($\angle$ O3-Dy2-O3A = 115.4°) | | | | |
	E / cm^{-1}	g_x	g_y	g_z	m_J*	E / cm^{-1}	g_x	g_y	g_z	m_J*
KD1	0	0.003	0.004	19.702	$\frac{15}{2}$	0	0.002	0.004	19.773	$\frac{15}{2}$
KD2	192	0.362	0.564	16.584	$\frac{13}{2}$	187	0.148	0.253	17.129	$\frac{13}{2}$
KD3	277	1.472	1.770	12.653	$\frac{11}{2}$	274	0.697	0.998	13.632	$\frac{11}{2}$
KD4	339	0.888	1.966	10.426	-	323	0.778	2.340	11.247	-
KD5	392	8.985	6.798	4.275	-	389	4.514	5.960	9.039	-
KD6	438	0.697	0.792	18.321	-	446	0.885	1.190	18.647	-
KD7	476	0.660	1.102	18.126	-	515	0.278	0.987	18.145	-
KD8	642	0.063	0.113	19.446	-	606	0.265	0.743	18.749	-
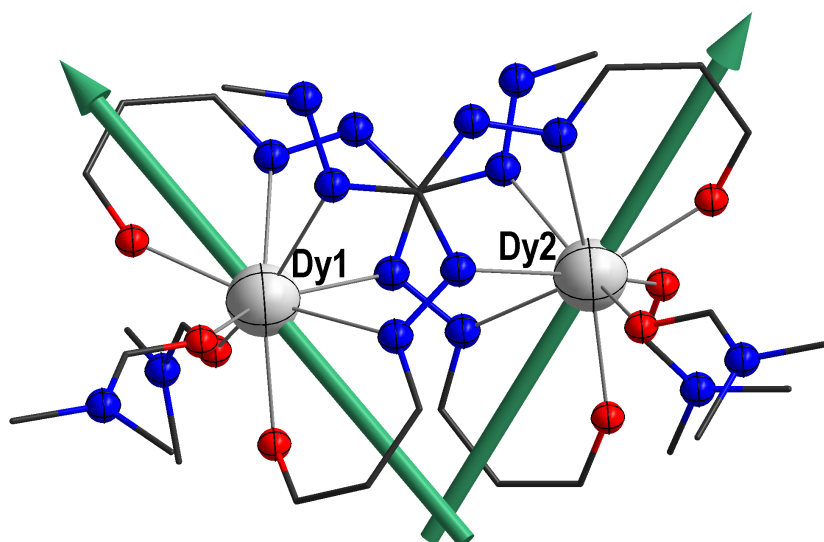
Figure B.2: Illustration of the g_z-component of the ground state Kramers doublet (KD1, easy axis of magnetisation, teal arrows) of both Dy centres in **15** as revealed by CAS-SCF calculations by Böhme[272] (see table B.4). An intersecting angle of both easy axes of 77.3° as well as dihedral angle with the both Dy centres of 37.7° is found.

Table B.5: Temperature dependence of the in-phase (χ' **top**) and out-of-phase (χ'' **middle**) component of the magnetic susceptibility as revealed by AC magnetic susceptibility measurements on **15** (**left**) and **15@Y** (**right**) with an AC field amplitude of $1\,\text{Oe}$ at the frequencies given in the graph. Fitting of the data to a generalised Debye model (eq. (1.20)) to extract relaxation times τ_T yields the Cole-Cole plots (**bottom**) in the temperature range given in the graph.

$[\text{Dy}_2(\text{H}_2\text{saltag}^{\text{Br}})_2(\text{dmf})_4] \cdot 1.75\text{H}_2\text{O}$ (**15**)	$[\text{DyY}(\text{H}_2\text{saltag}^{\text{Br}})_2(\text{dmf})_4] \cdot 1.75\text{H}_2\text{O}$ (**15@Y**)

$$H_{\text{DC}} = 0\,\text{Oe}$$

Table B.6: Temperature dependence of the in-phase (χ' **top**) and out-of-phase (χ'' **middle**) component of the magnetic susceptibility as revealed by AC magnetic susceptibility measurements on **15** (**left**) and **15@Y** (**right**) with an AC field amplitude of 1 Oe applied at the frequencies given in the graph and a static field $H_{DC} = 400$ Oe applied. Fitting of the data to a generalised Debye model (eq. (1.20)) to extract relaxation times τ_T yields the Cole-Cole plots (**bottom**) in the temperature range given in the graph.

$[\text{Dy}_2(\text{H}_2\text{saltag}^{\text{Br}})_2(\text{dmf})_4] \cdot 1.75\text{H}_2\text{O}$ (**15**)	$[\text{DyY}(\text{H}_2\text{saltag}^{\text{Br}})_2(\text{dmf})_4] \cdot 1.75\text{H}_2\text{O}$ (**15@Y**)

$$H_{DC} = 400\,\text{Oe}$$

Table B.7: Temperature dependence of the in-phase (χ' **top**) and out-of-phase (χ'' **middle**) component of the magnetic susceptibility as revealed by AC magnetic susceptibility measurements on **15** (**left**) and **15@Y** (**right**) with an AC field amplitude of 1 Oe applied at the frequencies given in the graph and a static field H_{DC} = 1000 Oe applied. Fitting of the data to a generalised Debye model (eq. (1.20)) to extract relaxation times τ_T yields the Cole-Cole plots (**bottom**) in the temperature range given in the graph.

$[Dy_2(H_2saltag^{Br})_2(dmf)_4] \cdot 1.75H_2O$ (**15**)	$[DyY(H_2saltag^{Br})_2(dmf)_4] \cdot 1.75H_2O$ (**15@Y**)

$$H_{DC} = 1000\,\text{Oe}$$

Figure B.3: Temperature dependence of molar magnetic susceptibility $\chi_{mol}T$ for **15** (**left**) and **15@Y** (**right**) at an applied magnetic field of $H = 2000$ Oe. In the left graph, also POLY-ANISO[222,291] simulation results based on CAS-SCF calculations by Böhme[272] revealing the dipolar and superexchange contributions of the weak magnetic interactions are illustrated.
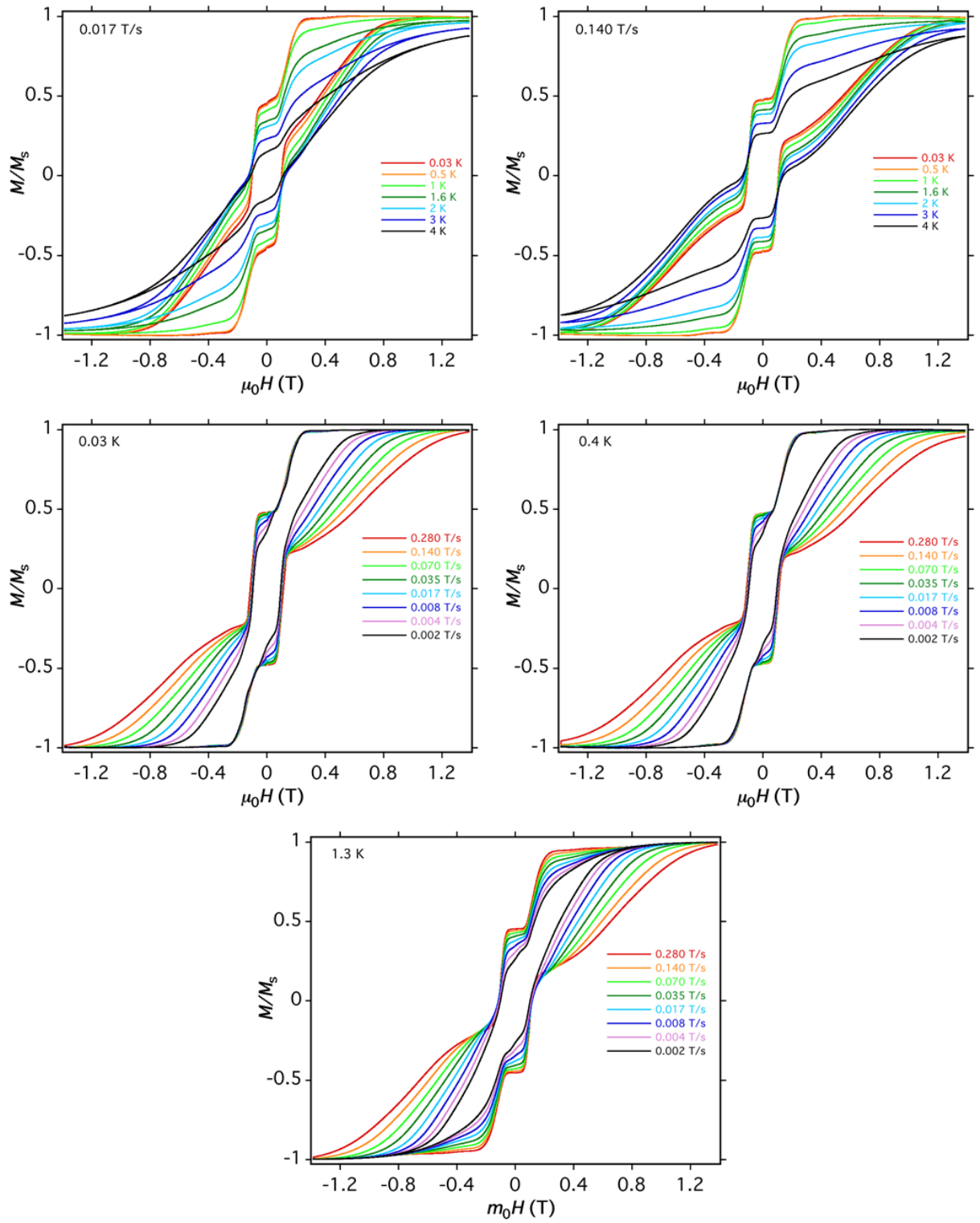
Figure B.4: Single crystal micro-SQUID hysteresis measurements carried out on **15** at different temperatures (also below 2 K) and magnetic field sweep rates by Marko Damjanović.[293]

[Dy$_2$(H$_2$saltag^{Br})$_2$(dmf)$_4$] · 2 DMF   (16)
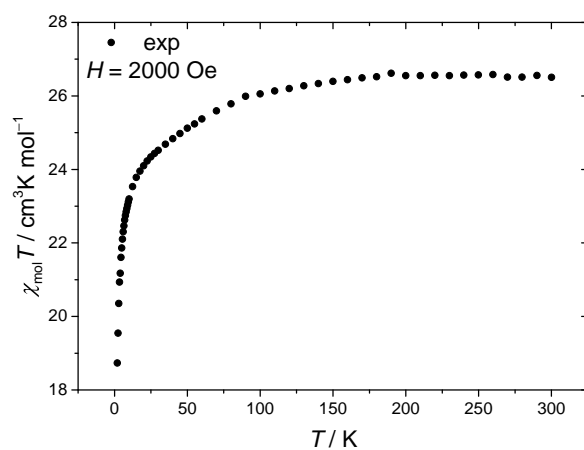
Figure B.5: Temperature dependence of molar magnetic susceptibility $\chi_{mol}T$ for **16** at an applied magnetic field of H = 2000 Oe.
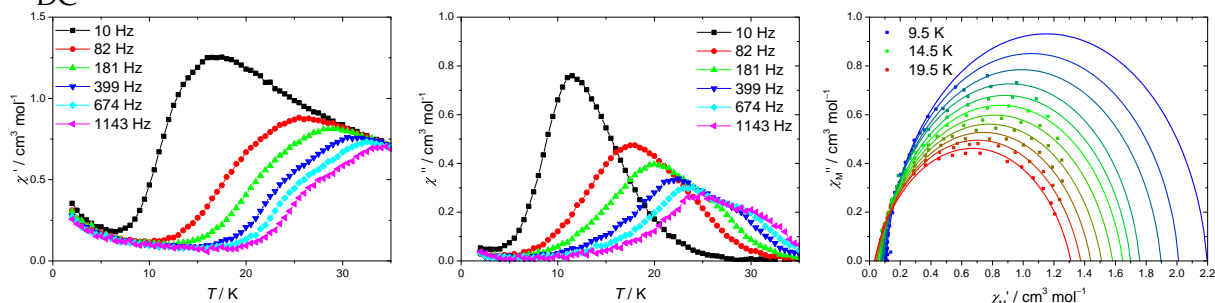
$H_{\mathrm{DC}} = 0\,\mathrm{Oe}$
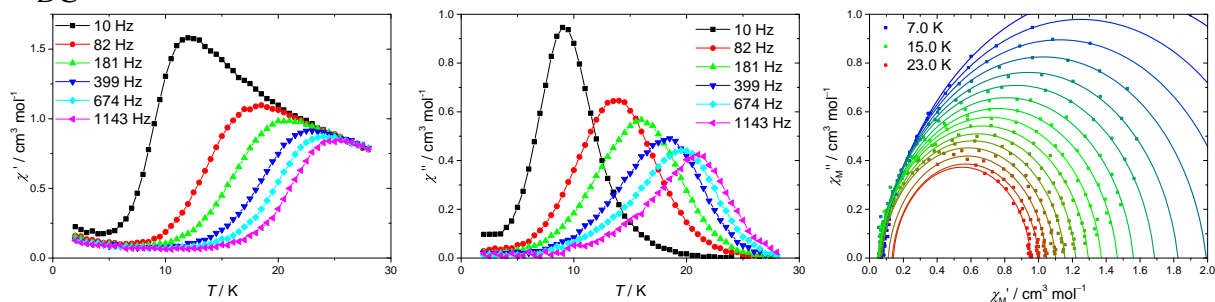
$H_{\mathrm{DC}} = 400\,\mathrm{Oe}$
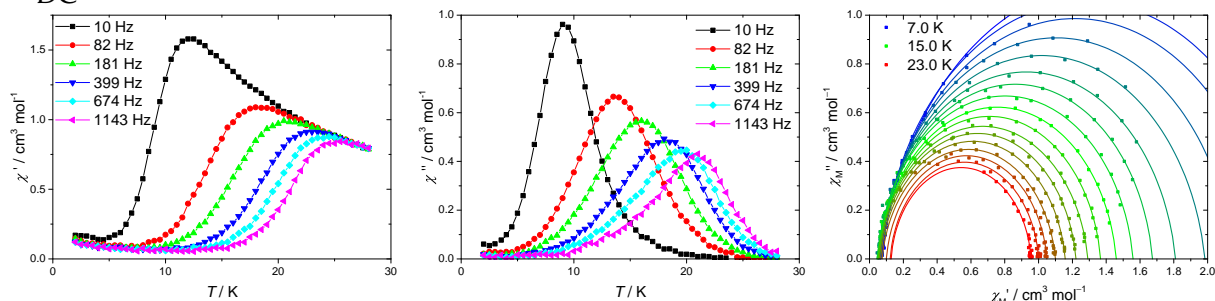
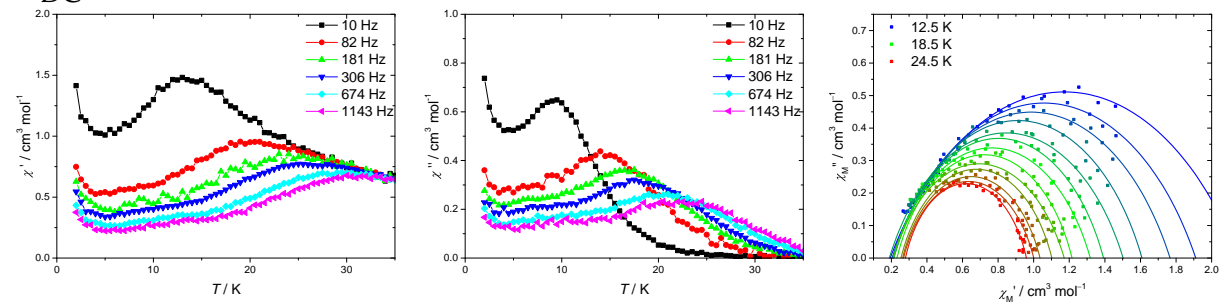$H_{\mathrm{DC}} = 1000\,\mathrm{Oe}$
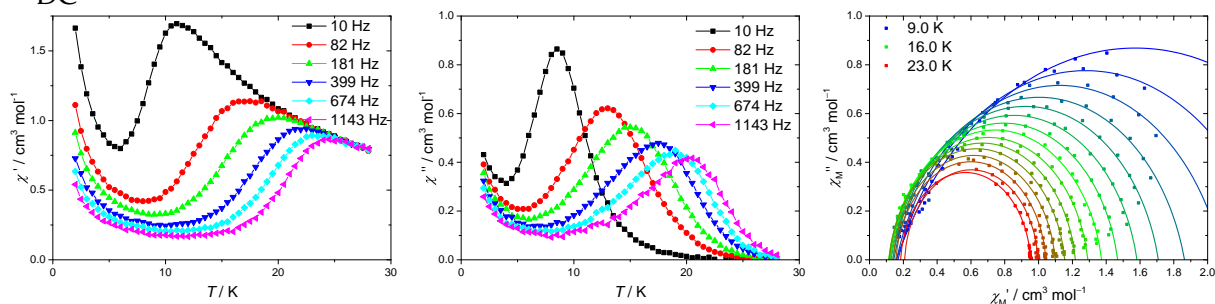
Figure B.6: Temperature dependence of the in-phase (χ' **left**) and out-of-phase (χ'' **middle**) compo-
nent of the magnetic susceptibility as revealed by AC magnetic susceptibility measure-
ments on **16** with an AC field amplitude of 1 Oe applied at the frequencies given in the
graph and static magnetic fields H_{DC} of 0 (**top**), 400 (**middle**) and 1000 Oe (**bottom**) ap-
plied. Fitting of the data to a generalised Debye model (eq. (1.20)) to extract relaxation times
τ_T yields the Cole-Cole plots (**right**) in the temperature range given in the graph.

[Dy₂(H₂saltag^Br)₂(py)₄]·H₂O·py (17)
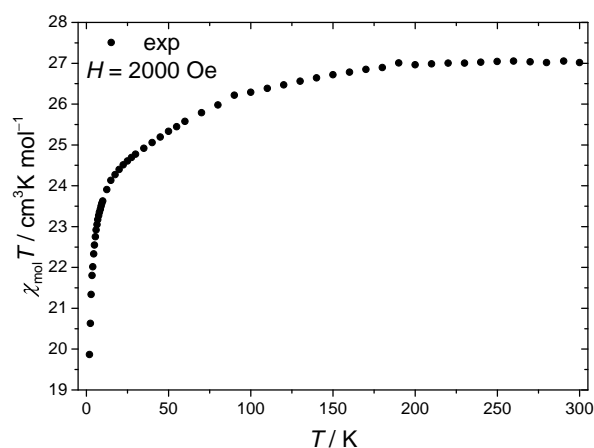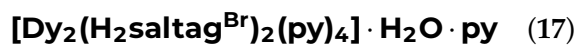
Figure B.7: Temperature dependence of molar magnetic susceptibility $\chi_{mol}T$ for **17** at an applied magnetic field of $H = 2000$ Oe.
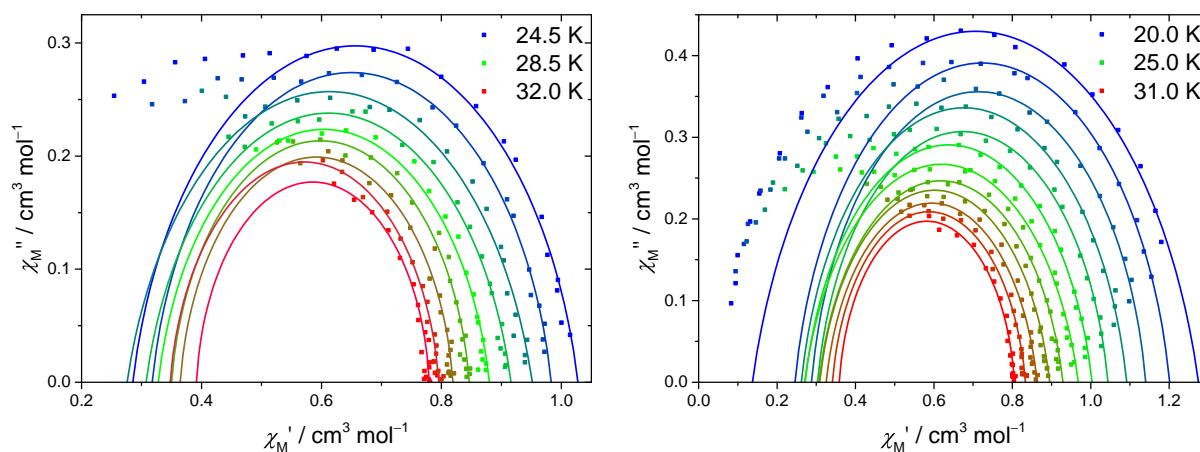
Figure B.8: Cole-Cole plots for **17** obtained from fits of τ_T at $H_{DC} = 0$ Oe (**left**) and 400 Oe (**right**) starting from 24.5 K and 20 K (complementary to the ones shown in fig. B.6), respectively. In these temperature ranges a clear splitting of two distinct processes appears. Since a simultaneous fit of both processes was not successful, only the process shifted to higher χ'-values was fitted and the data points with χ' below the maximum of the semicircle were not considered.

$H_{DC} = 0\,\text{Oe}$
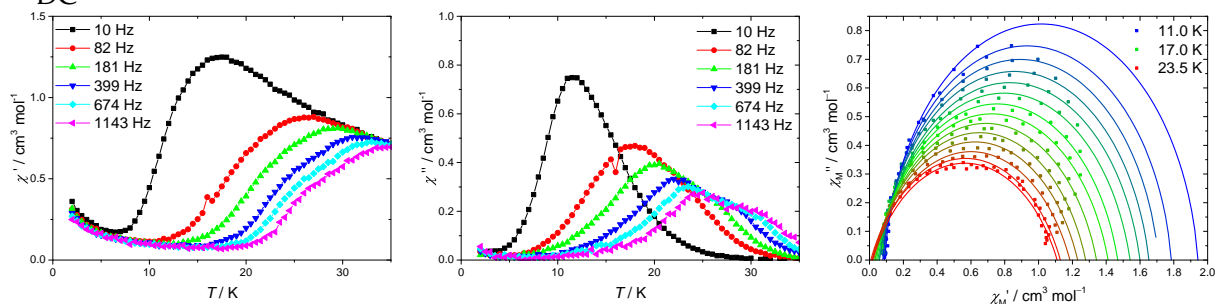
$H_{DC} = 400\,\text{Oe}$

$H_{DC} = 1000\,\text{Oe}$
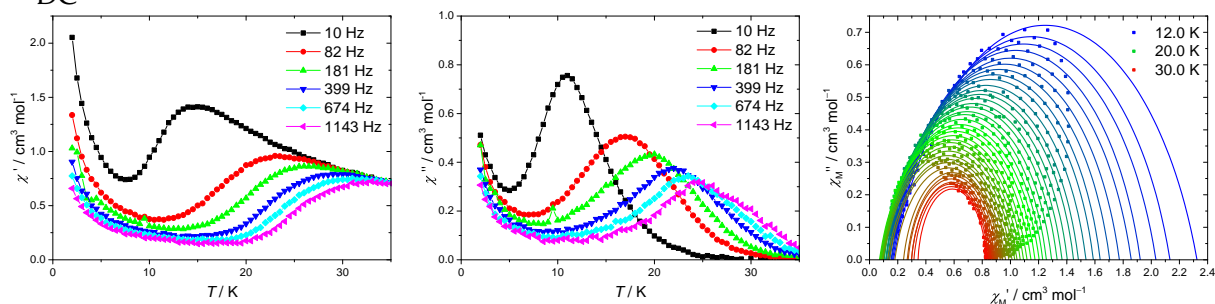
Figure B.9: Temperature dependence of the in-phase (χ' **left**) and out-of-phase (χ'' **middle**) component of the magnetic susceptibility as revealed by AC magnetic susceptibility measurements on **17** with an AC field amplitude of 1 Oe applied at the frequencies given in the graph and static magnetic fields H_{DC} of 0 (**top**), 400 (**middle**) and 1000 Oe (**bottom**) applied. Fitting of the data to a generalised Debye model (eq. (1.20)) to extract relaxation times τ_T yields the Cole-Cole plots (**right**) in the temperature range given in the graph.

[Dy$_2$(H$_2$saltag^{Br})$_2$(MeOH)$_4$]   (18)
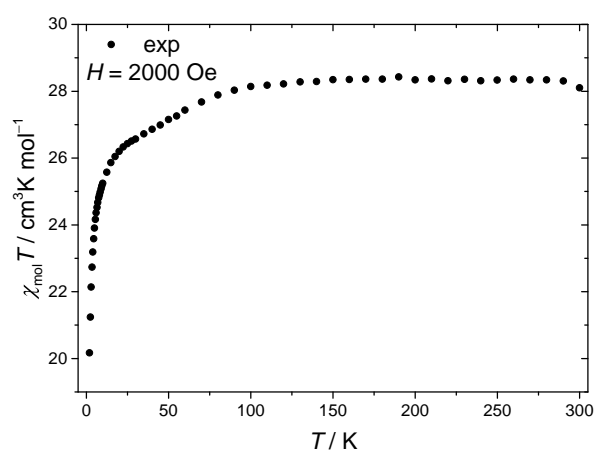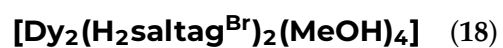
Figure B.10: Temperature dependence of molar magnetic susceptibility $\chi_{mol}T$ for **18** at an applied magnetic field of H = 2000 Oe.
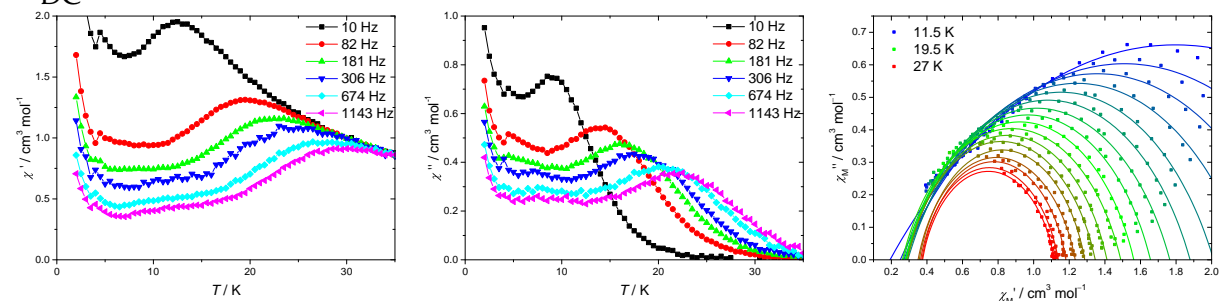
$H_{DC} = 0 \, \text{Oe}$

$H_{DC} = 400 \, \text{Oe}$
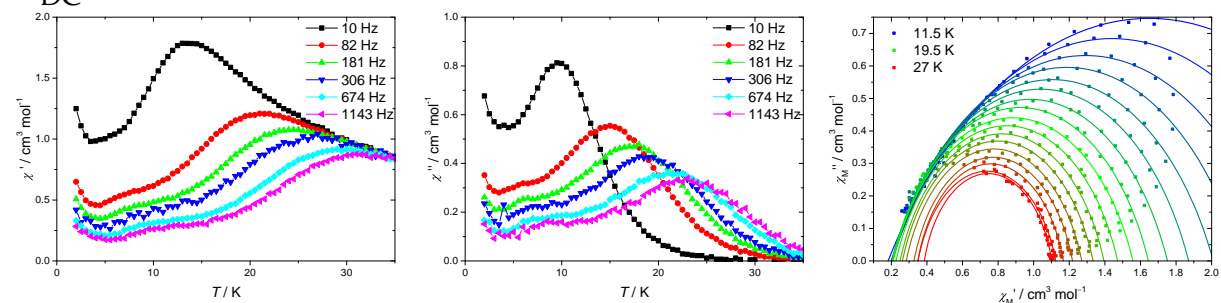
$H_{DC} = 1000 \, \text{Oe}$

Figure B.11: Temperature dependence of the in-phase (χ' **left**) and out-of-phase (χ'' **middle**) component of the magnetic susceptibility as revealed by AC magnetic susceptibility measurements on **18** with an AC field amplitude of 1 Oe applied at the frequencies given in the graph and static magnetic fields H_{DC} of 0 (**top**), 400 (**middle**) and 1000 Oe (**bottom**) applied. Fitting of the data to a generalised Debye model (eq. (1.20)) to extract relaxation times τ_T yields the Cole-Cole plots (**right**) in the temperature range given in the graph.

B.3 Trinuclear Lanthanoid Complexes (Section 4.3)

[Dy$_3$(H$_{0.5}$saltag^{Br})$_2$(MeOH)$_6$] · 3.5 MeOH   (19)

Table B.8: Relative energies of the Kramers doublets (KD) of all three Dy centres in **19** as revealed by CAS-SCF calculations by Böhme,[272] all energies are given in cm^{-1}. Besides, the intersecting angle of the easy axis of magnetisation in the ground state KD1 with the plane spanned by the three Dy centres $\angle \vec{g}_{zKD1}$-□Dy$_3$ and the intersecting angle with the easy axis of magnetisation in the ground state KD1 of the adjacent Dy centre $\angle \vec{g}_{zKD1}$-$\vec{g}'_{zKD1}$ is given. In the second row per atom, the respective angle $\angle O_{Ph}$–Dy–O_{Ph} is given as reference and the intersecting angle of the easy axis of magnetisation in the ground state KD1 with the line through the phenolate-O donors of the Dy centre $\angle O$–O_{Dy} - $\vec{g}_{zKD1}$ illustrates the discrepancy when approximating the easy axis by this very line.

|	KD2	KD3	KD4	KD5	KD6	KD7	KD8/ cm^{-1}	$\angle \vec{g}_{zKD1}$-□Dy$_3$	$\angle \vec{g}_{zKD1}$-$\vec{g}'_{zKD1}$
Dy1	216	357	442	546	626	674	773	23.1°	79.7°
$\angle O_{Ph}$–Dy–O_{Ph}=110.4°								$\angle O$–O_{Dy} - $\vec{g}_{zKD1}$=19.2°	
Dy2	211	315	417	545	662	724	773	21.8°	61.8°
$\angle O_{Ph}$–Dy–O_{Ph}=109.2°								$\angle O$–O_{Dy} - $\vec{g}_{zKD1}$=24.5°	
Dy3	216	293	403	502	593	647	696	17.3°	55.5°
$\angle O_{Ph}$–Dy–O_{Ph}=112.3°								$\angle O$–O_{Dy} - $\vec{g}_{zKD1}$=21.6°	
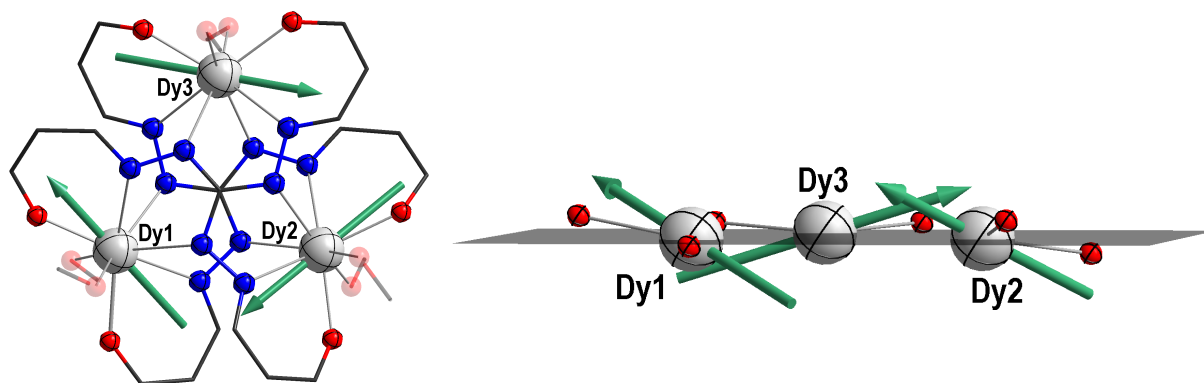
Figure B.12: Illustration of the alignment of the easy axes of magnetisation of the ground state KD1 ($\vec{g}_{zKD1}$, teal arrows) in **19** as obtained from CAS-SCF calculations by Böhme.[272] Wide parts of the molecules are omitted for clarity. In the right picture only the phenolate O-donors (red) and the □Dy$_3$-plane (dark grey) are drawn. The corresponding intersecting angles are given in table B.8.
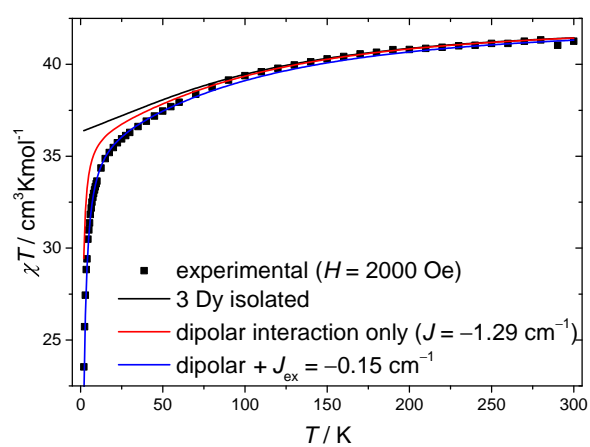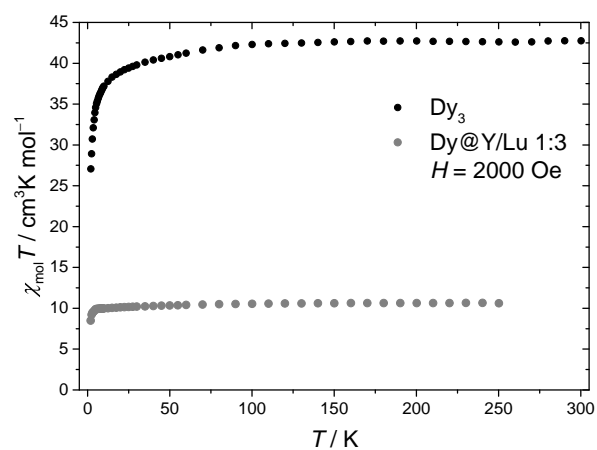
Figure B.13: Temperature dependence of molar magnetic susceptibility $\chi_{mol}T$ for **19** at an applied magnetic field of $H = 2000$ Oe. POLY-ANISO[222,291] simulation results based on CAS-SCF calculations by Böhme[272] revealing the dipolar and superexchange contributions of the weak magnetic interactions are also illustrated.
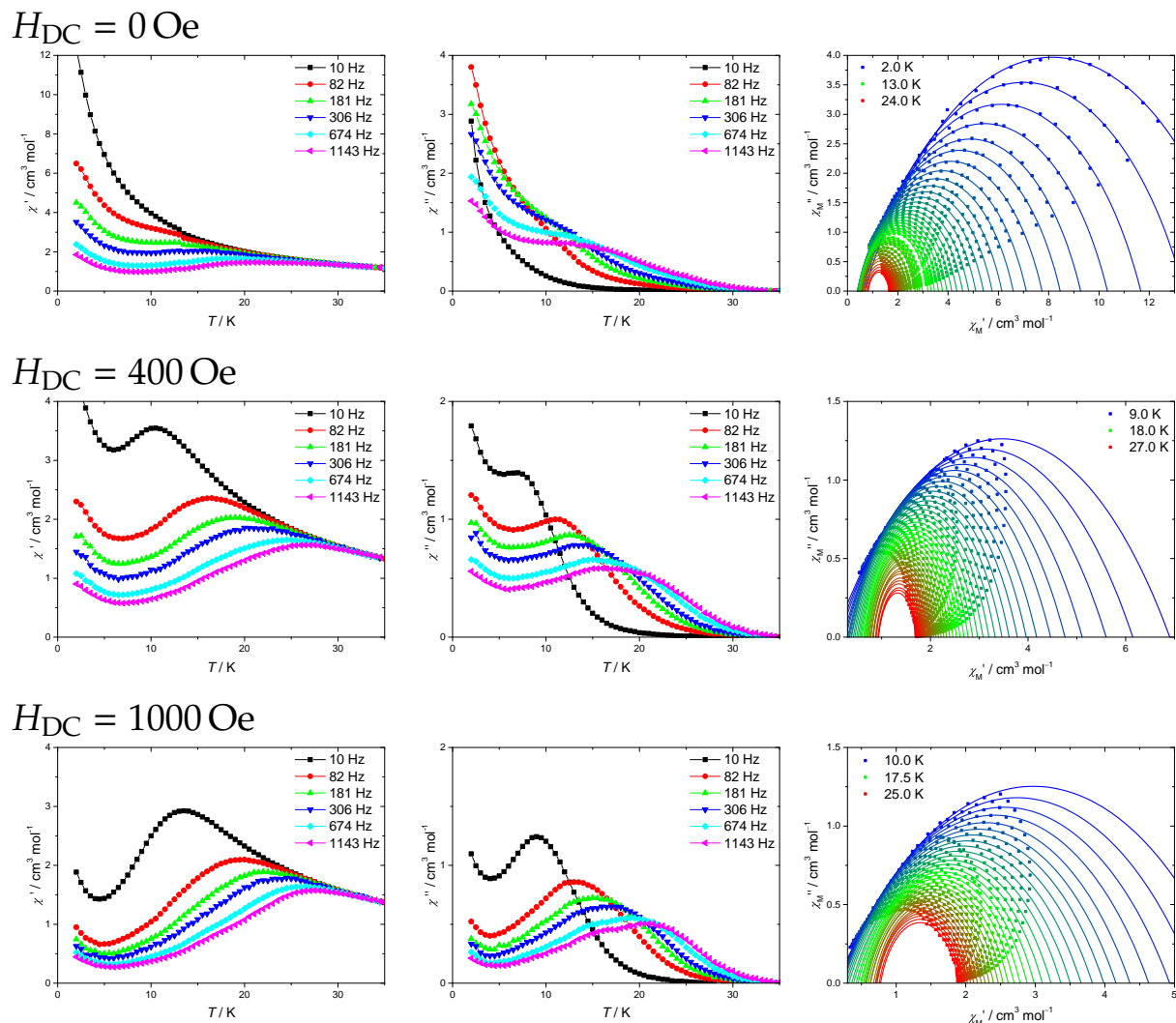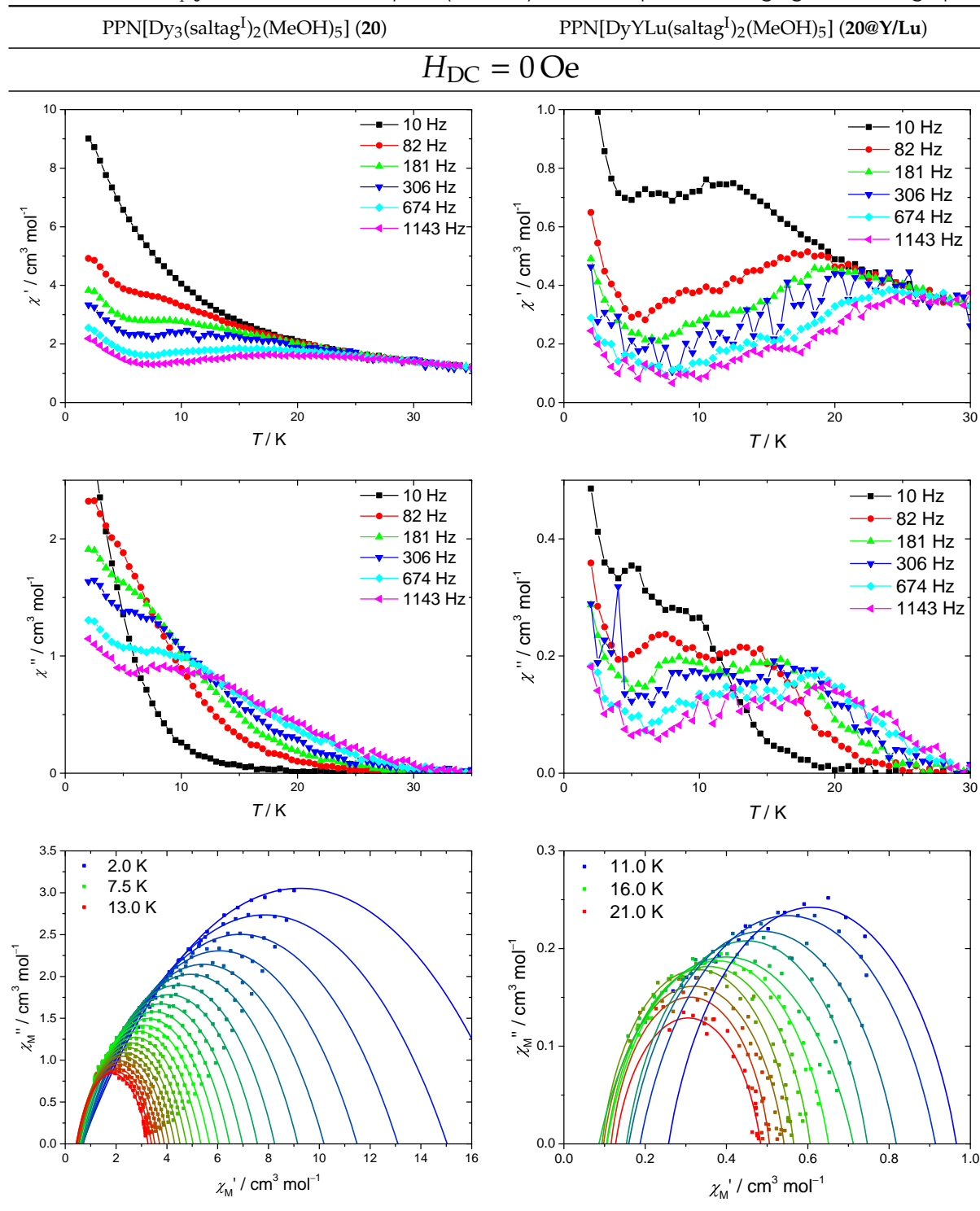
Figure B.14: Temperature dependence of the in-phase (χ' **left**) and out-of-phase (χ'' **middle**) compo-
nent of the magnetic susceptibility as revealed by AC magnetic susceptibility measure-
ments on **19** with an AC field amplitude of 1 Oe applied at the frequencies given in the
graph and static magnetic fields H_{DC} of 0 (**top**), 400 (**middle**) and 1000 Oe (**bottom**) ap-
plied. Fitting of the data to a generalised Debye model (eq. (1.20)) to extract relaxation
times τ_T yields the Cole-Cole plots (**right**) in the temperature range given in the graph.

PPN[Dy₃(saltag$^\text{I}$)₂(MeOH)₅] · 5 MeOH   (**20** and **20@Y/Lu**)
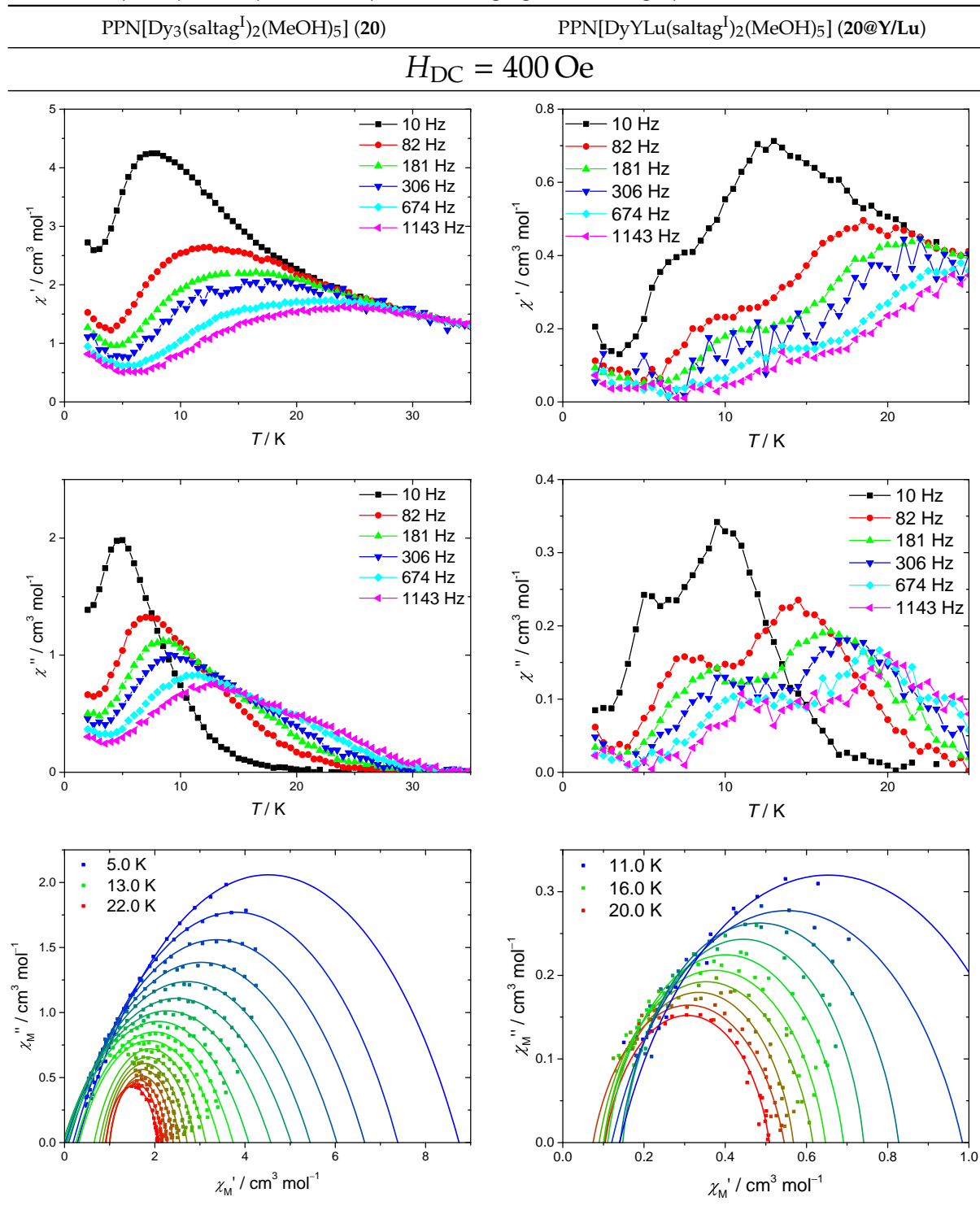

Figure B.15: Temperature dependence of molar magnetic susceptibility $\chi_{mol}T$ for **20** (black) and **20@Y/Lu** (grey) at an applied magnetic field of H = 2000 Oe.

Table B.9: Temperature dependence of the in-phase (χ' **top**) and out-of-phase (χ'' **middle**) component of the magnetic susceptibility as revealed by AC magnetic susceptibility measurements on **20** (**left**) and **20@Y/Lu** (**right**) with an AC field amplitude of 1 Oe at the frequencies given in the graph. Fitting of the data to a generalised Debye model (eq. (1.20)) to extract relaxation times τ_T yields the Cole-Cole plots (**bottom**) in the temperature range given in the graph.

PPN[Dy$_3$(saltag$^{\mathrm{I}}$)$_2$(MeOH)$_5$] (**20**)	PPN[DyYLu(saltag$^{\mathrm{I}}$)$_2$(MeOH)$_5$] (**20@Y/Lu**)

$$H_{\mathrm{DC}} = 0\,\mathrm{Oe}$$

Table B.10: Temperature dependence of the in-phase (χ' **top**) and out-of-phase (χ'' **middle**) component of the magnetic susceptibility as revealed by AC magnetic susceptibility measurements on **20** (**left**) and **20@Y/Lu** (**right**) with an AC field amplitude of 1 Oe applied at the frequencies given in the graph and a static field $H_{DC} = 400$ Oe applied. Fitting of the data to a generalised Debye model (eq. (1.20)) to extract relaxation times τ_T yields the Cole-Cole plots (**bottom**) in the temperature range given in the graph.

PPN[Dy$_3$(saltag^I)$_2$(MeOH)$_5$] (**20**)	PPN[DyYLu(saltag^I)$_2$(MeOH)$_5$] (**20@Y/Lu**)

$$H_{DC} = 400\,\text{Oe}$$

Table B.11: Temperature dependence of the in-phase (χ' **top**) and out-of-phase (χ'' **middle**) component of the magnetic susceptibility as revealed by AC magnetic susceptibility measurements on **20** (**left**) and **20@Y/Lu** (**right**) with an AC field amplitude of 1 Oe applied at the frequencies given in the graph and a static field $H_{DC} = 1000$ Oe applied. Fitting of the data to a generalised Debye model (eq. (1.20)) to extract relaxation times τ_T yields the Cole-Cole plots (**bottom**) in the temperature range given in the graph. Mind that the data for **20** could not be fitted reasonably, the thin lines in the bottom-left graph are guide for the eye.

PPN[Dy$_3$(saltag^I)$_2$(MeOH)$_5$] (**20**)	PPN[DyYLu(saltag^I)$_2$(MeOH)$_5$] (**20@Y/Lu**)

$$H_{DC} = 1000\,\text{Oe}$$
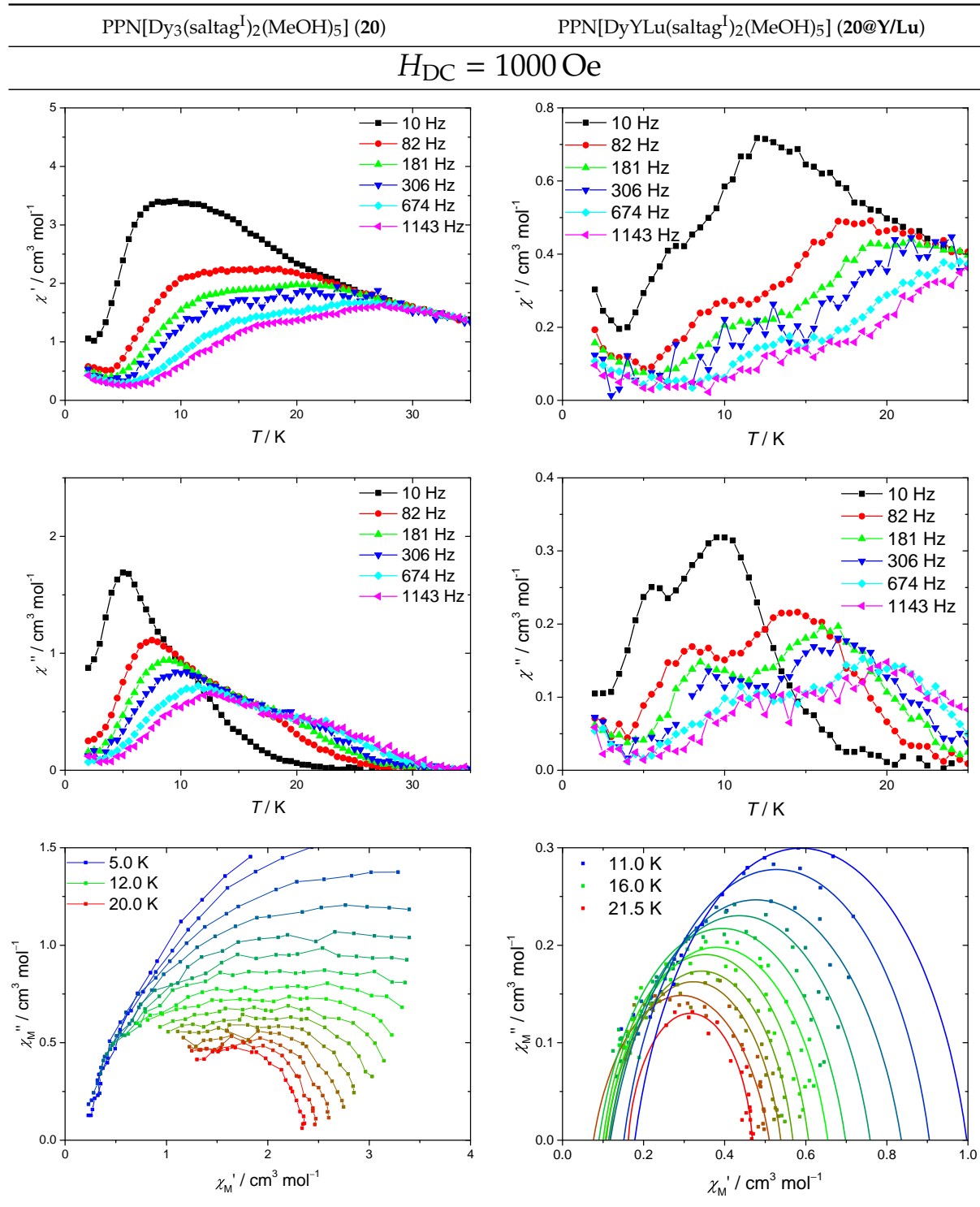
$(H_{0.5}DMAP)_2[Dy_3(saltag^I)_2(MeOH)_6] \cdot 2\,MeOH$ (**21** and **21@Y**)
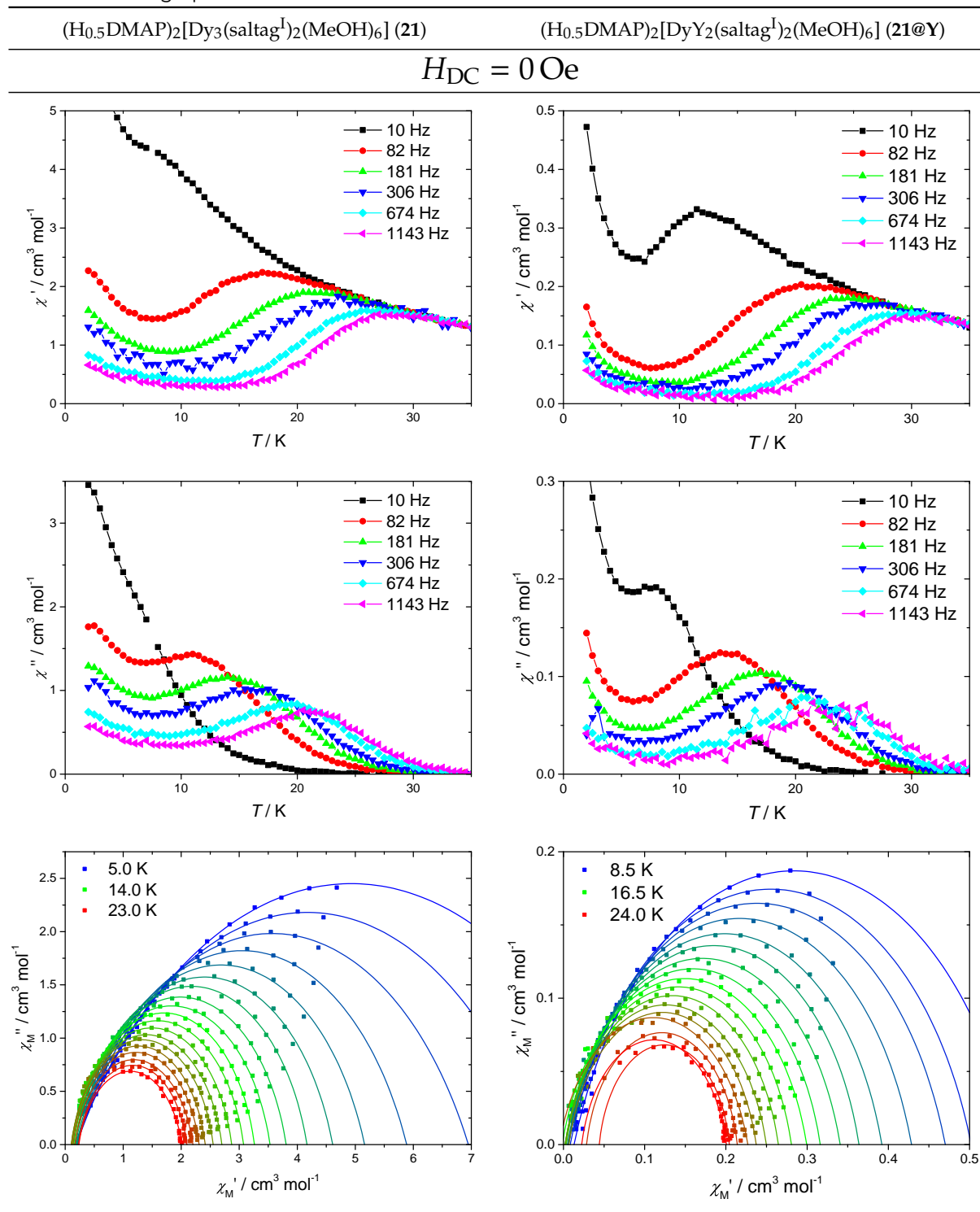
Table B.12: Relative energies of the Kramers doublets (KD) of all three Dy centres in **21** as revealed by CAS-SCF calculations by Böhme,[272] all energies are given in cm^{-1}. Besides, the intersecting angle of the easy axis of magnetisation in the ground state KD1 with the plane spanned by the three Dy centres $\angle\vec{g}_{zKD1}$-□Dy$_3$ and the intersecting angle with the easy axis of magnetisation in the ground state KD1 of the adjacent Dy centre $\angle\vec{g}_{zKD1}$-$\vec{g}'_{zKD1}$ is given. In the second row per atom, the respective angle $\angle O_{Ph}$–Dy–O_{Ph} is given as reference and the intersecting angle of the easy axis of magnetisation in the ground state KD1 with the line through the phenolate-O donors of the Dy centre $\angle O$–O_{Dy} - $\vec{g}_{zKD1}$ illustrates the discrepancy when approximating the easy axis by this very line.

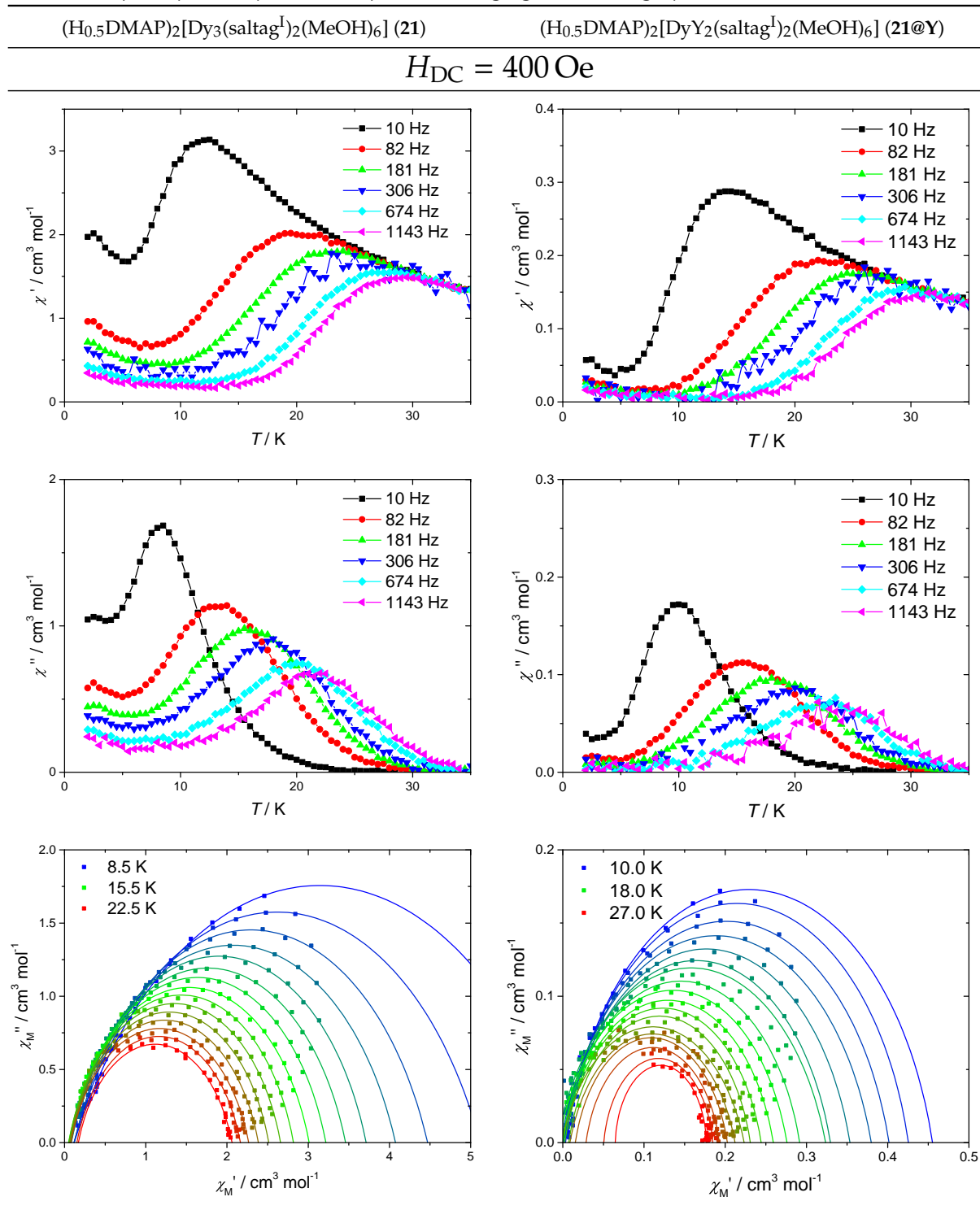|	KD2	KD3	KD4	KD5	KD6	KD7	KD8/ cm^{-1}	$\angle\vec{g}_{zKD1}$-□Dy$_3$	$\angle\vec{g}_{zKD1}$-$\vec{g}'_{zKD1}$
Dy1	235	326	438	554	665	728	764	18.4°	72.4°
$\angle O_{Ph}$–Dy–O_{Ph}=113.3°									$\angle O$–O_{Dy} - $\vec{g}_{zKD1}$=13.5°
Dy2	212	302	401	503	610	667	688	15.3°	58.0°
$\angle O_{Ph}$–Dy–O_{Ph}=113.8°									$\angle O$–O_{Dy} - $\vec{g}_{zKD1}$=12.9°
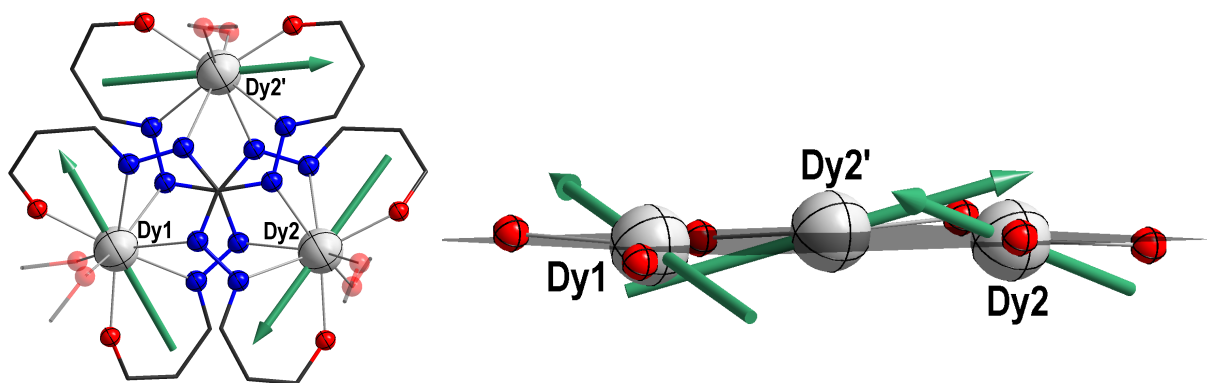
Figure B.16: Illustration of the alignment of the easy axes of magnetisation of the ground state KD1 ($\vec{g}_{zKD1}$, teal arrows) in **21** as obtained from CAS-SCF calculations by Böhme.[272] Wide parts of the molecules are omitted for clarity. In the right picture only the phenolate O-donors (red) and the □Dy$_3$-plane (dark grey) are drawn. The corresponding intersecting angles are given in table B.12.

Table B.13: Temperature dependence of the in-phase (χ' **top**) and out-of-phase (χ'' **middle**) component of the magnetic susceptibility as revealed by AC magnetic susceptibility measurements on **21** (**left**) and **21@Y** (**right**) with an AC field amplitude of 1 Oe at the frequencies given in the graph. Fitting of the data to a generalised Debye model (eq. (1.20)) to extract relaxation times τ_T yields the Cole-Cole plots (**bottom**) in the temperature range given in the graph.
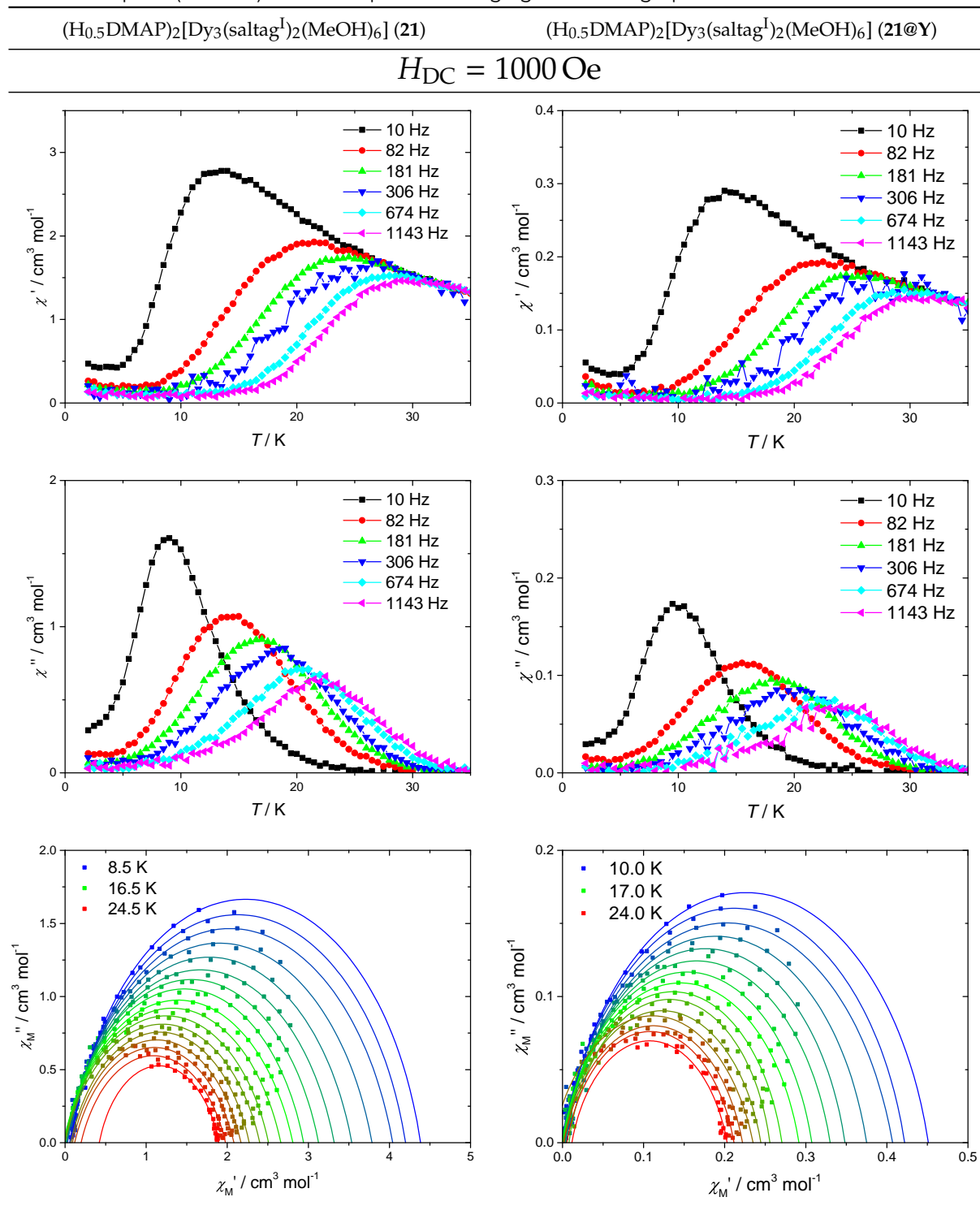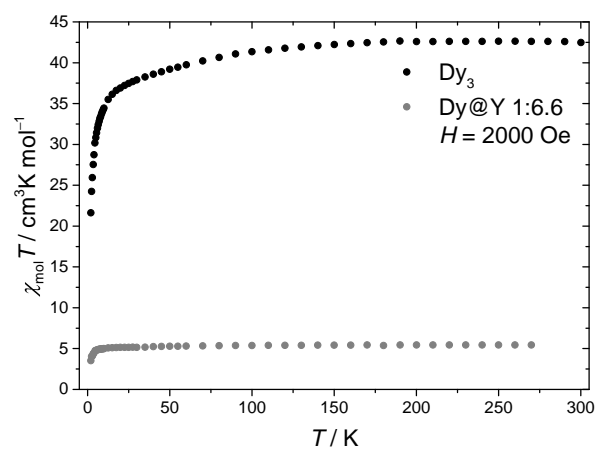
$(H_{0.5}DMAP)_2[Dy_3(saltag^I)_2(MeOH)_6]$ (**21**)	$(H_{0.5}DMAP)_2[DyY_2(saltag^I)_2(MeOH)_6]$ (**21@Y**)

$$H_{DC} = 0\,\text{Oe}$$

Table B.14: Temperature dependence of the in-phase (χ' **top**) and out-of-phase (χ'' **middle**) component of the magnetic susceptibility as revealed by AC magnetic susceptibility measurements on **21** (**left**) and **21@Y** (**right**) with an AC field amplitude of 1 Oe applied at the frequencies given in the graph and a static field $H_{DC} = 400$ Oe applied. Fitting of the data to a generalised Debye model (eq. (1.20)) to extract relaxation times τ_T yields the Cole-Cole plots (**bottom**) in the temperature range given in the graph.

$(H_{0.5}DMAP)_2[Dy_3(saltag^I)_2(MeOH)_6]$ (**21**)	$(H_{0.5}DMAP)_2[DyY_2(saltag^I)_2(MeOH)_6]$ (**21@Y**)

$$H_{DC} = 400\,\text{Oe}$$

Table B.15: Temperature dependence of the in-phase (χ' **top**) and out-of-phase (χ'' **middle**) component of the magnetic susceptibility as revealed by AC magnetic susceptibility measurements on **21** (**left**) and **21@Y** (**right**) with an AC field amplitude of 1 Oe applied at the frequencies given in the graph and a static field $H_{DC} = 1000$ Oe applied. Fitting of the data to a generalised Debye model (eq. (1.20)) to extract relaxation times τ_T yields the Cole-Cole plots (**bottom**) in the temperature range given in the graph.

$(H_{0.5}DMAP)_2[Dy_3(saltag^I)_2(MeOH)_6]$ (**21**)	$(H_{0.5}DMAP)_2[Dy_3(saltag^I)_2(MeOH)_6]$ (**21@Y**)

$$H_{DC} = 1000\,\text{Oe}$$

Figure B.17: Temperature dependence of molar magnetic susceptibility $\chi_{mol}T$ for **21** (black) and **21@Y** (grey) at an applied magnetic field of $H = 2000\,\text{Oe}$.
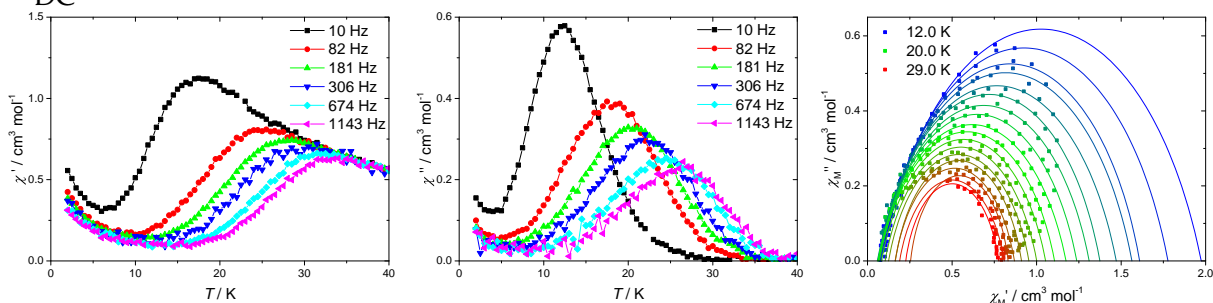
[Dy$_3$(H$_{0.5}$saltag^I)$_2$(thf)$_6$] (22)
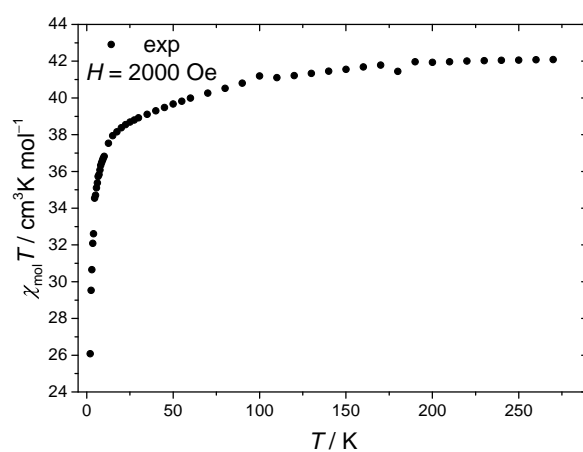
Figure B.18: Temperature dependence of molar magnetic susceptibility $\chi_{mol}T$ for **22** at an applied magnetic field of $H = 2000\,\text{Oe}$.
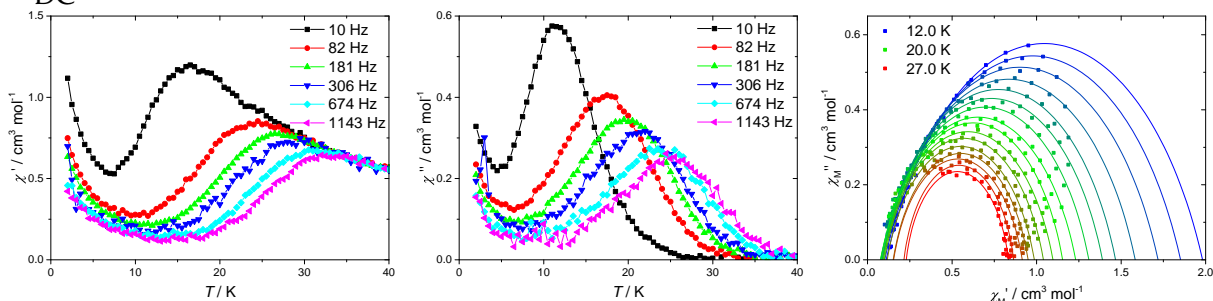
$H_{\mathrm{DC}} = 0\,\mathrm{Oe}$
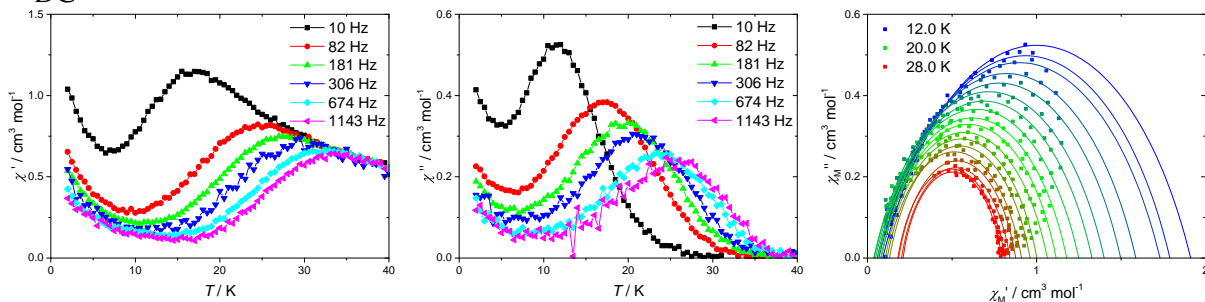
$H_{\mathrm{DC}} = 400\,\mathrm{Oe}$

$H_{\mathrm{DC}} = 1000\,\mathrm{Oe}$

Figure B.19: Temperature dependence of the in-phase (χ' **left**) and out-of-phase (χ'' **middle**) compo-
nent of the magnetic susceptibility as revealed by AC magnetic susceptibility measure-
ments on **22** with an AC field amplitude of 1 Oe applied at the frequencies given in the
graph and static magnetic fields H_{DC} of 0 (**top**), 400 (**middle**) and 1000 Oe (**bottom**) ap-
plied. Fitting of the data to a generalised Debye model (eq. (1.20)) to extract relaxation
times τ_T yields the Cole-Cole plots (**right**) in the temperature range given in the graph.